

Synthesis, Chemical Vapour Deposition and Structural Studies of Group 13 Alkoxides

This thesis is submitted in partial fulfilment of the requirements for the Degree of
Doctor of Philosophy (Chemistry)

Caroline Elizabeth Knapp

Supervised by Professor C. J. Carmalt

University College London
Christopher Ingold Laboratories,
20 Gordon Street,
WC1H 0AJ

2010

I, Caroline E. Knapp, confirm that the work presented in this thesis is my own.
Where information has been derived from other sources, I confirm that this has been indicated in the thesis.

Abstract

This work is concerned with the synthesis of precursors to group 13 oxide thin films, and the subsequent chemical vapour deposition (CVD) of group 13 mixed metal oxide films. Investigations into the mechanisms at work during their decomposition *via* various techniques including gas phase electron diffraction (GED) is also discussed.

A wide variety of group 13 alkoxides have been synthesised and characterised and described in this thesis. Significant findings support previous investigations showing the reaction of trialkyl group 13 complexes $[MR_3]$ with an excess of a donor functionalised alcohol does not yield a group 13 bis(alkoxide). However, compounds of the type $[Ga(OR')_nCl_{3-n}]$ ($n = 1, 2$) have been synthesised using direct routes from gallium amido precursors, which are also described herein. In addition a wide variety of novel group 13 precursors incorporating a mixture of ligands leading to enhanced properties, desirable for CVD are presented.

The gas phase structures of the dimethylalkoxygallanes, $[Me_2GaOCH_2CH_2NMe_2]_2$ and $[Me_2GaOCH_2CH_2OMe]_2$ have been obtained *via* gas-phase electron diffraction from studying the vapour produced upon heating. *Ab initio* molecular orbital calculations are presented for these compounds, as well as the gas phase structure of $[Me_2GaO^tBu]_2$. Only the monomeric forms $[Me_2GaOCH_2CH_2NMe_2]$ and $[Me_2GaOCH_2CH_2OMe]$ are observed in the gas phase with donor functionalised ligands, whereas the dimer $[Me_2GaO^tBu]_2$ remains intact in the gas phase.

Gallium oxide films were grown *via* AACVD using a variety of group 13 precursors. The films deposited were not oxygen deficient and little carbon contamination was observed, which is attributed to being a direct result of precursor design. Thin films of indium gallium oxide, and zinc gallium oxide were also produced from the *in situ* reactions of $InMe_3$, $GaMe_3$ and $HOCH_2CH_2OMe$ (for $Ga_xIn_{2-x}O_3$) and $ZnEt_2$, $GaMe_3$ and $HOCH_2CH_2OMe$ (for Ga_xZn_yO) *via* AACVD on silica substrates.

Acknowledgements

Firstly I would like to thank my supervisor, Prof. Claire J. Carmalt, for all of her encouragement, support and guidance. Also, thanks go to my second supervisor Prof. Paul F. McMillan for the long discussions and advice.

I would like to make special thanks to Dr. Geoff Hyett and Dr. Chris Blackman for their endless patience and advice, ranging from Rietveld refinement to XPS analysis and more. Also thanks go to Dr. David Pugh and Dr. Charlie Dunnill for help in and around the lab.

I thank again Dr. David Pugh, Prof. Derek Tocher and Dr. Sarah Barnett for carrying out all of the X-ray crystallography. I thank Dr. Abil Aliev for his help elucidating my NMR spectra. I thank Dr. Steve Firth for useful discussions about thermal analysis. I thank Lisa Harris and John Hill for mass spectra and Jill Maxwell for elemental analysis. I am extremely grateful to Kevin Reeves for WDX, EDXA and SEM. I would also like to thank Rob Palgrave, who recorded the X-ray photoelectron spectra. Thanks go to Prof. Franco Cacialli and Yong Shin for AFM and Kelvin probe measurements.

Mr. Dave Knapp, Mr. Mike Hill, Mr. Dave Ladd and Mr. Joe Nolan I will always be grateful for your invaluable advice and technical support. Also Dr. Derek Wann and Prof. David Rankin at the University of Edinburgh, who made my stay academically rewarding and enjoyable, thank you.

To name a few of the special people, in chronological order, I thank: Dr. Christina Baskaran, Dr. Siama Basharat, Dr. Naima Narband, Dr. Nicolas Boscher, Dr. Stephen Potts, Dr. Paolo Melgari, Dr. Kris Page, Dr. Russell Binions, Leah Pemberton, John Kilmartin, Dr. Ashkan Salamat, Amy Poole, Luanne Thomas, Tegan Thomas, Rosie Coates, Rachael Hazael, Mathew Waugh, Ross Colman, Colin Crick, Leanne Bloor, Sanjay Sathasivam, Savio Moniz, Davinder Bhachu and all members of the lab past and present.

Finally I would like to thank my parents, my brother Edward and dearest friend Gary: without their love and support I would not have been able to complete this thesis.

Contents

Title Page	<i>i</i>
Declaration	<i>ii</i>
Abstract	<i>iii</i>
Acknowledgements	<i>iv</i>
Contents	<i>v</i>
List of Figures	<i>xii</i>
List of Tables	<i>xvi</i>
List of Schemes	<i>xviii</i>
List of Abbreviations	<i>xx</i>
Chapter 1: Introduction	1
1.1 Deposition of films	2
1.1.1 Chemical Vapour Deposition	3
1.1.1.1 Single-Source Chemical Vapour Deposition	5
1.1.1.2 Aerosol-Assisted Chemical Vapour Deposition	6
1.2 Precursors to CVD	7
1.3 Group 13 oxides	10
1.3.1 Gallium oxide	10
1.3.1.1 Structure	10
1.3.1.2 Application	12
1.3.2 Indium oxide	13
1.3.2.1 Structure	13
1.3.2.2 Application	14
1.4 Overview	15
1.5 References	16
Chapter 2: Synthesis of Group 13 Alkoxides	19
2.1 Introduction	19
2.1.1 Gallium(III) and indium(III) mono(alkoxides)	21
2.1.2 Gallium(III) and indium(III) bis(alkoxides)	26
2.1.3 Gallium(III) and indium(III) tris(alkoxides)	30

2.2 Results and discussion	33
2.2.1 Gallium(III) and Indium(III) mono- and bis- (alkoxides)	35
2.2.1.1 Reaction of GaMe ₃ with HOCH ₂ CH ₂ OMe	35
2.2.1.2 Reaction of GaMe ₃ with HOCH ₂ CH ₂ NMe ₂	36
2.2.1.3 Reaction of GaMe ₃ with HOC(CH ₃) ₂ CH ₂ OMe	37
2.2.1.3.1 X-Ray crystallographic study of	39
[Me ₂ Ga(OC(CH ₃) ₂ CH ₂ OMe)] ₂	
2.2.1.4 Reaction of InMe ₃ with HOCH(CH ₃)CH ₂ OMe	41
2.2.1.4.1 X-Ray crystallographic study of	42
[Me ₂ In(OCH(CH ₃)CH ₂ OMe)] ₂	
2.2.1.5 The reaction of GaMe ₃ with HOCH(CF ₃) ₂	44
2.2.2 Gallium(III) mono- and bis- (alkoxides) via amine- alcohol exchange	45
2.2.2.1 Reaction of GaCl ₃ with LiNMe ₂	46
2.2.2.2 Reaction of GaCl ₃ with 2 equivalents of LiNMe ₂	47
2.2.2.3 Reaction of 6 with HOC(CH ₃) ₂ CH ₂ OMe	48
2.2.2.4 Reaction of 7 with 2 equivalents of HOCH(CH ₃)CH ₂ NMe ₂	48
2.2.2.5 Reaction of 7 with 2 equivalents of HOCH ₂ CH ₂ NMe ₂	49
2.2.3 Unsymmetrical gallium(III) bis(alkoxides)	50
2.2.3.1 Reaction of GaCl ₃ with LiN(SiMe ₃) ₂	52
2.2.3.2 Reaction of 11 with HOCH(CH ₃)CH ₂ NMe ₂	52
2.2.3.3 Reaction of 11 with HOCH ₂ CH ₂ NMe ₂	53
2.2.3.3.1 X-ray crystallographic study of	54
[Cl ₂ Ga(OCH ₂ CH ₂ NMe ₂)] ₂	
2.2.3.4 Reaction of 11 with HOCH ₂ CH ₂ OMe	56
2.2.3.5 Reaction of 13 with LiN(SiMe ₃) ₂	57
2.2.3.6 Reaction of 14 with LiN(SiMe ₃) ₂	58
2.2.3.7 Reaction of 16 with tertiary butanol	60
2.2.3.7.1 X-ray crystallographic analysis of [Me(Cl)Ga(O ^t Bu)] ₂	61
2.2.3.8 Reaction of 11 with HOCH ₂ CH ₂ NMe ₂	63
2.2.3.8.1 X-ray crystallographic study of	65
[MeGa(OCH ₂ CH ₂ NMe ₂)] ₂	
2.2.3.9 Reaction of 11 with 1 equivalent of HOCH ₂ CH ₂ NMe ₂	67

2.2.3.9.1 X-ray crystal study of [(MeGa{Cl}(N(SiMe ₃) ₂))(μ -OCH ₂ CH ₂ NMe ₂ (Ga){Me}(Cl))]	70
2.2.3.10 Summary of synthetic routes followed in section 2.2.3	72
2.2.4 Unsymmetrical indium(III) bis(alkoxides)	73
2.2.4.1 Reaction of InCl ₃ with LiN(SiMe ₃) ₂	75
2.2.4.2 Reaction of 20 with HOCH ₂ CH ₂ NMe ₂	75
2.2.4.3 Reaction of 20 with HOCH(CH ₃)CH ₂ OMe	76
2.2.4.3.1 X-ray structure of [Me{Cl}In(OCH(CH ₃)CH ₂ OMe)] ₂	77
2.2.4.4 Reaction of 20 with HOCH(CH ₂ NMe ₂) ₂	79
2.2.4.5 Reaction of 20 with HOCH ₂ CH ₂ OMe	80
2.2.4.6 Reaction of 21 with LiN(SiMe ₃) ₂	81
2.2.4.7 Reaction of 23 with LiN(SiMe ₃) ₂	82
2.2.4.8 Reaction of 25 with HO ^t Bu	83
2.2.4.9 Summary of synthetic routes followed in section 2.2.4	84
2.2.5 Gallium(III) and indium(III) tris(alkoxides)	85
2.2.5.1 Reaction of GaCl ₃ with barium isopropoxide	86
2.2.5.2 Reaction of InCl ₃ with barium isopropoxide	87
2.3 Conclusions	88
2.4 Experimental	90
2.4.1 General procedures	90
2.4.2 Physical measurements	90
2.4.3 Synthesis of precursors	91
2.4.3.1 Synthesis of [MeGa(OCH ₂ CH ₂ OMe)] ₂ (1)	91
2.4.3.2 Synthesis of [MeGa(OCH ₂ CH ₂ NMe ₂) ₂] (2)	91
2.4.3.3 Synthesis of [Me ₂ Ga(OC(CH ₃) ₂ CH ₂ OMe)] ₂ (3)	91
2.4.3.4 Synthesis of [Me ₂ In(OCH(CH ₃)CH ₂ OMe)] ₂ (4)	92
2.4.3.5 Synthesis of [Me ₂ Ga(OCH(CF ₃) ₂)] ₂ (5)	92
2.4.3.6 Synthesis of [Cl ₂ Ga(NMe ₂) ₂] (6)	93
2.4.3.7 Synthesis of [ClGa(NMe ₂) ₂] (7)	93
2.4.3.8 Synthesis of [Cl ₂ Ga(OC(CH ₃) ₂ CH ₂ OMe)] ₂ (8)	93
2.4.3.9 Synthesis of [ClGa(OCH(CH ₃)CH ₂ NMe ₂) ₂] (9)	94
2.4.3.10 Synthesis of [ClGa(OCH ₂ CH ₂ NMe ₂) ₂] (10)	94
2.4.3.11 Synthesis of [Me(Cl)GaN(SiMe ₃) ₂] (11)	94

2.4.3.12 Synthesis of $[\text{Cl}(\text{Me})\text{Ga}(\text{OCH}(\text{CH}_3)\text{CH}_2\text{NMe}_2)]_2$ (12)	95
2.4.3.13 Synthesis of $[\text{Cl}_2\text{Ga}(\text{OCH}_2\text{CH}_2\text{NMe}_2)]_2$ (13)	95
2.4.3.14 Synthesis of $[\text{Cl}(\text{Me})\text{Ga}(\text{OCH}_2\text{CH}_2\text{OMe})]_2$ (14)	96
2.4.3.15 Synthesis of $[\text{ClGa}\{\text{N}(\text{SiMe}_3)_2\}(\text{OCH}_2\text{CH}_2\text{NMe}_2)]_2$ (15)	96
2.4.3.16 Synthesis of $[\text{MeGa}\{\text{N}(\text{SiMe}_3)_2\}(\text{OCH}_2\text{CH}_2\text{OMe})]_2$ (16)	96
2.4.3.17 Synthesis of $[\text{Cl}(\text{Me})\text{Ga}(\text{O}^i\text{Bu})]_2$ (17)	97
2.4.3.18 Synthesis of $[\text{MeGa}(\text{OCH}_2\text{CH}_2\text{NMe}_2)_2]$ (18)	97
2.4.3.19 Synthesis of $[(\text{Ga}(\text{Cl})(\text{Me})(\text{N}(\text{SiMe}_3)_2))(\mu_2\text{-OCH}_2\text{CH}_2\text{NMe}_2(\text{Ga})(\text{Cl})(\text{Me}))]$ (19)	97
2.4.3.20 Synthesis of $[\text{Me}(\text{Cl})\text{InN}(\text{SiMe}_3)_2]_2$ (20)	98
2.4.3.21 Synthesis of $[\text{Me}(\text{Cl})\text{In}(\text{OCH}_2\text{CH}_2\text{NMe}_2)]_2$ (21)	98
2.4.3.22 Synthesis of $[\text{Me}(\text{Cl})\text{In}(\text{OCH}(\text{CH}_3)\text{CH}_2\text{OMe})]_2$ (22)	99
2.4.3.23 Synthesis of $[\text{Me}(\text{Cl})\text{In}(\text{OCH}(\text{CH}_2\text{NMe}_2))]_2$ (23)	99
2.4.3.24 Synthesis of $[\text{Me}(\text{Cl})\text{In}(\text{OCH}_2\text{CH}_2\text{OMe})]_2$ (24)	99
2.4.3.25 Synthesis of $[\text{MeIn}\{\text{N}(\text{SiMe}_3)_2\}(\text{OCH}_2\text{CH}_2\text{NMe}_2)]_2$ (25)	100
2.4.3.26 Synthesis of $[\text{MeIn}\{\text{N}(\text{SiMe}_3)_2\}(\text{OCH}(\text{CH}_2\text{NMe}_2)_2)]_2$ (26)	100
2.4.3.27 Synthesis of $[\text{Me}\{\text{O}^i\text{Bu}\}\text{In}(\text{OCH}_2\text{CH}_2\text{NMe}_2)]_2$ (27)	101
2.4.3.28 Synthesis of $[\text{Ga}(\text{O}^i\text{Pr})_3]_n$ (28)	101
2.4.3.29 Synthesis of $[\text{InO}^i\text{Pr}]_5(\mu_2\text{-O}^i\text{Pr})_4(\mu_3\text{-O}^i\text{Pr})_4(\mu_5\text{-O})]$ (29a)	101
2.5 References	103
Chapter 3: Gas Phase Electron Diffraction and Thermal Analysis	107
of Group 13 Alkoxides	
3.1 Introduction	107
3.1.1 Gas Phase Electron Diffraction	109
3.1.1.1 Background	110
3.1.1.2 Instrumentation	112
3.1.1.3 Data Analysis	115
3.1.1.4 Limitations of GED – and some solutions	115
3.1.1.5 Experimental equilibrium structures	118
3.1.1.6 <i>Ab initio</i> molecular orbital theory	119
3.1.1.7 Simplification of the Hamiltonian operator	120
3.1.1.8 Simplification of the molecular wavefunction	121

3.1.1.9 Density functional theory	122
3.1.1.10 Structural refinement in practice	123
3.1.2 Mechanistic studies in CVD	124
3.1.2.1 Coherent anti-stokes Raman scattering (CARS)	124
3.1.2.2 Density functional theory	126
3.1.3 Thermal Decomposition Studies	127
3.1.3.1 Background	127
3.1.3.2 Decomposition pathway	128
3.2 Results and Discussion	128
3.2.1 Gas phase electron diffraction studies	129
3.2.1.1 The reaction of GaMe ₃ with HOCH ₂ CH ₂ NMe ₂	129
3.2.1.2 The reaction of GaMe ₃ with HOCH ₂ CH ₂ OMe	134
3.2.1.3 The reaction of GaMe ₃ with HO ^t Bu	140
3.2.2 Thermal decomposition analysis	144
3.2.2.1 TGA of [Me ₂ In(OCH(CH ₃)CH ₂ OMe)] ₂ (4)	144
3.2.2.2 TGA analysis of [Cl(Me)Ga(OCH ₂ CH ₂ OMe)] ₂ (14)	145
3.2.2.3 TGA analysis of [Cl(Me)In(OCH ₂ CH ₂ NMe ₂)] ₂ (21)	146
3.2.2.4 Thermal analysis of [Me ₂ Ga(OCH ₂ CH ₂ NMe ₂)] ₂ (30)	147
3.2.2.5 Thermal analysis of [Me ₂ GaOCH ₂ CH ₂ OMe] ₂ (31)	148
3.2.2.6 Thermal analysis of [Me ₂ GaO ^t Bu] ₂ (32)	149
3.3 Conclusions	150
3.4 Experimental	151
3.4.1 General procedures	151
3.4.2 Physical measurements	151
3.4.3 Synthesis of compounds	152
3.4.3.1 Synthesis of [Me ₂ GaOCH ₂ CH ₂ NMe ₂] ₂ (30)	152
3.4.3.2 Synthesis of [Me ₂ GaOCH ₂ CH ₂ OMe] ₂ (31)	152
3.4.3.3 Synthesis of [Me ₂ GaO ^t Bu] ₂ (32)	153
3.4.4 GED experimental	153
4.4.4.1 Quantum chemical studies	153
4.4.4.2 Gas-phase electron diffraction	154
3.5 References	156

Chapter 4: Chemical Vapour Deposition of Metal Oxide Thin	159
Films	
4.1 Introduction	159
4.1.1 Chemical Vapour Deposition	159
4.1.2 Gallium indium oxide	161
4.1.3 Gallium zinc oxide	163
4.2 Results and discussion	165
4.2.1 Gallium oxide films	165
4.2.1.1 Energy dispersive X-ray analysis	167
4.2.1.2 Wavelength dispersive X-ray analysis	167
4.2.1.3 Scanning electron microscopy	167
4.2.1.4 X-ray Photoelectron Spectroscopy	167
4.2.1.5 X-ray Powder Diffraction	168
4.2.1.6 Summary	169
4.2.2 Gallium indium oxide films	169
4.2.2.1 Energy dispersive X-ray analysis	170
4.2.2.2 Wavelength dispersive X-ray analysis	170
4.2.2.3 Scanning electron microscopy	171
4.2.2.4 X-ray Photoelectron Spectroscopy	174
4.2.2.5 X-ray Powder Diffraction	178
4.2.2.6 Atomic Force Microscope Images	180
4.2.2.7 Kelvin Probe measurement	181
4.2.2.8 Summary	181
4.2.3 Gallium zinc oxide films	182
4.2.3.1 Energy dispersive X-ray analysis	183
4.2.3.2 Wavelength dispersive X-ray analysis	184
4.2.3.3 Scanning electron microscopy	184
4.2.3.4 X-ray Photoelectron Spectroscopy	187
4.2.3.5 X-ray Powder Diffraction	191
4.2.3.6 Summary	193
4.3 Conclusions	194

4.4 Experimental	194
4.4.1.1 General procedures - synthesis	195
4.4.1.2 General procedures - AACVD	195
4.4.1.3 AACVD reaction of GaMe ₃ and HOCH ₂ CH ₂ OMe	197
4.4.1.4 AACVD reaction of InMe ₃ , GaMe ₃ and HOCH ₂ CH ₂ OMe	197
4.4.1.5 AACVD reaction of GaMe ₃ , ZnEt ₂ and HOCH ₂ CH ₂ OMe	197
4.5 References	200
Chapter 5: Conclusions	204
5.1 Chapter 2	204
5.2 Chapter 3	205
5.3 Chapter 4	206
5.4 Summary	207
Appendices	209
A.1 List of Publications	210
A.2 Crystal data for [Me ₂ Ga(OC(CH ₃) ₂ CH ₂ OMe)] ₂ (3)	211
A.3 Crystal data for [Me ₂ In(OCH(CH ₃)CH ₂ OMe)] ₂ (4)	216
A.4 Crystal data for [Cl ₂ Ga(OCH ₂ CH ₂ NMe ₂)] ₂ (13)	221
A.5 Crystal data for [Me{Cl}Ga(O ^t Bu)] ₂ (17)	225
A.6 Crystal data for [MeGa(OCH ₂ CH ₂ NMe ₂)] ₂ (18)	229
A.7 Crystal data for [(Ga(Me){Cl}{N(SiMe ₃) ₂ })(μ ₂ - OCH ₂ CH ₂ NMe ₂)(Ga){Me}{Cl}] (19)	234
A.8 Crystal data for [Me{Cl}In(OCH(CH ₃)CH ₂ OMe)] ₂ (22)	240
A.9 Supplementary data for all gas phase electron diffraction experiments. (30a , 31a , 32)	244

List of Figures

Chapter 1: Introduction

- Fig. 1.1:** Overview of the CVD process. 4
- Fig. 1.2:** Molecular orbital diagram showing the different orbital interactions possible between a group 13 metal and its respective alkoxide ligand. 7
- Fig. 1.3:** Centro-symmetric M_2O_2 ring produced with a monofunctional R' group, A; and when a donor functionalised ligand, L, is used, B. 8
- Fig. 1.4:** The arrangement of Ga and O atoms in β - Ga_2O_3 (magenta spheres indicate Ga, red spheres indicate O). 12
- Fig. 1.5:** The arrangement of In and O atoms in In_2O_3 (Purple spheres indicate In, red spheres indicate O). 14

Chapter 2: Synthesis of Group 13 Alkoxides

- Fig. 2.1:** Representation of the formation of the M_2O_2 ring in the formation in mono(alkoxides). 22
- Fig. 2.2:** Structure for $[Me_2Ga(OC(CF_3)_2CH_2NRR')]_2$ ($R = H, R' = Me, R = H, R' = tBu, R = R' = Me$). 23
- Fig. 2.3:** Structure for $[Et_2Ga(OCH_2CH_2NMe_2)]_2$. 24
- Fig. 2.4:** Structure of $[Me_2In(OCH(CH_3)CH_2OMe)]_2$ and $[Me_2In(OCH(CH_2NMe_2)_2)]_2$. 25
- Fig. 2.5:** Monomeric structure of $[Me_2Ga(OR)]$ ($R = CH_2CH_2NHMe, CH_2CH_2NH^tBu, CH_2CH_2CH_2NHMe, CH_2CH_2CH_2NH^tBu$, and dimeric structure of $[^tBu_2Ga(OR)]_2$ ($R = CH_2CH_2NH^tBu, CH_2CH_2CH_2NH^tBu$). 25
- Fig. 2.5:** X-Ray crystal structure of $[Me_2Ga(OC(CH_3)_2CH_2OMe)]_2$ (**3**). 40
- Fig. 2.6:** X-Ray crystal structure of $[Me_2In(OCH(CH_3)CH_2OMe)]_2$ (**4**). 43
- Fig. 2.7:** X-ray crystal structure of $[Cl_2Ga(OCH_2CH_2NMe_2)]_2$ (**13**). 55
- Fig. 2.8:** X-ray crystal structure of $[Me(Cl)Ga(O^tBu)]_2$ (**17**). 62
- Fig. 2.9:** X-ray crystal structure of $[MeGa(OCH_2CH_2NMe_2)_2]$ (**18**). 66
- Fig. 2.10:** X-ray crystal structure of $[MeGa(Cl)\{N(SiMe_3)_2\}(\mu_2-OCH_2CH_2NMe_2)Ga(Me)\{Cl\}]$ (**19**). 71

Fig. 2.11: X-ray crystal structure of $[\text{Me}(\text{Cl})\text{In}(\text{OCH}(\text{CH}_3)\text{CH}_2\text{OMe})]_2$ (22).	78
Fig. 2.12: The proposed structure of (28) exhibited here as a tetramer.	87
Fig. 2.13: Proposed structure of $[\text{InO}^i\text{Pr})_5(\mu_2\text{-O}^i\text{Pr})_4(\mu_3\text{-O}^i\text{Pr})_4(\mu_5\text{-O})]$ (30).	88

Chapter 3: Gas Phase Electron Diffraction and Thermal Analysis of Group 13 Alkoxides

Fig. 3.1: Electron scattering data recorded on Kodak Electron Image film.	111
Fig. 3.2: Schematic diagram of a typical gas-phase electron diffraction apparatus.	112
Fig. 3.3: Shape of rotating sector used in Edinburgh.	113
Fig. 3.4 Application of two nozzle-to-film distances, (<i>a</i>) short and (<i>b</i>) long.	114
Fig. 3.5 The phase effect, caused by differences in wave contraction as the electron approaches a light atom (A) and heavy atom (B).	116
Fig. 3.6: Schematic diagram showing the vibration of a tri-atomic molecule.	117
Fig. 3.7: Comparison of a Gaussian function with an atomic radial function.	122
Fig. 3.8: Molecular structure of 30a including the atom numbering scheme.	132
Fig. 3.9: Radial-distribution curve from the GED refinement of 30a .	133
Fig 3.10: Molecular structure of 31a including the atom numbering scheme	137
Fig. 3.11: Radial-distribution curve from the GED refinement of 31a .	138
Fig. 3.12: Molecular structure of 32 including the atom numbering scheme.	142
Fig 3.13: Radial-distribution curve from the GED refinement of 32 . (Blue line shows experimental data, green sticks show model and red line shows difference).	143
Fig. 3.14: TGA of $[\text{Me}_2\text{In}(\text{OCH}(\text{CH}_3)\text{CH}_2\text{OMe})]_2$ (4).	145
Fig. 3.15: TGA/DSC of $[\text{Cl}(\text{Me})\text{Ga}(\text{OCH}_2\text{CH}_2\text{OMe})]_2$ (14).	146
Fig 3.16: TGA/DSC of $[\text{Cl}(\text{Me})\text{In}(\text{OCH}_2\text{CH}_2\text{NMe}_2)]_2$ (21).	147
Fig 3.17: TGA/DSC for $[\text{Me}_2\text{Ga}(\text{OCH}_2\text{CH}_2\text{NMe}_2)]_2$ (30).	148
Fig 3.18: TGA/DSC for $[\text{Me}_2\text{Ga}(\text{OCH}_2\text{CH}_2\text{OMe})]_2$ (31)	149
Fig 3.19: TGA/DSC for $[\text{Me}_2\text{GaO}^i\text{Bu}]_2$ (32).	150

Chapter 4: Chemical Vapour Deposition of Metal Oxide Thin Films

Fig 4.1: SEM images the film produced from the AACVD of GaMe ₃ and HOCH ₂ CH ₂ OMe at 450 °C.	167
Fig. 4.2: XPS of Ga 2p peaks for a film deposited at 450°C by AACVD form the <i>in situ</i> reaction of GaMe ₃ and excess HOCH ₂ CH ₂ NMe ₂ .	168
Fig. 4.3: SEM images of InGaO film on glass, deposition carried out at 350°C, before annealing.	171
Fig. 4.4: SEM images of InGaO film on glass, deposition carried out at 450 °C, films were annealed at 550 °C.	172
Fig 4.5: SEM images of InGaO film on quartz, deposition carried out at 450 °C, annealed overnight at 1000 °C.	173
Fig. 4.6: SEM images of InGaO film on quartz, deposition carried out at 450 °C, annealed for 1 hour at 1000°C.	174
Fig 4.7: XPS of In 3d peaks for a film deposited at 450 °C by AACVD form the <i>in situ</i> reaction of GaMe ₃ , InMe ₃ and excess HOCH ₂ CH ₂ OMe.	175
Fig.4.8: XPS of Ga 2p peaks for a film deposited at 450 °C by AACVD form the <i>in situ</i> reaction of GaMe ₃ , InMe ₃ and excess HOCH ₂ CH ₂ OMe.	176
Fig 4.9: XPS of O 1s peaks for a film deposited at 450°C by AACVD form the <i>in situ</i> reaction of GaMe ₃ , InMe ₃ and excess HOCH ₂ CH ₂ OMe.	177
Fig 4.10: XPS of all regions for a thin film deposited at 450 °C by AACVD form the <i>in situ</i> reaction of GaMe ₃ , InMe ₃ and excess HOCH ₂ CH ₂ OMe.	178
Fig 4.11: XRD pattern for film deposited on quartz and annealed at 1000 °C.	179
Fig. 4.12: Field size AFM image.	180
Fig. 4.13: SEM images of zinc gallium oxide film on quartz, deposition carried out at 550 °C, annealed overnight at 1000 °C.	185
Fig. 4.14: SEM images of zinc gallium oxide film on quartz, deposition carried out at 450°C, annealed overnight at 1000°C.	186
Fig. 4.15: SEM images of features on a zinc gallium oxide film on quartz, deposition carried out at 450 °C, annealed overnight at 1000 °C.	187
Fig. 4.16: XPS of Ga 2p peaks for a film deposited at 450 °C by AACVD form the <i>in situ</i> reaction of GaMe ₃ , ZnEt ₂ and excess HOCH ₂ CH ₂ OMe in toluene.	188
Fig. 4.17: XPS of Zn 2p peaks for a film deposited at 450 °C by AACVD	189

form the *in situ* reaction of GaMe₃, ZnEt₂ and excess HOCH₂CH₂OMe in toluene.

Fig 4.18: XPS of all regions for a thin film deposited at 450 °C by AACVD **191**

form the *in situ* reaction of GaMe₃, ZnEt₂ and excess HOCH₂CH₂OMe in toluene.

Fig 2.19: XRD pattern for film deposited on quartz and annealed at 1000 °C. **192**

Fig 4.20: AACVD apparatus, the deposition chamber. **195**

Fig 4.21: AACVD apparatus, the humidifier and bypass valve. **197**

List of Tables

Chapter 1: Introduction

Table 1.1: Crystal structures of gallium oxide	11
---	-----------

Chapter 2: Synthesis of Group 13 Alkoxides

Table 2.1: Selected bond lengths (Å) and angles (°) for [Me ₂ GaOC(CH ₃) ₂ CH ₂ OMe] ₂ (3).	39
Table 2.2: Selected bond lengths (Å) and angles (°) for Me ₂ InOCH(CH ₃)CH ₂ OMe (4).	42
Table 2.3: Selected bond lengths (Å) and angles (°) for [Cl ₂ Ga(OCH ₂ CH ₂ NMe ₂)] ₂ (13).	54
Table 2.4: Selected bond lengths (Å) and angles (°) for [Me(Cl)Ga(O ^t Bu)] ₂ (17).	61
Table 2.5: Selected bond lengths (Å) and angles (°) for [MeGa(OCH ₂ CH ₂ NMe ₂) ₂] (18).	65
Table 2.6: Selected bond lengths (Å) and angles (°) for [MeGa(Cl){N(SiMe ₃) ₂ }(μ ₂ -OCH ₂ CH ₂ NMe ₂)Ga(Me){Cl}] (19).	70
Table 2.7: Selected bond lengths (Å) and angles (°) for [Me{Cl}In(OCH(CH ₃)CH ₂ OMe)] ₂ (22).	77

Chapter 3: Gas Phase Electron Diffraction and Thermal Analysis of Group 13 Alkoxides

Table 3.1: GED-refined parameters (r_{h1}) for Me ₂ GaOCH ₂ CH ₂ NMe ₂ (30a).	131
Table 3.2: Selected calculated parameters and GED-refined parameters for Me ₂ GaOCH ₂ CH ₂ OMe (31a).	136
Table 3.3: Selected calculated parameters and GED-refined parameters for C _{2h} -symmetric [Me ₂ GaO ^t Bu] ₂ (32).	141
Table 3.4: Nozzle-to-film distances (mm), weighting functions (nm ⁻¹), scale factors, correlation parameters and electron wavelengths (pm) used in the electron diffraction studies of (30 – 32).	155

Chapter 4: Chemical Vapour Deposition of Metal Oxide Thin Films

- Table 4.1:** Deposition conditions and analysis of the films grown from the AACVD of GaMe₃, InMe₃ and ROH (R = CH₂CH₂OMe). **170**
- Table 4.2:** Deposition conditions and analysis of the films grown from the AACVD of GaMe₃, ZnEt₂ and ROH (R = CH₂CH₂OMe). **183**

List of Schemes

Chapter 2: Synthesis of Group 13 Alkoxides

Scheme 2.1: Reaction of GaMe ₃ and 2,2'-dihydroxy-1,1'-binaphthyl	27
Scheme 2.2: Reaction of GaCl ₃ and NaOR (R= C(CF ₃) ₂ CH ₂ NMe ₂ , C(CF ₃) ₂ CH ₂ C(CH ₃)NMe).	29
Scheme 2.3: Synthetic route for the formation of [MeIn(O ^t Bu) ₂] ₂ .	30
Scheme 2.4: Route 3 – Synthetic route for the formation of group 13 bisalkoxides.	34
Scheme 2.5: Synthesis of complexes of the type [Me ₂ M(μ-OR)] ₂ .	38
Scheme 2.6: Synthesis of gallium(III) mono and bis(alkoxides) using an amine-alcohol exchange reaction based on Route 2.	46
Scheme 2.7: Synthetic route for the formation of gallium(III) bis(alkoxides)	51
Scheme 2.8: Series of reactions resulting in the production of the monomeric compound [MeGa(OCH ₂ CH ₂ NMe ₂) ₂] (18)	64
Scheme 2.9: Series of reactions to produce the intermediate compound [(MeGa(Cl){N(SiMe ₃) ₂ }(μ ₂ -OCH ₂ CH ₂ NMe ₂)Ga(Me){Cl}] (19).	68
Scheme 2.10: Proposed mechanism for the formation of [(MeGa(Cl){N(SiMe ₃) ₂ }(μ ₂ -OCH ₂ CH ₂ NMe ₂)Ga(Me){Cl}] (19).	69
Scheme 2.11: Summary of the synthetic routes followed in section 2.3.3	73
Scheme 2.12: Synthetic route for the formation of indium(III) bis(alkoxides)	74
Scheme 2.13: Summary of synthetic routes used in section 2.2.4	85

Chapter 3: Gas Phase Electron Diffraction and Thermal Analysis of Group 13 Alkoxides

Scheme 3.1: Preparation of [Me ₂ GaOCH ₂ CH ₂ NMe ₂] ₂ (30) and [Me ₂ GaOCH ₂ CH ₂ NMe ₂] (30a).	131
Scheme 3.2: Preparation of [Me ₂ GaOCH ₂ CH ₂ NMe ₂] ₂ (31) and [Me ₂ GaOCH ₂ CH ₂ NMe ₂] (31a)	136

**Chapter 4: Chemical Vapour Deposition of Metal Oxide Thin
Films**

Scheme 4.1: Proposed route to gallium oxide thin films.

166

List of Abbreviations

Å	Angstrom
AACVD	Aerosol assisted chemical vapour deposition
APCVD	Atmospheric pressure chemical vapour deposition
Ar	Aryl
Calc.	Calculated
CARS	Coherent Anti-Stokes Raman Spectroscopy
CI	Chemical Ionisation
cm	Centimetre
CVD	Chemical vapour deposition
Cy	Cyclohexyl
d	Doublet
δ	Chemical shift / ppm
DSC	Differential scanning calorimetry
Et	Ethyl
EDXA	Energy dispersive X-ray analysis
eV	electron volts
g	Gram
GED	Gas Phase Electron Diffraction
h	Hour
J	Coupling constant
ⁱ Bu	iso-butyl
ⁱ Pr	iso-propyl
ⁿ Bu	Normal-butyl
^t Bu	Tertiary-butyl
IR	Infra-red
LPCVD	Low pressure chemical vapour deposition
m	Medium (in IR spectra)
Me	Methyl
mmol	Millimole
MOCVD	Metal-Organic Chemical Vapour Deposition

MS	Mass spectrometry
Py	Pyrdine
ⁿ Pr	Normal-propyl
NMR	Nuclear Magnetic Resonance
PECVD	Plasma enhanced chemical vapour deposition
Ph	Phenyl
ppm	Parts per million
PVD	Physical vapour deposition
Q	Quartet (in NMR spectra)
quin	Quintet (in NMR spectra)
R	Organic substituent
SEM	Scanning electron microscopy
S	Singlet (in NMR spectra)
S	Strong (in IR spectra)
Sept	Septet (NMR)
SiMe ₃	Trimethyl silyl
T	Triplet
THF	Tetrahydrofuran
TGA	Thermal gravimetric analysis
tmp	Trimethylpyridine
TFP	Thin Film Transistor
UV	Ultraviolet
vis	Visible
vs	Very strong
vw	Very weak
W	Weak
WDX	Wavelength dispersive analysis
XRD	X-ray diffraction
XPS	X-ray photoelectron spectroscopy

Chapter 1

Introduction

In recent years there has been increasing interest in gallium and indium alkoxides for use as precursors to group 13 oxide thin films. These materials find applications as gas sensors, amorphous oxide semiconductors within thin film transistor (TFT) technology, as photoelectric coatings and as transparent conducting coatings. Gallium and indium alkoxides have been shown to act as excellent precursors to their oxides *via* decomposition processes, at relatively low temperature, using chemical vapour deposition (CVD) to form thin films.

The aim of this work is to synthesise and characterise a range of gallium and indium alkoxide complexes incorporating donor-functionalised ligands. These group 13 alkoxides are ideal for use in aerosol-assisted (AA)CVD due to their good solubilities in a wide range of organic solvents. This thesis attempts to exploit the full potential of CVD by tailoring the properties of the precursor in order to optimise process parameters, such as deposition temperature, layer purity, uniformity and evaporation temperature. Whilst the initial aim of this work was to develop a range of group 13 alkoxide compounds, the mechanisms at work during decomposition of precursors was

also investigated *via* various techniques including gas phase electron diffraction (GED), and then subsequent CVD was carried out.

1.1. Deposition of thin films

The deposition of thin films is a relatively modern science, having only been explored in the past fifty years with expansive development in the last twenty. As it stands currently there are a huge variety of thin film deposition techniques readily available. Arguably the most popular methods of thin film deposition are CVD, atomic layer deposition (ALD) and physical vapour deposition (PVD).

There are a variety of factors to consider before choosing a method, and this choice will often depend on the properties of the desired film. Additionally, the choice of precursor and precursor source will be important decisions to make and are directly linked to the initial choice of deposition method.

The films produced can range from amorphous to epitaxial or polycrystalline in structure with the thickness ranging from a few microns in thickness down to a few atoms. The thin films can be described as a solid layer of a material, adhered to a substrate exhibiting different properties to those of the substrate, which has direct implications in making these products technologically important materials. As already alluded to there are several routes towards these thin films, solution phase techniques include dip coating, spraying and sol gel methodology. However, vapour phase routes are now increasingly being employed to prepare high quality thin films, and it is these techniques that will be discussed exclusively in this thesis.

There are a large range of reactors and precursor delivery systems currently available, these variations are a direct result of developments in CVD which have arisen out of the requirements of society. The developments are often made more rapidly when the current technique is proving problematic for production of the desired films. For example, when coating multiple samples in semiconductor devices or in scaling up when coating large surface areas, such as large scale functional coatings on glass.¹⁻⁴

An extensive range of materials are produced using CVD processes with application in several areas including; microelectronics, optoelectronics, protective, decorative and optical coatings.

1.1.1. Chemical Vapour Deposition

Chemical vapour deposition is essentially the formation of a thin film on a substrate, of varying description, by a chemical reaction of vapour phase precursors.^{5,6} The reaction in these instances occurs in the gas-phase, which is what distinguishes CVD from other physical vapour deposition processes, such as evaporation and reactive sputtering. With CVD the chemical reactions of precursors occur both in the gas phase and on the substrate, as outlined below. This thesis presents a study in metal-organic CVD (MOCVD) in that it utilizes metal-organic precursors. In the strictest sense organometallic compounds contain a direct σ or π metal to carbon bond, but in most instances concerning MOCVD the term ‘metal-organic’ is used to include precursors containing metal -oxygen, or -nitrogen bonds, which incorporates metal alkoxides, metal β - diketonates and metal alkylamides.

In a general overview of the CVD process, one or more of the aforementioned volatile precursors are transported in the gas phase into the reaction chamber. This is achieved either by sublimation or evaporation of the precursors *via* heating and introduction to a vacuum or bubbling an inert carrier gas through the precursor mixture. Once in the reaction chamber a number of gas phase reactions can occur, although little is known with respect to the variations in ‘gas phase’ reactions taking place. There are few studies in the literature dedicated to elucidating the mechanisms at work in CVD reactors and Chapter 3 in this thesis describes the use of gas phase electron diffraction to obtain information on the gas phase species.

It is thought that within the reaction chamber gas phase reactions may occur between the precursor molecules, and in some cases intermediate species can be formed. These gas phase species, chemically changed or otherwise, may be transported to the substrate and adsorbed onto the heated substrate. Surface reactions can then take place during which further decomposition of the precursors takes place to form the desired material

in the form of a thin film. It is during this step that volatile by products of the precursors are also formed, which desorb, along with any unrequired ligands, from the substrate and are transported out of the chamber *via* the inert carrier gas, or vacuum, depending on the type of CVD being used. Initially, at this stage, the atoms of the film are only weakly bound to the substrate and so are free to diffuse across the surface of the film. Eventually, and as a result of the heat of the substrate (≥ 200 °C) these weak van der Waals type interactions between the deposited material and substrate are replaced as the nucleation of the film occurs with several atoms bonding together. In addition, substrate defects act as nucleation points to which further atoms migrate, resulting in the growth of clusters of the desired material. The resulting island of material continues to grow, forming the film over time. An overview of the process is shown below in Fig. 1.1.

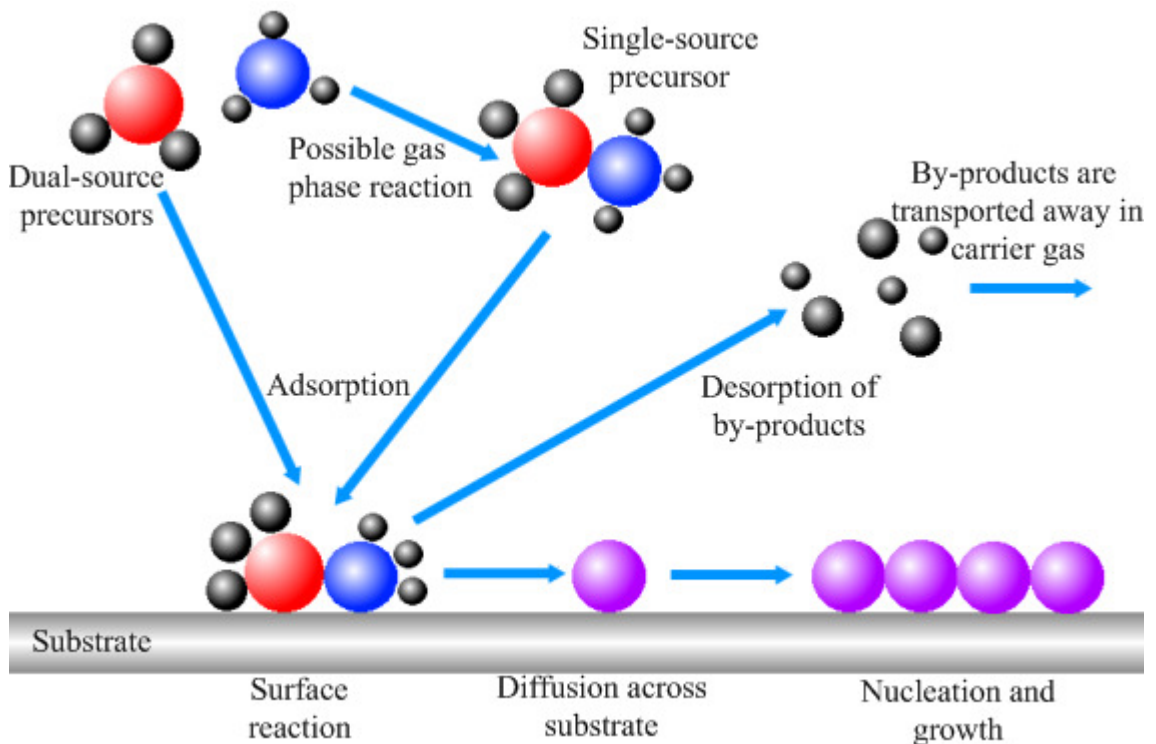


Fig. 1.1: Overview of the CVD process.

CVD has a number of advantages when compared to other methods of thin film deposition, such as physical vapour deposition (PVD). One of the biggest advantages has to be the production of highly dense and pure phase materials when using CVD. Additionally, films have excellent adhesion, are uniform and easily reproducible. Along with the reasonable deposition costs, the set up of CVD means that a large number of

parameters can be quickly and easily changed. Therefore, crystal structure, surface morphology and orientation of products can be controlled with ease. Further to this, deposition rates can be adjusted, a beneficial factor in regards to industrial scale up.

As already mentioned, CVD can utilise a wide range of precursors and uses relatively low deposition temperatures. Furthermore, as CVD is a non line-of-sight process, with excellent throwing power it can and is used to coat complex shaped components uniformly and to deposit films with good conformal coverage.⁷

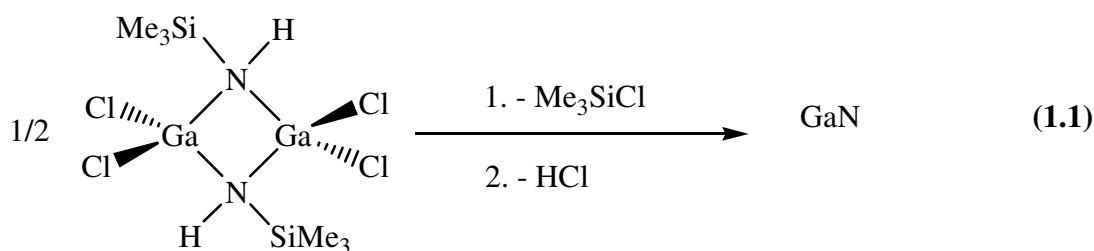
As previously described, the films produced have different properties to those of the substrate and are chemically bound to it, so they are strongly adhered to the substrate surface.⁸ These precursors can either be single-source, that is all of the desired film components are contained within one precursor or they can be dual source, where more than one molecule is employed.

1.1.1.1. Single-Source Chemical Vapour Deposition

It is argued that the single-source precursor approach to thin film production facilitates greater control over the stoichiometry of the film and can also create more homogenous materials. These, often simple precursors, contain preformed bonds between the elements that constitute the material in the film. For example, a gallium alkoxide precursor would contain at least one preformed Ga–O bond, ideal for the deposition of a Ga₂O₃ film. A single-source precursor should be simple, volatile, contain all of the appropriate atoms required for the film, and ideally these atoms are present in the same stoichiometry as in the final film⁹, that is the stoichiometry of the desired binary product (in Ga₂O₃ the M:O ratio is 1:1.5).

A direct result of including preformed bonds in the precursor is that lower temperature growth is possible with the single-source approach when directly compared to dual source methods. Additionally it stands to reason that these single-source precursors will be more air and moisture stable and therefore less reactive and hence less toxic compounds than conventional precursors, such as GaMe₃, InEt₃ or indeed ZnEt₂, to name a few examples.

Easily removable terminal ligands are essential for clean decomposition of CVD precursors, both dual and single-source. Unwanted contaminants, including carbon and chlorine often pose problems for the functionality of thin films.¹⁰ Equally compounds should be volatile and stable in the vapour phase so that they can be transported to the reaction chamber. A good example of a single-source CVD precursor is $[\text{Cl}_2\text{GaNH}(\text{SiMe}_3)]_2$, which can be used to make thin films of GaN.¹¹ On heating, the compound readily loses its ligands *via* condensation reactions producing Me_3SiCl and HCl , resulting in a facile, low temperature and clean deposition route to GaN (Egn. 1.1).



1.1.1.2. Aerosol-Assisted Chemical Vapour Deposition

This thesis presents a study in the design of group 13 alkoxide precursors to gallium and indium oxide thin films. The technique used exclusively in this thesis is aerosol assisted (AA)CVD, which will be discussed in more depth in Chapter 4. The main advantage of using AACVD, over other CVD techniques, is that this system eliminates the need for volatile precursors.¹² It utilizes an aerosol vaporisation technique¹³ where the precursor is dissolved in a suitable solvent and an aerosol mist is generated.

A piezoelectric transducer creates ultrasonic waves which pass through the solution, this produces a wave pattern on the surface of the liquid. When the height of the wave is sufficient, the crest of the wave is so unstable that droplets are ejected from the surface of the precursor solution, as this builds up it creates an aerosol mist.¹² This mist can be transported into the reaction chamber by diverting an inert carrier gas through the flask containing the precursor solution, to act as a bubbler.

Once in the reaction chamber, the solvent is evaporated and the chain of gas phase reactions begins in the production of the desired thin film. A description in fuller detail

describing this process, complete with a figure can be found in the introductory section of Chapter 4.

1.2. Precursors to CVD

Group 13 alkoxides have been used extensively in organic chemistry, particularly in the cross-coupling of aryl-triflates and aryl-halides, specifically utilising the intramolecularly donor-stabilised gallium alkoxides. A large number of alkylgallium(III) alkoxides, of the type $[\text{R}_{3-x}\text{Ga}(\text{OR}')_x]$ ($x = 1, 2$) and homoleptic gallium(III) alkoxides $[\text{Ga}(\text{OR}')_3]_n$, have also been reported. It is interesting to note that these gallium alkoxides are also intermediates to heterometallic complexes, such as $[\text{ZnGa}_2(\text{OR}_8)]_n$, which can serve as precursors to ZnGa_2O_4 materials. More importantly, with respect to this project, is the use of these gallium alkoxides as precursors to Ga_2O_3 films *via* various types of CVD, including low pressure (LP)CVD.

The alkoxide ligand is considered as a ‘hard’ base and so therefore shows a preference for ‘hard’ metal centres with high oxidation states (Fig. 1.2). The structural data (i.e. bond lengths and angles) for a multitude of gallium(III)/indium(III) alkoxide/aryloxide complexes has been reviewed as recently as 2003.¹⁴⁻¹⁷ The report extensively reviews the synthesis, structures and reactivities of these species however, they are at the forefront of interest in materials chemistry today.

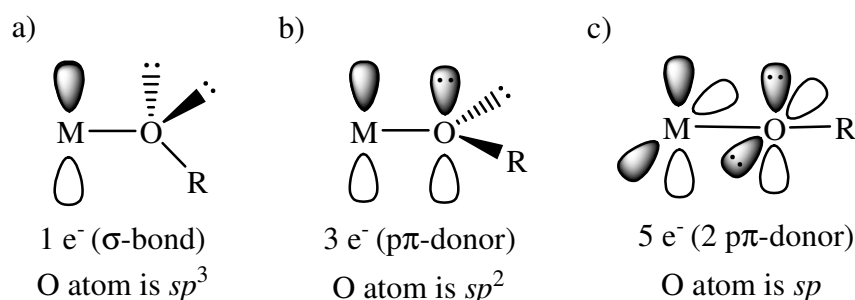


Fig. 1.2: Molecular orbital diagram showing the different orbital interactions possible between a group 13 metal and its respective alkoxide ligand.

Many of the known group 13 alkoxide complexes are characterised by a noticeable tendency to oligomerise due to the strong metal-oxygen bridges that are formed. Oligomerization can be a problem in CVD precursor design, with larger ligand clusters having decreased volatility and lower solubility, rendering the compounds poor precursors. Donor functionalised alkoxide ligands can act as 1-electron σ -donors, or as 3- or 5- electron π -donor ligands, as shown in Fig. 1.2. In gallium alkoxides the alkoxide ligand cannot act as a two-sided π -donor as it is energetically unfavourable for both of the gallium and oxygen centres to be sp hybridised. Studies have shown that π -bonding contributions in these compounds are small on account of the polar character of these bonds and the large size difference between the gallium and oxygen atoms.^{18,19}

Gallium and indium alkoxides are generally of the type $[\text{R}_2\text{M}(\text{OR}')_n]_n$, typically with the formation of strong metal-oxygen bridges. Donor functionalised alkoxide/amidoalkoxide ligands will be used to try to reduce oligomerisation, and thus create more volatile precursors for CVD. Additionally donor functionalised ligands should result in precursors which are less sensitive to air and moisture due to the stabilisation of the metal centre, *via* interactions between the metal centre and the donor atom, (usually an oxygen or nitrogen atom). In this thesis, the target compounds initially were $[\text{R}_2\text{Ga}(\text{OR}')_n]_n$ and $[\text{RGa}(\text{OR}')_2]_n$, although the latter are expected to be the better precursors due to the 1:2 ratio of Ga:O in the complexes (*cf.* 1:1.5 in M_2O_3), these compounds are discussed in length in Chapter 2. There are very few reports of gallium and indium bis(alkoxides) in the literature to date.

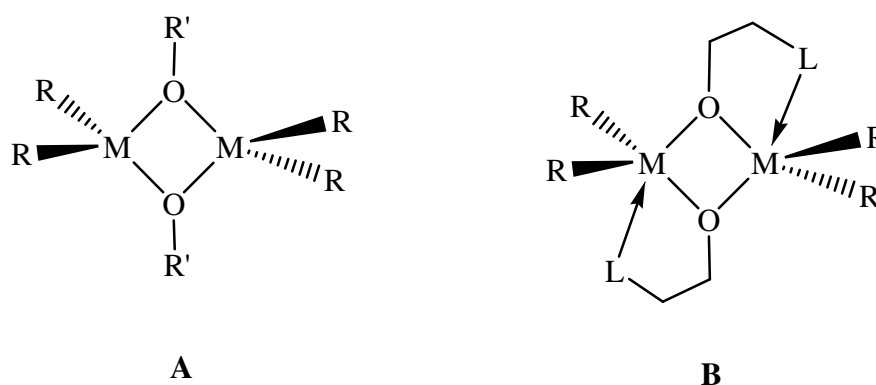


Fig. 1.3: Centro-symmetric M_2O_2 ring produced with a monofunctional R' group, A; and when a donor functionalised ligand, L, is used, B.

The precursors produced from the use of donor functionalised ligands adopt the structure of a centro-symmetric M_2O_2 ring (Fig. 1.3). This dimeric structure is derived from two sp^2 hybridised gallium or indium atoms which are bridged by two alkoxide ligands forming the aforementioned M_2O_2 ring. Therefore the first alkoxide ligand forms an M-O bond and lies within the equatorial plane of the metal centre. The second bridging alkoxide ligand forms a dative covalent M-O bond *via* electron-pair donation from the oxygen atom into a vacant p orbital on the metal and lies axial to the metal centre. The situation is reversed for the second gallium or indium metal centre and each alkoxide ligand is sp^3 hybridised at the oxygen atom.²⁰

In order to deposit thin films of high quality, there are certain requirements which need to be met by the precursor, generally whatever the form of CVD is used the same precursor requirements apply. Precursors can be designed for optimal performance, dependant on the desired outcome, however, in general the characteristics of an ideal CVD precursor are listed below:

- Precursors should have sufficient volatility (for LPCVD and APCVD) to generate active gaseous reactant species for achieving suitable growth rates within reasonable temperatures.
- In order to produce thin films, a low deposition rate is required.
- It is paramount to thin film growth that decomposition occurs below the temperature that the substrate would melt or undergo phase transformation.
- It is essential that precursors are adequately stable at room temperature, and do not decompose immediately when transported in the gas phase.
- Following this, the temperature difference between stable gas phase and decomposition for film growth should be considerable to prevent early decomposition.
- Precursors must be free from contaminants.
- It is vital that precursors decompose cleanly with all by products being removed *via* exhaust.
- When synthesising precursors for CVD it is important to tailor the design of the precursor towards the above optimum requirements.

- In addition, precursors should aim to exhibit low toxicity and low risk for safe handling. This, along with the need for precursors to be readily produced in high yield and at low cost is paramount for industrial application.

Looking into precursor design and their subsequent use in producing thin films can give an insight into the molecular decomposition pathways. However little is known in regards to mechanisms at work in CVD processes, with scarce documentation comparing precursor performance with film purity.

1.3. Group 13 oxides

Group 13 metal oxides play important roles in a variety of applications. Gallium oxide has application for gas sensing as well as in catalysis,²¹ phosphor host material for emissive display applications²² and blue light emitting nanowires.^{23,24} Doped and undoped indium oxide thin films are attractive materials for use as transparent conducting oxides (TCOs), in applications such as display panels and solar cell windows.^{25,26}

1.3.1. Gallium oxide

1.3.1.1. Structure

The function of gallium oxide thin films are able to switch with temperature, as discussed below. A variety of techniques have been used to deposit Ga₂O₃ films for gas sensing purposes, these include sputtering methods, sol-gel and MOCVD. To date it has been shown that MOCVD processes have the most practical approach to efficient preparation of large scale, reproducible and adhesive films with little impurity.

There are five known forms of crystalline gallium(III) oxide, Ga₂O₃, as summarised in Table 1.1. The crystalline structures are the most stable form of gallium oxide, and these vary depending on the conditions of their preparation.

Table 1.1: Crystal structures of gallium oxide

Form	Crystal structure
α -Ga ₂ O ₃	Trigonal $R\bar{3}c$
β -Ga ₂ O ₃	Monoclinic, $C2/m$
γ -Ga ₂ O ₃	Cubic, $Fd\bar{3}m$
δ -Ga ₂ O ₃	Cubic, $Ia\bar{3}$
ϵ -Ga ₂ O ₃	Orthorhombic

The trigonal and monoclinic forms of this gallium sesquioxide, α -Ga₂O₃ and β -Ga₂O₃ respectively, are the most stable of the five structures.²⁷ In the structure of α -Ga₂O₃ the oxygen ions are in an approximately hexagonal close packed array with all Ga³⁺ ions octahedrally coordinated to O²⁻ ions. In this structure the octahedra share faces and edges with each other which consequently brings the metal ions in close proximity with one another. This α -phase is known to be metastable.

Differing markedly from that of α -Ga₂O₃, the structure of β -Ga₂O₃ exhibits a ‘distorted cubic’ close packed array, as shown below in Fig. 1.3.²⁸ The unit cell consists of two crystallographically non-equivalent gallium atoms and three non-equivalent oxygen ions, with each Ga³⁺ ion being surrounded by a distorted tetrahedron of oxygen ions. Unlike the metastable α -Ga₂O₃, β -Ga₂O₃, owing to its low density, is the thermodynamically stable phase at room temperature.²⁹

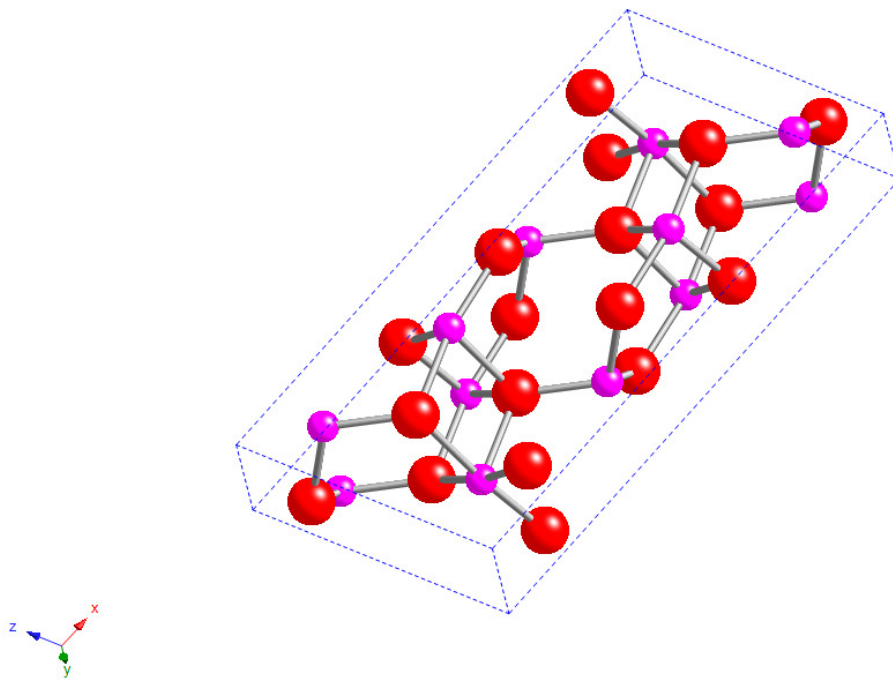


Fig. 1.4: The arrangement of Ga and O atoms in β -Ga₂O₃ (magenta spheres indicate Ga, red spheres indicate O).

It is interesting to compare the average bond distances of the two known stable gallium oxide structures. The gallium oxygen distances in both the α -Ga₂O₃ and β -Ga₂O₃ phases are the same, at 2.00 Å, however there is a difference in the O–O distances of 2.80 Å and 2.84 Å for the α -Ga₂O₃ and β -Ga₂O₃ phases, respectively.^{27,29} This larger distance in the β -Ga₂O₃ phase is attributed to the packing of atoms, and is the rationale behind the lower density of the phase.

1.3.1.2. Application

Gallium oxide (Ga₂O₃) is an electrical insulator at room temperature and semiconducting above 500 °C.³⁰ Because of these attributes, gallium oxide (Ga₂O₃) is considered to be one of the most ideal materials for application as thin-film gas sensors at high temperatures and finds uses in optoelectronic devices.³¹⁻³³ Additionally it shows practical use in monitoring and controlling systems of combustion engine's waste gases.

This thermally stable material adopts a monoclinic structure, is semiconducting above 500 °C and at temperatures above 900 °C the electric conductivity changes depend on

the concentration of oxygen.³⁴ This sensitivity to oxygen concentration means that Ga_2O_3 can be used as a sensor. Oxygen gas sensors have practical use in monitoring and controlling oxygen concentrations in exhaust gases of automobiles, as well as waste gases and chemical processes.³⁵ Below 900 °C, gallium oxide thin film operate as a surface-control-type sensor to reducing gases, *e.g.* H_2 , EtOH and CO .^{36,37} So by a simple change of temperature the function of the sensor can be switched.

As previously alluded to, $\beta\text{-Ga}_2\text{O}_3$ and amorphous Ga_2O_3 has received attention as a new phosphor host material for thin film electroluminescent (TFEL) devices.^{22,38,39} $\beta\text{-Ga}_2\text{O}_3$ can exhibit up to three different emissions, UV, blue and green depending on the dopant and preparation of the sample, this is a direct effect observed after optical excitation through the band gap.³⁹

Due to the materials high ion-exchange selectivity and capacity, Ga_2O_3 can also be used as a catalyst.⁴⁰⁻⁴² The large ion capacity also means that the framework can be easily doped, giving rise to a host of other functional materials.²⁵⁻²⁷ Tin doped $\beta\text{-Ga}_2\text{O}_3$ films for example are unique oxide films which are transparent to deep UV light and are electrically conductive.⁴³ These commercially desirable materials can be used in such applications as UV transparent electrodes for UV light emitting diodes.⁴⁴

1.3.2. Indium oxide

1.3.2.1. Structure

Unlike its gallium equivalent, the indium sesquioxide is only found to be stable in one crystalline form, with cubic *C* modification.⁴⁵ The indium ions are six coordinate with the oxygen atoms displaying four coordinate geometry, the unit cell consists of two crystallographically non-equivalent indium atoms and one type of oxygen atom. As shown below in Fig. 1.4, each indium atom is surrounded by six equidistant oxygen atoms, which lie close to the corners of a cube, the two body diagonally opposite corners of this cube remain unoccupied. The other crystallographically non-equivalent In atom is surrounded by six oxygen atoms which lie close to the corners of a cube again, this time leaving the two face-diagonally opposite corners unoccupied. In this

polyhedra the In–O distances differ marginally in each arrangement with an average bond distance of 2.18 Å.

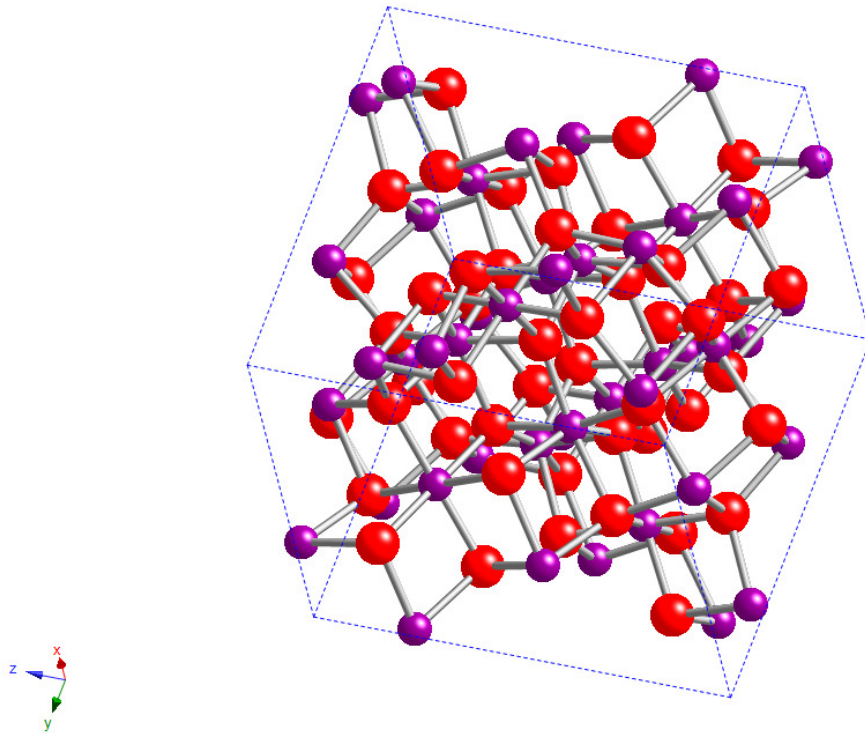


Fig. 1.5: The arrangement of In and O atoms in In_2O_3 (Purple spheres indicate In, red spheres indicate O).

1.3.2.2. Application

Due to their high conductivity and high transparency in the visible region transparent conducting oxide (TCO) materials are at the forefront of interest today. Indium oxide thin films are generally polycrystalline and can be prepared *via* spray pyrolysis,⁴⁶ magnetron sputtering,⁴⁷ sol gel⁴⁸ and MOCVD,^{49,50} to name a few. There is little reported in the literature in regards to CVD of indium oxide films, as precursor development in the area is relatively untouched. Whilst a recent study has reported the use of fluorine to increase precursor volatility in LPCVD,⁵¹ subsequent films resulted in fluorine contamination. To eliminate the need for volatile precursors, AACVD would seem an obvious choice, and yet to date, there is only one study.⁵⁰

Indium oxide has a direct band gap of 3.75 eV⁵² for single crystals. Indium oxide can be doped with other metals to enhance its electronic properties. Indium tin oxide thin films for example are widely used in optoelectronic devices, including flat panel displays,⁵³

photovoltaic cells⁵⁴ and in transparent electrodes for light emitting diodes.⁵⁵ Doping the indium oxide framework with tin can reduce the optical band gap to 3.4 eV,⁵⁶ making it a highly desirable material.

Because of their potential in commercially viable materials, indium oxide thin films, either doped or otherwise, are attractive compounds for application in display panels and solar cell windows.²⁶ As a direct result of its transparency, conductivity, low electric resistivity, chemical stability and excellent adhesion to substrate⁵⁷ undoped indium oxide finds use in industrial and technological applications such as toxic / dangerous gas detection in chemical plants.

1.4. Overview

Over the last twenty years, chemical vapour deposition has been developed into a highly advanced and efficient thin film growth technology. It can be argued that some steps are yet to be defined⁵⁸ but methods are developed to the point where basic computer simulations are beginning to be able to model the growth rates in a variety of reactor geometries. The advances in these film deposition techniques and better analytical equipment available has gone hand in hand with the development of highly efficient chemical precursors to the desired materials.

1.5. References

1. C. F. Powell, J. H. Oxley, J. M. Blocher, *Vapour Deposition*, ed. T. E. Society. 1966, Pennington NJ.
2. E. M. Sherwood, J. M. Blocher, *J. Metals*, 1965, **17**, 594.
3. R. L. Moon, Y.-M. Houngh, *Chemical Vapour Deposition*, ed. M. L. Hitchman, K. F. Jensen. 1989, New York, Academic Press. Chapter 6.
4. M. L. Hitchman, K. F. Jensen, *Chemical Vapour Deposition*, ed. M. L. Hitchman, K. F. Jensen. 1989, New York, Academic Press. Chapter 1.
5. M. Ohring, *The Materials Science of Thin Films*. 1992, London, Academic Press.
6. W. S. R. Jr., *CVD of Nonmetals*. 1996, New York, VCH Publishers.
7. K. L. Choy, *Prog. Mater. Sci.*, 2003, **48**, 57.
8. M. O. Aboelfotoh, B. G. Svensson, *Semicond. Sci. Technol.*, 1991, **6**, 647.
9. T. S. Lewkebandara, C. H. Winter, *Adv. Mater.*, 1994, **6**, 237.
10. K. G. Caulton, L. G. Hubert-Pfalzgraf, *Chem. Rev.*, 2002, **90**, 969.
11. M. L. Hitchman, K. F. Jensen, *Chemical Vapour Deposition Principles and Applications*. 1993, London, Academic Press.
12. T. T. Kodas, M. J. Hampden-Smith, *Aerosol Processing of Materials*. 1999, Chichester, Wiley VCH. 537.
13. C. J. Carmalt, J. D. Mileham, A. J. P. White, D. J. Williams, J. W. Steed, *Inorg. Chem.*, 2001, **40**, 6035.
14. H. C. Chen, B. H. Tseng, M. P. Houngh, Y. H. Wang, *Thin Solid Films*, 2003, **445**, 112.
15. C. Mitterer, P. H. Mayrhofer, *Key Eng. Mater.*, 2004, **264-268**, 453.
16. D. J. Blackwood, *Corros. Rev.*, 2003, **21**, 97.
17. G. B. Smith, A. Ben-David, P. D. Swift, *Renew. Energ.*, 2001, **22**, 79.
18. P. P. Power, *Chem. Rev.*, 1999, **99**, 3463.
19. P. J. Brothers, P. P. Power, *Adv. Organomet. Chem.*, 1996, **39**, 1.
20. C. J. Carmalt, S. J. King, *Coord. Chem. Rev.*, 2006, **250**, 682.
21. P. Michorczyk, J. Ogonowski, *App. Cat. A - Gen.*, 2003, **251**, 425.
22. T. Miyata, T. Nakatani, T. Minami, *Thin Solid Films*, 2000, **373**, 145.

23. S. Mishra, S. Daniele, S. Petit, E. Jeanneau, M. Rolland, *Dalton Trans.*, 20092568.
24. Z. R. Dai, Z. W. Pan, Z. L. Wang, *J. Phys. Chem. B*, 2002, **106**, 902.
25. J. N. Avaritsiotis, R. P. Howson, *Thin Solid Films*, 1981, **80**, 63.
26. S. Sharma, M. K. Sunkara, *J. Am. Chem. Soc.*, 2002, **124**, 12288.
27. M. Mareizo, J. P. Remeika, *J. Chem. Phys.*, 1966, **46**, 1862.
28. S. Geller, *J. Chem. Phys.*, 1960, **33**, 676.
29. L. M. Foster, H. C. Stump, *J. Am. Chem. Soc.*, 1951, **73**, 1590.
30. M. Fleischer, H. Mexiner, *Sensor. Actuat. B*, 1995, **26**, 81.
31. M. Fleischer, L. Hollbauer, H. Mexiner, *Sensor. Actuat. B Chem.*, 1994, **18**, 119.
32. M. Ogita, K. Higo, Y. Hatanaka, *Appl. Surf. Sci.*, 2001, **175**, 721.
33. M. Ogita, S. Yausa, K. Kobayashi, Y. Yamada, Y. Natanishi, Y. Hatanaka, *Appl. Surf. Sci.*, 2003, **212**, 397.
34. T. Schwebel, M. Fleischer, H. Mexiner, C.-D. Kohl, *Sensor. Actuat. B Chem.*, 1998, **49**, 46.
35. Y. Li, A. Trinchi, W. Wlodarski, K. Galatsis, K. Kalantar-Zadeh, *Sensor. Actuat. B Chem.*, 2003, **93**, 431.
36. M. Fleischer, S. Kornely, T. Weh, J. Frank, H. Meixner, *Sensor. Actuat. B Chem.*, 2000, **69**, 205.
37. M. Ogita, N. Saika, Y. Nakanishi, Y. Hatanaka, *Appl. Surf. Sci.*, 1999, **142**, 188.
38. J. Hao, M. Cocivera, *J. Phys. D. Appl. Phys.*, 2002, **35**, 433.
39. L. Binet, D. Gourier, *J. Phys. Chem. Solids*, 1998, **59**, 1241.
40. A. L. Petre, J. A. Peredigon-Melon, H. H. M. Hirano, *Thin Solid Films*, 2002, **411**, 134.
41. A. L. Petre, A. Auroux, P. Gelin, M. Caldararu, N. I. Ionescu, *Thermochim. Acta*, 2001177.
42. C. O. Arean, A. L. Bellan, M. P. Menruit, M. R. Delagdo, G. T. Palomino, *Micro. Meso. Mat.*, 2000, **40**, 35.
43. M. Orita, H. Hiramatsu, H. Ohta, M. Hirano, H. Hosono, *Thin Solid Films*, 2002, **411**, 135.
44. H. Ohta, K. Kawamura, M. Orita, M. Hirana, N. Sarukura, H. Hosono, *Appl. Phys. Lett.*, 2000, **77**, 475.
45. M. Mareizo, *Acta Cryst.*, 1996, **20**, 723.

46. J. J. Prince, S. Ramamurthy, B. Subramanian, C. Sanjeeviraja, M. Jayachandran, *J. Cryst. Growth*, 2002, **240**, 142.
47. J. Hu, F. Zhu, J. Zhang, H. Gong, *Sensor. Actuat. B Chem.*, 2003, **93**, 175.
48. M. A. Flondoza, R. Castanedo-Perez, G. Torres-Delgado, J. M. Martin, O. Zelaya-Angel, *Thin Solid Films*, 2008, **517**, 681.
49. J. Park, G. A. Horley, P. O'Brien, A. C. Jones, M. Motevalli, *J. Mater. Chem.*, 2001, **11**, 2346.
50. S. Basharat, C. J. Carmalt, S. A. Barnett, D. A. Tocher, H. O. Davies, *Inorg. Chem.*, 2007, **46**, 9473.
51. T.-Y. Chou, Y. Chi, S.-F. Huang, C.-S. Liu, A. J. Carty, L. Scoles, K. A. Udachin, *Inorg. Chem.*, 2003, **42**, 6041.
52. H. K. Muller, *Phys. Status Solidi*, 1969, **27**, 723.
53. S.-F. Hsu, C.-C. Lee, S.-W. Wang, C. H. Chen, *Appl. Phys. Lett.*, 2005, **86**, 1.
54. E. Kymakis, G. A. J. Amaratunga, *Appl. Phys. Lett.*, 2002, **80**, 112.
55. J. H. Burroughes, D. D. C. Bradley, A. R. Brown, R. N. Marks, K. Mackay, R. H. Friend, P. L. Burns, A. B. Holmes, *Nature*, 1990, **347**, 539.
56. C. Xirouchaki, G. Kiriakidis, T. F. Pedersen, H. Fritzsche, *J. Appl. Phys.*, 1996, **79**, 9349.
57. Z. Z. You, J. Dong, *J. Colloid. Sci.*, 2006, **300**, 687.
58. J.-H. Ryou, R. Kanjolia, R. D. Dupuis, *Chemical Vapour Deposition, Precursors Processes and Application*, ed. A. C. Jones, M. L. Hitchman. 2009, Cambridge, RSC. Chapter 6.

Chapter 2

Synthesis of Group 13 Alkoxides

This chapter describes the synthesis and characterization of a range of gallium(III) and indium(III) alkoxides. The compounds were prepared with a view to application as single-source precursors for the chemical vapour deposition (CVD) of group 13 oxide thin films, as discussed in Chapter 4. Section 2.1 gives an overview of known gallium(III) and indium(III) alkoxide complexes in the literature. The synthesis and characterization of the group 13 alkoxides prepared for this study are discussed in section 2.2, with conclusions in section 2.3 and experimental details given in section 2.4.

2.1. Introduction

Toward the end of the last century and continuing into the next, the development of molecular precursors for metal oxides has become the subject of much study.^{1,2} Research into the synthesis of precursors to these materials has expanded hugely in order to tailor compounds such that the desired thin film is produced readily at low cost and in high purity, with the precursor having sufficient volatility and ability to follow a clean decomposition path with all by-products leaving *via* an exhaust.³⁻⁵

The focus of this study will be the synthesis of group 13 alkoxide precursors for use in the preparation of gallium and indium oxide thin films. The chemical and physical properties of these precursors can be fine tuned by altering the structure of the ligand,⁶ for example volatility can be increased by substituting fluorinated groups or using ligands with larger steric bulk. However these changes to the precursors often lead to metal oxide thin films high in carbon and/or fluorine contamination.⁷ Furthermore, the use of bulky alkoxide ligands, or donor functionalised alcohol groups is a popular choice to shield metal centres from intermolecular interactions and thus inhibit oligomerisation. Oligomerisation is likely to occur around an incomplete coordination sphere, rendering the compounds insoluble with low volatility; both properties undesirable for CVD.

In 2008 investigations into the advantages of relatively low temperature depositions of metal oxide thin films *via* the use of group 13 alkoxides have reported the production of films with little or no carbon contamination.^{8,9} These studies have incorporated the use of donor functionalised alcohols, which have the ability to chelate *via* an extra donor atom incorporated along the carbon chain, this commonly is an oxygen or nitrogen atom. In turn these additional donor groups lead to a fully saturated metal centre with oligomerisation prevented.¹⁰

A range of diorganoalkoxometallanes of gallium and indium of the type $[R_2MOR']_n$, incorporating donor-functionalised alkoxides have been structurally characterised.^{9,11-17} In general, these compounds are synthesized either *via* the reaction of MR_3 with an alcohol, or from the salt metathesis reaction of R_2MX and $M'OR$ (M' = alkali metal, X = Cl, Br, R = Me, Et).¹⁸ Interestingly, the reaction of MR_3 with excess $R'OH$ usually results in the formation of sesquialkoxides,^{19,20} rather than bis- or tris(alkoxides). However, a monomeric gallium bis(alkoxide), $[EtGa(OCH_2CH_2NMe_2)_2]$, incorporating a donor functionalized alkoxide has been isolated *via* the reaction of $GaEt_3$ with an excess of $HOCH_2CH_2NMe_2$ under reflux conditions.¹³

2.1.1. Gallium(III) and indium(III) mono(alkoxides)

A number of different methods have been used to synthesise mono(alkoxides) of gallium(III) and indium(III).^{18,21-31} The most common route is the reaction of trivalent gallium or indium organometallics, MR_3 , with alcohols at elevated temperatures, Eqn. 2.1.²⁷



R = Me, Et; R' = alkyl or aryl.

Salt elimination is another efficient and widely used route for the synthesis of gallium and indium mono(alkoxides). This involves the reaction of di-alkyl/aryl metal halide complexes $[R_2MX]$ (R = alkyl or aryl, M = Ga or In, X = halide) with lithiated or other early main group reagents (e.g. $LiOR'$), Eqn. 2.2. The elimination of the salt provides the driving force for the reaction.



A third route to group 13 mono(alkoxide) complexes involves amine-alcohol exchange, Eqn. 2.3.



Group 13 mono(alkoxides), of the type $[R_2MOR']_n$ (R = alkyl or aryl; M = Ga or In; R' = alkyl, aryl), have been structurally characterised for both gallium(III) and indium(III).³² The electronic and steric properties of both the alkoxide and alkyl/aryl ligands govern the structure of these compounds. Gallium and indium alkoxides are generally air/moisture sensitive compounds and highly soluble in a range of organic solvents. Two main structural types have been identified for gallium and indium alkoxides, either dimers with alkoxy bridges or monomers.¹⁶

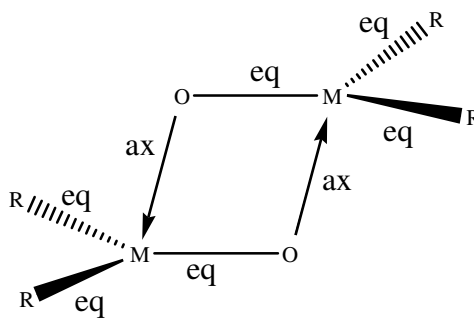


Fig. 2.1: Representation of the formation of the M_2O_2 ring in the formation in mono(alkoxides).

The dimeric structure is derived from two sp^2 hybridised M atoms, which are then bridged by two alkoxide ligands forming a M_2O_2 ring, according to Fig. 2.1. Thus, the first alkoxide ligand forms an M–O bond and lies within the equatorial, MR_2 plane of M. The second bridging alkoxide ligand forms a dative covalent M–O bond *via* electron pair donation from O into a vacant p orbital on M and lies axial to the M centre. The situation is reversed for the second M and each alkoxide ligand is sp^3 hybridised at O.¹⁸

Compounds of the type $[Me_2M(OR)]_n$ are reported in the literature spanning back over 50 years (M = Ga; R = Me,³³ CH₃, CD₃, C₂H₅,³⁴ *t*Bu, *n*Bu, Me, PhCH₂,³⁵⁻³⁷ OCy;³⁸ M = In, R = Me,³⁹ CD₃,⁴⁰ *t*Bu,⁴¹ SiMe₃⁴²). These complexes were produced from the reaction of MMe₃ and ROH. In all cases when M = In, $n = 2$, however, when M = Ga, $n = 3$ with vibrational data showing trimeric puckered six-membered M_3O_3 ring systems, with one exception, when R = OCy, here $n = 2$, exhibiting a planar Ga_2O_2 ring.

Similar complexes of the type $[R_2Ga(O^tBu)]_2$ (R = CH₃,⁴³ *t*Bu⁴⁴) were afforded from the reaction of GaR₃ with one equivalent of *t*BuOH. Treatment of GaR₃ with excess *t*BuOH did not yield any further reaction, this is probably due to electronic rather than steric effects, since the strongly electron donating alkoxides in organogroup 13 metal complexes generally reduce the reactivity of the M–R bond towards protonolysis.²⁸

There are many known structures incorporating monofunctional alkoxides, yet fewer species incorporating donor functionalised alkoxide ligands, which is central to this research, are known. The use of donor functionalised ligands helps to stabilise the

complexes and can help to achieve dimeric species, as opposed to polymers. The use of donor functionalised ligands has resulted in the isolation of dimeric species of group 13 alkoxides, as outlined below.

The monomeric complexes $[\text{Me}_2\text{Ga}(\text{OC}(\text{CF}_3)_2\text{CH}_2\text{NRR}')]$ ($\text{R} = \text{H}$, $\text{R}' = \text{Me}$, $\text{R} = \text{H}$, $\text{R}' = \text{'Bu}$, $\text{R} = \text{R}' = \text{Me}$) (Fig. 2.2) have been reported and show an interesting four coordinate gallium centre. The compounds have been isolated by the treatment of GaMe_3 with fluorinated aminoalcohols.⁴⁵ The structure of $[\text{Me}_2\text{Ga}(\text{OC}(\text{CF}_3)_2\text{CH}_2\text{NRR}')]$ ($\text{R} = \text{R}' = \text{Me}$), determined by X-ray crystallography, revealed that the four-coordinate gallium centre adopts a distorted tetrahedral environment with bond angles in the range $107.6\text{--}125.0^\circ$. The Ga–N bond distance of $2.082(2) \text{ \AA}$ is significantly shorter than the Ga–N bond length observed in related dimeric gallium complexes incorporating non-fluorinated aminoalkoxide ligands, such as $[\text{Me}_2\text{Ga}(\text{OCH}(\text{CH}_3)\text{CH}_2\text{NMe}_2)]_2$ (Ga–N $2.525(2) \text{ \AA}$).¹⁶ Thus, it appears that the coordinative unsaturation of the gallium atom is satisfied by the dative interaction with the nitrogen atom.¹⁸ The presence of electron-withdrawing CF_3 groups on the aminoalkoxide, as well as steric repulsion, reduces the bridging capability of the oxygen atom and thus preventing dimer formation. The Ga–O bond distance of $1.890(2) \text{ \AA}$ is comparable to that observed in the monomeric compound $[\text{Me}_2\text{Ga}(\text{OCPh}(\text{CH}_2\text{Ph})\text{CH}(\text{CH}_3)\text{CH}_2\text{NMe}_2)]$.⁴⁶

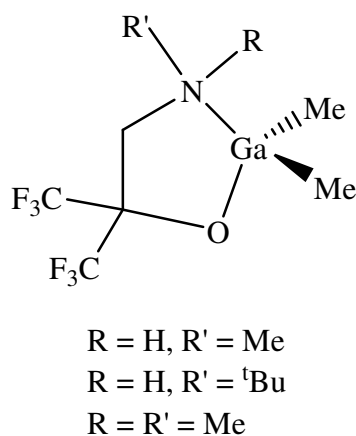


Fig. 2.2: Structure of $[\text{Me}_2\text{Ga}(\text{OC}(\text{CF}_3)_2\text{CH}_2\text{NRR}')]$ ($\text{R} = \text{H}$, $\text{R}' = \text{Me}$, $\text{R} = \text{H}$, $\text{R}' = \text{'Bu}$, $\text{R} = \text{R}' = \text{Me}$).

The dimeric gallium mono(alkoxides), $[\text{Et}_2\text{Ga}(\text{OR})]_2$ have been reported. These compounds were prepared from the reaction of GaEt_3 with one equivalent of ROH ($\text{R} = \text{CH}_2\text{CH}_2\text{NMe}_2$, $\text{CH}(\text{CH}_2\text{NMe}_2)_2$, $\text{CH}(\text{CH}_3)\text{CH}_2\text{NMe}_2$, $\text{C}(\text{CH}_3)_2\text{CH}_2\text{OMe}$, $\text{CH}_2\text{CH}_2\text{OMe}$, $\text{CH}_2\text{CH}_2\text{OMe}$ and $\text{CH}(\text{CH}_3)_2$) under reflux conditions for 24 hours.¹⁸ These complexes were found to adopt dimeric structures with a planar Ga_2O_2 ring, with each gallium atom adopting a distorted trigonal bipyramidal geometry with the ethyl groups taking the equatorial positions and the bridging alkoxide group filling the axial position (Fig. 2.3). The subsequent use of these precursors to deposit thin films of gallium oxide resulted in oxygen deficient films.⁹

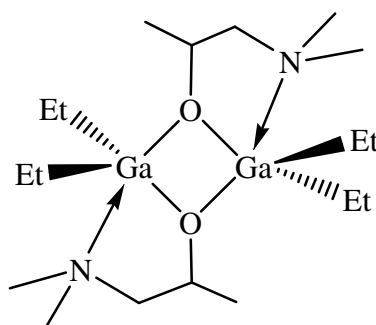


Fig. 2.3: Structure of $[\text{Et}_2\text{Ga}(\text{OCH}_2\text{CH}_2\text{NMe}_2)]_2$.

More recently, the successful preparation and characterization of dimeric indium mono(alkoxides), $[\text{Me}_2\text{In}(\text{OR})]_2$, ($\text{R} = \text{CH}_2\text{CH}_2\text{NMe}_2$, $\text{CH}(\text{CH}_2\text{NMe}_2)_2$, $\text{CH}(\text{CH}_3)\text{CH}_2\text{NMe}_2$ and $\text{C}(\text{CH}_3)_2\text{CH}_2\text{OMe}$) have been reported.¹⁴ These compounds were synthesised from the reaction of InMe_3 with the addition of one equivalent of ROH under reflux conditions for 24 hours. As with their aforementioned gallium analogues, these complexes, as determined by X-ray crystallography, reveal a centrosymmetric planar In_2O_2 ring. Each indium atom, adopts a distorted trigonal bipyramidal geometry with the methyl groups taking the equatorial positions and the bridging alkoxide group filling the axial position (Fig. 2.4). Interestingly, when $\text{R} = \text{CH}(\text{CH}_2\text{NMe}_2)_2$, the two nitrogen atoms of the alkoxide ligand interact with both indium centres. It is the stabilising effect of these donor functionalised ligands that enable the isolation of dimeric, and not polymeric species.

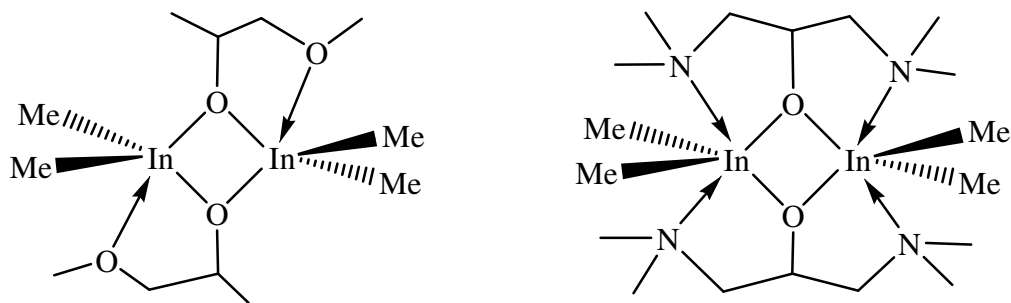


Fig. 2.4: Structure of $[\text{Me}_2\text{In}(\text{OCH}(\text{CH}_3)\text{CH}_2\text{OMe})]_2$, left, and $[\text{Me}_2\text{In}(\text{OCH}(\text{CH}_2\text{NMe}_2)_2)]_2$, right.

A more recent report of gallium mono(alkoxide) synthesis⁴⁷ used a variety of donor functionalized amino alcohol ligands have been used. The reaction of GaMe_3 with ROH afforded the corresponding aminoalkoxides of the type $[\text{Me}_2\text{Ga}(\text{OR})]$ ($\text{R} = \text{CH}_2\text{CH}_2\text{NHMe}$, $\text{CH}_2\text{CH}_2\text{NH}^t\text{Bu}$, $\text{CH}_2\text{CH}_2\text{CH}_2\text{NHMe}$, $\text{CH}_2\text{CH}_2\text{CH}_2\text{NH}^t\text{Bu}$), and $[\text{}^t\text{Bu}_2\text{Ga}(\text{OR})]_2$ ($\text{R} = \text{CH}_2\text{CH}_2\text{NH}^t\text{Bu}$, $\text{CH}_2\text{CH}_2\text{CH}_2\text{NH}^t\text{Bu}$). The structures of the compounds were crystallographically elucidated, showing the monomeric species to form intramolecular Ga–N bonds. The dimeric structures had no Ga–N interaction, instead forming characteristic Ga_2O_2 rings (Fig. 2.5).

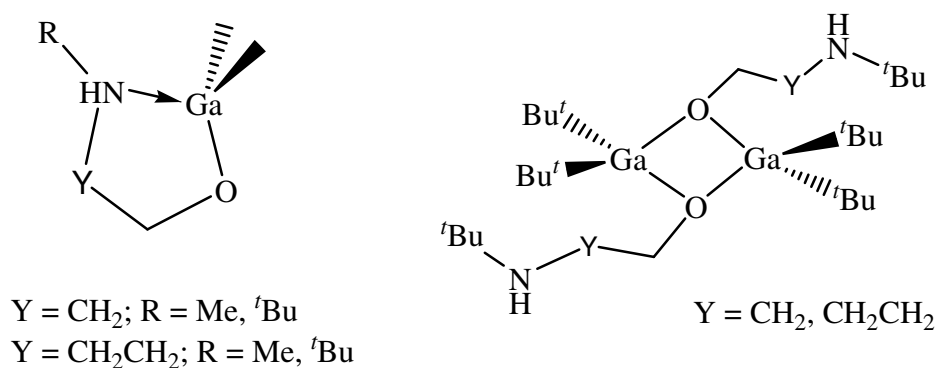


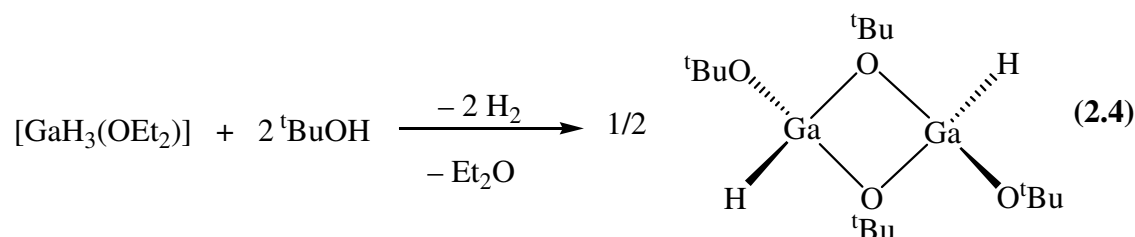
Fig. 2.5: Monomeric structure of $[\text{Me}_2\text{Ga}(\text{OR})]$ ($\text{R} = \text{CH}_2\text{CH}_2\text{NHMe}$, $\text{CH}_2\text{CH}_2\text{NH}^t\text{Bu}$, $\text{CH}_2\text{CH}_2\text{CH}_2\text{NHMe}$, $\text{CH}_2\text{CH}_2\text{CH}_2\text{NH}^t\text{Bu}$), left, and dimeric structure of $[\text{}^t\text{Bu}_2\text{Ga}(\text{OR})]_2$ ($\text{R} = \text{CH}_2\text{CH}_2\text{NH}^t\text{Bu}$, $\text{CH}_2\text{CH}_2\text{CH}_2\text{NH}^t\text{Bu}$), right.⁴⁷

The majority of gallium and indium mono(alkoxides) reported are dimeric and are considered to have lower volatility than required by certain types of CVD. Therefore these complexes are often overlooked in favour of more volatile precursors.

2.1.2. Gallium(III) and Indium(III) bis(alkoxides)

There are very few direct paths to gallium and indium bis(alkoxide) compounds reported in the literature. These rare species are in contrast to the well-known mono(alkoxides) of gallium and indium.¹⁸ The reaction of MR_3 ($M = \text{In, Ga}$; $R = \text{Me, Et, etc}$) with two equivalents or an excess of alcohol does not typically yield the expected gallium and indium bis(alkoxide) compounds, $[RM(OR')_2]_n$. Instead, reaction of MMe_3 with an excess of alcohol often results in the formation of sesquialkoxides.³²

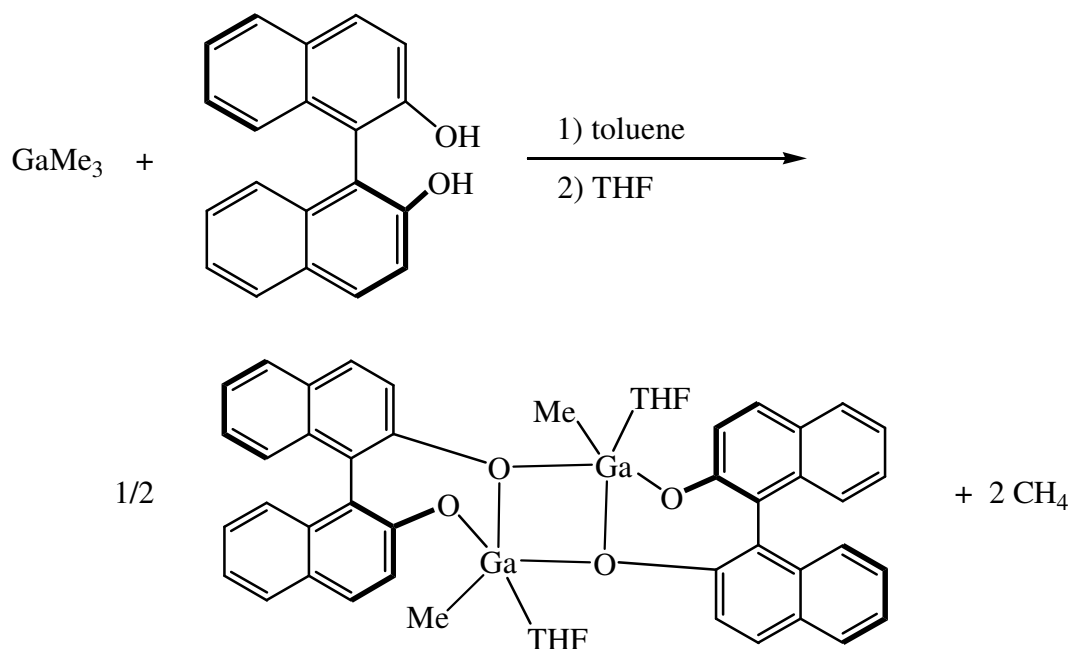
The structure of a dimeric gallium bis(alkoxide) has been reported. The complex was synthesised from the reaction of $[GaH_3(OEt_2)]$ with two equivalents of ${}^t\text{BuOH}$, a simple monodentate alkoxide group.⁴⁸ The reaction scheme can be seen in Eq. 2.4.



The structure of $[HGa(O{}^t\text{Bu})_2]_2$ was determined and was found to be dimeric with each gallium centre being four-coordinate and approximately tetrahedral (terminal Ga–O 1.783(4) Å; av. bridging Ga–O 1.906(4) Å). The bridging oxygen atoms were found to be in a trigonal planar environment.

The first preparation of a gallium bis(alkoxide) with a chelating alkoxide ligand was subsequently reported. The alkane elimination reaction between $GaMe_3$ and one

equivalent of the chelating ligand BINOL (2,2'-dihydroxy-1,1'-binaphthyl) led to the formation of a dimeric gallium bis(alkoxide), as shown in Scheme 2.1.⁴⁹

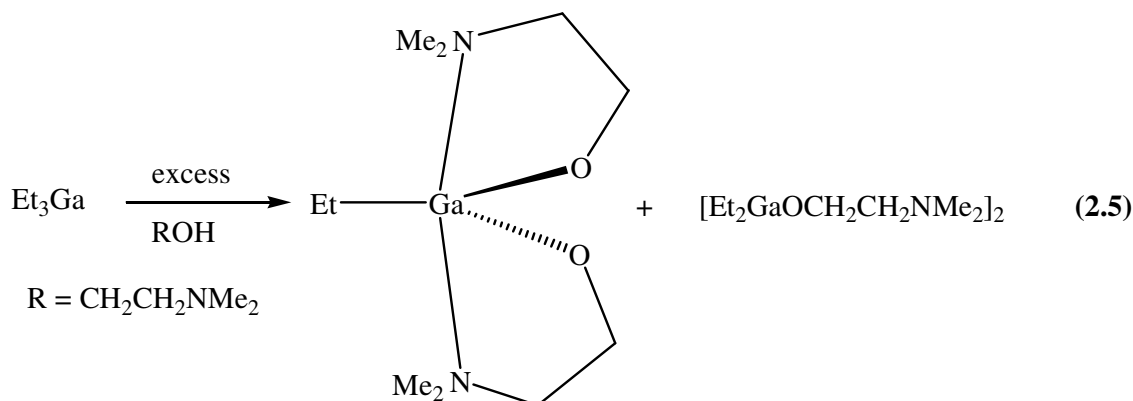


Scheme 2.1: Reaction of GaMe_3 and 2,2'-dihydroxy-1,1'-binaphthyl.

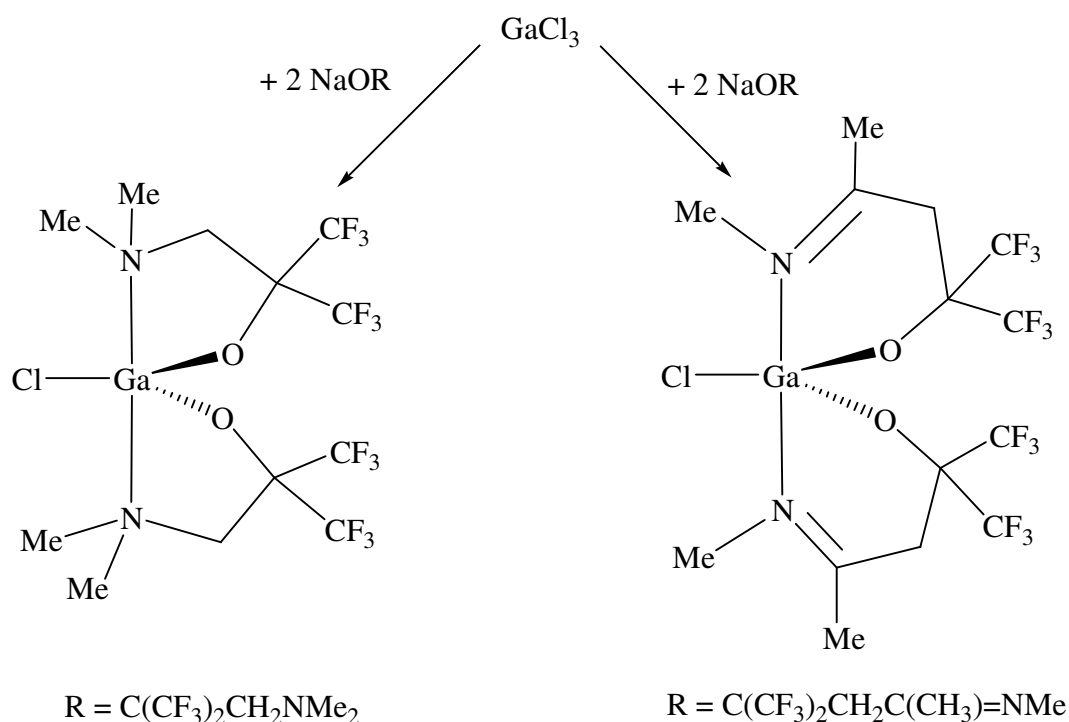
As with previous studies, initial conclusions suggested that the resultant product comprised of a coordination polymer of the type $[\text{MeGa}(\text{S})\text{-BINOL}]_n$.¹⁸ THF was used in order to break the polymer chains, by coordinating to the gallium centre. From recrystallisation in THF the compound, $[(\text{THF})\text{MeGa}(\text{S})\text{-BINOL}]_2$, was yielded. This structure was found to be dimeric by X-ray crystallography, with each gallium centre adopting a distorted trigonal bipyramidal geometry with the THF and O atom of one BINOL ligands in the axial positions. Two bridging O atoms from the BINOL ligands are in equatorial positions (bridging Ga–O 2.072(4) Å; terminal Ga–O (BINOL) 1.834(6) Å).¹⁸

There are several, recent reports of mixtures of gallium mono and bis(alkoxide) compounds. A monomeric gallium bis(alkoxide) incorporating a donor functionalised ligand was prepared by the reaction of GaEt_3 with an excess of $\text{HOCH}_2\text{CH}_2\text{NMe}_2$ under

reflux conditions.²⁵ Sublimation of the reaction mixture resulted in the isolation of a 1:1 mixture of $[\text{Et}_2\text{Ga}(\text{OCH}_2\text{CH}_2\text{NMe}_2)]_2$ and the gallium bis(alkoxide) $[\text{EtGa}(\text{OCH}_2\text{CH}_2\text{NMe}_2)_2]$, as shown in Eqn. 2.5. Further studies using similar reagents in a 1:6 ratio have all yielded 1:1 mixtures of the gallium mono and bis(alkoxide) compounds. Thus, reaction of GaEt_3 with six equivalents of ROH ($\text{R} = \text{CH}_2\text{CH}_2\text{NMe}_2$, $\text{CH}(\text{CH}_2\text{NMe}_2)_2$, $\text{CH}(\text{CH}_3)\text{CH}_2\text{NMe}_2$, $\text{C}(\text{CH}_3)_2\text{CH}_2\text{OMe}$, $\text{CH}_2\text{CH}_2\text{OMe}$, $\text{CH}_2\text{CH}_2\text{OMe}$ and $\text{CH}(\text{CH}_3)_2$) all yielded mixtures.



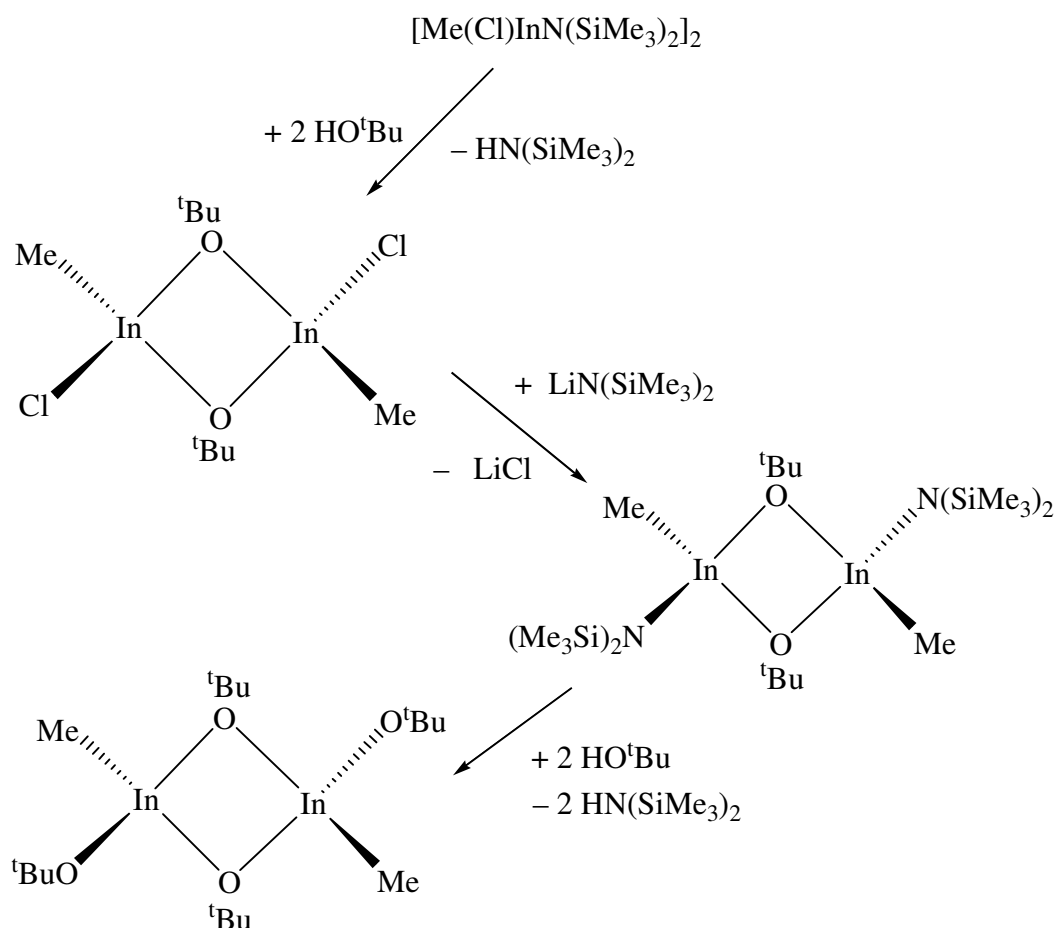
Disubstituted gallium bis(alkoxides) of the type $[\text{ClGa}(\text{OR})_2]$, are also already known. These compounds can be produced by the reaction of GaCl_3 with two equivalent of NaOR , as outlined in Scheme 2.2 ($\text{R} = \text{C}(\text{CF}_3)_2\text{CH}_2\text{NMe}_2$, $\text{C}(\text{CF}_3)_2\text{CH}_2\text{C}(\text{CH}_3)\text{NMe}$).⁴⁵ The structure of these compounds are similar to $[\text{EtGa}(\text{OCH}_2\text{CH}_2\text{NMe}_2)]_2$ ¹³ with a trigonal bipyramidal geometry adopted at the monomeric gallium centre.



Scheme 2.2: Reaction of GaCl_3 and NaOR ($\text{R} = \text{C}(\text{CF}_3)_2\text{CH}_2\text{NMe}_2$, $\text{C}(\text{CF}_3)_2\text{CH}_2\text{C}(\text{CH}_3)\text{NMe}$).

The synthesis and characterization of $[\text{MeGa}(\text{OR})_2]_n$ has been reported from the reaction of GaMe_3 and either butanol or ethanol in boiling toluene. The reaction evolved methane and both of the compounds reported were found to exist as centrosymmetrical dimers, which are then connected to form infinite chains.⁵⁰

$[\text{MeIn}(\text{O}^t\text{Bu})_2]_2$ is one of the only structurally characterised examples of an indium bis(alkoxide) incorporating a monodentate alkoxide.⁵¹ Scheme 2.3 below outlines the amine/alcohol exchange reaction that takes place in its synthesis. Initially, the amido complex $[\text{Me}(\text{Cl})\text{InN}(\text{SiMe}_3)_2]_2$ was reacted with two equivalents of $^t\text{BuOH}$ to give the indium mono(alkoxide) $[\text{Me}(\text{Cl})\text{InO}^t\text{Bu}]_2$. Reaction of $\text{LiN}(\text{SiMe}_3)_2$ with $[\text{Me}(\text{Cl})\text{InO}^t\text{Bu}]_2$ followed by ligand exchange with $^t\text{BuOH}$ resulted in the formation of $[\text{MeIn}(\text{O}^t\text{Bu})_2]_2$.



Scheme 2.3: Synthetic route for the formation of $[\text{MeIn}(\text{O}^t\text{Bu})_2]_2$.

The solid-state structure of $[\text{MeIn}(\text{O}^t\text{Bu})_2]_2$ comprises of a dimeric molecule with bridging alkoxide groups (In–O–In 103.6(2)°, O–In–O 76.4(2)°).¹⁸ The indium centre adopts a distorted tetrahedral coordination geometry with the In–O bond lengths to the terminal oxygen atoms being 0.12 Å shorter than the bond lengths in the In₂O₂ ring (bridging In–O 2.128(8) Å; terminal In–O 2.006(4) Å).

2.1.3. Gallium(III) and Indium(III) tris(alkoxides)

In recent years there has been increasing interest in group 13 alkoxides, for use as precursors to group 13 oxide thin films, for application as amorphous oxide semiconductors (AOS) within thin film transistor (TFT) technology, as photoelectric coatings and as transparent conducting coatings. These materials can be used singly or

together in combination with tin and/or zinc analogues. Indium oxide films are both transparent in the visible region of the electromagnetic spectrum and also conductive.⁵²

Gallium and indium tris(alkoxides) have been shown to act as excellent precursors to metal oxides, *via* decomposition processes, at relatively low temperature, in chemical vapour deposition (CVD) to create thin films.¹⁸ A major problem in the CVD technique stems from the large organic groups, that are utilised to increase solubility and/or volatility of the precursors, however these synthetic routes routinely lead to carbon, or halide incorporation into the films.¹²

Chlorine contamination is a problem, especially when applied in commercial application in production lines. An independent report carried out at Kojundo Ltd.,^{53,54} found that in order to eliminate chlorine contamination a further equivalent of base is required, however, base contamination then becomes a problem.

A large number of homoleptic gallium(III) alkoxides with the formula $[\text{Ga}(\text{OR}')_3]_n$ have been reported, however there are relatively few reports on the chemistry of the indium(III) alkoxides. There are several routes used to synthesise tris(alkoxides) of the form $[\text{M}(\text{OR})_3]_n$. The first reported attempts involved the reaction of the group 13 metal trihalides with sodium alkoxides. The gallium tris(alkoxides), of the type $[\text{Ga}(\text{OR})_3]_n$ (where $\text{R} = \text{Et}, ^i\text{Pr}$), were synthesised *via* the reaction of GaCl_3 with the respective NaOR .^{55,56} $[\text{Ga}(\text{O}^i\text{Pr})_3]_n$ was also reported to have been synthesized by an alternative alkoxide/alcohol exchange reaction, where $[\text{Ga}(\text{OEt})_3]$ and three equivalents of $^i\text{PrOH}$ yielded the gallium tris(isopropoxide).⁵⁶ Literature reports show the structures of these gallium tris(alkoxides) to vary depending on the ligand. For example, many are tetramers, whilst $[\text{Ga}(\text{O}^i\text{Bu})_3]_2$ was shown to be dimeric.⁵⁷ Interestingly $[\text{Ga}(\text{O}^i\text{Pr})_3]$ exists as an equilibrium mixture of a tetramer and dimer (Eqn. 2.6):



More recently, a new synthetic route has greatly improved the yield of gallium tris(alkoxides). The amide/alcohol exchange reaction of $[\text{Ga}(\text{NMe}_2)_3]_2$ with three

equivalents of ROH resulted in the formation of the homoleptic gallium alkoxides, no mixtures were observed.⁵⁸ However, many of these compounds were isolated as oils and only characterised by ¹H NMR spectra. The gallium isopropoxide analogue was found, by X-ray crystallography to be tetrameric, and related to the In and Al compounds, $\text{In}[(\mu\text{-OCHEt}_2)_2\text{In}(\text{OCHEt}_2)_2]_3$ and $\text{Al}[(\mu\text{-O}^i\text{Pr})_2\text{Al}(\text{O}^i\text{Pr})_2]_3$, respectively,^{59,60} with a formula of $\text{Ga}[(\mu\text{-O}^i\text{Pr})_2\text{Ga}(\text{O}^i\text{Pr})_2]_3$. Gallium alkoxides of the type $[\text{Ga}(\text{OR})_3(\text{HNMe}_2)]$ incorporating fluoroalkoxide groups, (R = $\text{CH}(\text{CF}_3)_2$, $\text{CMe}_2(\text{CF}_3)$, $\text{CMe}(\text{CF}_3)_2$) have also been prepared from the reaction of $[\text{Ga}(\text{NMe}_2)_3]_2$ and six equivalents of ROH.⁶¹

Films of indium oxide have also been reported and were formed *via* the use of the CVD.⁶²⁻⁶⁴ There has been interest in the development of suitable precursors to these indium oxide films, with tris(acetylacetonato) indium being one compound widely investigated.⁶⁵ Other indium compounds were explored as precursors with little success due to various problems, including solubility, and the pyrophoric nature of the compounds which caused problems with precursor handling.

Literature reports on the synthesis of gallium tris(alkoxides) and their analogous indium tris(alkoxides) differ. There is very little reported on the synthesis of the indium analogues. However, indium tris(isopropoxide) has been reported to be synthesised by reaction of InCl_3 with NaO^iPr , and then used as a starting material to make other tris(alkoxides) *via* alcohol/alkoxide exchange reactions (R = Me, Et, ⁿBu, ^sBu, and pentyl) or transesterification (R = ^tBu).⁶⁶ Interestingly, the isopropoxide complex was reported to have a molecular complexity of four in boiling propanol, with oligomerisation occurring due to water contamination. However later reports following the same synthetic route showed, *via* crystallographic analysis, that the cluster compound $[(\text{InO}^i\text{Pr})_5(\mu_2\text{-O}^i\text{Pr})_4(\mu_3\text{-O}^i\text{Pr})_4(\mu_5\text{-O})]$ was formed.⁶⁷ This work, as well as subsequent reports,²³ show that the oxo group was not due to water contamination, but the formation of a cluster.

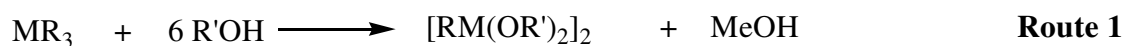
A novel synthetic approach to homoleptic indium alkoxide complexes involved the reaction of $\text{In}[\text{N}^t\text{Bu}(\text{SiMe}_3)]_3$ with sterically demanding alcohols, ROH (R = ^tO^tBu, OCMe_2Et , OCMe_2^iPr). These compounds form simple edge-shared tetrahedral dimers,

however the isopropoxide derivative is found to be an insoluble, presumably polymeric, compound.⁵⁹

2.2. Results and Discussion

Four different routes were attempted towards the synthesis of gallium and indium alkoxides incorporating donor functionalised ligands.

The first route (Route 1) involves the reaction of MR_3 ($R = Me$, $M = Ga, In$) with donor functionalised alcohols. As has already been established, the reaction of MR_3 with one equivalent of $R'OH$ yields dimeric alkoxy-metalloanes, of the type $[R_2MOR']_2$. It was hoped that the addition of excess donor functionalised alcohols in route 1 would result in the formation of alkyl gallium or indium bis(alkoxides). These complexes would also serve as precursors to gallium or indium oxide thin films and could decompose *via* α - or β -hydrogen elimination, minimising carbon contamination in the resulting films. Donor functionalised ligands were chosen to increase the volatility of the complexes for LPCVD and solubility for AACVD. In the presence of excess alcohol, high temperatures were employed in an attempt to synthesise novel group 13 bis(alkoxides). Previous attempts to prepare gallium bis(alkoxides) using simple monofunctional alcohols have failed and generally result in the formation of gallium mono(alkoxides) or sesquialkoxides. Gallium and indium bis(alkoxides), as well as being novel compounds, are expected to be superior precursors to the respective metal oxide. The $M : O$ ratio in the group 13 bis(alkoxides) are 1 : 2 rather than 1 : 1 as found in the group 13 mono(alkoxides). A ratio of 1 : 1.5 is required for the resulting M_2O_3 material and therefore the mono(alkoxides) could lead to oxygen deficient films. Furthermore, the group 13 bis(alkoxides) incorporating donor functionalised ligands are expected to be monomeric and hence more volatile.



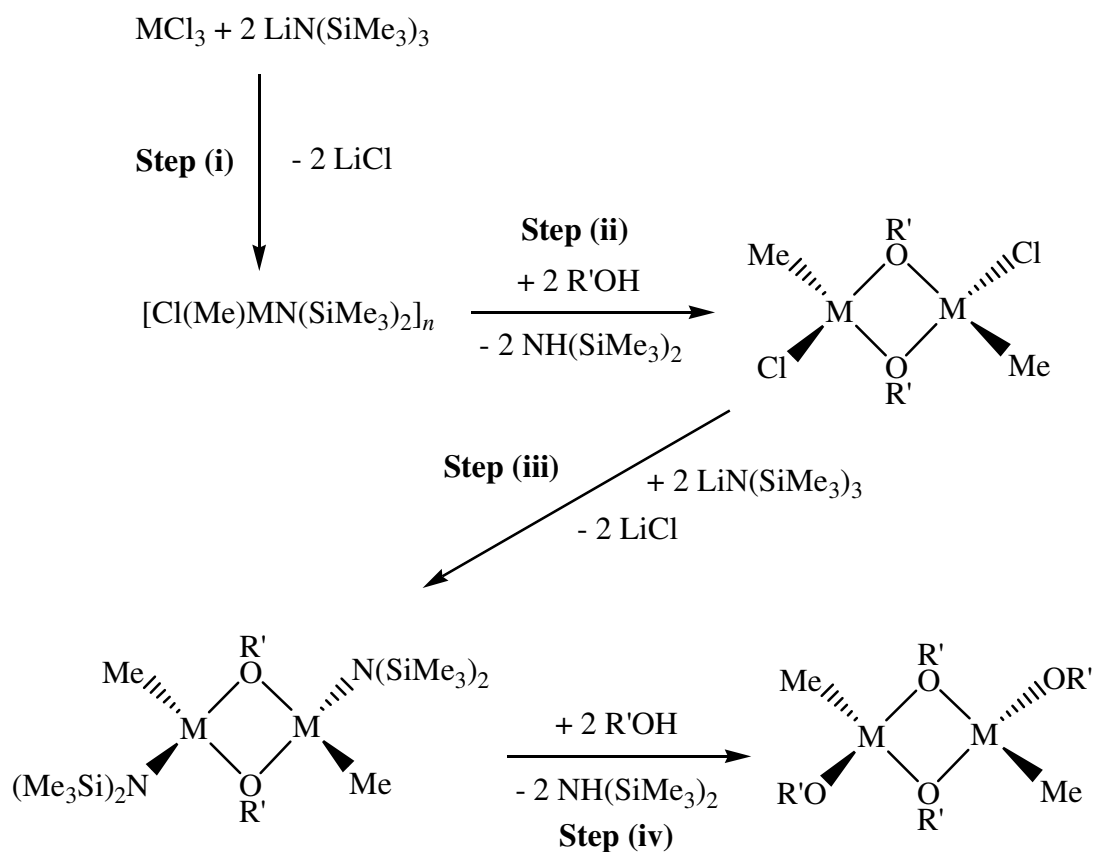
M = In, Ga; R = Me, Et, R' = CH₂CH₂NMe₂, CH(CH₂NMe₂)₂, CH(CH₃)CH₂NMe₂, C(CH₃)₂CH₂OMe, CH(CF₃)₂ and CH₂CH₂OMe.

The use of gallium amides (Route 2) for the synthesis of the corresponding alkoxide was prompted by the earlier successes of this route.¹²



R' = CH₂CH₂NMe₂, CH(CH₂NMe₂)₂, CH(CH₃)CH₂NMe₂ and CH₂CH₂OMe).

The third route (Route 3) followed in this chapter is shown below in Scheme 2.4, and was attempted in order to isolate unsymmetrical group 13 bis(alkoxides).



M = In, Ga; R' = CH₂CH₂NMe₂, CH(CH₂NMe₂)₂, CH(CH₃)CH₂NMe₂, C(CH₃)₂CH₂OMe, and CH₂CH₂OMe)

Scheme 2.4: **Route 3** – Synthetic route for the formation of group 13 bis(alkoxides).

It is proposed that methyl transfer would occur in the first step, according to Scheme 2.4, as described previously.⁵¹ This is an advantage since the final result would be the production of group 13 bis(alkoxide) precursors that contain no chlorine. It is preferential that precursors do not contain atoms such as chlorine or bromine as they are often a source of contamination in the resulting metal oxide thin film. After the initial salt elimination step with methyl transfer, a second step involving reaction with two equivalents of a donor functionalized alcohol should yield the mono(alkoxide) dimer as shown in Scheme 2.4. In a third step, the remaining chloride group is removed *via* a second salt elimination reaction, with a final protonolysis/alcoholysis reaction with a simple alcohol yielding a novel group 13 bis(alkoxide). The use of a simple alcohol group will not just introduce a ligand that follows a clean decomposition path *via* β -hydride elimination, but should also increase volatility, a desired outcome for LPCVD precursors. This size difference will hinder efficient packing between molecules and thus increase the solubility of the compounds, a desired attribute for AACVD precursors.

The fourth route (Route 4) followed in this chapter involves a novel barium chloride salt elimination, resulting in the clean formation of group 13 tris(alkoxides).

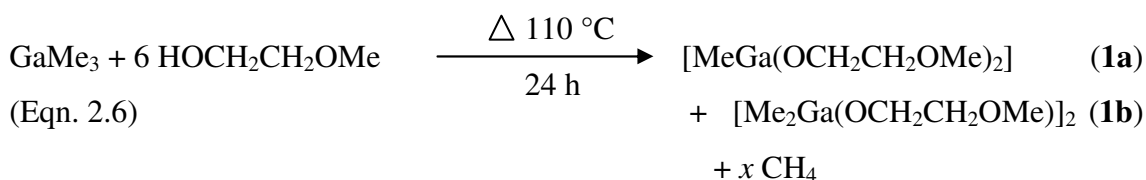


M = Ga, In; R = *i*Pr

2.2.1. Gallium(III) and Indium(III) mono- and bis- (alkoxides).

2.2.1.1. Reaction of GaMe₃ with HOCH₂CH₂OMe

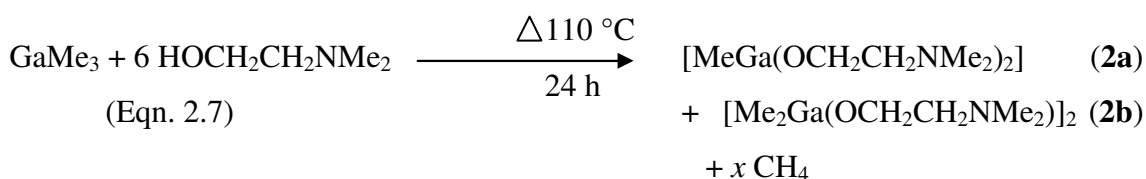
The reaction of GaMe₃ with six equivalents of HOCH₂CH₂OMe in toluene under reflux conditions for 24 hours afforded a mixture of methylgallium bis(alkoxide) [MeGa(OCH₂CH₂OMe)₂] (**1a**) and dimethylgallium alkoxide [Me₂Ga(OCH₂CH₂OMe)₂] (**1b**). ¹H and ¹³C NMR spectroscopic data confirmed the formation of compounds **1a** and **1b**.



The reaction shown in Eqn. 2.6 was successfully carried out, which is based on Route 2, as previously described. In an attempt to isolate the bis(alkoxide) as the sole product, an excess (six equivalents) of alcohol was used, however this resulted in the production of the gallium bis(alkoxide) (**1a**) and the mono(alkoxide) (**1b**). The peaks in the ^1H NMR, whilst displaying broad multiplets did show evidence of the production of **1a**. Peaks at 3.83, 3.37 and 3.26 ppm correspond to the OCH_2CH_2 , CH_2OMe and $\text{O}(\text{CH}_3)$ environments and are in a 14:3 ratio with the peak at -0.22 ppm corresponding to GaCH_3 which is consistent with the formation of the bis(alkoxide) (**1a**). Additional peaks at 3.81, 3.31 and 3.25 ppm corresponding to OCH_2CH_2 , CH_2OMe and $\text{O}(\text{CH}_3)$ of the mono(alkoxide) (**1b**) are in a 7:6 ratio with a peak at -0.21 ppm (GaCH_3). The gallium atom in **1a** is attached to only one methyl group as opposed to three in the starting material, GaMe_3 , which causes a downfield resonance shift of the methyl group in the ^1H NMR, from 0.03 ppm in GaMe_3 to -0.22 ppm in **1a**, a peak observed at -0.21 ppm is also observed for the GaMe_2 in **1b**. The $^{13}\text{C}\{^1\text{H}\}$ NMR spectrum shows two close peaks for the GaCH_3 environment, at 3.26 and 5.26 ppm, the appearance of these peaks would suggest the gallium bis(alkoxide) (**1a**) as well as gallium mono(alkoxide) (**1b**) is present. Mass spectrometry confirms the presence of fragments consistent with the formation of **1a** and **1b**.

2.2.1.2. Reaction of GaMe_3 with $\text{HOCH}_2\text{CH}_2\text{NMe}_2$

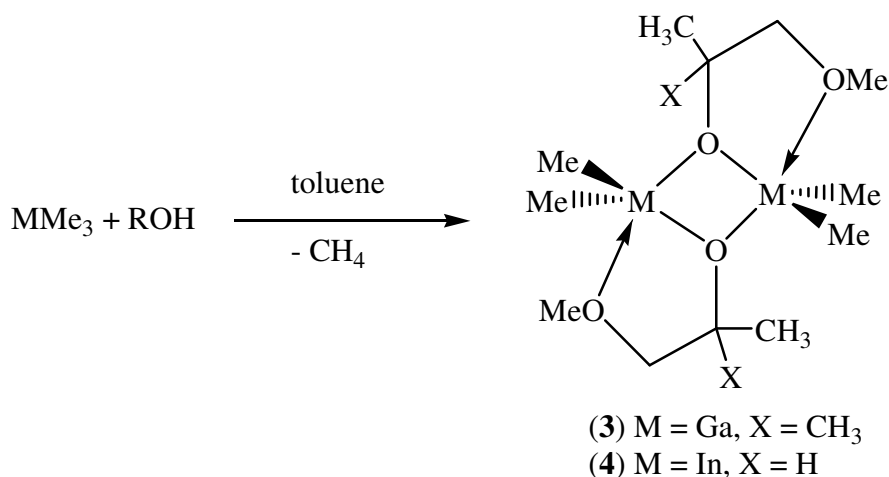
An analogous reaction of GaMe_3 with six equivalents of $\text{HOCH}_2\text{CH}_2\text{NMe}_2$ in toluene under reflux conditions for 24 hours afforded a mixture of the methylgallium bis(alkoxide) $[\text{MeGa}(\text{OCH}_2\text{CH}_2\text{NMe}_2)_2]$ (**2a**) and the dimethylgallium mono(alkoxide) $[\text{Me}_2\text{Ga}(\text{OCH}_2\text{CH}_2\text{NMe}_2)]_2$ (**2b**) (Eqn. 2.7). Spectroscopic data confirmed the formation of compounds **2a** and **2b**.



The reaction shown in Eqn. 2.7 was successfully carried out, which is based on Route 2, as previously described. As with Eqn. 2.6, the excess of alcohol used resulted in the production of the gallium bis(alkoxide). ^1H NMR data shows the methyl group on the gallium in **2a** (-0.12 ppm) to be significantly more upfield than that of the starting material, GaMe_3 (0.03 ppm), a similar peak observed at -0.21 ppm can be assigned to the corresponding GaMe_2 for **2b**. Peaks at 3.68, 2.37 and 2.31 can be assigned to the environments OCH_2CH_2 , CH_2NMe_2 and $\text{N}(\text{CH}_3)_2$, respectively, and are in a 20:3 ratio with the peak at -0.12, assigned to GaMe indicating the presence of **2a**. Similarly peaks observed at 3.71, 2.38 and 2.34 ppm (OCH_2CH_2 , CH_2NMe_2 and $\text{N}(\text{CH}_3)_2$), are in a 5:3 ratio with the peak at -0.21 ppm assigned to GaMe_2 indicating the presence of **2b**. The appearance of two close peaks for the GaMe environment in the $^{13}\text{C}\{^1\text{H}\}$ NMR spectrum, at 11.4 ppm (**2a**) and 11.7 ppm (**2b**) indicate the mixture of **2a** and **2b**, as observed for **1a** and **1b**, all peaks in the $^{13}\text{C}\{^1\text{H}\}$ NMR show evidence of the formation of **2a** and **2b**. The mass spectrum also supports the formation of a mixture. A molecular peak at 261 corresponds to the bis(alkoxide) **2a**, whilst other molecular ion peaks at 172, 88 and 72 correspond to $(\text{MeGaOCH}_2\text{CH}_2\text{NMe}_2)$, $(\text{OCH}_2\text{CH}_2\text{NMe}_2)$ and $(\text{CH}_2\text{CH}_2\text{NMe}_2)$, respectively, which could be due to the presence of either **2a** or **2b**. In the above two examples, it can be concluded that this route does not yield solely the gallium bis(alkoxide) but rather yields a mixture of the gallium mono and bis(alkoxides), **1a**, **2a** and **1b**, **2b** respectively.

2.2.1.3. Reaction of GaMe_3 with $\text{HOC}(\text{CH}_3)_2\text{CH}_2\text{OMe}$

Treatment of GaMe_3 with an excess of $\text{HOC}(\text{CH}_3)_2\text{CH}_2\text{OMe}$ in toluene under reflux conditions for 24 hours afforded $[\text{Me}_2\text{Ga}(\text{OC}(\text{CH}_3)_2\text{CH}_2\text{OMe})]_2$ (**3**). A white powder was isolated after work-up of the reaction mixture from which colourless crystals of **3** suitable for single crystal X-ray diffraction, were afforded. Analytical and spectroscopic data for **3** indicated that the dimeric complex **3** had been isolated (Scheme 2.5).



Scheme 2.5: Synthesis of complexes of the type $[\text{Me}_2\text{M}(\mu\text{-OR})]_2$.

Peaks observed in the ^1H NMR spectrum at 3.34, 3.11 and 1.17 ppm corresponding to the OCH_3 , CH_2 and CH_3 groups of the alkoxide ligand respectively, were in a 11:6 ratio with a peak at -0.33 ppm assigned to GaMe_2 . This is consistent with the formation of compound **3**. Single peaks at 2.5, 27.2, 58.1, 72.6 and 81.7 ppm in the ^{13}C $\{^1\text{H}\}$ NMR were also consistent with the expected OCCH_2 , OCCH_2 , OCH_3 , OCCH_3 and GaCH_3 carbon environments, respectively. FT-IR confirmed the presence of ring modes with frequencies at 534 cm^{-1} which are attributable to characteristic ring modes of the Ga_2O_2 unit. In the mass spectrum obtained from a solution of **3** in toluene, the molecular ion minus a methyl group peak at $m/z = 391$ was observed, supporting the proposed dimeric structure of the complex. This is further confirmed by intense peaks ($m/z = 303$ and 187) corresponding to molecular fragmentation of the dimeric structure. Interestingly a large peak corresponding to the ligand fragment ($\text{OC}(\text{CH}_3)_2\text{CH}_2\text{CH}_2\text{OMe}_2$) was observed and could provide some evidence of a potential decomposition pathway to gallium oxide. Therefore, combination of spectroscopic techniques confirmed the isolation of **3**, and there was no evidence for the formation of any bis(alkoxide). The structure of **3** was also confirmed by X-ray crystallography, the details of which are described in section 2.2.1.3.1.

2.2.1.3.1. X-Ray crystallographic studies of $[\text{Me}_2\text{GaOC}(\text{CH}_3)_2\text{CH}_2\text{OMe}]_2$
(3)

Table 2.1. Selected bond lengths (Å) and angles (°) for $[\text{Me}_2\text{Ga}(\text{OC}(\text{CH}_3)_2\text{CH}_2\text{OMe})]_2$
(3)

Ga(1)-O(1)	1.9331(11)	Ga(1)-C(6)	1.9672(18)
Ga(1)-O(1) ⁱ	2.0051(11)	Ga(1)-C(7)	1.9605(19)
Ga(1)-O(2)	2.6282(18)		
Ga(1) ⁱ -O(1)-Ga(1)	102.91(5)	O(1)-Ga(1)-C(6)	111.28(7)
O(1) ⁱ -Ga(1)-O(1)	77.09(5)	O(1)-Ga(1)-C(7)	115.29(7)
C(2)-O(1)-Ga(1)	129.07(1)	C(6)-Ga(1)-C(7)	127.75(10)
C(2)-O(1)-Ga(1)	126.14(1)	C(6)-Ga(1)-O(1A)	106.56(7)
C(5)-O(2)-C(4)	112.43(15)	C(7)-Ga(1)-O(1A)	105.37(7)

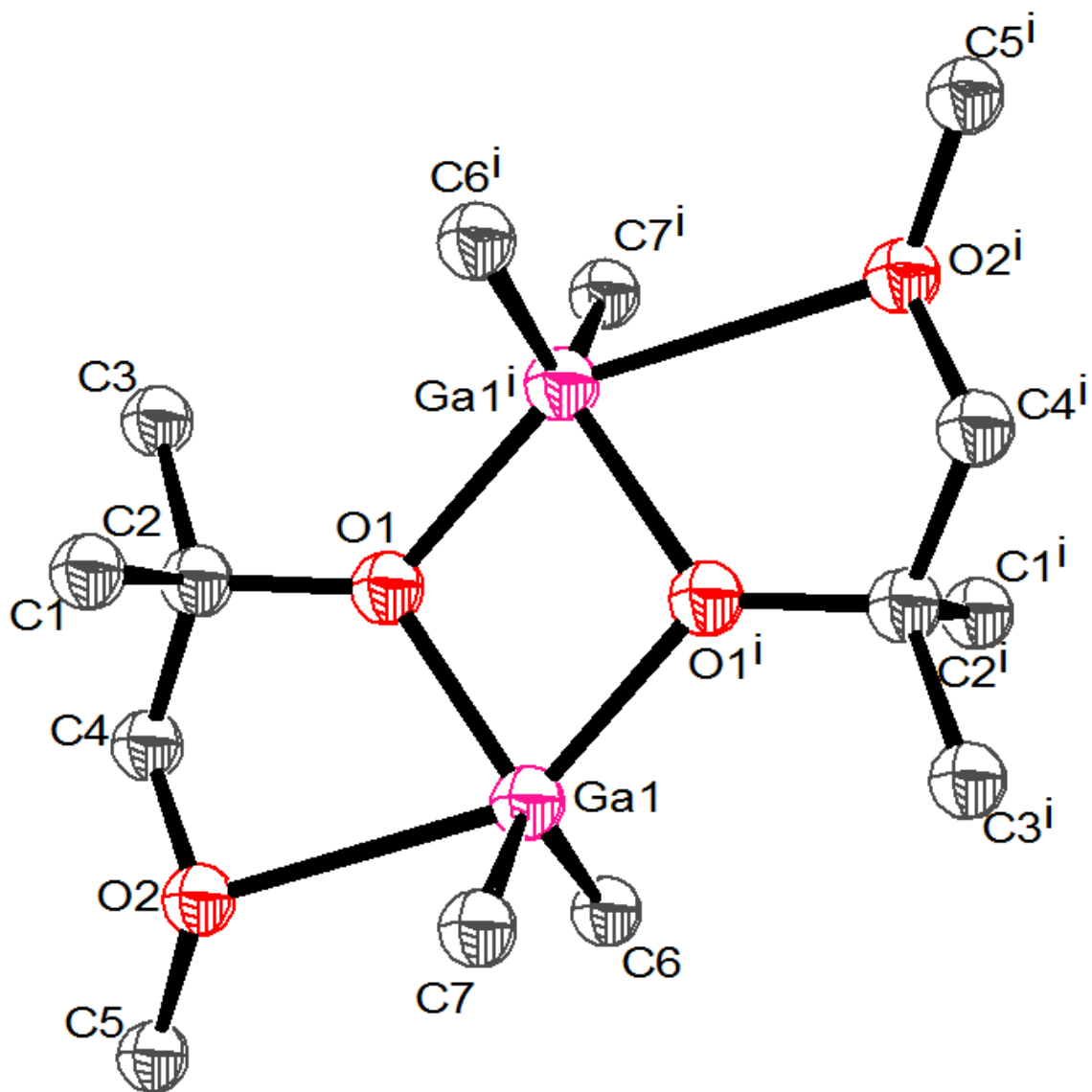


Fig. 2.5: X-Ray crystal structure of $[\text{Me}_2\text{Ga}(\text{OC}(\text{CH}_3)_2\text{CH}_2\text{OMe})_2]$ (**3**).

The crystal structure of compound **3** was determined by single crystal X-ray diffraction and the results are shown in Fig. 2.5; selected bond lengths and angles are given in Table 2.1. Compound **3** crystallised in the monoclinic space group $P2_1/n$ and lies on an inversion centre in the unit cell. It is dimeric in the solid state with the two gallium cations and two alkoxide oxygen anions forming a centrosymmetric, planar four-membered Ga_2O_2 ring that is common to this type of compound. Each monomeric unit is composed of one gallium cation, two methyl groups and a bidentate alkoxide ligand which forms a 5-membered gallacycle ring.

Each gallium atom in **3** adopts a distorted trigonal bipyramidal geometry with the methyl groups in equatorial positions. The alkoxide [crystallographic O(1)] of one bidentate ligand is located in the equatorial position whereas the bridging alkoxide O(1ⁱ) from the other gallium centre is in an axial position, along with the oxygen atom of the neutral methoxy group [crystallographic O(2)]. The equatorial Ga(1)–O(1) bond length of 1.9331(11) Å is significantly shorter than the bridging Ga(1)–O(1ⁱ) bond distance of 2.0051(11) Å. The Ga(1)–O(2) distance of 2.6282(14) Å can be attributed to O→Ga dative bonding.

The axial bond angle [crystallographic O(1ⁱ)–Ga(1)–O(2)] is 148.31(4)°: this large deviation from the ideal is due to the constraints of the internal O–Ga–O angle [77.09(5)°] in the Ga_2O_2 ring and the geometry of the bidentate ligand. The sum of the bond angles in the equatorial plane of **3** is 354°, which is a measure of the planarity of the equatorial groups.

2.2.1.4. Reaction of $InMe_3$ with $HOCH(CH_3)CH_2OMe$

Treatment of $InMe_3$ with an excess of $HOCH(CH_3)CH_2OMe$ in toluene resulted in the formation of $[Me_2In(OCH(CH_3)CH_2OMe)]_2$ (**4**). An oil was isolated after work-up of the reaction mixture from which colourless crystals of **4**, suitable for single crystal X-ray diffraction, were afforded in high yield. Analytical and spectroscopic data for **4** indicated that the expected dimeric complex of the type $[Me_2M(\mu-OR)]_2$ had been isolated (Scheme 2.5). The reaction of $InMe_3$ with other donor-functionalized alcohols

has been previously reported to yield the complexes of type, $[\text{Me}_2\text{In}(\mu\text{-OR})]_2$.^{14,16,17} Peaks in the ^1H NMR of **4** at 3.95, 3.27, 3.04 and 1.04 ppm are consistent with the hydrogen environments at InOCHCH_3 , OCH_3 , InOCHCH_2 and InOCHCH_3 , respectively and are in a 3:2 ratio with the peak at 0.43 ppm consistent with the InMe_2 environment. The presence of 5 clean peaks in the $^{13}\text{C}\{^1\text{H}\}$ NMR at 79.39, 66.25, 58.04, 20.85 and 0.99 ppm were consistent with all carbon environments in the mono(alkoxide), **4** (CHCH_2OMe , $\text{OCH}(\text{CH}_3)$, CH_2OCH_3 , InCH_3 and $\text{InCH}(\text{CH}_3)\text{CH}_2$). In the mass spectrum obtained from a solution of **4** in toluene, the molecular ion minus a methyl group peak at $m/z = 453$ was observed, supporting the proposed dimeric structure of the complex. This is further confirmed by intense peaks ($m/z = 407$ and 319) corresponding to molecular fragmentation of the dimeric structure. An intense peak for the monomeric structure ($m/z = 219$) is observed, these fragments may arise from the symmetric cleavage of the In_2O_2 ring, during decomposition. A combination of spectroscopic techniques confirmed the isolation of **4**. The structure of **4** was confirmed by X-ray crystallography, the details of which are described in section 2.2.1.4.1.

2.2.1.4.1. X-Ray crystallographic studies of $[\text{Me}_2\text{In}(\text{OCH}(\text{CH}_3)\text{CH}_2\text{OMe})]$ (**4**)

Table 2.2. Selected bond lengths (Å) and angles (°) for $[\text{Me}_2\text{In}(\text{OCH}(\text{CH}_3)\text{CH}_2\text{OMe})]$ (**4**)

$\text{In}(1)\text{-O}(1)$	2.107(4)	$\text{In}(1)\text{-C}(1)$	2.102(7)
$\text{In}(1)\text{-O}(1)^i$	2.179(4)	$\text{In}(1)\text{-C}(2)$	2.092(8)
$\text{In}(1)\text{-O}(2)$	2.584(5)		
$\text{In}(1)^i\text{-O}(1)\text{-In}(1)$	105.23(17)	$\text{O}(1)\text{-In}(1)\text{-C}(1)$	87.9(2)
$\text{O}(1)^i\text{-In}(1)\text{-O}(1)$	74.77(17)	$\text{O}(1)\text{-In}(1)\text{-C}(2)$	92.8(3)
$\text{C}(5)\text{-O}(1)\text{-In}(1)$	122.5(4)	$\text{C}(1)\text{-In}(1)\text{-C}(2)$	137.6(3)
$\text{C}(5)\text{-O}(1)\text{-In}(1)$	128.6(4)	$\text{C}(1)\text{-In}(1)\text{-O}(1)^i$	100.5(2)
$\text{C}(3)\text{-O}(2)\text{-C}(4)$	114.8(5)	$\text{C}(2)\text{-In}(1)\text{-O}(1)^i$	103.2(3)

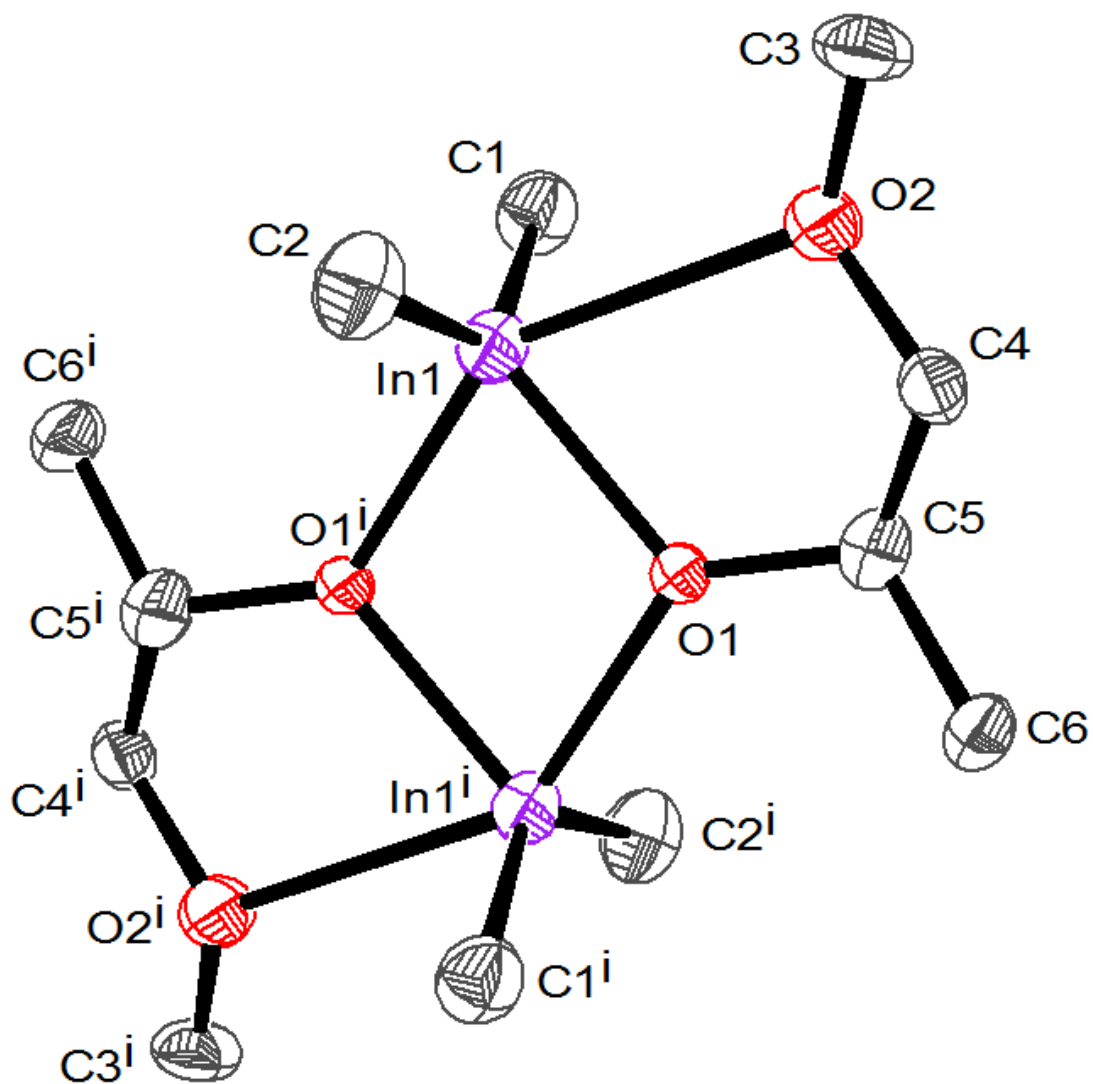


Fig. 2.6: X-Ray crystal structure of $[\text{Me}_2\text{In}(\text{OCH}(\text{CH}_3)\text{CH}_2\text{OMe})_2]$ (4).

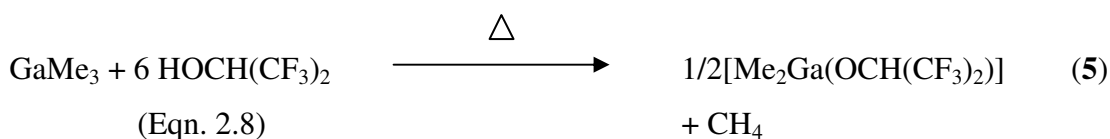
The crystal structure of compound **4** is shown in Fig. 2.6; selected bond lengths and angles are also given in Table 2.2 above. Compound **4** crystallised in the monoclinic space group $P2_1/c$ and also lies on an inversion centre in the unit cell. Like compound **3**, it is dimeric in the solid state with the indium cations and alkoxide oxygen anions forming a centrosymmetric, four-membered In_2O_2 planar ring and the bidentate ligand forming a five-membered indacycle ring. The geometry at the indium atoms is very similar to that in compound **3** with two methyl groups and an alkoxide oxygen anion in the equatorial positions whereas the bridging alkoxide group and neutral methoxy donor are located in the axial positions.

The $\text{O}(1)\text{--In}(1)\text{--O}(2)$ bond angle is $144.23(15)^\circ$; similarly to **3**, the large deviation from ideal is due to the bidentate ligand, but the deviation is slightly larger which is probably due to the larger ionic radius of indium compared to gallium. As expected, the equatorial $\text{In}(1)\text{--O}(1)$ bond length of $2.107(4)$ Å is significantly shorter than the axial bridging $\text{In}(1)\text{--O}(1')$ bond distance of $2.179(4)$ Å. The $\text{In}(1)\text{--O}(2)$ distance of $2.504(5)$ Å in **4** can be attributed to $\text{O}\rightarrow\text{In}$ dative bonding, although interestingly it is shorter than the corresponding axial $\text{Ga}(1)\text{--O}(2)$ distance in compound **3**.

The structures of compounds **3** and **4** are similar to related compounds of the type $[\text{R}_2\text{M}(\mu\text{-OR}')_2]$ ($\text{R}' =$ donor functionalized group) which have been previously reported; all bond lengths and angles are comparable.^{9,15-17,68}

2.2.1.5. The reaction of GaMe_3 with $\text{HOCH}(\text{CF}_3)_2$

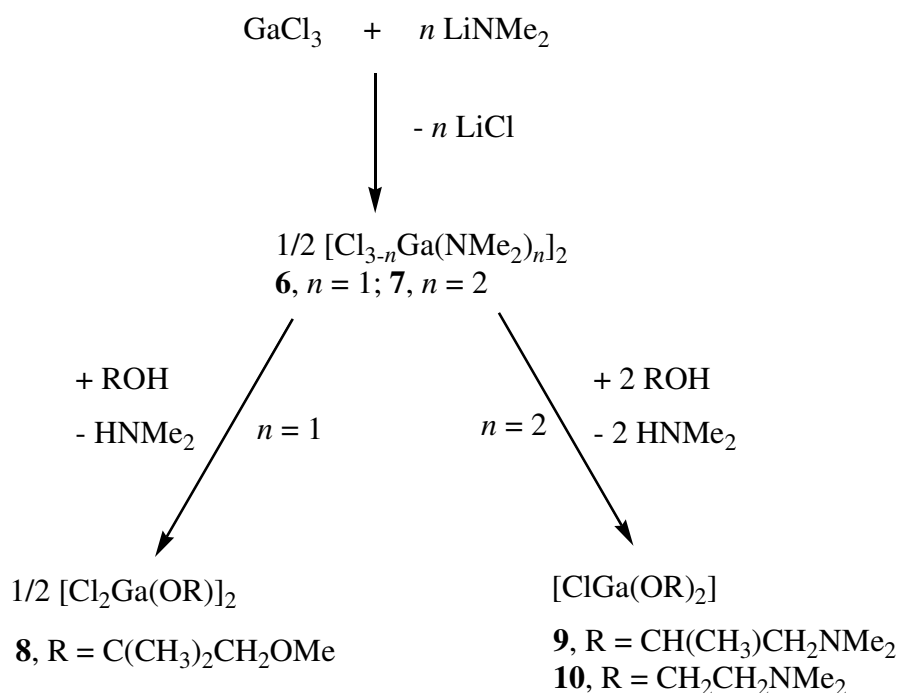
The reaction of GaMe_3 with six equivalents of $\text{HOCH}(\text{CF}_3)_2$ in toluene under reflux conditions for 24 hours afforded the dimethylgallium fluorinated alkoxide $[\text{Me}_2\text{Ga}(\text{OCH}(\text{CF}_3)_2)]_2$ (**5**), as a dark brown oil. Spectroscopic data confirmed the formation of compound **5**.



The reaction shown in Eqn. 2.8 was successfully carried out, which is based on Route 1, as previously described. Compound **5** was isolated solely as a gallium mono(alkoxide), and there was no evidence for the presence of the bis(alkoxide), despite excess alcohol being used. It was hoped that the presence of the electron withdrawing CF₃ groups on the alkoxide ligand, as well as adding steric repulsion, would reduce the bridging capacity of the oxygen atom and thus prevent the dimer formation, much like it does in the compound [Me₂Ga(OC(CF₃)₂CH₂NMe₂)].¹³ The main peaks in the ¹H NMR spectrum at 0.20 and 4.46 ppm can be assigned to the GaCH₃ and OCH hydrogen environments, with a 6:1 ratio being consistent with the formation of the mono(alkoxide) **5**. Three peaks at 120.0, 71.8 and 1.0 ppm in the ¹³C{¹H} NMR are consistent with the carbon environments in **5**. Complex NMR spectra suggest that whilst the major product is **5**, monomers, dimers and tetramers are present in solution. In ¹H NMR data, a multiplet is observed for GaCH₃ at 0.20 ppm, which suggests a mixture of products. The peak observed at 0.20 ppm is a downfield shift from the starting material GaMe₃ (observed at 0.03 ppm). This downfield shift indicates the electron density being pulled away from the metal centre and thus the methyl group. The Ga₂O₂ ring modes were observed at 535 cm⁻¹ in the IR spectrum, consistent with the dimeric structure of **5**, as well as C-F bonds at 1374, 1292 and 1194 cm⁻¹. The mass spectrum shows several molecular ion peaks indicating a presence of mixtures in the compound, including 221 indicating ((CF₃)₂MeGa), 169 indicating (GaCF₃CHO), and 149 ((CF₃)₂C).

2.2.2. Gallium(III) mono and bis (alkoxides) via amine-alcohol exchange.

The synthesis of gallium(III) mono and bis(alkoxides) was investigated using an amine-alcohol exchange route shown in Scheme 2.5.

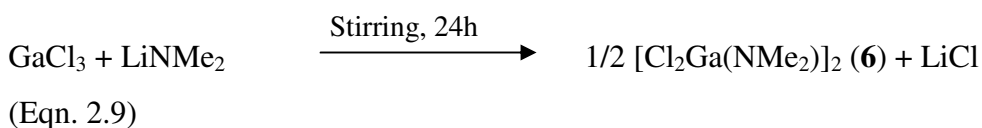


Scheme 2.6: Synthesis of gallium(III) mono and bis(alkoxides) using an amine-alcohol exchange reaction based on Route 2.

The first step is the reaction of GaCl_3 with either one or two equivalents of LiNMe_2 , resulting in a chlorogallium amide, of the type $[\text{Cl}_{3-x}\text{Ga}(\text{NMe}_2)_x]_n$ ($x = 1$ (**6**); 2 (**7**)). The second step involved the treatment of **6** or **7** with ROH to produce the mono or bis alkoxide ($\text{R} = \text{OC}(\text{CH}_3)_2\text{CH}_2\text{OMe}$ (**8**), $\text{OCH}(\text{CH}_3)\text{CH}_2\text{NMe}_2$ (**9**), $\text{OCH}_2\text{CH}_2\text{NMe}_2$ (**10**)) as detailed in sections 2.2.2.3 – 2.2.2.5.

2.2.2.1. Reaction of GaCl_3 with $\text{Li}(\text{NMe}_2)$

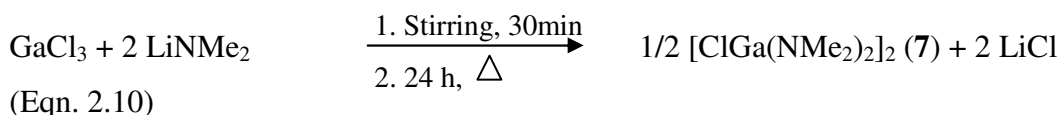
The reaction of GaCl_3 with the dropwise addition of one equivalent of LiNMe_2 , in toluene initially at -78°C with stirring for 24 hours at room temperature afforded the dichloro gallium amide $[\text{Cl}_2\text{Ga}(\text{NMe}_2)]_2$ (**6**), as a free flowing white powder in high yield (Eqn. 2.9). ^1H NMR spectroscopic data confirmed the formation of compound **6**.



The reaction shown in Eqn. 2.9 was successfully carried out, which is based on Route 2 as previously described. The ^1H NMR of **6** shows one clear peak at 2.76 ppm corresponding to the single hydrogen environment ($-\text{N}(\text{CH}_3)_2$). A single peak at 44.0 ppm in the $^{13}\text{C}\{^1\text{H}\}$ NMR supports the formation of **6**. In the mass spectrum obtained from a solution of **6** in toluene, a peak was observed for the molecular ion at $m/z = 366$, supporting the proposed dimeric structure of the complex. This is further confirmed by an intense peak at $m/z = 297$ corresponding to molecular fragmentation of the dimeric structure. An intense peak for the monomeric structure ($m/z = 148$) was also observed, these fragments may arise from the symmetric cleavage of the Ga_2N_2 ring, during decomposition.

2.2.2.2. Reaction of GaCl_3 with 2 equivalents of $\text{Li}(\text{NMe}_2)$

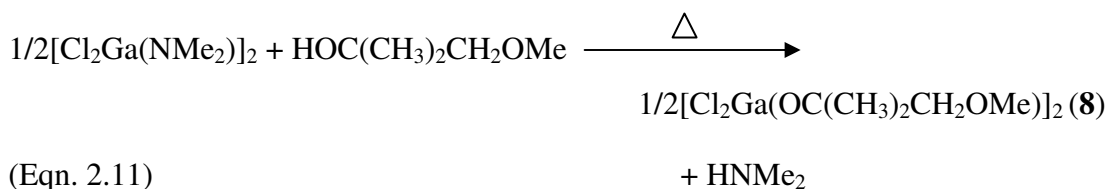
The reaction of GaCl_3 with two equivalents of LiNMe_2 in toluene initially at $-78\text{ }^\circ\text{C}$ with stirring for 24 hours at room temperature, afforded the chloro-gallium dimethyl amide [$\text{ClGa}(\text{NMe}_2)_2$] (**7**), as a free flowing white powder in high yield (Eqn. 2.10). Analytical and spectroscopic data confirmed the formation of compound **7**.



The reaction shown in Eqn. 2.10 is based on Route 2 and compound **7** was successfully isolated for use as a precursor. ^1H NMR of **7** shows peaks at 2.30 and 2.75 ppm corresponding to the terminal and bridging dimethylamido environments seen in **7**. In the mass spectrum of **7** taken in toluene, a peak was observed for the molecular ion at $m/z = 387$, supporting the proposed dimeric structure of **7**. This is further confirmed by an intense peak at $m/z = 308$ corresponding to molecular fragmentation of the dimeric structure. This compound was used *in situ* to produce gallium bis(alkoxides), as shown in Route 3 and detailed in sections 2.2.2.4 and 2.2.2.5.

2.2.2.3. Reaction of **6** with HOC(CH₃)₂CH₂OMe

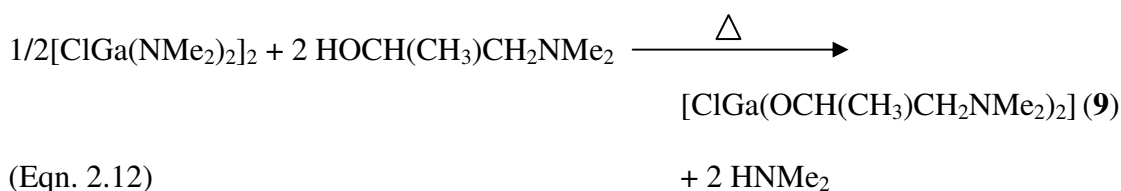
The reaction of **6** with one equivalent of HOC(CH₃)₂CH₂OMe in toluene, afforded the dichloro gallium alkoxide, [Cl₂Ga(OC(CH₃)₂CH₂OMe)]₂ (**8**), as a pale yellow solid (Eqn. 2.11).



The reaction shown in Eqn. 2.11 is based on Route 3, as described in section 2.2. Analytical and spectroscopic data for **8** was consistent with the formulation [Cl₂Ga(OC(CH₃)₂CH₂OMe)]₂. Peaks observed in the ¹H NMR spectrum at 3.60, 2.58 and 1.48 ppm, assigned to the hydrogen environments OCH₃, OCCH₂ and OC(CH₃), respectively, provide evidence for the isolation of **8**. Corresponding peaks in the ¹³C{¹H} NMR at 79.9 (OCCH₂), 70.1 (OCCH₂), 58.9 (OCH₃), 26.1 (OC(CH₃)) are also consistent with the synthesis of **8**. Importantly the shift in ¹H NMR of **6** at 2.75 ppm corresponding to the Ga-NMe₂ group, was not present in the ¹H NMR spectrum of **8**, indicating there is no mixture of products. The resonance of protons positioned α to the donor heteroatom showed a downfield shift in the ¹H NMR of **8**, compared to the free ligand indicating a dative ligand-metal interaction. In the mass spectrum of **8**, taken in toluene, peaks observed at *m/z* = 451 and 290 are consistent with molecular fragmentation of the dimeric structure.

2.2.2.4. Reaction of **7** with 2 equivalents of HOCH(CH₃)CH₂NMe₂

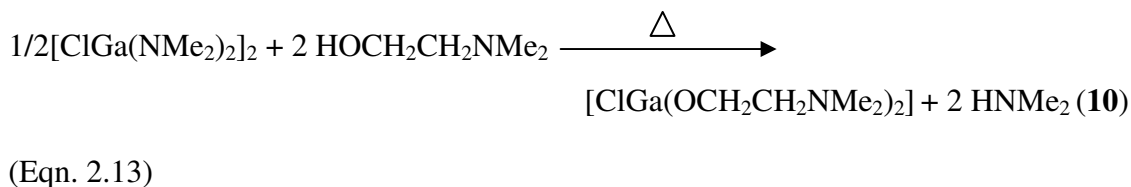
The reaction of **7** with two equivalents of HOCH(CH₃)CH₂NMe₂ in toluene under reflux conditions for 24 hours, afforded the monomeric chloro-gallium bis(alkoxide): [ClGa(OCH(CH₃)CH₂NMe₂)₂] (**9**), as a yellow viscous oil. Analytical and spectroscopic data confirmed the formation of compound **9**. The reaction is based on Route 3, as detailed in section 2.2, shown below in Eqn. 2.12.



The peaks in the ^1H NMR spectrum, show evidence of the production of **9**. Peaks were observed at 1.31, 2.29, 2.41, 2.49 and 3.95 ppm, corresponding to the $\text{OCH}(\text{CH}_3)$, OCHCH_2N , NCH_3 and $\text{OCH}(\text{CH}_3)\text{CH}_2$, and are in a 6:4:12:2 ratio, which is consistent with the formation of **9**. A downfield shift in the resonance of protons positioned α to the donor heteroatom was observed and confirms a dative-ligand metal interaction in **9**. In the mass spectrum of **9** taken in toluene, a peak is observed for the molecular ion at $m/z = 309$, supporting the proposed monomeric structure of **9**. This is further confirmed by an intense peak at $m/z = 273$, corresponding to molecular fragmentation of this structure. Interestingly a large peak corresponding to the ligand fragment $\text{OCH}(\text{CH}_3)\text{CH}_2\text{NMe}_2$ was observed, which could provide some evidence of a potential decomposition pathway to gallium oxide.

2.2.2.5. Reaction of **7** with 2 equivalents of $\text{HOCH}_2\text{CH}_2\text{NMe}_2$

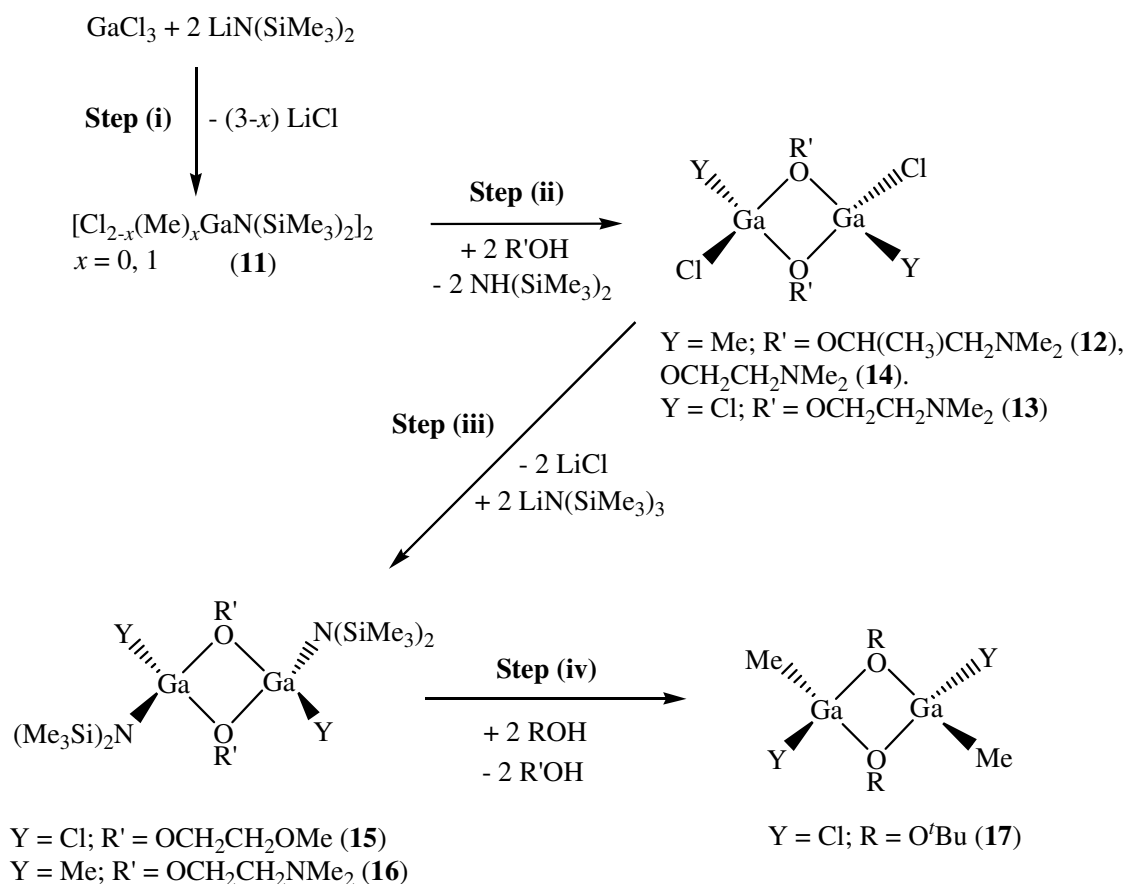
The reaction of **7** with two equivalents of $\text{HOCH}_2\text{CH}_2\text{NMe}_2$ in toluene, under reflux conditions for 24 hours, afforded the monomeric chlorogallium bis(alkoxide), $[\text{ClGa}(\text{OCH}_2\text{CH}_2\text{NMe}_2)_2]$ (**10**), as a yellow viscous oil (Eqn. 2.13). Analytical and spectroscopic data confirmed the formation of compound **10**.



The reaction shown in Eqn. 2.13 is based on Route 3, as previously described (section 2.2). Peaks observed in the ^1H NMR spectrum at 2.00, 2.27 and 3.93 ppm can be assigned to the NCH_3 , $\text{OCH}_2\text{CH}_2\text{N}$ and $\text{OCH}_2\text{CH}_2\text{N}$ hydrogen environments respectively, and are in a 12:4:4 ratio, which is consistent with the formation of **10**. As with **9**, a downfield shift in the ^1H NMR in the resonance of protons positioned α to the donor heteroatom confirms a dative ligand-metal interaction in **10**. In the mass spectrum of **10** taken in toluene, a peak is observed for the molecular ion at $m/z = 281$ which supports the proposed monomeric structure of **10**. This is further confirmed by intense peaks at $m/z = 246$, 194 and 158 corresponding to molecular fragmentation of this structure. Interestingly a large peak corresponding to the ligand fragment $\text{OCH}_2\text{CH}_2\text{NMe}_2$ ($m/z = 88$) was observed which could provide some evidence of a potential decomposition pathway to gallium oxide. Furthermore, it can be concluded, the reaction of $[\text{ClGa}(\text{NMe}_2)_2]$ and two equivalents of ROH, as reported for the synthesis of **9** and **10**, provide a clean route to the novel gallium bis(alkoxides).

2.2.3. Unsymmetrical gallium(III) bis(alkoxides)

The attempted synthesis of unsymmetrical gallium(III) bis(alkoxides) was investigated using the four step synthetic route shown in Scheme 2.4 in section 2.2. In light of this work a slightly amended Scheme 2.6 details the routes followed in the synthesis described in sections 2.2.3.1 - 2.2.3.7.



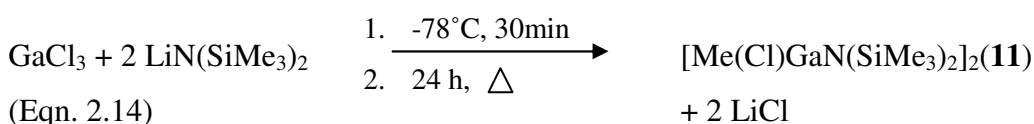
Scheme 2.7: Synthetic route for the formation of gallium(III) bis(alkoxides).

It is proposed that methyl transfer would occur in the first step, according to Scheme 2.7, as with the indium analogue, described previously.⁵¹ This is an advantage since the production of a group 13 bis(alkoxide) precursor that contains no chlorine would result. After the initial salt elimination step (**Step (i)**) with methyl transfer, **Step (ii)** involves the addition of two equivalents of a donor functionalized alcohol, yielding a mono(alkoxide) dimer (Scheme 2.7). In **Step (iii)**, the remaining chloride group is removed *via* a second salt elimination reaction. However, it has been observed that in **Step (i)** the proposed methyl transfer does not always occur, meaning that a chloride group can still be present in the compound. **Step (iv)** involves a protonolysis/alcoholysis reaction with a monofunctional alcohol, which results in a novel gallium(III) bis(alkoxide). The use of a simple alcohol group in **Step (iv)** should yield a precursor, that, follows a clean decomposition path *via* β -hydride elimination and is highly volatile, both desired outcomes for LPCVD precursors. It was hoped that **Step (iv)** would result in the isolation of an unsymmetrical gallium(III) bis(alkoxide), of the type $[\text{MeGa}(\text{OR})(\text{OR}')_2]$. It is proposed that size difference would hinder efficient packing

between molecules and thus increase the solubility of the compounds, a desired attribute for AACVD precursors. However, exchange of the donor functionalised alcohol with the monofunctional alcohol occurred to afford $[\text{Me}(\text{Y})\text{GaOR}]_2$.

2.2.3.1. Reaction of GaCl_3 with $\text{LiN}(\text{SiMe}_3)_2$

The reaction of GaCl_3 with two equivalents of $\text{LiN}(\text{SiMe}_3)_2$ in toluene, at -78°C initially, then under reflux conditions for 24 hours afforded the methyl-chloro-gallium amide dimer, $[\text{Me}(\text{Cl})\text{Ga}\{\text{N}(\text{SiMe}_3)_2\}]_2$ (**11**). A white viscous liquid was isolated, which was purified by sublimation. Analytical and spectroscopic data indicated the formation of compound **11**, which involved a methyl group transfer from the Me_3Si group to the gallium centre, as previously reported.⁵¹

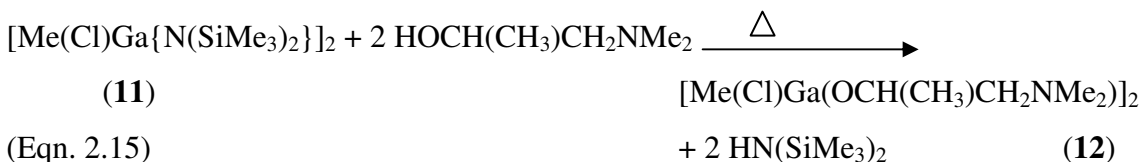


The reaction shown in Eqn. 2.14 was successfully carried based on **Step (i)** detailed in section 2.2 and Scheme 2.7. A peak observed in the ^1H NMR spectrum of the product at 0.28 ppm corresponds to the $\text{N}(\text{Si}(\text{CH}_3)_3)$ hydrogen environment and is in a 6:1 ratio with a peak at 0.03 ppm consistent with the GaCH_3 environment, confirming the formation of **11**. Peaks observed in the $^{13}\text{C}\{^1\text{H}\}$ NMR spectrum for the GaCH_3 and $\text{N}(\text{Si}(\text{CH}_3)_3)$ environments at 23.2 and 4.7 ppm, respectively, also support the formation of **11**. In the mass spectrum of **11** taken in toluene, a peak is observed for the molecular ion at $m/z = 279$ which provides evidence for the proposed dimeric structure of **11**. This is confirmed by large peaks at $m/z = 244$ and 201 consistent with fragments of the dimeric structure reported for **11**. Compound **11** has been isolated for use as a precursor as shown in scheme 2.6, and will feature largely in the following sections.

2.2.3.2. Reaction of **11** with $\text{HOCH}(\text{CH}_3)\text{CH}_2\text{NMe}_2$

Compound **11** was prepared *in situ* as described in section 2.2.3.1. The dropwise addition of two equivalents of $\text{HOCH}(\text{CH}_3)\text{CH}_2\text{NMe}_2$ in toluene, to compound **11** followed by heating under reflux conditions for 24 hours afforded the dimeric methyl-

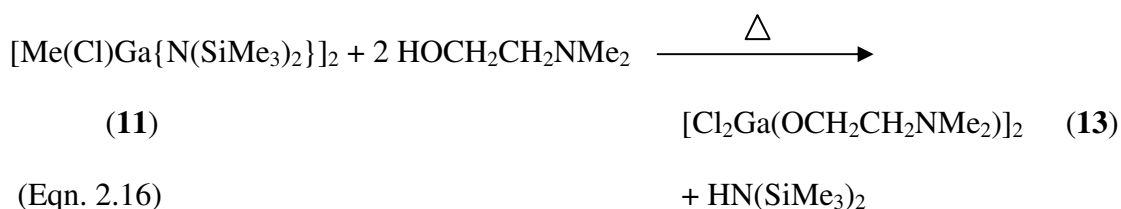
chloro-gallium alkoxide, $[\text{Me}(\text{Cl})\text{Ga}(\text{OCH}(\text{CH}_3)\text{CH}_2\text{NMe}_2)]_2$ (**12**). Compound **12** was isolated as small colourless crystals after sublimation in a long Schlenk flask over an oil bath at 50 °C under a dynamic vacuum. Analytical and spectroscopic data confirmed the formation of compound **12**.



The reaction shown in Eqn. 2.15 was successfully carried out, which is based on Step (ii) in Scheme 2.6. Evidence of the formation of **12** was obtained from the ^1H NMR spectrum, with peaks at 4.05, 2.31 and 0.22 ppm which can be assigned to the hydrogen environments: $\text{OCH}(\text{CH}_3)$, $\text{OCH}(\text{CH}_3)\text{CH}_2$ and $\text{N}(\text{CH}_3)_2$, and are in an overall 4:1 ratio with the peak observed at 0.06 ppm which is assigned to the GaCH_3 moiety. Five clear peaks observed in the $^{13}\text{C}\{^1\text{H}\}$ NMR spectrum at 23.0, 48.2, 64.5, 66.3 and 67.8 ppm can be assigned to the carbon environments of GaCH_3 , $\text{OCH}(\text{CH}_3)$, $\text{N}(\text{CH}_3)_2$, $\text{CH}(\text{CH}_3)\text{CH}_2$ and $\text{OCH}_2(\text{CH}_3)$. In the mass spectrum, a molecular ion was observed at $m/z = 4429$, supporting the proposed dimeric structure of **12**. This is confirmed by large peaks at $m/z = 412$ and 293 consistent with fragments of the dimeric structure reported for **12**.

2.2.3.3. Attempted reaction of **11** with $\text{HOCH}_2\text{CH}_2\text{NMe}_2$

The dropwise addition of two equivalents of $\text{HOCH}_2\text{CH}_2\text{NMe}_2$ to compound **11** prepared *in situ* (section 2.2.3.1), in toluene under reflux conditions for 24 hours afforded the dimeric dichlorogallium alkoxide, $[\text{Cl}_2\text{Ga}(\text{OCH}_2\text{CH}_2\text{NMe}_2)]_2$ (**13**). Compound **13** was isolated as small colourless crystals suitable for single crystal diffraction after sublimation in a long Schlenk flask over an oil bath at 50 °C under a dynamic vacuum. Spectroscopic and analytical techniques confirmed the formation of compound **13**.



The synthesis of **13** is unusual, a compound of the type $[\text{Me}(\text{Cl})\text{Ga}(\text{OCH}_2\text{CH}_2\text{NMe}_2)]_2$ was expected. However, there is no peak in the ^1H NMR spectrum of **13** corresponding to Ga-Me which suggests that no methyl transfer from the silyl amide had occurred in the first step (**Step (i)**) in Scheme 2.6 in the synthesis of **11**. As solutions of the precursor to this reaction (**11**) are used *in situ* it is proposed that in this instance the synthesis of **11** produced mixtures of $[\text{Me}(\text{Cl})\text{Ga}\{\text{N}(\text{SiMe}_3)_2\}]_2$ and $[\text{Cl}_2\text{GaN}(\text{SiMe}_3)_2]_2$. Therefore, the reaction of $[\text{Cl}_2\text{GaN}(\text{SiMe}_3)_2]_2$ with two equivalents of $\text{HOCH}_2\text{CH}_2\text{NMe}_2$ then results in the formation of compound, **13**. In an attempt to grow crystals suitable for single crystal analysis **13** was isolated solely and is thought to be the major product. Peaks in the ^1H NMR are consistent with the production of **13** only, with peaks at 3.59, 2.57 and 0.22 ppm being assigned to OCH_2CH_2 , CH_2NMe_2 , $\text{N}(\text{CH}_3)_2$, in a 1:1:3 ratio. The $^{13}\text{C}\{^1\text{H}\}$ NMR spectra also shows peaks consistent to compound **13**; three peaks being clearly observed for the carbon environments CH_2NMe_2 , OCH_2 and $\text{N}(\text{CH}_3)_2$, at 60.2, 57.9 and 44.9 ppm, respectively. In the mass spectrum of **13** taken in toluene, a peak was observed for the molecular ion at $m/z = 383$ which supports the proposed dimeric structure of **13**. This is confirmed by an additional peak at $m/z = 311$ consistent with a fragment of the dimeric structure reported for **13**.

2.2.3.3.1. X-ray crystallographic study of $[\text{Cl}_2\text{Ga}(\text{OCH}_2\text{CH}_2\text{NMe}_2)]_2$

Table 2.3. Selected bond lengths (Å) and angles (°) for $[\text{Cl}_2\text{Ga}(\text{OCH}_2\text{CH}_2\text{NMe}_2)]_2$ (**13**).

O(1)-Ga(1)	1.9195(19)	Cl(1)-Ga(1)	2.2017(8)
Ga(1)-O(1) ⁱ	1.9571(19)	Cl(2)-Ga(1)	2.1533(9)
N(1)-Ga(1)	2.103(2)		
O(1)-Ga(1)-Cl(1)	137.84(8)	O(1)-Ga(1)-O(1) ⁱ	73.68(9)
O(1) ⁱ -Ga(1)-Cl(1)	94.55(7)	O(1)-Ga(1)-Cl(2)	110.80(8)
Cl(2)-Ga(1)-Cl(1)	111.13(4)	O(1) ⁱ -Ga(1)-Cl(2)	100.59(8)
O(1)-Ga(1)-N(1)	80.13(9)	N(1)-Ga(1)-Cl(1)	94.43(7)
O(1) ⁱ -Ga(1)-N(1)	149.46(9)	N(1)-Ga(1)-Cl(2)	103.22(7)

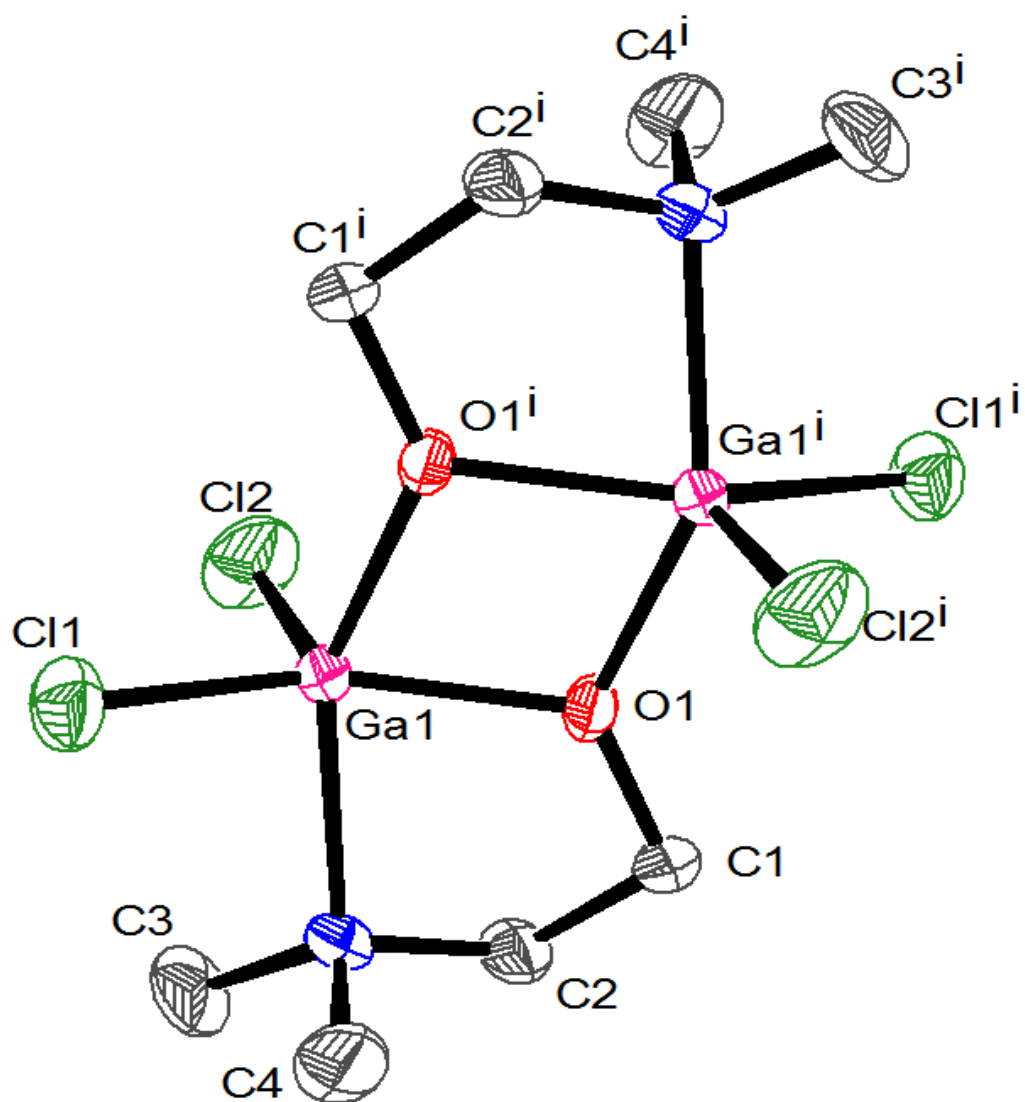


Fig. 2.7: X-ray crystal structure of $[\text{Cl}_2\text{Ga}(\text{OCH}_2\text{CH}_2\text{NMe}_2)]_2$ (13).

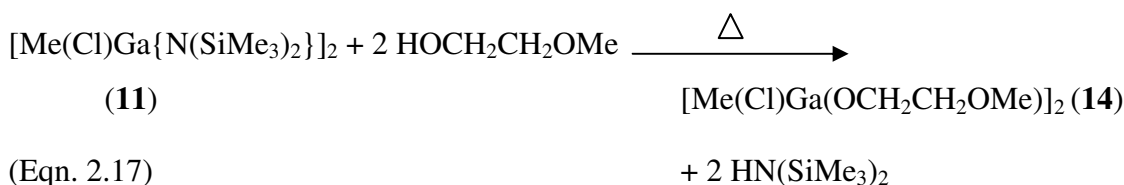
The crystal structure of compound **13** was determined by X-ray crystallography, the results are shown in Figure 2.7; selected bond lengths and angles are given in Table 2.3. Compound **13** crystallised into the monoclinic, $P2_1/n$ space group. As shown in Figure 2.7, the compound adopts a dimeric molecular arrangement. The centrosymmetric, four-membered Ga_2O_2 ring, that is common to this type of complex,⁵¹ is planar, and the bidentate ligand forms a five-membered ring. Each gallium atom in **13** adopts a distorted trigonal bipyramidal geometry with a chlorine atom in each of the two equatorial positions. The bridging alkoxide groups are located in both axial and equatorial positions, while the nitrogen atom (N1) of the alkoxide group is in the axial position with the O1#1–Ga–N1 bond angle to the opposite, axial alkoxide group being $149.46(9)^\circ$. This large deviation from 180° is due to the constraints of the internal O#1–Ga–O1 angle ($73.68(9)^\circ$) in the Ga_2O_2 ring and the geometry of the ligand. The sum of the bond angles in the equatorial plane of **13** is 359.77° , which is a measure of the planarity of the equatorial groups. The equatorial Ga–O bond length ($1.920(2) \text{ \AA}$) is slightly shorter than the axial Ga–O#1 bond distance ($1.9571(19) \text{ \AA}$) which is indicative of two active bonding Ga–O bond types. The longer Ga–N1 distance ($2.103(2) \text{ \AA}$) in **13**, can be attributed to N1→Ga dative bonding.

The structure of compound **13** is similar to related compounds of the type $[\text{R}_2\text{M}(\mu\text{-OR}')_2]$ ($\text{R}' =$ donor functionalized group) which have been previously reported; all bond lengths and angles are comparable.^{9,15-17,68} In comparison to a similar indium dimeric compound, namely: $[\text{Me}_2\text{In}(\text{OCH}_2\text{CH}_2\text{NMe}_2)]_2$,¹⁴ where the bond lengths are all longer. In this compound the equatorial In–O bond length is ($2.1432(14) \text{ \AA}$) and longer than the equatorial Ga–O bond length ($1.9195(19) \text{ \AA}$) is longer in **13**. Equally the axial M–O bond distance in **13** is shorter than in the equivalent $[\text{Me}_2\text{In}(\text{OCH}_2\text{CH}_2\text{NMe}_2)]_2$ ($2.5161(16) \text{ \AA}$ for the In analogue and $1.9571(19) \text{ \AA}$ for the Ga–O axial bond length). The longer bond distance in the indium derivative is due to the larger covalent radius of indium with respect to gallium and the greater Lewis acidity of indium.

2.2.3.4. Reaction of **11** with $\text{HOCH}_2\text{CH}_2\text{OMe}$

The dropwise addition of two equivalents of $\text{HOCH}_2\text{CH}_2\text{OMe}$ to compound **11** prepared *in situ* in toluene, under reflux conditions for 24 hours, afforded the dimeric methyl-

chloro-gallium alkoxide, $[\text{Me}(\text{Cl})\text{Ga}(\text{OCH}_2\text{CH}_2\text{OMe})_2]$ (**14**). A free flowing crystalline solid was isolated after sublimation in a long Schlenk flask over an oil bath at 50°C under a dynamic vacuum. Analytical and spectroscopic data indicated that compound **14** had been formed.

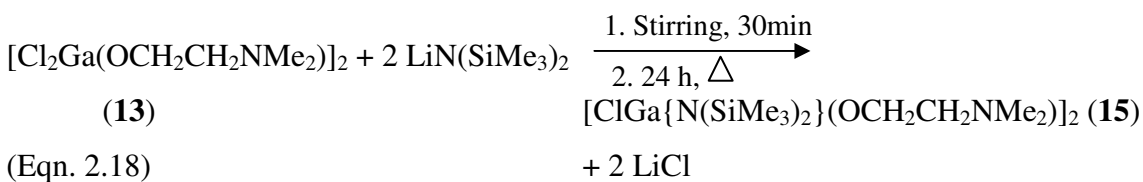


The reaction shown in Eqn. 2.17 was successfully carried out, which is based on Step (ii) of Scheme 2.6. The ^1H NMR of **14** showed the expected peak corresponding to GaMe at 0.05 ppm confirming methyl transfer to the metal centre had occurred. As expected. Other peaks observed in the ^1H NMR spectrum at 3.72, 3.30 and 3.16 ppm corresponding to the OCH_2CH_2 , CH_2OMe , $\text{O}(\text{CH}_3)$ hydrogen environments, respectively, are in a 7:3 ratio with the peak for GaMe observed at 0.05 ppm. In the $^{13}\text{C}\{^1\text{H}\}$ NMR spectrum of **14** the four environments CH_2OMe OCH_2 $\text{O}(\text{CH}_3)$ and GaMe are observed at 73.1, 62.1, 57.9 and 5.7 ppm respectively. In the mass spectrum of **14** recorded in toluene, a peak is observed for the molecular ion at $m/z = 388$ which supports the proposed dimeric structure of **14**. This is confirmed by additional peaks at $m/z = 353$ and 276, which are consistent with a fragments of the dimeric structure reported for **14**. Interestingly a large peak corresponding to the ligand fragment $\text{Me}(\text{OCH}_2\text{CH}_2\text{OMe})$ is observed and could provide some evidence of a potential decomposition pathway to gallium oxide.

2.2.3.5. Reaction of **13** with $\text{Li}(\text{N}(\text{SiMe}_3)_2)$

The third step of the synthesis described in Scheme 2.6 (Step (iii)) involves the reaction of $[\text{Me}_x(\text{Cl})_{2-x}\text{Ga}(\text{OR})_2]$ with two equivalents of $\text{LiN}(\text{SiMe}_3)_2$. When $x = 0$, $[\text{Cl}_2\text{Ga}(\text{OCH}_2\text{CH}_2\text{NMe}_2)_2]$ (**13**), was prepared, as described in section 2.2.2.6, and used *in situ* to yield $[\text{ClGa}(\text{OR})\{\text{N}(\text{SiMe}_3)_2\}]_2$. Thus, reaction of $[\text{Cl}_2\text{Ga}(\text{OCH}_2\text{CH}_2\text{NMe}_2)_2]$ (**13**) with two equivalents of $\text{LiN}(\text{SiMe}_3)_2$ in toluene with stirring for 30 minutes, then under reflux conditions for 24 hours afforded the dimeric chloro-gallium

amido/alkoxide $[\text{ClGa}\{\text{N}(\text{SiMe}_3)_2\}(\text{OCH}_2\text{CH}_2\text{NMe}_2)]_2$ (**15**), as a yellow viscous oil (Eqn. 2.18). Analytical and spectroscopic data confirm the formation of compound **15**.

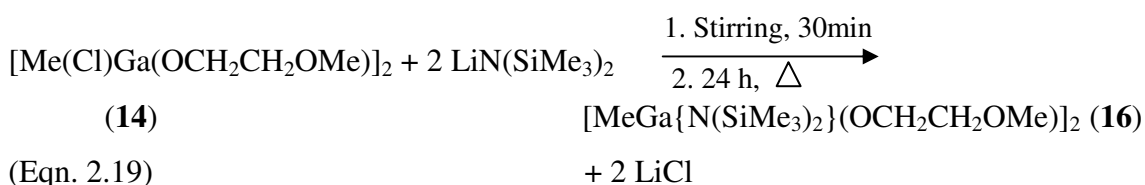


The reaction shown in Eqn. 2.18 was successfully carried out, which is based on **Step (iii)** of Scheme 2.6. In contrast to the ^1H NMR of compound **14**, no peak corresponding to the GaMe hydrogen environment was observed in the ^1H NMR of **15**. This is further evidence of the lack of methyl transfer to the gallium centre that can occur in the synthesis of compound **11**, in this instance, (**Step (i)** of Scheme 2.6). Peaks were observed in the ^1H NMR spectrum of **15**, corresponding to the alkoxide and amide ligands respectively, observed in a 5:9 ratio which is consistent with the formation of **15**. Peaks at 3.90, 2.31 and 2.24 ppm correspond to the OCH, $\text{CH}_2\text{CH}_2\text{N}$ and NCH_3 hydrogen environments in the alkoxide ligand, respectively, and are in a 4:4:12 ratio. An additional multiplet observed at 0.08 ppm can be assigned to the amide ligand, $\text{N}(\text{SiCH}_3)_2$. In the $^{13}\text{C}\{^1\text{H}\}$ NMR spectrum taken of compound **15** the four environments CH_2NMe_2 , OCH_2 , NMe_2 and $\text{N}(\text{SiMe}_3)_2$ are observed at 62.9, 46.1, 44.9 and 5.4 ppm, respectively. In the mass spectrum of **15** recorded in toluene, a peak was observed for the molecular ion at $m/z = 704$ which supports the proposed dimeric structure of **15**, confirmed by an additional peak at $m/z = 474$, which is consistent with a fragments of the dimeric structure. An intense peak observed at $m/z = 352$ corresponding to the monomeric structure, may have arisen from the symmetric cleavage of the Ga_2O_2 ring, during decomposition. Interestingly a peak corresponding to the ligand fragment, $\text{OCH}_2\text{CH}_2\text{NMe}_2$ was observed and could provide some evidence of a potential decomposition pathway to gallium oxide.

2.2.3.6. Reaction of **14** with $\text{Li}(\text{N}(\text{SiMe}_3)_2)$

The third step of the synthesis described in Scheme 2.6 (**Step (iii)**) involves the reaction of $[\text{Me}_x(\text{Cl})_{2-x}\text{GaOR}]_2$ with two equivalents of $\text{LiN}(\text{SiMe}_3)_2$. However, when $x = 1$, compound **14**, was isolated, as described in section 2.2.2.7 and used *in situ* to yield

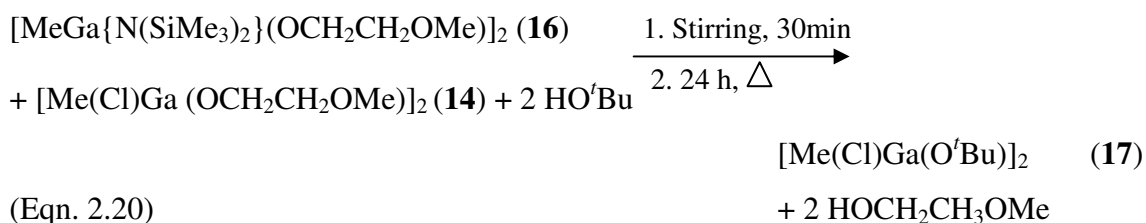
$[\text{MeGa}\{\text{N}(\text{SiMe}_3)_2\}(\text{OR})]_2$. The reaction of two equivalents of $\text{LiN}(\text{SiMe}_3)_2$ in toluene with a solution of **14**, prepared *in situ* with stirring for 30 min, then under reflux conditions for 24 hours afforded the dimeric methyl-gallium amido/alkoxide, $[\text{MeGa}\{\text{N}(\text{SiMe}_3)_2\}(\text{OCH}_2\text{CH}_2\text{OMe})]_2$ (**16**), as a yellow viscous oil (Eqn. 2.19). Analytical and spectroscopic data suggest the formation of compound **16**.



As observed in the ^1H NMR spectrum of the precursor (**14**) for this reaction, shown in Eqn. 2.19, a peak corresponding to the GaMe hydrogen environment was observed in the ^1H NMR spectrum of compound **16**, at 0.07 ppm. This is further evidence that the methyl transfer to the metal centre in the synthesis of compound **11** occurs, in this instance, which follows **Step (i)** of Scheme 2.7 (detailed in section 2.2.3.3). Peaks were observed in the $^{13}\text{C}\{^1\text{H}\}$ NMR and ^1H NMR spectra of **16**, for the alkoxide, amido and methyl ligands respectively, observed in a 7:18:3 ratio which is consistent with the formation of **16**. Peaks at 3.79, 3.35 and 3.25 ppm correspond to the OCH_2 , CH_2O and OCH_3 hydrogen environments in the alkoxide ligand, as well as a multiplet observed at 0.23 ppm assigned to SiCH_3 and a sharp single peak at 0.07 ppm for the GaMe hydrogen environment. In the $^{13}\text{C}\{^1\text{H}\}$ NMR spectrum of compound **16** peaks are observed for the alkoxide and amido ligand carbon environments, CH_2OMe , OCH_2 , $\text{O}(\text{CH}_3)$ and $\text{N}(\text{SiMe}_3)_2$ as well as a peak at 5.1 for the GaMe carbon environment (74.1, 62.0, 58.5, 5.7 and 5.1 ppm respectively). In the mass spectrum taken of compound **16**, a peak was observed for the molecular ion at $m/z = 638$ supporting the proposed dimeric structure of **16**. Peaks observed at $m/z = 478$, 404, 318 and 74 are consistent with fragments of the dimeric structure and with ligand fragments, providing some evidence of a potential decomposition pathway to gallium oxide. An intense peak observed at $m/z = 319$ corresponding to the monomeric structure, may have arisen from the symmetric cleavage of the Ga_2O_2 ring, during decomposition.

2.2.3.7. Reaction of **16** with HO^tBu

The fourth step of the synthesis described in Scheme 2.6 (**Step (iv)**) involves the reaction of [MeGa{N(SiMe₃)₂}(OR')]₂ with two equivalents of HO^tBu. It was originally proposed that this reaction would yield the unsymmetrical gallium(III) bis(alkoxide), of the type [MeGa(OR')(O^tBu)], *via* elimination of HN(SiMe₃)₂. However, the addition of two equivalents of HO^tBu to a solution of **16**, prepared *in situ* in toluene with stirring for 30 min, then under reflux conditions for 24 hours afforded the dimeric chloromethyl-gallium alkoxide, [Me(Cl)Ga(O^tBu)]₂ (**17**), as yellow viscous oil. Analytical and spectroscopic data confirm the formation of compound **17**.



The formation of the expected product [MeGa(OCH₂CH₂NMe₂)(O^tBu)] did not occur and compound **17** was the only product isolated. It is proposed that because compound **16** was prepared and used *in situ* as a precursor (Eqn. 2.20), some [Me(Cl)Ga(OCH₂CH₂NMe₂)₂] (compound **14**) was left unreacted in the flask when compound **16** was initially synthesised (from an *in situ* solution of **14**), as described in section 2.2.3.6. It follows that, upon the addition of two equivalents of HO^tBu (Eqn. 2.20) to **14**, alcohol exchange between HO^tBu and OCH₂CH₂OMe (reaction with **14**) is more facile than an amine elimination (reaction with **16**), and so HO^tBu reacts preferentially with **14**, not with **16**, as initially intended (Scheme 2.4, Route 3, Step (iv)). Due to the increased sensitivity in air and moisture of **16**, when compared with **14**, it is thought that compound **16** decomposes, as analytical and spectroscopic data show no evidence for a mixture of unreacted **16** and the product (**17**). It is proposed that the highly volatile decomposition products of **16** would be removed *in vacuo* with the solvent upon work up of the reaction.

As observed in the ^1H NMR spectra of the precursors (**14** and **16**) to this reaction, a peak corresponding to the GaMe hydrogen environment was observed for compound **17**, at 0.22 ppm. Peaks were also observed in the ^1H NMR spectrum of **17** for the tertiary butyl group at 1.20 ppm and methyl group hydrogen environment at 0.22 ppm, in a 3:1 ratio, consistent with formation of **17**. In the $^{13}\text{C}\{^1\text{H}\}$ NMR spectrum, two peaks, at 80.2 and 48.3 ppm were observed for the two carbon environments in the tertiary butyl ligand, as well as a peak at 5.12 ppm for the GaMe carbon environment. In the mass spectrum of **17**, taken in toluene, a peak was observed for the molecular ion at $m/z = 384$ supporting the proposed dimeric structure of **17**. Peaks observed at $m/z = 327$, 312, 277 and 257 are consistent with fragments of the dimeric structure and with ligand fragments, providing some evidence of a potential decomposition pathway to gallium oxide. Despite the inclusion of a chloride group in **17**, this compound shows promise as an excellent CVD precursor as the tertiary butyl group would decompose cleanly *via* β -hydride elimination.

2.2.3.7.1. X-ray crystallographic analysis of $[\text{Me}(\text{Cl})\text{Ga}(\text{O}^t\text{Bu})]_2$ (**17**)

Table 2.4. Selected bond lengths (Å) and angles (°) for $[\text{Me}(\text{Cl})\text{Ga}(\text{O}^t\text{Bu})]_2$ (**17**).

C(1)-Ga(1)	1.928(3)	Cl(1)-Ga(1)	2.1856(9)
Ga(1)-O(1) ⁱ	1.909(2)		
O(1)-Ga(1)	1.916(2)		
O(1) ⁱ -Ga(1)-O(1)	79.60(9)	O(1) ⁱ -Ga(1)-Cl(1)	106.85(7)
O(1) ⁱ -Ga(1)-C(1)	119.53(14)	O(1)-Ga(1)-Cl(1)	106.44(7)
O(1)-Ga(1)-C(1)	119.98(13)	C(1)-Ga(1)-Cl(1)	117.86(12)
C(2)-O(1)-Ga(1)	128.46(18)	Ga(1) ⁱ -O(1)-Ga(1)	100.40(9)

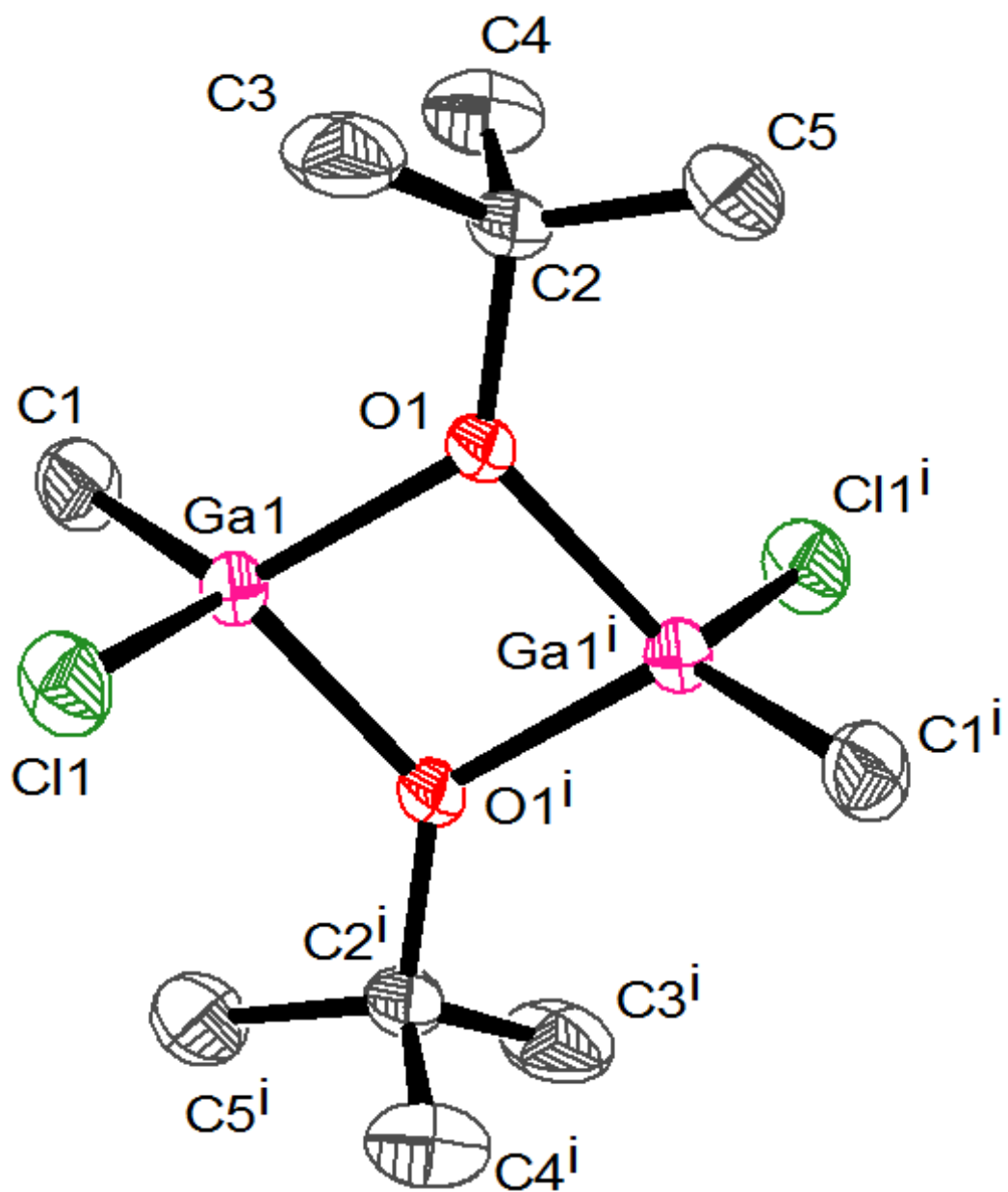


Figure 2.8: X-ray crystal structure of $[\text{Me}(\text{Cl})\text{Ga}(\text{O}^t\text{Bu})]_2$ (**17**).

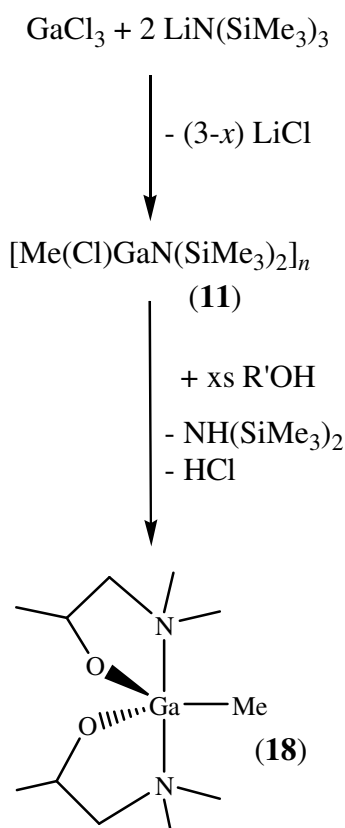
The crystal structure of compound **17** was determined by X-ray crystallography, the results are shown in Figure 2.10; selected bond lengths and angles are given in Table 2.4. Compound **17** crystallised into the monoclinic, $P2_1/n$ space group. As shown in Figure 2.10, the compound adopts a dimeric molecular arrangement. The centrosymmetric, four-membered Ga_2O_2 ring, that is common to this type of complex,⁵¹ is planar. The bridging oxygen atoms of the Ga_2O_2 centrosymmetric ring make up two of the corners of the gallium centred tetrahedra, whilst methyl and chloro terminal groups make up the remaining two.

Comparable bond lengths suggest that both methyl and chloro groups are tightly bound to both gallium centres (C1-Ga1 1.928(3) Å and Cl1-Ga1 2.1856(9) Å). A slightly shorter bond distance is observed between Ga1-O^i (1.909(2) Å) than Ga1-O1 (1.916(2) Å), however the difference is not large enough to be indicative of two active bonding Ga-O bond types.

The gallium centred tetrahedra are slightly distorted, exhibiting bond angles which vary only slightly from the desired 109° seen in typical tetrahedra. The bond angles in the tetrahedra show a range of values from $106.44(7) - 119.98(13)^\circ$ with the exception of O1Ga1O^i ($79.60(9)^\circ$), this large deviation from 109° is due to the steric constraints of in the Ga_2O_2 ring, this can be compared to compound **13** which exhibits an internal $\text{O}^i\text{-Ga-O1}$ angle of $73.68(9)^\circ$.

2.2.3.8. Reaction of **11** with $\text{HOCH}_2\text{CH}_2\text{OMe}_2$

Reaction of a solution of compound **11**, prepared as described in section 2.2.3.1 and used *in situ*, with two equivalents of $\text{HOCH}(\text{CH}_3)\text{CH}_2\text{NMe}_2$, yielded $[\text{Cl}_2\text{Ga}(\text{OCH}(\text{CH}_3)\text{CH}_2\text{NMe})]_2$ (**13**) (section 2.2.3.3). However, if an excess of alcohol is added in Step (iii) of Scheme 2.7, a gallium(III) bis(alkoxide), was isolated which is monomeric rather than dimeric, creating a precursor with increased volatility and thus enhancing its appeal as a CVD precursor.



Scheme 2.8: Series of reactions resulting in the production of the monomeric compound $[\text{MeGa}(\text{OCH}(\text{CH}_3)\text{CH}_2\text{NMe}_2)_2]$ (**18**).

As shown in Scheme 2.8, the reaction of excess $\text{HOCH}(\text{CH}_3)\text{CH}_2\text{NMe}_2$ with compound **11** (prepared *in situ*) in toluene under reflux conditions for 24 hours, afforded the monomeric methyl-gallium bis(alkoxide), $[\text{MeGa}(\text{OCH}(\text{CH}_3)\text{CH}_2\text{NMe}_2)_2]$ (**18**). Small colourless crystals of **18** were isolated after sublimation in a long Schlenk flask over an oil bath at 50 °C under a dynamic vacuum of crystallographic quality. Analytical and spectroscopic data confirmed the formation of compound **18**.

The reaction shown in Scheme 2.8 was successfully carried out, which is based on **Step (ii)** in Scheme 2.7. Evidence for the formation of **18** was obtained from the ^1H NMR spectrum, with peaks at 3.60, 2.35 and 2.31 ppm which can be assigned to the hydrogen environments, OCH_2 , OCH_2CH_2 and NMe_2 , respectively. These peaks are in a 20:3 ratio to the peak observed at 0.05 ppm which is assigned to the GaMe hydrogen environment. Four clear peaks observed in the $^{13}\text{C}\{^1\text{H}\}$ NMR spectrum at 61.2, 59.0, 45.4 and 5.8 ppm can be assigned the carbon environments at CH_2NMe_2 , OCH_2 ,

$\text{N}(\text{CH}_3)_2$ and GaMe , respectively. In the mass spectrum of **18** taken in toluene, a peak was observed for the molecular ion at $m/z = 261$, in agreement with the monomeric structure of **18**. This is confirmed by peaks at $m/z = 162$ and 88 , consistent with fragments of the monomeric structure and ligand fragments reported for **18**.

Compound **18** was initially formed as a minor product in the synthesis of $[\text{Cl}_2\text{GaOCH}(\text{CH}_3)\text{CH}_2\text{NMe}_2]_2$ (**13**). However after repeating the synthesis, with an excess of $\text{HOCH}(\text{CH}_3)\text{CH}_2\text{NMe}_2$, according to Scheme 2.8, spectroscopic data supported the formation of **18** in higher yield. The use of compound **11** as an *in situ* reagent means that the yield of this compound can only be estimated. Therefore, initially **18** was formed when **11** was reacted with an excess of $\text{HOCH}(\text{CH}_3)\text{CH}_2\text{NMe}_2$.

2.2.3.8.1. X-ray crystallographic studies of

$[\text{MeGa}(\text{OCH}(\text{CH}_3)\text{CH}_2\text{NMe}_2)_2]$ (**18**)

Table 2.5. Selected bond lengths (Å) and angles (°) for $[\text{MeGa}(\text{OCH}(\text{CH}_3)\text{CH}_2\text{NMe}_2)_2]$ (**18**).

O(1)-Ga(1)	1.8538(16)	N(2)-Ga(1)	2.2250(19)
O(2)-Ga(1)	1.8554(16)	C(1)-Ga(1)	1.983(2)
N(1)-Ga(1)	2.2424(19)		
O(1)-Ga(1)-O(2)	112.46(7)	O(2)-Ga(1)-N(2)	82.71(7)
O(1)-Ga(1)-N(1)	82.34(7)	O(2)-Ga(1)-C(1)	124.36(8)
O(1)-Ga(1)-N(2)	87.60(7)	C(1)-Ga(1)-N(1)	99.02(8)
O(1)-Ga(1)-C(1)	123.18(8)	C(1)-Ga(1)-N(2)	99.13(8)
O(2)-Ga(1)-N(1)	87.22(7)	N(2)-Ga(1)-N(1)	161.85(7)

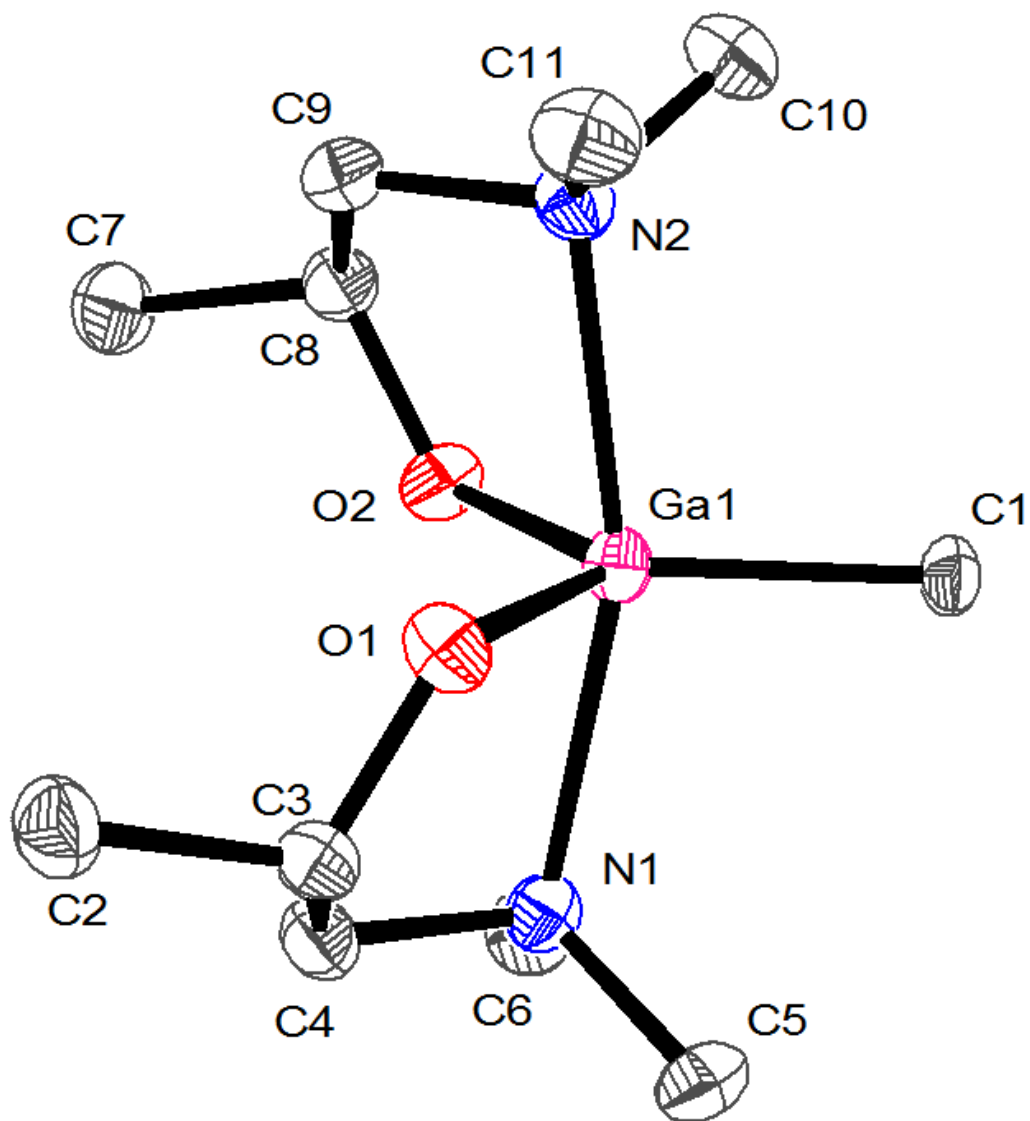


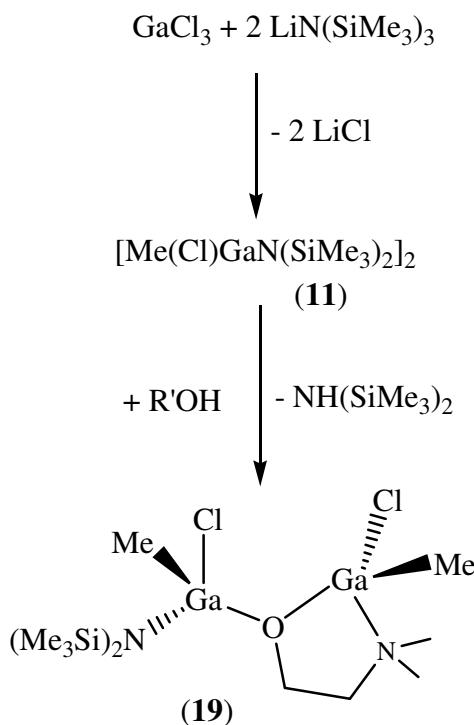
Fig. 2.9: X-ray crystal structure of $[\text{MeGa}(\text{OCH}(\text{CH}_3)\text{CH}_2\text{NMe}_2)_2]$ (**18**).

The crystal structure of compound **18**, shown in Fig. 2.8, was determined by single crystal X-ray diffraction and selected bond lengths and angles are given in Table 2.5. Compound **18** crystallised into the triclinic space group *P*-1, it is monomeric in the solid state with the gallium atom adopting a distorted trigonal bipyramidal geometry. The oxygen atoms of each alkoxide ligand and the methyl group occupy the equatorial positions whilst the nitrogen atoms of the donor functionalised group reside in the axial positions (Fig. 2.8). The N1–Ga–N2 bond angle is 161.85(7)°, which deviates from 180°, although it is not as pronounced as with the dimeric alkoxogallanes, such as **13**, due to the lack of constraint in the monomer versus the dimer. The sum of the bond angles in the equatorial plane of **18** is 360.00°, which is a measure of the planarity of the equatorial groups. The two equatorial Ga–O bond lengths are the same (1.8538(16) and 1.8554(16) Å) which is indicative of the same Ga–O bond type. The Ga–N distances are 2.2424(19) and 2.2250(19) Å and are significantly shorter than the sum of the van der Waals radii and so indicative of a strong dative bonding interaction.

Related trigonal bipyramidal related alkoxogallanes [EtGa(OCH₂CH₂NMe₂)₂] and [ClGa(OR)₂] (R = CH₂CH₂NMe₂, C(CF₃)₂CH₂C(CH₃)=NMe and C(CF₃)₂CH₂NMe₂)^{12,13,45} show Ga–O and Ga–N bond distances similar to those observed here. As with **18** and [ClGa(OCH₂CH₂NMe₂)₂] the axial N1–Ga–N2 bond angle (165.11(11)°) again shows less deviation from the expected 180° due to the lack of internal constraint observed as a direct result of the planar Ga₂O₂ rings exhibited in the dimeric structures (*c.f.* **13**).

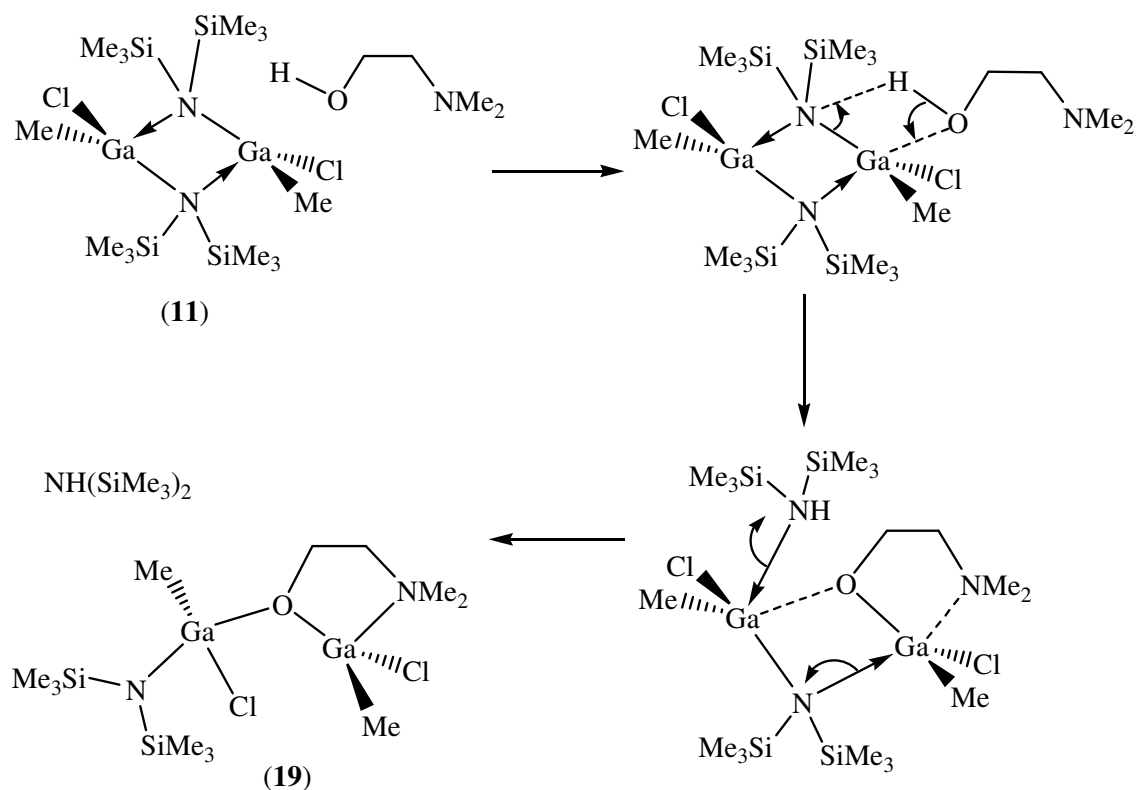
2.2.3.9. Reaction of **11** with 1 equivalent of HOCH₂CH₂NMe₂

As described in section 2.2.3.3, the reaction of a solution of compound **11**, prepared and used *in situ*, with two equivalents of HOCH₂CH₂NMe₂, yielded [Cl₂Ga(OCH₂CH₂NMe)₂] (**13**). However, when one equivalent of alcohol is added in Step (iii) of Scheme 2.7 rather than two, an intermediate gallium(III) amido/alkoxide could be isolated.



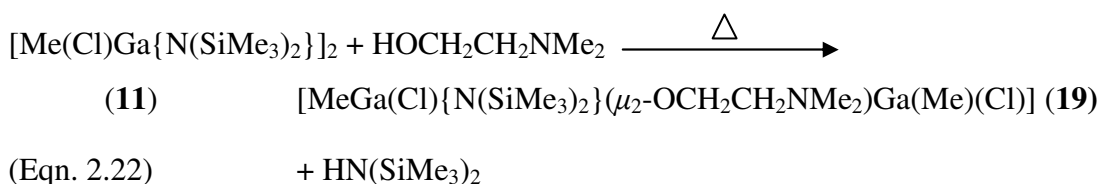
Scheme 2.9: Series of reactions to produce the intermediate compound $[\text{MeGa}(\text{Cl})\{\text{N}(\text{SiMe}_3)_2\}(\mu_2\text{-OCH}_2\text{CH}_2\text{NMe}_2)\text{Ga}(\text{Me})\{\text{Cl}\}]$ (**19**).

Compound **19** was initially formed as a by product during the synthesis of compound **13**. However after repeating the reaction of **11** with one equivalent of $\text{HOCH}_2\text{CH}_2\text{NMe}_2$, according to Scheme 2.9, spectroscopic data supported the formation of **19**. The use of compound **11** as an *in situ* reagent means that the yield of this compound can only be estimated. Compound **11** $[\text{Me}(\text{Cl})\text{Ga}\{\text{N}(\text{SiMe}_3)_2\}]_2$ and $[\text{Me}(\text{Cl})\text{Ga}(\text{OCH}_2\text{CH}_2\text{NMe}_2)]_2$ are linked *via* an oxygen bridge and probably form due to insufficient $\text{HOCH}_2\text{CH}_2\text{NMe}_2$ being present to enable the formation of compound **13** solely. Therefore, compound **19** is the result of adding one equivalent of the donor functionalized alcohol and can be thought of as an intermediate to $[\text{Me}(\text{Cl})\text{Ga}(\text{OCH}_2\text{CH}_2\text{NMe}_2)]_2$. The formation of **19** is interesting since it shows the presence of a methyl and chlorine atom on the gallium centre and provides evidence of a methyl transfer at the metal centre. In addition, compound **19** gives an insight into how these reactions take place and a proposed mechanism for the formation of **19** is depicted in Scheme 2.10.



Scheme 2.10: Proposed mechanism for the formation of [MeGa(Cl){N(SiMe₃)₂}(μ₂-OCH₂CH₂NMe₂)Ga(Me)(Cl)] (**19**).

The reaction of **11** with the dropwise addition of one equivalent of HOCH₂CH₂NMe₂ in toluene under reflux conditions for 24 hours afforded [MeGa(Cl){N(SiMe₃)₂}(μ₂-OCH₂CH₂NMe₂)Ga(Me)(Cl)] (**19**). Small colourless crystals of **19** were isolated after sublimation in a long Schlenk flask over an oil bath at 50°C under a dynamic vacuum. Analytical and spectroscopic data confirmed the formation of compound **19**.



The reaction shown in Eqn. 2.22 was successfully carried out, which is based on Step (ii) in Scheme 2.6. Evidence of the formation of **19** was obtained from the ¹H NMR spectrum, with peaks at 3.47, 2.22 and 2.12 ppm assigned to the hydrogen environments, in the alkoxide ligand. Additional peaks observed at 0.34, 0.06 and 0.03

ppm can be assigned to the amido and two GaMe hydrogen environments, respectively. Peaks for the alkoxide, amido and methyl environments are in a 10:18:3:3 ratio, which is consistent with the isolation of **19**. Three peaks observed in the $^{13}\text{C}\{^1\text{H}\}$ NMR spectrum at 60.5, 58.7 and 45.1 can be assigned to the carbon environments in the alkoxide ligand (CH_2NMe_2 , OCH_2 and $\text{N}(\text{CH}_3)_2$ respectively), whilst peaks at 22.7 and 6.0 ppm can be assigned to the two GaMe carbon environments, with a peak at 4.9 ppm being assigned to the carbon environment in the amido ligand ($\text{N}(\text{SiMe}_3)$).

2.2.3.9.1. X-ray crystal study of $[\text{MeGa}(\text{Cl})\{\text{N}(\text{SiMe}_3)_2\}(\mu_2\text{-OCH}_2\text{CH}_2\text{NMe}_2)\text{Ga}(\text{Me})\{\text{Cl}\}]$ (19**)**

Table 2.6. Selected bond lengths (Å) and angles (°) for $[\text{MeGa}(\text{Cl})\{\text{N}(\text{SiMe}_3)_2\}(\mu_2\text{-OCH}_2\text{CH}_2\text{NMe}_2)\text{Ga}(\text{Me})(\text{Cl})]$ (**19**).

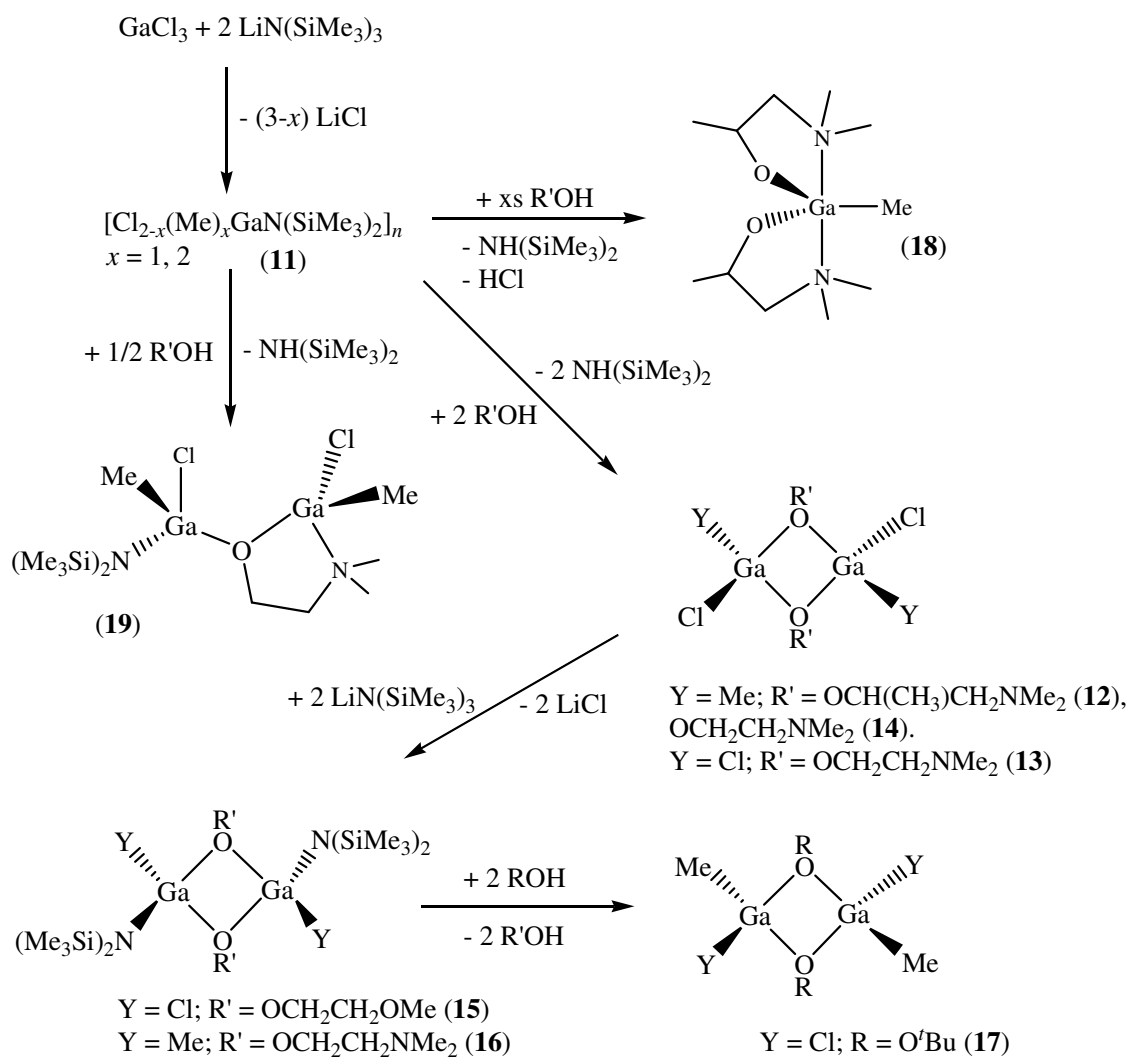
C(1)-Ga(1)	1.929(11)	C(6)-Ga(2)	2.027(11)
O(1)-Ga(1)	1.904(8)	O(1)-Ga(2)	1.966(9)
Cl(1)-Ga(1)	2.165(4)	Cl(2)-Ga(2)	2.236(4)
Ga(1)-N(1)	2.033(12)	Ga(2)-N(2)	1.860(10)
Ga(1)-O(1)-Ga(2)	124.1(5)		
O(1)-Ga(1)-C(1)	120.0(4)	O(1)-Ga(2)-C(6)	103.0(4)
O(1)-Ga(1)-N(1)	85.9(4)	N(2)-Ga(2)-O(1)	108.3(5)
C(1)-Ga(1)-N(1)	113.0(5)	N(2)-Ga(2)-C(6)	125.6(4)
O(1)-Ga(1)-Cl(1)	105.5(3)	O(1)-Ga(2)-Cl(2)	95.5(3)
C(1)-Ga(1)-Cl(1)	121.7(4)	C(6)-Ga(2)-Cl(2)	105.6(4)
N(1)-Ga(1)-Cl(1)	104.1(3)	N(2)-Ga(2)-Cl(2)	114.1(4)

The crystal structure of compound **19** was determined by X-ray crystallography, the results are shown in Figure 2.9; selected bond lengths and angles are given in Table 2.5. Compound **19** crystallised into the trigonal R3c space group. As shown in Figure 2.9, the compound can be viewed as two tetrahedrally coordinated gallium centres bridged by an oxygen atom. One of the gallium centred tetrahedra have a methyl, chlorine, nitrogen and oxygen atom in each corner, the oxygen atom bridging to the second gallium tetrahedra, which has an additional methyl, chlorine and nitrogen atom at its corners. The nitrogen atom at the corner of the second gallium centred tetrahedra is linked to the bridging oxygen atom via a hydrocarbon backbone, forming a five membered cyclic ring with the central gallium atom. Comparable bond lengths suggest that both methyl and chloro groups are tightly bound to both gallium centres (C1–Ga1, 1.929(11) Å, C6–Ga2, 2.027(11) Å, and Cl1–Ga1, 2.033(12) Å, Cl2–Ga2, 2.236(4) Å) with a slightly shorter bond distance observed between Ga1–O1 (1.904(8) Å) than Ga2–O1 (1.966(9) Å). It is interesting to note that the Ga–N bond distances differ considerably for the two gallium centres, indicative of two different bonding modes; the shorter distance of 1.860(10) Å for Ga2–N2 can be assigned to a covalent bond, the Ga1–N1 distance (2.033(12) Å) whilst considerably longer is still significantly shorter than the sum of the van der Waals radii and so indicative of a strong dative bonding interaction.

The oxygen bridged tetrahedra are both distorted, exhibiting bond angles which can vary significantly from the desired 109° seen in typical tetrahedra. The bond angles in the tetrahedra centred on Ga1 show a range of values from 104.1(3)–121.7(4)° with the exception of O1–Ga1–N1 (85.9(4)°), this large deviation from 109° is due to the steric constraints of the donor functionalized ligand which makes up the aforementioned five membered ring.

2.2.3.10. Summary of synthetic routes followed in section 2.2.3.

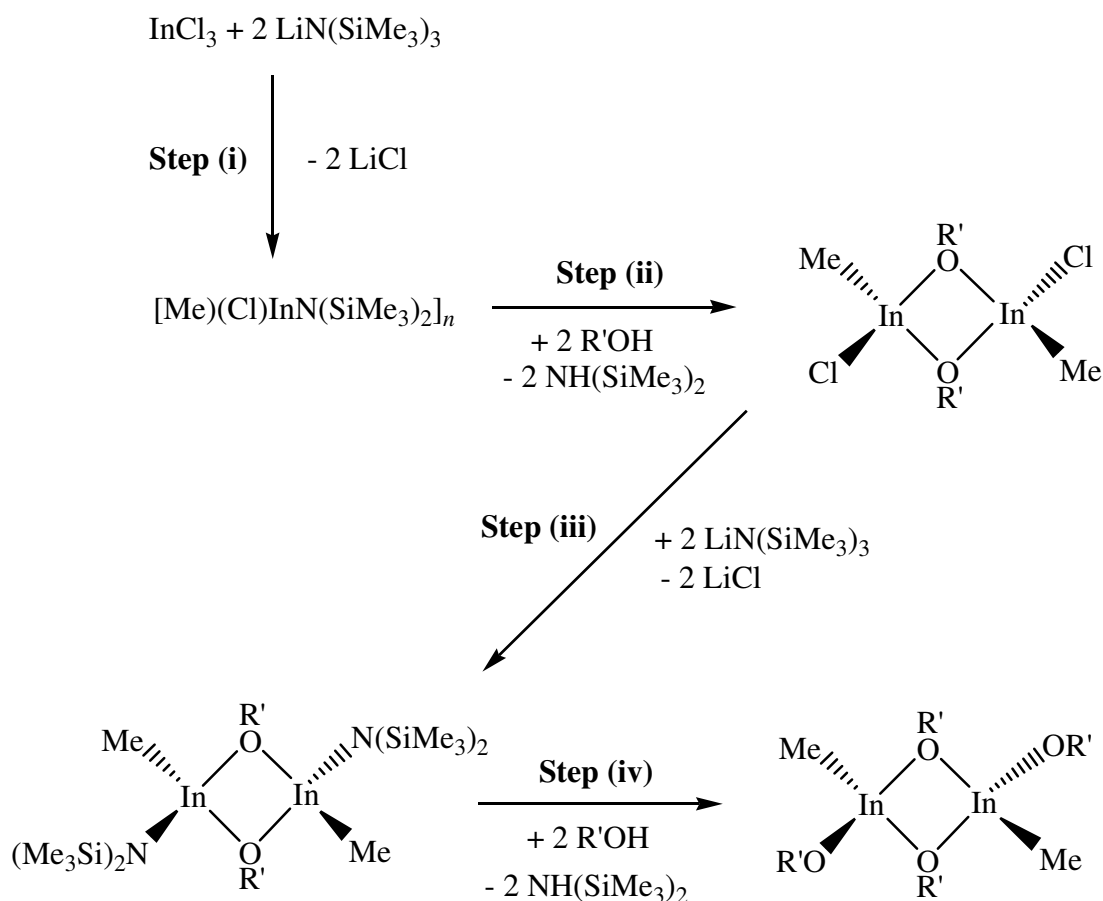
The attempted synthesis of unsymmetrical gallium (III) bis(alkoxides) was investigated using the four step synthetic routes shown in Scheme 2.4 in section 2.2. In light of this work a slightly amended Scheme 2.11 detail the routes followed in the synthesis described in sections 2.2.3.



Scheme 2.11: Summary of the synthetic routes followed in section 2.2.3

2.2.4. Unsymmetrical indium(III) bis(alkoxides)

The attempted synthesis of unsymmetrical indium (III) bis(alkoxides) was investigated using the four step synthetic routes shown in Scheme 2.4 in section 2.2. In light of this work a slightly amended Scheme 2.12 detail, the routes followed in the synthesis described in sections 2.2.4.1 - 2.2.4.8.



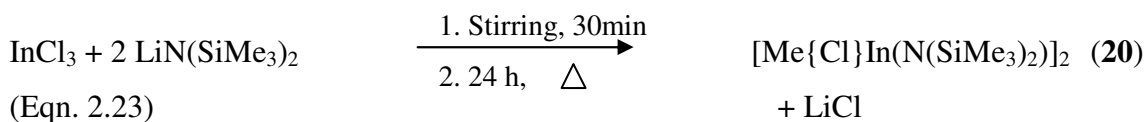
Scheme 2.12: Synthetic route for the formation of indium(III) bis(alkoxides).

The four step synthetic route described in Scheme 2.12 was investigated, as a novel path to unsymmetrical indium(III) bis(alkoxides). Whilst **Steps (i)–(ii)** are based on reactions previously reported,⁵¹ **Step (iii)–(iv)** have been developed and are described herein. It is proposed that methyl transfer would occur in the first step, according to Scheme 2.12, the advantage of which being the production of indium(III) bis(alkoxide) precursors that contain no chlorine. After the initial salt elimination step with methyl transfer, **Step (ii)** involves the addition of two equivalents of a donor functionalized alcohol, yielding an indium(III) mono(alkoxide) dimer (Scheme 2.12). In **Step (iii)**, the remaining chloride group is removed *via* a second salt elimination reaction. **Step (iv)** involves a protonolysis/alcoholysis reaction with a simple alcohol, which results in a novel indium(III) bis(alkoxide), $[\text{MeIn}(\text{OR})(\text{OR}')_2]$. The use of a monofunctional alcohol group in **Step (iv)** will yield a precursor, that, follows a clean decomposition path *via* β -hydride elimination and is highly volatile, both desired outcomes for LPCVD precursors. It is proposed that size difference will hinder efficient packing between

molecules and thus increase the solubility of the compounds, a desired attribute for AACVD precursors.

2.2.4.1. The reaction of InCl_3 with $\text{LiN}(\text{SiMe}_3)_2$

In order to isolate an unsymmetrical indium(III) bis(alkoxide) the four step synthetic procedure, outlined in Scheme 2.10 was employed. Step (i) involves the formation of the precursor $[\text{Me}(\text{Cl})\text{In}\{\text{N}(\text{SiMe}_3)_2\}]_2$ (**20**) and this compound has been isolated and used *in situ* in other reactions as detailed in sections 2.2.4.2 – 2.2.4.5. Thus, the reaction of InCl_3 with two equivalents of $\text{LiN}(\text{SiMe}_3)_2$ in toluene with stirring for 30 min, then under reflux conditions for 24 hours, afforded the methyl-chloro-indium amide dimer, $[\text{Me}(\text{Cl})\text{In}\{\text{N}(\text{SiMe}_3)_2\}]_2$ (**20**), as a yellow solid. Analytical and spectroscopic data confirmed the formation of compound **20**.

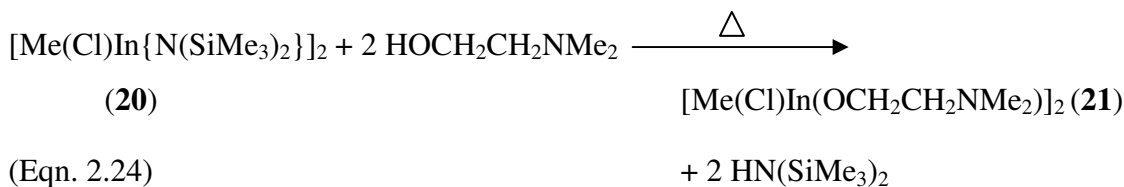


The reaction shown in Eqn. 2.23 was successfully carried based on **Step (i)** detailed in Scheme 2.12. A peak observed in the ^1H NMR spectrum at 0.28 ppm was consistent with the $\text{N}(\text{Si}(\text{CH}_3)_3)$ hydrogen environment and was in a 6:1 ratio with a peak at 0.31 corresponding to the InMe environment, confirming the formation of **20**. Peaks observed in the $^{13}\text{C}\{^1\text{H}\}$ NMR spectrum for the InMe and $\text{N}(\text{Si}(\text{CH}_3)_3)$, environments at 6.1 and 5.5 ppm, respectively, also confirm **20**. In the mass spectrum of **20**, taken in toluene, peaks observed at $m/z = 579$ and 324 are consistent with fragments of the proposed dimeric structure of **20**. Compound **20** has been isolated for use as a precursor as shown in scheme 2.6, and will feature largely in the following sections.

2.2.4.2. Reaction of **20** with $\text{HOCH}_2\text{CH}_2\text{NMe}_2$

Step (ii) in the procedure to prepare unsymmetrical indium(III) bis(alkoxides) involves the reaction of $[\text{Me}(\text{Cl})\text{In}\{\text{N}(\text{SiMe}_3)_2\}]_2$ (**20**) with $\text{R}'\text{OH}$ in order to form compounds of the type $[\text{Me}(\text{Cl})\text{In}(\text{OR}')_2]$ (**Step (ii)**, Scheme 2.12). Therefore, reaction of **20** with two equivalents of $\text{HOCH}_2\text{CH}_2\text{NMe}_2$ was carried out in toluene under reflux conditions for

24 hours. The dimeric methyl-chloro-indium alkoxide, $[\text{Me}(\text{Cl})\text{In}(\text{OCH}_2\text{CH}_2\text{NMe}_2)]_2$ (**21**), was isolated as small colourless crystals after sublimation. Analytical and spectroscopic data confirmed the formation of compound **21**.

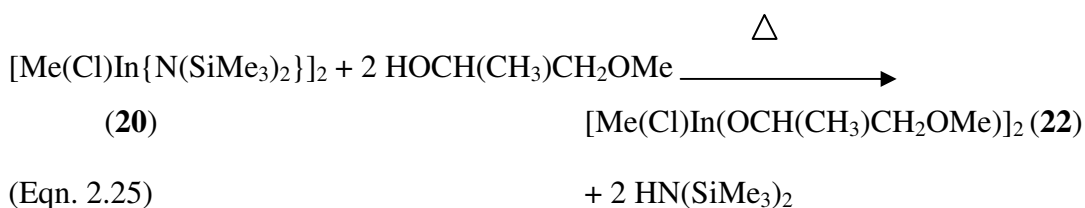


The reaction shown in Eqn. 2.24 is based on **Step (ii)** in Scheme 2.12. Compound **21** was isolated and will also be used as a precursor in **Step (iii)** (Scheme 2.12). Evidence of the formation of **21** was obtained from the ^1H NMR spectrum, peaks at 3.87, 2.49 and 2.28 ppm can be assigned to the hydrogen environments, OCH_2CH_2 , CH_2NMe_2 and $\text{N}(\text{CH}_3)_2$, and are in a 10:3 ratio with the peak observed at 0.31 ppm which is assigned to the hydrogen environment for InMe . Four peaks observed in the $^{13}\text{C}\{^1\text{H}\}$ NMR spectrum at 61.2, 56.7, 46.2 and 5.6 ppm can be assigned the carbon environments at CH_2NMe_2 , OCH_2 , $\text{N}(\text{CH}_3)_2$ and InMe , respectively. A peak is observed for the molecular ion at $m/z = 504$, in the mass spectrum, which supports the proposed dimeric structure of **21**. This is confirmed by peaks at $m/z = 435$ and 363 consistent with fragments of the dimeric structure reported for **21**. Interestingly a peak corresponding to the ligand fragment $\text{OCH}_2\text{CH}_2\text{NMe}_2$ is observed ($m/z = 90$) and could provide some evidence of a potential decomposition pathway to indium oxide.

2.2.4.3. Reaction of **20** with $\text{HOCH}(\text{CH}_3)\text{CH}_2\text{OMe}$

In order to synthesise unsymmetrical indium(III) bis(alkoxides), **Step (ii)** of Route 3 (Scheme 2.12) was carried out with other donor functionalised alcohols. The reaction of **20**, prepared *in situ*, with two equivalents of $\text{HOCH}(\text{CH}_3)\text{CH}_2\text{OMe}$ in toluene under reflux conditions for 24 hours, afforded the dimeric methyl-chloro-indium alkoxide, $[\text{Me}(\text{Cl})\text{In}(\text{OCH}(\text{CH}_3)\text{CH}_2\text{OMe})]_2$ (**22**). Small colourless crystals of **22** were formed after sublimation in a long Schlenk flask over an oil bath at 50°C under a dynamic vacuum. The dimeric nature of **22** was also confirmed by the X-ray crystallographic

data which was obtained from the crystals, the data is given in Table 2.7 and Fig. 2.11. Analytical and spectroscopic data also confirmed the formation of compound **22**.



The reaction shown in Eqn. 2.25 was successfully carried out, which is based on **Step (ii)** (Scheme 2.12) and **22** was isolated. In the ^1H NMR spectrum of **22**, peaks observed at 4.60, 3.64, 3.58 and 3.45 ppm can be assigned to the hydrogen environments, $\text{OCH}(\text{CH}_3)$, $\text{OCH}(\text{CH}_3)\text{CH}_2$, $\text{OCH}(\text{CH}_3)\text{CH}_2$ and OCH_3 , respectively, and are in an 18:6 ratio with the peak observed at 0.36 ppm corresponding to InMe , which is consistent with the formation of **22**. The five carbon environments present in **22**, namely OCHCH_3 , OCH_3 , OCHCH_3 , OCHCH_3 and InMe , are observed at 66.7, 58.7, 57.2, 6.6 and 5.6 ppm, respectively. In the mass spectrum of **22** taken in toluene, a peak is observed for the molecular ion at $m/z = 507$, which supports the proposed dimeric structure of **22**. This is confirmed by peaks at $m/z = 436$ and 434 consistent with fragments of the dimeric structure reported for **22**.

2.2.4.3.1. X-ray structure of $[\text{Me}(\text{Cl})\text{In}(\text{OCH}(\text{CH}_3)\text{CH}_2\text{OMe})]_2$ (**22**)

Table 2.7: Selected bond lengths (Å) and angles (°) for

$[\text{Me}(\text{Cl})\text{In}(\text{OCH}(\text{CH}_3)\text{CH}_2\text{OMe})]_2$ (**22**)

In1–O1	2.106(3)	In1–C5	2.135(4)
In1–O1 ⁱ	2.170(3)	In1–Cl1	2.3867(12)
In1–O2	2.406(3)		
O1–In1–C5	129.48(16)	O1–In1–O1 ⁱ	74.03(11)
C5–In1–O1 ⁱ	109.94(14)	O1–In1–Cl1	106.53(9)
C5–In1–Cl1	122.06(13)	O1 ⁱ –In1–Cl1	97.20(9)
O1–In1–O2	71.88(10)	C5–In1–O2	93.10(14)
O1 ⁱ –In1–O2	145.87(9)	Cl1–In1–O2	90.91(8)

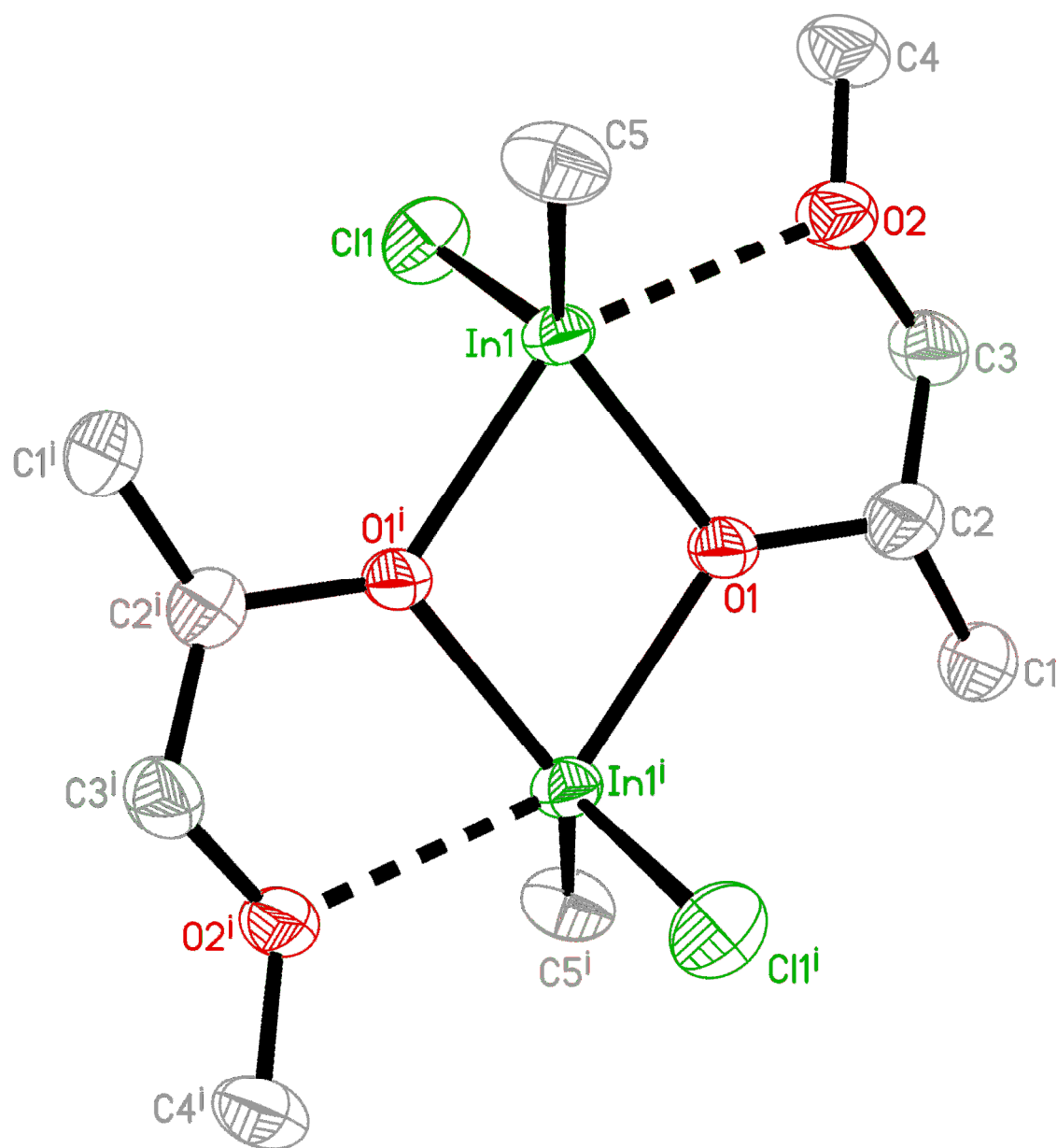


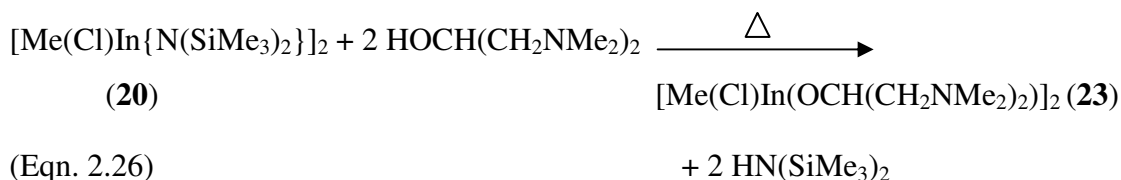
Fig. 2.11: X-ray crystal structure of $[\text{Me}(\text{Cl})\text{In}(\text{OCH}(\text{CH}_3)\text{CH}_2\text{OMe})]_2$ (**22**).

The crystal structure of compound **22** was determined by X-ray crystallography, the results are shown in Figure 2.11; selected bond lengths and angles are given in Table 2.7. Compound **22** crystallised into the monoclinic, $P2_1/c$ space group. As shown in Figure 2.11, the compound adopts a dimeric molecular arrangement. The centrosymmetric, four-membered In_2O_2 ring, that is common to this type of complex,⁵¹ is planar. Each indium atom in **22** adopts a distorted trigonal bipyramidal geometry with a methyl and chlorine group in equatorial positions. The bridging alkoxide groups are located in both axial and equatorial positions, while the oxygen atom (O2) of the donor (OMe) group is in the axial position with the O1–In–O2 bond angle to the opposite, axial alkoxide group being $145.87(9)^\circ$. This large deviation from 180° is due to the constraints of the internal O–In–O angle ($74.03(11)^\circ$) in the In_2O_2 ring and the geometry of the ligand. The sum of the bond angles in the equatorial plane of **22** is 358.07° , which is a measure of the planarity of the equatorial groups. The equatorial In–O bond length ($2.106(3) \text{ \AA}$) is significantly shorter than the axial In–O bond distance ($2.170(3) \text{ \AA}$) indicative of two active bonding In–O bond types. The In–O2 distance ($2.406(3) \text{ \AA}$) in **22**, can be attributed to $\text{O}_2 \rightarrow \text{In}$ dative bonding. In comparison to a gallium analogue, namely, $[\text{Ga}(\text{OC}(\text{CH}_3)_2\text{CH}_2\text{OMe})\text{Cl}_2]_2$, the bond lengths are shorter. The equatorial Ga–O bond length is $1.886(2) \text{ \AA}$ and so shorter than the equivalent equatorial In–O bond length ($2.106(3) \text{ \AA}$) in **22**. Equally the axial M–O bond distance in **22** is longer than in the equivalent $[\text{Ga}(\text{OC}(\text{CH}_3)_2\text{CH}_2\text{OMe})\text{Cl}_2]_2$ ($2.170(3) \text{ \AA}$ for the In analogue and $1.9753(17) \text{ \AA}$ for the Ga–O bond length). The longer bond distance in the indium derivative is due to the larger covalent radius of indium with respect to gallium and the greater Lewis acidity of indium.

2.2.4.4. Reaction of **20** with $\text{HOCH}(\text{CH}_2\text{NMe}_2)_2$

The formation of compounds **21** and **22** indicate that the methodology in Route 3 (described in section 2.2) can be used to prepare a range of indium(III) alkoxides. Further reactions were investigated using the donor functionalised alcohol $\text{HOCH}(\text{CH}_2\text{NMe}_2)_2$ in which two donor functionalised groups are present. Thus, the reaction of **20** with two equivalents of $\text{HOCH}(\text{CH}_2\text{NMe}_2)_2$ in toluene, under reflux conditions for 24 hours, afforded the dimeric methyl-chloro-indium amido/alkoxide, $[\text{Me}(\text{Cl})\text{In}(\text{OCH}(\text{CH}_2\text{NMe}_2)_2)]_2$ (**23**). Small colourless crystals of **23** were isolated after

sublimation in a long Schlenk flask over an oil bath at 50°C under a dynamic vacuum, however crystals were not of sufficient quality for single X-ray crystallographic analysis. Analytical and spectroscopic data confirmed the formation of compound **23**.

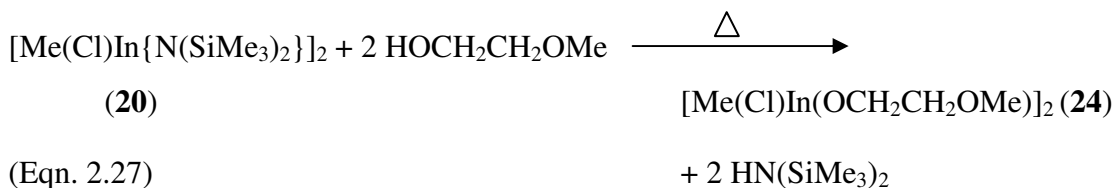


The reaction shown in Eqn. 2.26 based on **Step (ii)** (Scheme 2.12), isolated compound **23**. This compound will be used as a precursor in reactions based on **step (iii)** of Scheme 2.12. In the ¹H NMR spectrum of **23**, peaks observed at 2.61, 2.32 and 2.24 ppm can be assigned to the hydrogen environments, OCH, OCHCH₂N and N(CH₃)₂, respectively, and are in a 3:1 ratio with the peak observed at 0.06 ppm corresponding to InMe, which is consistent with the formation of **23**. The four carbon environments present in **23**, namely OCH, OCH(CH₂N), N(CH₃) and InMe are observed at 67.3, 64.3, 46.1 and 5.3 ppm, respectively. In the mass spectrum of **23** taken in toluene, a peak is observed for the molecular ion at *m/z* = 620, which supports the proposed dimeric structure of **23**. This is confirmed by large peaks at *m/z* = 527 and 440 consistent with fragments of the dimeric structure reported for **23**. Interestingly, peaks corresponding to the ligand fragments CH(CH₂NMe₂)₂ and CH(CH₂NMe₂) are observed (*m/z* = 128, 71) and could provide some evidence of a potential decomposition pathway to indium oxide.

2.2.4.5. Reaction of **20** with HOCH₂CH₂OMe

Given the successful formation of compounds **21–23**, reaction of **20** with two equivalents of HOCH₂CH₂OMe in toluene under reflux conditions for 24 hours was investigated. The dimeric methyl–chloro–indium alkoxide, [Me(Cl)In(OCH₂CH₂OMe)]₂ (**24**), similar to **21–23** was isolated as small colourless crystals after sublimation in a long Schlenk flask over an oil bath at 50 °C under a dynamic vacuum. However, crystals were not of suitable quality for single X-ray

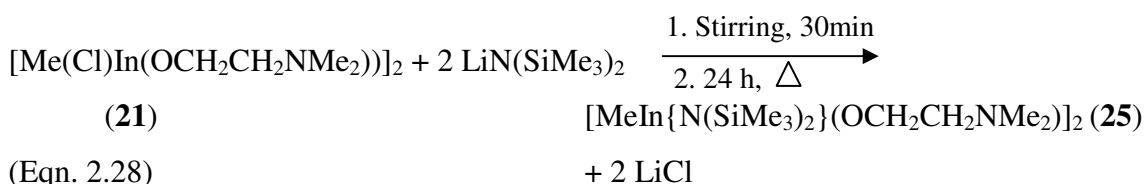
crystallographic analysis. Other analytical and spectroscopic techniques confirm the formation of **24**.



The reaction shown in Eqn. 2.27 was successfully carried out, which is based on Step (ii) (Scheme 2.10). In the ^1H NMR spectrum of **24** peaks were observed at 3.82, 3.41 and 3.21 ppm which can be assigned to the hydrogen environments, OCH_2CH_2 , CH_2OMe and $\text{O}(\text{CH}_3)$, respectively, and are in an 14:6 ratio with the peak observed at 0.15 ppm corresponding to InMe , which is consistent with the formation of **24**. Shifts observed in $^{13}\text{C}\{^1\text{H}\}$ NMR at 69.1, 58.1, 56.7 and 11.7 ppm can be assigned to CH_2OMe , OCH_2 , $\text{O}(\text{CH}_3)$ and InCH_3 , respectively. In the mass spectrum of **24** taken in toluene, a peak is observed for the molecular ion at $m/z = 479$, which supports the proposed dimeric structure of **24**. This is confirmed by large peaks consistent with fragments of the dimeric structure reported for **24** ($m/z = 464$, 420 and 394). Interestingly a peak corresponding to the ligand fragment $\text{OCH}_2\text{CH}_2\text{OMe}$ is observed at $m/z = 75$ and could provide some evidence of a potential decomposition pathway to indium oxide.

2.2.4.6. Reaction of **21** with $\text{LiN}(\text{SiMe}_3)_2$

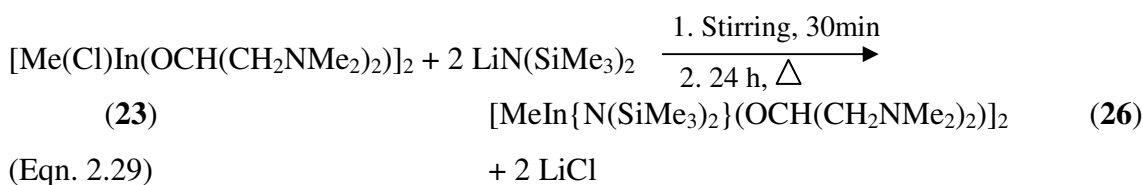
Step (iii) in Route 3 (Scheme 2.12) involves the reaction of compounds of the type $[\text{Me}(\text{Cl})\text{In}(\text{OR}')_2]$ with two equivalents of $\text{LiN}(\text{SiMe}_3)_2$ in order to isolate precursors of the type $[\text{MeIn}\{\text{N}(\text{SiMe}_3)_2\}(\text{OR}')_2]$. The *in situ* reaction of **21** with two equivalents of $\text{LiN}(\text{SiMe}_3)_2$ in toluene, with stirring for 30 min, then under reflux conditions for 24 hours, afforded the dimeric methyl-indium amido/alkoxide $[\text{MeIn}\{\text{N}(\text{SiMe}_3)_2\}(\text{OCH}_2\text{CH}_2\text{NMe}_2)]_2$ (**25**), as a yellow viscous oil. Analytical and spectroscopic data confirm the formation of compound **25**.



The reaction shown in Eqn. 2.28 is based on Route 3 (Scheme 2.12) and yielded **25** which will be used in reactions investigating **Step (iv)** also described in Scheme 2.12. Peaks were observed in the ^1H and $^{13}\text{C}\{^1\text{H}\}$ NMR spectra of **25**, for the alkoxide, amido and methyl ligands respectively, observed in a 10:18:3 ratio, which is consistent with the formation of **25**. Peaks were observed at 3.87, 2.48 and 2.23 ppm corresponding to the OCH_2 , CH_2N and $\text{N}(\text{CH}_3)_2$ hydrogen environments in the alkoxide ligand, as well as a multiplet at 0.28 ppm assigned to SiCH_3 and a single peak at 0.30 ppm for the InMe hydrogen environment. In the $^{13}\text{C}\{^1\text{H}\}$ NMR spectrum of **25**, peaks were observed for the alkoxide and amido ligand carbon environments, CH_2NMe_2 , OCH_2 , NMe_2 , $\text{N}(\text{SiMe}_3)_2$ and for the InMe carbon environment (60.2, 57.7, 46.5, 6.2 and 5.77 ppm respectively). In the mass spectrum of compound **25**, peaks observed at $m/z = 471$, 436, 398 and 348 are consistent with fragments of the dimeric structure of **25**. A peak observed at $m/z = 90$ is consistent with ligand fragments, providing some evidence of a potential decomposition pathway to gallium oxide.

2.2.4.7. Reaction of **23** with $\text{LiN}(\text{SiMe}_3)_2$

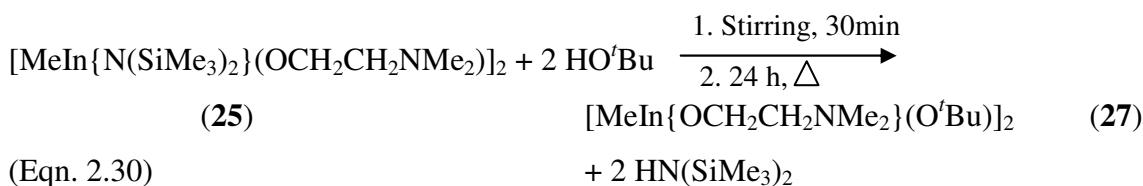
As detailed in section 2.2.4.6, **Step (iii)** in Route 3 (Scheme 2.12) involves the reaction of compounds of the type $[\text{Me}(\text{Cl})\text{In}(\text{OR}')_2]$ with two equivalents of $\text{LiN}(\text{SiMe}_3)_2$ in order to isolate precursors of the type $[\text{MeIn}\{\text{N}(\text{SiMe}_3)_3\}(\text{OR}')_2]$. Following the successful isolation of **25**, the *in situ* reaction of compound **23** with two equivalents of $\text{LiN}(\text{SiMe}_3)_2$ in toluene, with stirring for 30 minutes, then under reflux conditions for 24 hours, as carried out. The dimeric methyl-indium amido/alkoxide, $[\text{MeIn}\{\text{N}(\text{SiMe}_3)_2\}(\text{OCH}(\text{CH}_2\text{NMe}_2)_2)]_2$ (**26**) was isolated as a yellow viscous oil (Eqn. 2.29). Analytical and spectroscopic data confirms the formation of compound **26**.



Peaks were observed in the ^1H and $^{13}\text{C}\{^1\text{H}\}$ NMR spectra of **25**, corresponding to the alkoxide, amido and methyl ligands in a 17:18:3 ratio which is consistent with the formation of **26**. The peaks at 3.90, 2.31 and 2.24 ppm correspond to the OCH, CH_2N and $\text{N}(\text{CH}_3)_2$ hydrogen environments in the alkoxide ligand. A multiplet was observed at 0.08 ppm assigned to SiCH_3 and a single peak at 1.25 ppm for the InMe hydrogen environment. In the mass spectrum of compound **26**, taken in toluene peaks observed at $m/z = 812, 754, 710$ and 581 were consistent with fragments of the dimeric structure of **26**. Interestingly, peaks are observed for the ligand fragments $\text{N}(\text{SiMe}_3)_2$ and $\text{CH}(\text{CH}_2\text{NMe}_2)_2$ ($m/z = 160, 129$), providing some evidence of a potential decomposition pathway to indium oxide.

2.2.4.8. Reaction of **25** with HO^tBu

The fourth step of the synthesis described in Scheme 2.12 (**Step (iv)**) involves the reaction of compounds of the type $[\text{MeIn}\{\text{N}(\text{SiMe}_3)_2\}(\text{OR}')_2]$ with two equivalents of HO^tBu . This reaction would produce an unsymmetrical indium(III) bis(alkoxide), of the type $[\text{MeIn}\{\text{OR}'\}(\text{OR})_2]$, as described in Scheme 2.12, in **Step (iv)** of Route 3. Unlike the gallium analogues described in section 2.2.3, a methyl transfer to the indium metal centre is always observed in **Step (i)**, and it follows that **Steps (ii) – Step (iv)** proceed towards the facile synthesis of unsymmetrical indium(III) bis(alkoxides). Thus, the *in situ* reaction of the **25** with two equivalents of tertiary butanol in toluene, with stirring for 30 min, then under reflux conditions for 24 hours, afforded the dimeric methyl-indium bis(alkoxide), $[\text{MeIn}\{\text{OCH}_2\text{CH}_2\text{NMe}_2\}(\text{O}^t\text{Bu})_2]$ (**27**), as an orange viscous oil (Eqn. 2.30). Analytical and spectroscopic data confirm the formation of compound **27**.

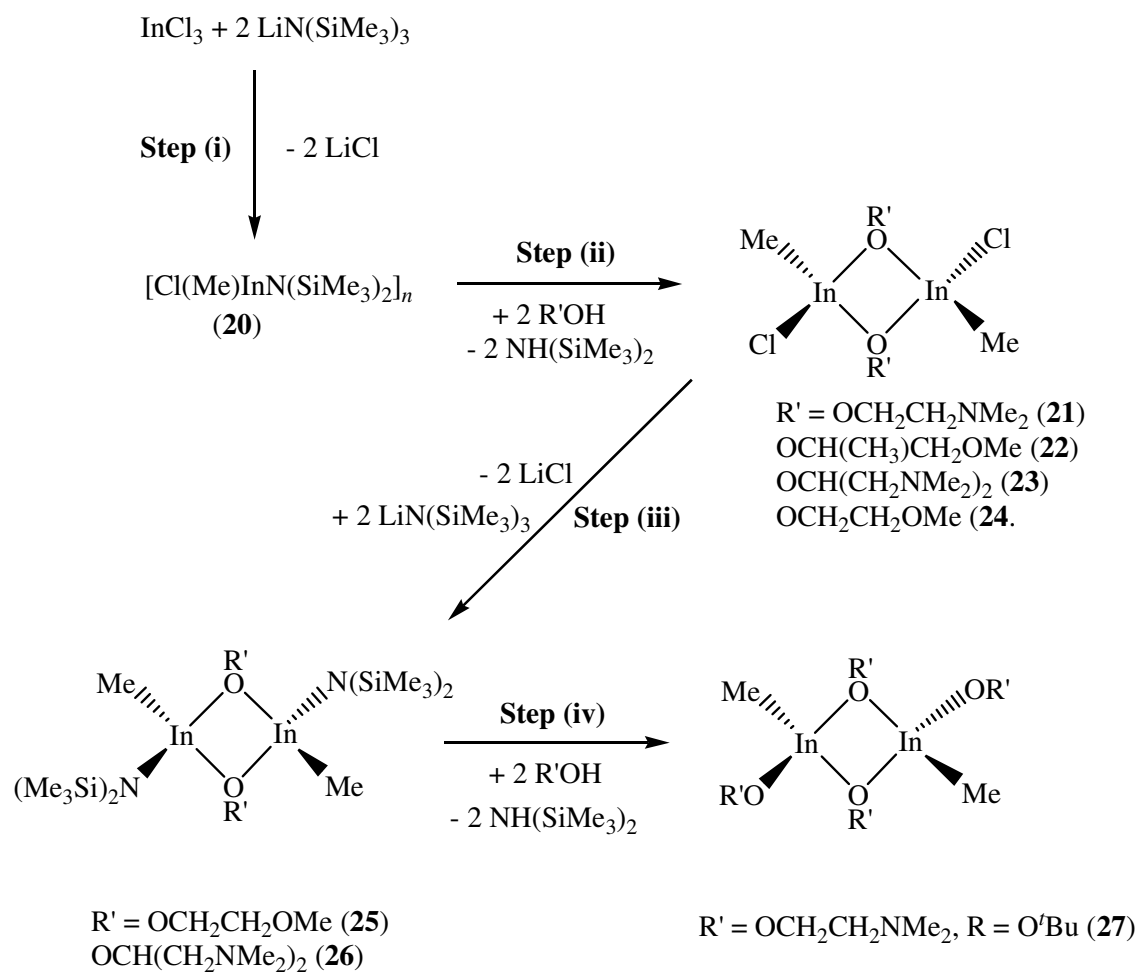


In the ^1H NMR spectrum of **27** peaks were observed for the donor functionalised alkoxide, tertiary butyl and methyl ligands, consistent with the synthesis of **27**. Peaks observed for the tertiary butyl group hydrogen environment at 1.20 ppm, methyl group hydrogen environment at 0.06 ppm, and donor functionalised alkoxide ligand at 2.61, 2.32 and 2.24 ppm (OCH_2 , $\text{CH}_2\text{CH}_2\text{N}$ and NCH_3 , respectively), were observed in a 18:20:6 ratio, which is consistent with the formation of **27**. In the $^{13}\text{C}\{^1\text{H}\}$ NMR spectrum of compound **27** two peaks, at 78.7 and 46.5 ppm are observed for the two carbon environments in the tertiary butyl ligand. Peaks were also observed at 67.3, 64.3 and 46.1 ppm for the three carbon environments in the donor functionalised alkoxide ligand (OCH_2 , $\text{OCH}_2\text{CH}_2\text{N}$ and NCH_3), as well as a peak observed at 5.30 ppm for the InMe carbon environment. In the mass spectrum of compound **27**, taken in toluene peaks observed at $m/z = 471, 429, 401, 371$ and 90 were consistent with fragments of the dimeric structure and with ligand fragments, providing some evidence of a potential decomposition pathway to indium oxide.

Compound **27** shows promise as an excellent CVD precursor, as a liquid its solubility is suitable for dissolution in a wide range of organic solvents. Additionally the incorporation of a tertiary butyl group will aid clean decomposition *via* β -hydride elimination, and the coordination of two alcohol groups results in a M:O ratio of 1:2 in the precursor, with the view to the production of In_2O_3 thin films that are not oxygen deficient.

2.2.4.9. Summary of synthetic routes used in section 2.2.4.

The attempted synthesis of unsymmetrical indium (III) bis(alkoxides) was investigated using the four step synthetic routes shown in Scheme 2.4 in section 2.2. In light of this work a slightly amended Scheme 2.13 detail the routes followed in the synthesis described in sections 2.2.4. It is interesting to note that when compared to the similar reactions investigated with gallium (Scheme 2.11), with indium reactions are much cleaner.



Scheme 2.13: Summary of synthetic routes used in section 2.2.4.

2.2.5. Gallium(III) and indium(III) tris(alkoxides).

The attempted synthesis of gallium(III) and indium(III) tris(alkoxides) was investigated using the Route 4, as described in section 2.2. This synthesis follows a barium chloride salt elimination, resulting in the clean formation of group 13 tris(alkoxides).



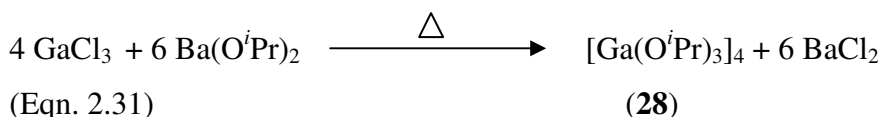
M = Ga, In; R = *i*Pr

Previous routes to group 13 tris(alkoxides) include the reaction of MCl₃ with three equivalents of Na(OR). Exchanging sodium with the doubly charged barium atom allows the group 13 metal to retain a high coordination number.

The synthetic route reported here removes any chlorine contamination by using an extra equivalent of the barium isopropoxide. In previous reported procedures an excess of sodium isopropoxide resulted in contamination of the product with the base, stoichiometric amounts resulted in chlorine contamination. However, the increased insolubility of barium chloride means that the excess base can be removed by recrystallising the group 13 alkoxide with hexane, giving a pure product with good yields.

2.2.5.1. Reaction of GaCl₃ with barium isopropoxide

The treatment of GaCl₃ with one and a half equivalents of barium isopropoxide resulted in the formation of Ga(O^{*i*}Pr)₃ (**28**) which was isolated as a yellow crystalline solid in good yield (Eqn. 2.31). Analytical and spectroscopic data confirm the formation of compound **28**, which exists as a tetramer.



The synthesis of **28** is based on Route 4, described in section 2.2 and detailed in Scheme 2.14. The solubility of the compound was poor in hexanes and benzene and clean NMR spectrum were only achieved in deuterated chloroform. In the ¹H NMR spectrum of **28** peaks observed at 4.35, 3.93, 1.39 and 1.51 ppm can be assigned to the hydrogen environments, OCH, OCH, CHCH₃ and CHCH₃, respectively, consistent with the formation of **28** as a tetramer (Fig. 2.12). Four peaks observed in the ¹³C{¹H} NMR spectrum of **28** at 65.1, 64.1, 27.4 and 25.3 correspond to the carbon environments, CH, CH, HCH₃ and CHCH₃. In the mass spectrum of **28**, taken in toluene, peaks observed are consistent with fragments of the tetramer and the ligand OCH(CH₃)₂ (*m/z* = 383, 315, 246, 187 and 118).

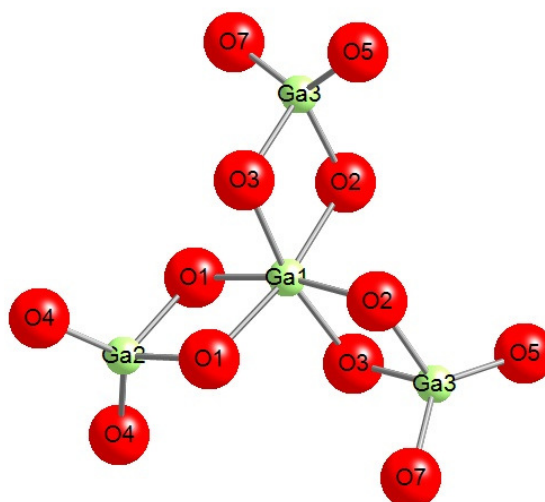
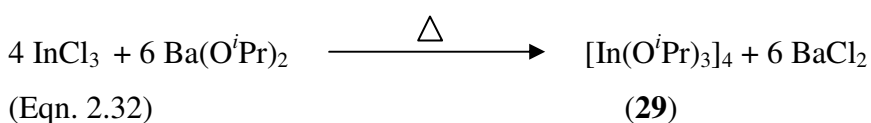


Fig. 2.12: The proposed structure of (**28**) exhibited here as a tetramer, the gallium tris(alkoxides) units oligomerise, bridging through one oxygen atom from each gallium tris(isopropoxide) unit rendering each gallium centre four coordinate with a tetrahedral geometry (carbon and hydrogen atoms are omitted for clarity).

The proposed mechanism for the synthesis of the group 13 tris(alkoxides) is shown in Scheme 2.14. The methodology was successful for the gallium analogue, however the formation of $[\text{In}(\text{O}^i\text{Pr})_3]_n$ is not observed, as detailed in section 2.2.5.2.

2.2.5.2. Reaction of InCl_3 with barium isopropoxide

The treatment of InCl_3 with one and a half equivalents of barium isopropoxide does not result in the formation of $[\text{In}(\text{O}^i\text{Pr})_3]$ (**29**), as proposed in Eqn. 2.32. It is thought that the isopropoxide ligands are not bulky enough to stabilise the indium centre as a tris(alkoxide), in fact there is no literature report of $[\text{In}(\text{O}^i\text{Pr})_3]$. Indium, with its larger atomic radius, when compared to gallium cannot exist as **29** and instead oligomerisation is observed and the indium cluster $[(\text{InO}^i\text{Pr})_5(\mu_2\text{-O}^i\text{Pr})_4(\mu_3\text{-O}^i\text{Pr})_4(\mu_5\text{-O})]$ (**29a**) (Fig. 2.13) isolated as a white crystalline solid in good yield. Analytical and spectroscopic data confirm the formation of compound **29a**, on comparison with literature values.⁶⁷



The solubility of **29a** was poor in hexanes and benzene and clean NMR spectrum were only achieved in deuterated chloroform. In the ^1H NMR spectrum of **29a** peaks observed at 4.36, 1.44 and 1.21 ppm can be assigned to the hydrogen environments, CH , CHCH_3 and CHCH_3 , respectively, in a 13:48:30 ratio, consistent with the formation of **29a** as a cluster. Four peaks observed in the $^{13}\text{C}\{^1\text{H}\}$ NMR spectrum of **29a** at 68.2, 68.9, 28.6 and 27.1 ppm correspond to the carbon environments, O-CH , OCH , $\text{O-CH}(\text{CH}_3)_2$ and $\text{OCH}(\text{CH}_3)_2$. In the mass spectrum of **29a**, taken in toluene, peaks observed are consistent with fragments of the cluster and ligand fragments ($m/z = 485, 405, 346, 248$ and 173).

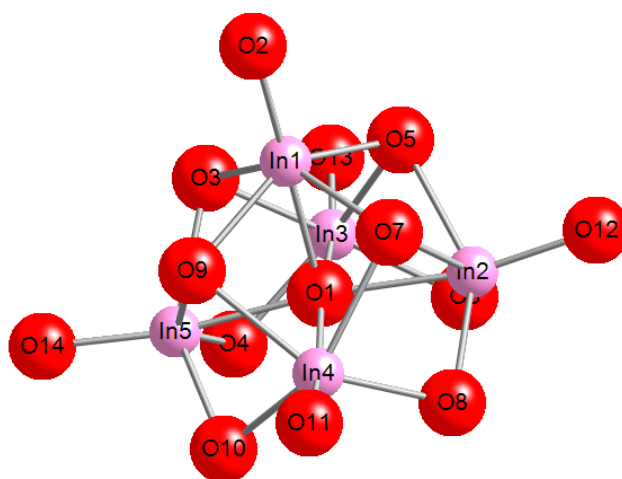


Fig. 2.13: Proposed structure of $[(\text{InO}^i\text{Pr})_5(\mu_2\text{-O}^i\text{Pr})_4(\mu_3\text{-O}^i\text{Pr})_4(\mu_5\text{-O})]$ (**29a**) as reported previously.⁶⁷ It can be observed the central oxygen atom (O1) is surrounded by five highly distorted octahedral indium centres in a square pyramidal arrangement, with four μ_3 isopropoxide groups capping the indium atoms above the plane and four μ_2 isopropoxide groups bridging the indium atoms below the plane (carbon and hydrogen atoms are omitted for clarity).

2.3. Conclusions

A wide variety of group 13 alkoxides have been synthesised and characterised in this thesis. Significant findings in Chapter 2 support previous investigations showing the reaction of MR_3 with excess of a donor functionalised alcohol does not solely yield a group 13 bis(alkoxide) in high yield. In addition, compounds of the type $[\text{Ga}(\text{OR}')_n\text{Cl}_3]$.

n] (**8-10**) were synthesised using direct routes from gallium amides prepared (**6, 7**), as well as a wide variety of novel group 13 precursors (M = Ga (**11 – 19**); M = In (**20 – 27**)) incorporating a mixture of ligands. The unsymmetrical nature of the compounds should lead to enhanced properties, desirable for CVD. Additionally, the synthesis of group 13 tris(alkoxides) **28** and **29a** via a barium chloride elimination route is reported as characterized by spectroscopic data.

The group 13 monoalkoxometallanes of the type $[\text{Me}_2\text{M}(\text{OR}')_2]$ were synthesised by the reaction of GaMe_3 or InMe_3 with $\text{R}'\text{OH}$ (M = Ga, $\text{R}' = \text{CH}_2\text{CH}_2\text{OMe}$, $\text{CH}_2\text{CH}_2\text{NMe}_2$, $\text{C}(\text{CH}_3)_2\text{CH}_2\text{OMe}$, $\text{CH}(\text{CF}_3)_2$ (**1-3, 5**); M = In, $\text{R}' = \text{CH}(\text{CH}_3)\text{CH}_2\text{OMe}$ (**4**)) in toluene.

Additionally, compounds of the type $[\text{Ga}(\text{OR}')_n\text{Cl}_{3-n}]$, were synthesised directly from the reaction of $\text{R}'\text{OH}$ with $[\text{Ga}(\text{NMe}_2)_n\text{Cl}_{3-n}]$ ($n = 1$ (**6**), **2** (**7**); $n = 1$, $\text{R}' = \text{C}(\text{CH}_3)_2\text{CH}_2\text{OMe}$ (**8**); $n = 2$, $\text{R}' = \text{CH}(\text{CH}_3)\text{CH}_2\text{NMe}_2$ (**9**), $\text{CH}_2\text{CH}_2\text{NMe}_2$ (**10**)).

With a view to further enhancing the properties of these group 13 alkoxide precursors a series of protonolysis and alcoholysis steps were devised and carried out to synthesis a wide range of group 13 compounds of the type $[\text{Me}_x(\text{Cl})_{2-(x+z)}\text{M}\{\text{N}(\text{SiMe}_3)_2\}_{1-y}(\text{OR}')_y(\text{OR})_z]_2$ (M = Ga (**11 – 19**); M = In (**20 – 27**)) incorporating a variety of donor functionalised alkoxide ligands ($\text{R}' = \text{OCH}_2\text{CH}_2\text{OMe}$, $\text{OCH}_2\text{CH}_2\text{NMe}_2$, $\text{OCH}(\text{CH}_3)\text{CH}_2\text{OMe}$, $\text{OC}(\text{CH}_3)_2\text{CH}_2\text{NMe}_2$) and a simple alkoxide ligand ($\text{R} = \text{O}'\text{Bu}$) to act as precursors to group 13 oxide thin films. The variety in size of ligands surrounding the metal centre further enhances solubility, lowers the temperature of vapourisation and enables facile decomposition; all of which are all desired properties for CVD.

Many of these compounds have been characterised by a variety of techniques including X-ray crystallography, which show that compounds of the form $[\text{X}_2\text{M}(\text{OR}')_2]$ (X = Cl, Et, Me) are dimeric in the solid state whilst compounds of the type $[\text{XM}(\text{OR}')_2]$ (X = Cl, Et, Me) are monomeric in the solid state. In addition, it is interesting to note that the reactions with gallium compounds often resulted in mixtures of products, however, in comparison to reactions with analogous indium compounds, reactions were much cleaner.

Finally the synthesis of homoleptic group 13 tris(alkoxide) $[\text{Ga}(\text{O}^i\text{Pr})_3]$ (**28**) and cluster compound $[(\text{InO}^i\text{Pr})_5(\mu_2\text{-O}^i\text{Pr})_4(\mu_3\text{-O}^i\text{Pr})_4(\mu_5\text{-O})]$ (**29a**) was achieved by reaction of MCl_3 with three equivalents of $\text{Ba}(\text{O}^i\text{Pr})_2$ as characterized by spectroscopic data.

The reaction of GaCl_3 with one and a half equivalents of barium isopropoxide resulted in the formation of $[\text{Ga}(\text{O}^i\text{Pr})_3]_4$ (**28**) in good yield with no chlorine contamination. The routes described have been shown to be unsuccessful in isolating the indium analogue (**29**) and instead give the cluster compound $[(\text{InO}^i\text{Pr})_5(\mu_2\text{-O}^i\text{Pr})_4(\mu_3\text{-O}^i\text{Pr})_4(\mu_5\text{-O})]$ (**29**) also in high yield and without chlorine contamination. Compounds **28** and **29a** are fully characterised by ^1H and ^{13}C NMR, IR and mass spectroscopy.

2.4. Experimental

2.4.1. General procedures

All manipulations were performed under a dry, oxygen-free dinitrogen atmosphere using standard Schlenk techniques or in an Mbraun glovebox. All solvents used were stored in alumina columns and dried with anhydrous engineering equipment, such that the water concentration was 5 – 10 ppm. Chemicals were supplied by Multivalent or procured commercially from Aldrich and used without further purification, with the exception of alcohols which were further distilled and degassed and stored over molecular sieves. Analytical data were obtained at UCL.

2.4.2. Physical Measurements

All ^1H and ^{13}C NMR spectra were obtained on a Bruker AMX300 and AMX400 spectrometer, operating at 299.87 MHz and 400.12 MHz respectively. All spectra were recorded using C_6D_6 and CD_2Cl_2 which were dried and degassed over molecular sieves prior to use; ^1H and ^{13}C chemical shifts are reported relative to SiMe_4 (δ 0.00). All IR spectra were recorded using a Shimadzu FTIR-8200 spectrometer, operating in the region of $4000\text{-}400\text{ cm}^{-1}$. The IR samples were prepared using nujol. The mass spectra were obtained using a Micromass 70-SE spectrometer using Chemical Ionisation (CI) with methane reagent gas. The Elemental Analysis (elemental analysis) was carried using Elemental Analyser (CE-440) (Exeter Analytical Inc). The instrument used for thermal analysis was the Netzsch Jupiter.

2.4.3. Synthesis of precursors

2.4.3.1. Synthesis of [MeGa(OCH₂CH₂OMe)₂] (1)

Trimethylgallium (0.9968 g, 8.77 mmol) was dissolved in toluene (20 cm³) and cooled to -78 °C. 2-Methoxyethanol (4.15 cm³, 52 mmol) was added dropwise to the cooled solution. This was allowed to warm to room temperature with stirring. The reaction was then heated under reflux for 24 h giving a cloudy solution. The solvent was removed *in vacuo* to give a white viscous liquid (0.9850 g, yield 48%). ¹H NMR δ/ppm (CDCl₃): Compound **1**: 3.83 (m, OCH₂CH₂, 4H), 3.37 (m, CH₂OMe, 4H), 3.26 (s, O(CH₃), 6H), -0.22 (s, GaCH₃, 3H). Compound **1a**: 3.81 (m, OCH₂CH₂, 2H), 3.31 (m, CH₂OMe, 2H), 3.25 (s, O(CH₃), 3H), -0.21 (s, GaCH₃, 6H). ¹³C{¹H} NMR δ/ppm (CDCl₃): Compound **1**: 74.0 (CH₂OMe), 62.2 (OCH₂), 58.8 (O(CH₃)), 3.26 (GaCH₃). Compound **1a**: 74.2 (CH₂OMe), 62.0 (OCH₂), 59.0 (O(CH₃)), 5.26 (GaCH₃). Mass spec. (CI): (*m/z*) 159 [MeGa(OCH₂CH₂OMe)], 90 [Me(OCH₂CH₂OMe)], 99 (GaMe₂).

2.4.3.2. Synthesis of [MeGa(OCH₂CH₂NMe₂)₂] (2)

Trimethylgallium (1.0028 g, 8.7 mmol) was dissolved in toluene (20 cm³) and cooled to -78 °C. 2-Dimethylaminoethanol (5.2 cm³, 52 mmol) was added dropwise to the cooled solution. This was allowed to warm to room temperature with stirring. The reaction was then heated under reflux for 24 h giving a brown solution. The solvent was removed *in vacuo* to give a viscous liquid (1.2567 g, 55% yield). ¹H NMR δ/ppm (CDCl₃): Compound **2**: 3.68 (m, OCH₂CH₂, 4H), 2.37 (m, CH₂NMe₂, 4H), 2.31 (s, N(CH₃)₂, 12H), -0.12 (s, GaCH₃, 3H). Compound **2a**: 3.71 (m, OCH₂CH₂, 2H), 2.38 (m, CH₂NMe₂, 2H), 2.34 (s, N(CH₃)₂, 6H), -0.21 (s, GaCH₃, 6H). ¹³C{¹H} NMR δ/ppm (CDCl₃): Compound **2**: 61.5 (CH₂NMe₂), 59.6 (OCH₂), 46.0 (N(CH₃)₂), 11.4 (GaCH₃). Compound **2a**: 61.6 (CH₂NMe₂), 60.1 (OCH₂), 46.3 (N(CH₃)₂), 11.7 (GaCH₃). Mass spec. (CI): (*m/z*) 261 MeGa(OCH₂CH₂NMe₂), 172 (MeGaOCH₂CH₂NMe₂), 88 (OCH₂CH₂NMe₂), 72 (CH₂CH₂NMe₂).

2.4.3.3. Synthesis of [Me₂Ga(OC(CH₃)₂CH₂OMe)]₂ (3)

1-Methoxy-2-methyl-2-propanol (2.0 cm³, 17.5 mmol) was added dropwise to trimethylgallium (0.53 g, 4.61 mmol) in toluene (20 cm³) cooled to -78 °C. This was allowed to warm to room temperature with stirring. The reaction was then heated under reflux for 24 h, resulting in a cloudy solution. The solvent was removed *in vacuo*

affording a white solid, this was dissolved in hexane and cooled to $-80\text{ }^{\circ}\text{C}$; after 30 days a white solid (0.45 g, 24% yield) had formed. Anal. Calc. (%) for $\text{C}_{14}\text{H}_{34}\text{O}_4\text{Ga}_2$: C, 41.23; H, 8.34. Found (%): C, 40.31; H, 8.49. ^1H NMR δ/ppm (CDCl_3): 3.34 (s, OCH_3 , 6H), 3.11 (s, GaOCCH_2 , 4H), 1.17 (s, GaOCCH_3 , 12H), -0.33 (s, GaCH_3 , 12H,). ^{13}C NMR δ/ppm (CDCl_3): 81.7 (OCCH_2), 72.6 (OCCH_2), 58.1 (OCH_3), 27.2 (GaOCCH_3), 2.5 (GaCH_3). FT-IR (Nujol, KBr, cm^{-1}): 2977 m, 2884 m, 2834 m, 1458 m, 1363 m, 1260 w, 1198 m, 1180 s, 1002 w, 960 s, 939 m, 798 m, 739 m, 637 m, 585 m, 534 m, 494 w. Mass spec (CI): (m/z) 391 ($[\text{M}]_2 - \text{Me}$), 303 ($[\text{M}]_2 - \text{Me}_4\text{O}_2\text{CH}_3$), 187 ($[\text{M}] - \text{Me}$), 87 ($\text{C}(\text{CH}_3)_2\text{CH}_2\text{CH}_2\text{OCH}_3$). After several weeks, small clear crystals of X-ray crystallography quality formed.

2.4.3.4. Synthesis of $[\text{Me}_2\text{In}(\text{OCH}(\text{CH}_3)\text{CH}_2\text{OMe})]_2$ (4)

1-Methoxy-2-propanol (5.1 cm^3 , 5.2 mmol) was added dropwise to trimethylindium (0.67 g, 4.21 mmol) dissolved in toluene (20 cm^3) and cooled to $-78\text{ }^{\circ}\text{C}$. This was allowed to warm to room temperature with stirring. The reaction was then heated under reflux for 24 h, resulting in a cloudy yellow solution. The solvent was removed in vacuo to give a yellow viscous liquid (1.13 g, 58% yield). After several weeks, small clear crystals formed from the oil. Anal. Calc. (%) for $\text{C}_{12}\text{H}_{30}\text{O}_4\text{In}_2$: C, 30.90; H, 6.44. Found (%): C, 31.86; H, 6.67. ^1H NMR δ/ppm (CDCl_3): 3.95 (m, InOCHCH_3 , 1H), 3.27 (m, OCH_3 , 3H), 3.04 (m, InOCHCH_2 , 2H), 1.04 (m, InOCHCH_3 , 3H), 0.43 (s, InCH_3 , 6H). $^{13}\text{C}\{^1\text{H}\}$ NMR δ/ppm (CDCl_3): 79.4 (CHCH_2OMe), 66.3 ($\text{OCH}(\text{CH}_3)$), 58.0 (CH_2OCH_3), 20.9 ($\text{InCH}(\text{CH}_3)\text{CH}_2$), 1.0 (InCH_3). Mass spec (CI): (m/z) 453 ($[\text{M}]_2 - \text{Me}$), 407 ($[\text{M}]_2 - \text{Me}_4$), 319 ($[\text{M}]_2 - \text{Me}_4\text{OCH}(\text{CH}_3)\text{CH}_2\text{OMe}$), 219 ($\text{MeIn}(\text{OCH}(\text{CH}_3)\text{CH}_2\text{OMe})$).

2.4.3.5. Synthesis of $[\text{Me}_2\text{Ga}(\text{OCH}(\text{CF}_3)_2)]_2$ (5)

Trimethylgallium (0.9970 g, 8.77 mmol) was dissolved in toluene (20 cm^3) and cooled to $-78\text{ }^{\circ}\text{C}$. 1,1,1,3,3,3-Hexafluoro-2-propanol (4.15 cm^3 , 52 mmol) was added dropwise to the cooled solution, which was then allowed to warm to room temperature with stirring. The reaction was then heated under reflux for 24 h giving a cloudy solution. The solvent was removed in vacuo to give a white viscous liquid (1.47 g, 61% yield). Anal. Calc. for $\text{C}_{10}\text{H}_{14}\text{O}_2\text{F}_{12}\text{Ga}_2$: C, 22.56; H, 2.63; N, 0.00. Found: C, 21.91; H, 2.55; N, 0.00 %. ^1H NMR δ/ppm (C_6D_6): 4.46 (m, OCH , 2H), 0.20 (m, GaCH_3 , 12H). $^{13}\text{C}\{^1\text{H}\}$ NMR δ/ppm (C_6D_6): 1.0 (GaCH_3), 71.8 (OCH), 120.0 (CCF_3). IR (cm^{-1}): 2924

m, 2282 w, 2149 w, 1996 w, 1570 m, 1374 s, 1292 s, 1194 s, 1106 s, 895 s, 862 s, 814 w, 751 m, 688 m, 621 w, 601 m, 535 m. Mass spec (CI): (m/z) 407 ($[M]_2 - CF_6$), 297 ($[M]_2 - (CF_3)_2CHOHGa$), 221 ($(CF_3)_2MeGa$), 169 ($GaCF_3CHO$), 149 ($(CF_3)_2C$).

2.4.3.6. Synthesis of $[Cl_2Ga(NMe_2)]_2$ (6)

A slurry of lithium dimethylamide (0.2934 g, 5.0 mmol) in hexane (15 cm³) was added dropwise to a stirred solution of gallium trichloride (0.8900 g, 5.0 mmol) in hexane (15 cm³) at -78 °C, and stirred for 2 h. The reaction mixture was allowed to warm to room temperature and stirred for a further 24 h. The resulting white slurry was filtered and the solvent removed *in vacuo* to yield a free flowing white powder (0.8784 g, 76%). Anal. Calc. for C₄H₁₂N₂Cl₄Ga₂: C, 13.11; H, 3.28; N, 7.65. Found: C, 12.96; H, 2.97; N, 7.31 %. ¹H NMR δ /ppm (C₆D₆): 2.76 (s, NCH₃, 12H). ¹³C{¹H} NMR δ /ppm (C₆D₆): 44.0 (NCH₃). Mass spec. (CI): (m/z) 366 ([M]), 297 ([M] - Ga), 148 (ClGaNMe₂), 113 (Ga(NMe)).

2.4.3.7. Synthesis of $[ClGa(NMe_2)]_2$ (7)

A slurry of lithium dimethylamide (0.5867 g, 11 mmol) in hexane (15 cm³) was added dropwise to a stirred solution of gallium trichloride (1.0067 g, 5.7 mmol) in hexane (15 cm³) at -78 °C, and stirred for 2 h. The reaction mixture was allowed to warm to room temperature and stirred for a further 24 h. The resulting white slurry was filtered and the solvent removed *in vacuo* to yield a free flowing white powder (0.8477 g, 82%). Anal. Calc. for C₈H₂₄N₄Cl₂Ga₂: C, 24.85; H, 6.26; N, 14.49. Found: C, 24.19; H, 6.12; N, 13.87 %. ¹H NMR δ /ppm (C₆D₆): 2.30 (s, μ_2 -NCH₃, 12H), 2.75 (s, NCH₃, 12H). ¹³C{¹H} NMR δ /ppm (C₆D₆): 42.9 (NCH₃). Mass spec. (CI): (m/z) 387 ([M]), 308 ([M] - NMe₂, - Cl), 238 ([M] - Ga).

2.4.3.8. Synthesis of $[Cl_2Ga(OC(CH_3)_2CH_2OMe)]_2$ (8)

1-Methoxy-2-methyl-2-propanol, (0.4 cm³, 3.26 mmol) was added dropwise to a stirred solution of **6** (0.6027 g, 3.26 mmol) in hexane (20 cm³) at -78 °C. The reaction mixture was allowed to warm to room temperature and stirred for 24 h. Removal of the solvent *in vacuo* afforded a white crystalline solid (0.4936 g, 62% yield). Anal. Calc. for C₁₀H₂₂Cl₄Ga₂O₄: C, 24.64; H, 4.55. Found: C, 25.02; H, 4.26 %. ¹H NMR δ /ppm (C₆D₆): 3.60 (s, OCH₃, 6H), 2.58 (s, GaOCCH₂, 4H), 1.48 (s, OC(CH₃), 12H). ¹³C{¹H} NMR δ /ppm (C₆D₆): 79.9 (OCCH₂) 70.1 (OCCH₂), 58.9 (OCH₃), 26.1 (OC(CH₃)).

Mass spec. (CI): (m/z) 451 [Ga(OC(CH₃)₂CH₂OMe)₃Cl₂], 290 [Ga(OC(CH₃)CH₂OMe)₂Cl₂ – OC(CH₃)₂CH₂OMe], 245 [Ga(OC(CH₃)CH₂OMe)₂Cl₂], 87 [C(CH₃)₂CH₂OMe].

2.4.3.9. Synthesis of [ClGa(OCH(CH₃)CH₂NMe₂)₂] (9)

1-Methylamino-2-propanol (1.1 cm³, 8.30 mmol) was added dropwise to a stirred solution of **7** (0.8023 g, 4.15 mmol) in hexane (20 cm³) at -78 °C. The reaction mixture was allowed to warm to room temperature and stirred for 24 h. Removal of the solvent *in vacuo* afforded a white crystalline solid (0.6923 g, 54 % yield). Anal. Calc. for C₁₀H₂₄ClGaN₂O₂: C, 38.81; H, 7.81; N, 9.05. Found: C, 38.88; H, 7.08; N, 9.67 %. ¹H NMR δ /ppm (C₆D₆): 1.31 (d, OCH(CH₃), 6H, J = 6.10 Hz), 2.29-2.41 (br, OCHCH₂N, 4H), 2.49 (br, NCH₃, 12H), 3.95 (m, OCH(CH₃)CH₂, 2H). Mass spec. (CI): (m/z) 309 [M], 273 [M] – OCH(CH₃)CH₂NMe₂, 102 [OCH(CH₃)CH₂NMe₂], 86 OCH(CH₃)CH₂NMe₂.

2.4.3.10. Synthesis of [ClGa(OCH₂CH₂NMe₂)₂] (10)

2-Dimethylaminoethanol, (0.75 cm³, 7.37 mmol) was added dropwise to a solution of **7** (0.7126 g, 3.69 mmol) in hexane (20 cm³) at -78 °C. The reaction was allowed to warm to room temperature and stirred for 24 h. removal of the solvent *in vacuo* afforded a pale yellow solid (0.6203 g, 60 % yield). Anal. Calc. for C₈H₂₀ClGaN₂O₂: C, 34.14; H, 7.16; N, 9.95. Found: C, 34.66; H, 7.72; N, 9.05 %. ¹H NMR δ /ppm (C₆D₆): 2.00 (NCH₃, 12H), 2.27 (t, OCH₂CH₂N, 4H), 3.93 (t, OCH₂CH₂N, 4H). ¹³C{¹H} NMR δ /ppm (C₆D₆): 43.9 (NCH₃), 58.7 (OCH₂CH₂N), 60.4 (OCH₂CH₂N). Mass spec. (CI): (m/z) 281 [M], 246 [M] – Cl, 194 [M] – OCH₂CH₂NMe₂, 158 [Ga(OCH₂CH₂NMe₂)₂], 88 [OCH₂CH₂NMe₂].

2.4.3.11. Synthesis of [Me(Cl)GaN(SiMe₃)₂]₂ (11)

A suspension of lithium hexamethyldisilylamide (0.5867 g, 11 mmol) in toluene (15 cm³) was added dropwise to a suspension of gallium trichloride (0.9786 g, 5.7 mmol) in toluene (15 cm³) at -78 °C and was stirred for 30 minutes. The reaction mixture was allowed to warm to room temperature with stirring and then heated, under reflux, for 24 h giving a cloudy solution. After cooling the solution was filtered and the solvent removed *in vacuo* to give a white viscous liquid. The product was purified by sublimation (10⁻² Torr/100 °C, 1.04 g, 67% yield). Anal. Calc. for C₁₄H₄₂Cl₂Si₄Ga₂N₂:

C, 29.96; H, 7.54; N, 4.99. Found: C, 30.67; H, 7.22; N, 5.11 %. ^1H NMR δ/ppm (C_6D_6): 0.28 (m, $\text{N}(\text{Si}(\text{CH}_3)_3)$, 36H), 0.03 (s, GaCH_3 , 6H). $^{13}\text{C}\{^1\text{H}\}$ NMR δ/ppm (C_6D_6): 23.2 (GaCH_3), 4.7 ($\text{N}(\text{Si}(\text{CH}_3)_3)$). Mass spec. (CI): (m/z) 279 [M], 244 [M] – Cl, 201 [$\text{GaN}(\text{SiMe}_3)_2$], 199 [M] – Me – Cl, 171 [M] – Cl – (SiMe_3).

2.4.3.12. Synthesis of $[\text{Me}(\text{Cl})\text{Ga}(\text{OCH}(\text{CH}_3)\text{CH}_2\text{NMe}_2)]_2$ (12)

1-Dimethylamino-2-propanol (0.3 cm^3 , 3.1 mmol) was added to a solution of **11** (1.0098 g, 1.7 mmol) in toluene (20 cm^3) prepared from an *in situ* reaction. The mixture was heated under reflux for 24 h giving a cloudy solution. After cooling the solution was filtered and the solvent and volatiles removed *in vacuo* to give a yellow viscous oil. The oil was sublimed in a long Schlenk flask over an oil bath at 50°C under a dynamic vacuum affording small clear crystals (0.56 g, 79% yield). Anal. Calc. (%) for $\text{C}_{12}\text{H}_{30}\text{N}_2\text{O}_2\text{Ga}_2\text{Cl}_2$: C, 32.58; H, 6.79; N, 6.33 Found (%): C, 31.98; H, 6.67; N, 6.01. ^1H NMR δ/ppm (C_6D_6): 4.05 (m, $\text{OCH}(\text{CH}_3)$, 2H), 2.31 (br, $\text{OCH}(\text{CH}_3)\text{CH}_2$, 4H), 0.22 (br, $\text{N}(\text{CH}_3)_2$, 12H), 0.07 (s, $\text{OCH}(\text{CH}_3)$, 6H), 0.06 (GaCH_3 , 6H). $^{13}\text{C}\{^1\text{H}\}$ NMR δ/ppm (C_6D_6): 23.0 (GaCH_3), 48.2 ($\text{OCH}(\text{CH}_3)$), 64.5 ($\text{N}(\text{CH}_3)_2$), 66.3 ($\text{CH}(\text{CH}_3)\text{CH}_2$), 67.8 ($\text{OCH}_2(\text{CH}_3)$). Mass spec (CI): (m/z) 442 ([M]), 412 ([M] – Me_2), 293 ([M] – $\text{Me}_4\text{OCH}(\text{CH}_3)\text{CH}_2\text{OMe}$).

2.4.3.13. Synthesis of $[\text{Cl}_2\text{Ga}(\text{OCH}_2\text{CH}_2\text{NMe}_2)]_2$ (13)

2-Dimethylaminoethanol, (0.3 cm^3 , 2.8 mmol) was added dropwise to a solution of **11** (0.9987 g, 1.7 mmol) in toluene (20 cm^3) prepared *in situ*. The reaction was heated under reflux for 24 h giving a cloudy solution. After cooling the solution was filtered and the solvent and other volatiles were removed *in vacuo* to give a yellow viscous oil. The oil was sublimed in a long Schlenk flask over an oil bath at 50°C under a dynamic vacuum and afforded crystals of X-ray crystallographic quality (0.5897 g, 42% yield). Anal. Calc. (%) for $\text{C}_8\text{H}_{20}\text{N}_2\text{O}_2\text{Ga}_2\text{Cl}_4$: C, 25.06; H, 5.22; N, 7.31 Found (%): C, 25.98; H, 5.37; N, 7.01. ^1H NMR δ/ppm (C_6D_6): 3.59 (m, OCH_2CH_2 , 2H), 2.57 – 2.15 (br, CH_2NMe_2 , 2H), 2.11 (m, $\text{N}(\text{CH}_3)_2$, 6H). $^{13}\text{C}\{^1\text{H}\}$ NMR δ/ppm (C_6D_6): 60.2 (CH_2NMe_2), 57.9 (OCH_2), 44.9 ($\text{N}(\text{CH}_3)_2$). Mass spec (CI): (m/z) 383 ([M]), 311 ([M] – $\text{CH}_2\text{CH}_2\text{NMe}_2$), 72 ($\text{CH}_2\text{CH}_2\text{NMe}_2$).

2.4.3.14. Synthesis of [Me(Cl)Ga(OCH₂CH₂OMe)]₂ (14)

2-Methoxyethanol, (0.4 cm³, 3.1 mmol) was added a solution of **11** (1.012 g, 1.7 mmol) in toluene (20 cm³) prepared *in situ*. The reaction was heated under reflux for 24 h giving a cloudy solution. After cooling the solution was filtered and the solvent and volatiles removed *in vacuo* to give a yellow viscous oil. The oil was sublimed in a long Schlenk flask over an oil bath at 50°C under a dynamic vacuum and afforded a free flowing crystalline solid (0.52 g, 73% yield). Anal. Calc. (%) for C₈H₂₀O₄Ga₂Cl₂: C, 24.74; H, 5.15; N, 0.00 Found (%): C, 25.12; H, 5.21; N, 0.00. ¹H NMR δ/ppm (C₆D₆): 3.72 (m, OCH₂CH₂, 2H), 3.30 (m, CH₂OMe, 2H), 3.16 (s, O(CH₃), 3H), 0.05 (s, GaCH₃, 3H). ¹³C{¹H} NMR δ/ppm (C₆D₆): 73.1 (CH₂OMe), 62.1 (OCH₂), 57.9 (O(CH₃)), 5.7 (GaCH₃). Mass spec. (CI): (m/z) 388 [M], 353 [M] – Cl, 276 [M] – Cl – (OCH₂CH₂OMe), 193 [MeGa(OCH₂CH₂OMe)], 159 [MeGa(OCH₂CH₂OMe)], 90 [Me(OCH₂CH₂OMe)].

2.4.3.15. Synthesis of [ClGa{N(SiMe₃)₂}(OCH₂CH₂NMe₂)]₂ (15)

A suspension of lithium hexamethyldisilylamide (0.8902 g, 5.3 mmol) in toluene (15 cm³) was added to a solution of **13** (0.5012 g, 1.3 mmol) in toluene (20 cm³) which was prepared *in situ*. The reaction was then heated under reflux for 24 h giving a cloudy solution. After cooling the solution was filtered and the solvent removed *in vacuo* to give a yellow viscous oil, which was purified *via* sublimation to yield a crystalline solid (0.2071 g, 23% yield). Anal. Calc. (%) for C₂₀H₅₆N₄O₂Si₄Ga₂Cl₂: C, 34.09; H, 7.95; N, 7.95 Found (%): C, 34.12; H, 7.89; N, 8.13. ¹H NMR (C₆D₆): δ/ppm: 3.90 (m, OCH, 2H), 2.31 (m, CH₂CH₂N, 2H), 2.24 (m, NCH₃, 6H), 0.08 (m, SiCH₃, 18H). ¹³C{¹H} NMR δ/ppm (C₆D₆): 62.9 (CH₂NMe₂), 46.1 (OCH₂), 44.9 (N(CH₃)₂), 5.4 (N(Si(CH₃)₃)). Mass spec. (CI): (m/z) 704 [M], 474 [M] – 2 (N(SiMe₃)₂), 352 ½[M], 314 [M] – Cl₂(N(SiMe₃)₂)₂, 90 [OCH₂CH₂NMe₂].

2.4.3.16. Synthesis of [MeGa{N(SiMe₃)₂}(OCH₂CH₂OMe)]₂ (16)

A suspension of lithium hexamethyldisilylamide (0.8902 g, 5.3 mmol) in toluene (15 cm³) was added to a solution of **14** (0.4992 g, 1.3 mmol) in toluene (20 cm³) which was prepared *in situ*. The reaction was then heated under reflux for 24 h giving a cloudy solution. After cooling the solution was filtered and the solvent removed *in vacuo* to give a yellow viscous oil. (0.4071 g, 37% yield). Anal. Calc. (%) for C₂₀H₃₂N₂O₂Si₄Ga₂: C, 37.61; H, 5.02; N, 4.38 Found (%): C, 37.33; H, 5.29; N, 4.13. ¹H NMR δ/ppm

(C₆D₆): 3.79 (m, OCH₂CH₂, 4H), 3.35 (m, CH₂OMe, 4H), 3.15 (s, O(CH₃), 6H), 0.23 (br, SiCH₃, 36H), 0.07 (s, GaCH₃, 6H). ¹³C{¹H} NMR δ/ppm (C₆D₆): 74.1 (CH₂OMe), 62.0 (OCH₂), 58.5 (O(CH₃)), 5.7 (GaCH₃), 5.1 (N(Si(CH₃)₃). Mass spec. (CI): (*m/z*) 638 [M], 478 [M] – (N(SiMe₃)₂), 404 [M] – N(SiMe₃)₂ – CH₂CH₂OMe₂, 319 ½[M], 318 [M] – (N(SiMe₃)₂)₂, 74 [-CH₂CH₂OMe₂].

2.4.3.17. Synthesis of [Cl(Me)Ga(O^tBu)]₂ (17)

Tertiary butanol (0.55 cm³, 5.8 mmol) was added to a solution of **16** (0.1851 g, 2.9 mmol) in toluene (20 cm³) which was prepared *in situ*. The reaction was heated under reflux for 24 h, giving an orange solution. After cooling solvent and volatiles were removed *in vacuo* yielding an orange viscous oil (0.4225 g, 37 %). Anal. Calc. for C₁₀H₂₄O₂Ga₂Cl₂: C, 31.25; H, 6.25; N, 0.00 (%). Found: C, 29.89; H, 6.01; N 0.00 (%). ¹H NMR δ/ppm (C₆D₆): 1.2 (m, C(CH₃)₃, 18H), 0.22 (s, GaCH₃, 6H). ¹³C{¹H} NMR δ/ppm (C₆D₆): 80.2 (C(CH₃)₃), 48.3 (C(CH₃)₃), 5.12 (GaCH₃). Mass spec. (CI): (*m/z*) 384 [M], 327 [M] – C(CH₃)₃, 312 [M] – (CH₃)₃ – Me, 277 [M] – Cl – C(CH₃)₃ – Me, 257 [Me₂Ga₂(O^tBu)₂], 142 [Me₂GaO(C(CH₃)₃)], 69 [Ga], 57 [C(CH₃)₃].

2.4.3.18. Synthesis of [MeGa(OCH₂CH₂NMe₂)₂] (18)

2-Dimethylaminoethanol, (0.6 cm³, 5.5 mmol) was added to a solution of **11** (0.9702 g, 2.5 mmol) in toluene (20 cm³) which was prepared *in situ*. The reaction was heated under reflux for 24 h giving a cloudy solution. After cooling the solution was filtered and the solvent and other volatiles were removed *in vacuo* to give a yellow viscous oil. The oil was sublimed in a long Schlenk flask over an oil bath at 100°C under a dynamic vacuum and afforded small clear crystals of X-ray crystallographic quality (0.8201 g, 58% yield). Anal. Calc. for C₉H₂₃N₂O₂Ga: C, 41.5; H, 8.84; N, 10.8 (%). Found: C, 39.89; H, 8.51; N 9.98 (%). ¹H NMR δ/ppm (C₆D₆): 3.60 (m, OCH₂CH₂, 4H), 2.35 (br, CH₂NMe₂, 4H), 2.31 (m, N(CH₃)₂, 12H), 0.05 (s, GaCH₃, 3H). ¹³C{¹H} NMR δ/ppm (C₆D₆): 61.2 (CH₂NMe₂), 59.0 (OCH₂), 45.4 (N(CH₃)₂), 5.8 (GaCH₃). Mass spec. (CI): (*m/z*) 261 [M], 162 MeGa(OCH₂CH₂NMe₂), 88 (OCH₂CH₂NMe₂), 72 (CH₂CH₂NMe₂).

2.4.3.19. Synthesis of [MeGa(Cl){N(SiMe₃)₂}(μ₂-OCH₂CH₂NMe₂)Ga(Me)Cl] (19)

2-Dimethylaminoethanol, (0.15 cm³, 1.1 mmol) was added to a solution of **11** (1.2754 g, 2.2 mmol) in toluene (20 cm³), which was prepared *in situ*. The reaction was then

heated under reflux for 24 h giving a cloudy solution. After cooling the solution was filtered and the solvent and other volatiles were removed *in vacuo* to give a yellow viscous oil. The oil was sublimed in a long Schlenk flask over an oil bath at 80 °C under a dynamic vacuum and afforded small clear crystals of X-ray crystallography quality (0.3016 g, 21% yield). Anal. Calc. for $C_{12}H_{34}N_2O_1Si_2Ga_2Cl_2$: C, 29.63; H, 7.00; N, 5.8 (%). Found: C, 30.02; H, 7.51; N 5.5 (%). 1H NMR δ /ppm (C_6D_6): 3.47 (m, OCH_2CH_2 , 2H), 2.22 (br, CH_2NMe_2 , 2H), 2.12 (m, $N(CH_3)_2$, 6H), 0.34 (m, $N(Si(CH_3)_3)$, 18H), 0.06 (s, $GaCH_3$, 3H), 0.03 (s, $GaCH_3$, 3H). $^{13}C\{^1H\}$ NMR δ /ppm (C_6D_6): 60.5 (CH_2NMe_2), 58.7 (OCH_2), 45.1 ($N(CH_3)_2$), 22.7 ($GaCH_3$), 6.0 ($GaCH_3$), 4.9 ($N(Si(CH_3)_3)$).

2.4.3.20. Synthesis of $[Me(Cl)InN(SiMe_3)_2]_2$ (**20**)

A suspension of lithium hexamethyldisilylamide (0.8902 g, 5.3 mmol) in toluene (15 cm^3) was added dropwise to a suspension of indium trichloride (0.5123 g, 2.3 mmol) in toluene (15 cm^3) and stirred for 30 minutes. The reaction was then heated under reflux for 24 h giving a cloudy solution. After cooling the solution was filtered and the solvent removed *in vacuo* to give a yellow viscous oil, the product was purified by sublimation (10^{-2} Torr/100 °C, 0.5209 g, 67% yield). Anal. Calc. for $C_{14}H_{42}N_2In_2Si_2Cl_2$: C, 25.8; H, 6.49; N, 4.30. Found: C, 25.9; H, 7.0; N, 4.6 %. 1H NMR δ /ppm (C_6D_6): 0.31 (s, $InCH_3$, 6H), 0.28 (s, $N(Si(CH_3)_3)_2$, 36H). $^{13}C\{^1H\}$ NMR δ /ppm (C_6D_6): 5.5 ($NSi(CH_3)_3)_2$), 6.1 ($InCH_3$). Mass spec. (CI): (m/z) 579 [M] – $N(SiMe_3)$ – Me, 324 [$ClMeInN(SiMe_3)_2$], 290 [$MeInN(SiMe_3)_2$], 251 [$ClMeInN(SiMe_3)$], 216 [$MeInN(SiMe_3)$].

2.4.3.21. Synthesis of $[Me(Cl)In(OCH_2CH_2NMe_2)]_2$ (**21**)

2-Dimethylaminoethanol, (0.3 cm^3 , 2.8 mmol) was added to a solution of **20** (0.9086 g, 1.4 mmol) in toluene (20 cm^3), which was prepared *in situ*. The reaction was then heated under reflux for 24 h giving a cloudy solution. After cooling the solution was filtered and the solvent removed *in vacuo* to give a yellow viscous oil, the product was purified by sublimation (10^{-2} Torr/100°C) and afforded small clear crystals (0.5994 g, 42% yield). Anal. Calc. for $C_{10}H_{26}N_2In_2Cl_2O_2$: C, 23.8; H, 5.1; N, 5.5. Found: C, 24.8; H, 6.1; N, 4.98 %. 1H NMR δ /ppm (C_6D_6): 3.87 (m, OCH_2CH_2 , 2H), 2.49 (m, CH_2NMe_2 , 2H), 2.28 (s, $N(CH_3)_2$, 6H), 0.31 (s, $InCH_3$, 3H). $^{13}C\{^1H\}$ NMR δ /ppm (C_6D_6): 61.2 (CH_2NMe_2), 56.7 (OCH_2), 46.2 ($N(CH_3)_2$), 5.6 ($InCH_3$). Mass spec. (CI): (m/z) 504 [M], 435 [M] – Cl_2 , 363 [M] – Cl – Me – $OCH_2CH_2NMe_2$, 290 [$In(OCH_2CH_2NMe_2)_2$], 207 [$In(OCH_2CH_2NMe_2)$], 146 [$InMe$], 90 [$OCH_2CH_2NMe_2$].

2.4.3.22. Synthesis of [Me(Cl)In(OCH(CH₃)CH₂OMe)]₂ (22)

2-Methoxyethanol, (0.3 cm³, 3.1 mmol) was added to a solution of **20** (1.0043 g, 1.5 mmol) in toluene (20 cm³), which was prepared *in situ*. The reaction was then heated under reflux for 24 h giving a cloudy solution. After cooling the solution was filtered and the solvent removed *in vacuo* to give a yellow viscous oil, the product was purified by sublimation (10⁻² Torr/100°C) and afforded clear crystals (0.5021 g, 32% yield). Anal. Calc. for C₁₀H₂₄In₂Cl₂O₄: C, 23.66; H, 4.7; N, 0.0. Found: C, 24.12; H, 5.1; N, 0.00 %. ¹H NMR δ/ppm (C₆D₆): 4.60 (m, OCH(CH₃), 1H), 3.64 (m, OCH(CH₃)CH₂, 2H), 3.58 (m, OCH(CH₃)CH₂, 3H), 3.45 (m, OCH₃, 3H) 0.36 (InCH₃, 3H). ¹³C{¹H} NMR δ/ppm (C₆D₆): 66.7 (OCHCH₃), 58.7 (OCH₃), 57.2 (OCHCH₃), 6.6 (OCHCH₃), 5.6 (InCH₃). Mass spec. (CI): (m/z) 507 [M], 436 [M] – Cl₂, 434 [M] – OCH(CH₃)CH₂OMe, 349 [M] – Cl₂ – Me – CH(CH₃)CH₂OMe, 146 [InMe].

2.4.3.23. Synthesis of [Me(Cl)In(OCH(CH₂NMe₂)₂)]₂ (23)

1,3-Bis(dimethylamino)-2-propanol (0.25 cm³, 2.9 mmol) was added to a solution of **20** (0.9735 g, 1.5 mmol) in toluene (20 cm³), which was prepared *in situ*. The reaction was then heated under reflux for 24 h giving a cloudy solution. After cooling the solution was filtered and the solvent removed *in vacuo* to give a yellow viscous oil (0.4221 g, 29% yield). The oil was sublimed in a long Schlenk over an oil bath at 50°C under a dynamic vacuum and afforded small clear crystals. Anal. Calc. for C₁₆H₄₀N₄O₂In₂Cl₂: C, 30.96; H, 6.45; N, 9.00. Found: C, 30.54; H, 6.26; N, 8.92. ¹H NMR (C₆D₆): δ/ppm: 2.61 (m, OCH, 1H), 2.32 (m, CHCH₂N, 4H), 2.24 (m, NCH₃, 12H), 0.06 (m, InCH₃, 3H). ¹³C{¹H} NMR δ/ppm (C₆D₆): 67.3 (OCH), 64.3 (OCH(CH₂N)), 46.1 (NCH₃), 5.3 (InMe). Mass spec. (CI): (m/z) 620 [M], 527 [M] – Cl – CH₂NMe₂, 440 [M] – Cl – Me – CH(CH₂NMe₂)₂, 164 InMeCl, 128 CH(CH₂NMe₂)₂, 71 CH(CH₂NMe₂).

2.4.3.24. Synthesis of [Me(Cl)In(OCH₂CH₂OMe)]₂ (24)

2-Methoxyethanol (0.4 cm³, 3.1 mmol) was added to a solution of **20** (0.9765 g, 1.5 mmol) in toluene (20 cm³). The reaction was heated under reflux for 24 h giving a cloudy solution. After cooling the solution was filtered and the solvent removed *in vacuo* to give a orange/yellow viscous oil (0.6810 g, 44% yield). Anal. Calc. (%) for C₈H₂₀O₄In₂Cl₂: C, 20.04; H, 4.18; N, 0.00 Found (%): C, 20.12; H, 5.01; N, 0.00. ¹H NMR δ/ppm (C₆D₆): 3.82 (m, OCH₂CH₂, 4H), 3.41 (m, CH₂OMe, 4H), 3.21 (s, O(CH₃), 6H), 0.15 (s, InCH₃, 6H). ¹³C{¹H} NMR δ/ppm (C₆D₆): 69.1 (CH₂OMe), 58.1 (OCH₂),

56.7 (O(CH₃)), 11.7 (InCH₃). Mass spec. (CI): (*m/z*) 479 [M], 464 [M] – Me, 394 [M] – Cl₂ – Me, 420 [M] – CH₂CH₂OMe, 385 [M] – Cl – CH₂CH₂OMe, 204 MeInOCH₂CH₂OMe, 189 InOCH₂CH₂OMe, 75 OCH₂CH₂OMe.

2.4.3.25. Synthesis of [MeIn{N(SiMe₃)₂}(OCH₂CH₂NMe₂)₂] (25)

A suspension of lithium hexamethyldisilylamide (0.8902 g, 5.3 mmol) in toluene (15 cm³) was added to a solution of **21** (1.1904 g, 2.5 mmol) in toluene (20 cm³), which was prepared *in situ*. The reaction was heated under reflux for 24 h giving a cloudy solution. After cooling the solution was filtered and the solvent removed *in vacuo* to give a yellow viscous oil. The oil was sublimed in a long Schlenk flask over an oil bath at 50°C under a dynamic vacuum and afforded small clear crystals (0.3207 g, 32% yield). Anal. Calc. for C₂₂H₆₂N₄In₂Si₄O₂: C, 36.0; H, 8.2; N, 7.4. Found: C, 35.42; H, 7.9; N, 6.92 %. ¹H NMR δ/ppm (C₆D₆): 3.87 (m, OCH₂CH₂, 2H), 2.48 (m, CH₂NMe₂, 2H), 2.23 (s, N(CH₃)₂, 6H), 0.30 (s, InCH₃, 3H), 0.28 (m, N(Si(CH₃)₃), 18H). ¹³C{¹H} NMR δ/ppm (C₆D₆): 60.2 (CH₂NMe₂), 57.7 (OCH₂), 46.5 (N(CH₃)₂), 6.2 (N(Si(CH₃)₃), 5.7 (InCH₃). Mass spec. (CI): (*m/z*) 471 [M] –N(SiMe₃)₂ – OCH₂CH₂NMe₂ – Me, 436 [M] – 2 (N(SiMe₃)₂), 398 [MeIn₂N(SiMe₃)₂], 348 [Me₂In₂(OCH₂CH₂NMe₂)], 291 [MeInN(SiMe₃)₂], 218 [MeInOCH₂CH₂NMe₂], 145 [Me₂In], 115 [In], 90 [OCH₂CH₂NMe₂].

2.4.3.26. Synthesis of [MeIn{N(SiMe₃)₂}(OCH(CH₂NMe₂)₂)₂] (26)

A suspension of lithium hexamethyldisilylamide (0.8902 g, 5.3 mmol) in toluene (15 cm³) was added to a solution of **23** (1.4846 g, 2.5 mmol) in toluene (20 cm³), which was prepared *in situ*. The reaction was then heated under reflux for 24 h giving a cloudy solution. After cooling the solution was filtered and the solvent removed *in vacuo* to give a yellow viscous oil. The oil was sublimed in a long Schlenk flask over an oil bath at 50°C under a dynamic vacuum and afforded small clear crystals. Anal. Calc. for C₂₈H₇₆N₆In₂Si₄O₂: C, 38.62; H, 8.7; N, 10.0. Found: C, 36.92; H, 7.9; N, 9.92 %. ¹H NMR (C₆D₆): δ/ppm: 3.90 (m, OCH, 1H), 2.31 (m, CHCH₂N, 2H), 2.24 (m, NCH₃, 3H), 1.25 (m, InCH₃, 3H), 0.08 (m, SiCH₃, 18H). (0.3207 g, 32% yield). Mass spec. (CI): (*m/z*) 812 [M] – CH₂NMe₂, 754 [M] – (CH₂NMe₂)₂, 710 [M] – N(SiMe₃)₂, 581 [M] – N(SiMe₃)₂ – CH(CH₂NMe₂)₂, 434 [M] – 2 N(SiMe₃)₂ – 2 CH₂NMe₂, 160 N(SiMe₃)₂, 129 CH(CH₂NMe₂)₂.

2.4.3.27. Synthesis of [MeIn{OCH₂CH₂NMe₂}(O^tBu)]₂ (27)

Tertiary butanol (0.25 cm³, 2.6 mmol) was added to a solution of **25** (0.9054 g, 1.3 mmol) in toluene (20 cm³), which was prepared *in situ*. The reaction was heated under reflux for 24 h, giving a yellow solution. After cooling solvent and volatiles were removed *in vacuo* yielding a light yellow viscous oil (0.2916 g, 38.5 %). Anal. Calc. for C₁₈H₄₄N₂O₄In₂: C, 37.11; H, 7.56; N, 4.8. Found: C, 36.58; H, 6.86; N 4.42 %. ¹H NMR (C₆D₆): δ/ppm: 2.61 (m, OCH₂, 1H), 2.32 (m, CH₂CH₂N, 4H), 2.24 (m, NCH₃, 12H), 1.2 (m, C(CH₃)₃, 9H), 0.06 (m, InCH₃, 3H). ¹³C{¹H} NMR δ/ppm (C₆D₆): 78.7 (C(CH₃)₃), 67.3 (OCH₂), 64.3 (OCH₂CH₂N), 46.5 (C(CH₃)₃), 46.1 (NCH₃), 5.3 (InMe). Mass spec. (CI): (*m/z*) 471 [M] – (OCH₂CH₂NMe₂) – Me, 429 [M] – 2(O^tBu), 401 [MeIn₂(OCH₂CH₂NMe₂)(O^tBu)], 371 [In₂(O^tBu)₂], 355 [Me₂In₂(OCH₂CH₂NMe₂)], 290 ½ [M], 281 [In(OCH₂CH₂NMe₂)(O^tBu)], 207 [In(OCH₂CH₂NMe₂)], 145 [Me₂In], 115 [In], 90 [OCH₂CH₂NMe₂].

2.4.3.28. Synthesis of [Ga(OⁱPr)₃] (28).

Barium metal (7.8201 g, 0.5708 mol) was stirred with isopropanol (100 cm³) under reflux for 24 hours, H₂ gas evolved. Gallium trichloride (5.0916 g, 0.0293 mol) was dissolved in hexane (30 cm₃) and added dropwise to the barium isopropoxide solution (75 cm³) under reflux for ca. 30 minutes. After addition the hexane was removed via distillation of the hexane/isopropoxide azeotrope at 80 °C. Isopropanol (50 cm³) was added and the mixture refluxed for 24 h. The barium chloride was left to settle and the decanted section was pumped to dryness to yield **28** (5.0018g, 70.8% yield). Anal. Calc. for Ga(OⁱPr)₃: C, 44.0; H, 8.5; N, 0.0%. Found: C, 39.80; H, 7.21%. ¹H NMR δ/ppm (C₆D₆): 4.35 (m, CH, 1H), 3.93 (m, CH, 1H), 1.39 (d, CHCH₃, 6H), 1.51 (d, CHCH₃, 3H). ¹H NMR δ/ppm (CDCl₃): 4.00 (m, CH, 1H), 1.17 (br, CHCH₃, 6H). ¹³C NMR δ/ppm (CDCl₃): 65.1 (CH), 64.1 (CH), 27.4 (CHCH₃), 25.3 (CHCH₃). FTIR cm⁻¹ (nujol): 3150, 2961, 2629, 1464, 1376, 1250, 1128, 1030, 969, 878, 828, 780, 720, 615. Mass spec (CI): (*m/z*): 383 (Ga₃(OCH(CH₃)₂)₃), 315 (Ga₂(OCH(CH₃)₂)₃), 246 (Ga(OCH(CH₃)₂)₃), 187 (Ga(OCH(CH₃)₂)₂), 118 (OCH(CH₃)₂)₂.

2.4.3.29. Synthesis of [(InOⁱPr)₅(μ₂-OⁱPr)₄(μ₃-OⁱPr)₄(μ₅-O)] (29a).

Barium metal (5.1026 g, 0.0372 mol) was stirred with isopropanol (60 cm³) under reflux and evolved H₂ gas. Indium trichloride (5.2019 g, 0.0237 mol) was dissolved in DME (30 cm³) and isopropanol (50 cm³) and added dropwise to the decanted solution

of barium isopropoxide (40 cm³) under reflux with stirring for *ca.* 1.5 h. After addition the formation of a white ppt. was observed. Further barium isopropoxide (10 cm³) was added and refluxed for another 2 h. The barium chloride salt was left to settle overnight and the decanted section was pumped to dryness to yield **29a** (4.298 g, 67 % yield, based on InCl₃). ¹H NMR δ /ppm (CDCl₃): 4.36 (m, CH, 13H), 1.44 (d, CHCH₃, 48H), 1.21 (d, CHCH₃, 30H). ¹³C NMR δ /ppm (CDCl₃): 68.2 (In-CH), 68.9 (OCH), 28.6 (In-CH(CH₃)₂), 27.1 (OCH(CH₃)₂). FTIR cm⁻¹ (nujol): 2921, 1462, 1376, 1158, 952, 721. Mass spec. (CI): (*m/z*): 485 (In(OCH(CH₃)₂)₃), 405 (InO^{*i*}Pr)₂(O^{*i*}Pr), 346 ((InO^{*i*}Pr)₂), 248 (InO^{*i*}Pr(O^{*i*}Pr)(O), 173 (InO^{*i*}Pr), 60 (HO^{*i*}Pr).

2.5. References

1. K. G. Caulton, L. G. Hubert-Pfalzgraf, *Chem. Rev.*, 2002, **90**, 969.
2. R. C. Mehrotra, A. Singh, S. Sogani, *Chem. Rev.*, 2002, **94**, 1643.
3. A. C. Jones, T. J. Leedham, P. J. Wright, M. J. Crosbie, D. J. Williams, H. O. Davies, K. A. Fleeting, P. O'Brien, M. E. Pemble, *Mater. Sci. Semi. Proc.*, 1999, **2**, 165.
4. A. C. Jones, S. A. Rushworth, J. Auld, *J. Cryst. Growth*, 1995, **146**, 503.
5. M. Veith, S. Mathur, C. Mathur, *Polyhedron*, 1998, **17**, 1005.
6. D. J. Otway, W. S. Rees, *Coord. Chem. Rev.*, 2000, **210**, 279.
7. A. P. Purdy, A. D. Berry, R. T. Holm, M. Fatemi, D. K. Gaskill, *Inorg. Chem.*, 2002, **28**, 2799.
8. S. Basharat, C. J. Carmalt, R. Binions, R. Palgrave, I. P. Parkin, *Dalton Trans.*, 2008, 591.
9. S. Basharat, C. J. Carmalt, R. Palgrave, S. A. Barnett, D. A. Tocher, H. O. Davies, *J. Organomet. Chem.*, 2008, **693**, 1787.
10. A. H. Wolfgang, W. H. Norbert, R. Oliver, *Angew. Chem. Int. Edit.*, 1995, **34**, 2187.
11. T.-Y. Chou, Y. Chi, S.-F. Huang, C.-S. Liu, A. J. Carty, L. Scoles, K. A. Udachin, *Inorg. Chem.*, 2003, **42**, 6041.
12. S. Basharat, C. E. Knapp, C. J. Carmalt, S. A. Barnett, D. A. Tocher, *N. J. Chem.*, 2008, **32**, 1513.
13. S. Basharat, C. J. Carmalt, S. J. King, E. S. Peters, D. A. Tocher, *Dalton Trans.*, 2004, 3475.
14. S. Basharat, C. J. Carmalt, S. A. Barnett, D. A. Tocher, H. O. Davies, *Inorg. Chem.*, 2007, **46**, 9473.
15. H. Schumann, S. Wernik, B. C. Wasserman, F. Girgsdies, *J. Organomet. Chem.*, 2001, **621**, 317.
16. K. H. Thiele, E. Hecht, T. Gelbrich, U. Dumichen, *J. Organomet. Chem.*, 1997, **540**, 89.
17. S. Herbert, D. Sebastian, G. Frank, H. Bernd, H. Markus, H. Ji-Young, K. Jens, S. Stefan, W. Sonja, C. W. Birgit, *Z. Anorg. Allg. Chem.*, 2006, **632**, 251.
18. C. J. Carmalt, S. J. King, *Coord. Chem. Rev.*, 2006, **250**, 682.

19. S. Basharat, W. Betchley, C. J. Carmalt, S. Barnett, D. A. Tocher, H. O. Davies, *Organometallics*, 2007, **26**, 403.
20. B. Neumuller, *Chem. Soc. Rev.*, 2003, **32**, 50.
21. J. McMurrin, D. Dai, K. Balasubramanian, C. Steffek, J. Kouvetakis, J. L. Hubbard, *Inorg. Chem.*, 1998, **37**, 6638.
22. P. P. Power, *Chem. Rev.*, 1999, **99**, 3463.
23. P. J. Brothers, K. Hubler, U. Hubler, B. C. Noll, M. M. Olmstead, P. P. Power, *Angew. Chem. Int. Edit.*, 1996, **35**, 2355.
24. G. E. Coates, *J. Chem. Soc.*, 1953, 2519.
25. G. Mann, H. Olapinski, R. Ott, J. Weidlein, *Z. Anorg. Allg. Chem.*, 1974, **410**, 195.
26. H. U. Schwering, E. Jungk, J. Weidlein, *J. Organomet. Chem.*, 1975, **91**, C4.
27. M. B. Power, W. M. Cleaver, A. W. Apblett, A. R. Barron, J. W. Ziller, *Polyhedron*, 1992, **11**, 477.
28. M. D. Healy, J. T. Leman, A. R. Barron, *J. Am. Chem. Soc.*, 1991, **113**, 2776.
29. Y. A. Aleksandrov, N. V. Chikinova, G. I. Makin, *Zh. Obsh. Khim.*, 1989, **59**, 2545.
30. Y. A. Aleksandrov, N. V. Chikinova, G. I. Makin, V. A. Alferov, I. G. Stepanova, *Zh. Obsh. Khim.*, 1984, **54**, 963.
31. S. Chitsaz, E. Iravani, B. Neumuller, *Z. Anorg. Allg. Chem.*, 2002, **628**, 2279.
32. S. J. Rettig, A. Storr, J. Trotter, *Can. J. Chem.*, 1975, **53**, 58.
33. S. Daniele, D. Tchekoukov, L. G. Hubert-Pfalzgraf, *J. Mater. Chem.*, 2002, **12**, 2519.
34. G. Mann, H. Olapinski, J. W. R. Ott, *Z. Anorg. Allg. Chem.*, 1974, **410**, 195.
35. N. Chikinova, V. Alferov, V. Alyasov, Y. Aleksandrov, N. Vyshinskii, V. Tsvetkov, *Zh. Obsh. Khim.*, 1989, **59**, 1795.
36. Y. Aleksandrov, N. Chikinova, G. I. Makin, V. I. Bregadze, L. M. Golubinskaya, *Metallorgan. Khim.*, 1989, **2**, 524.
37. Y. Aleksandrov, N. Chikinova, G. I. Makin, V. Alferov, I. Stepanova, *Zh. Obsh. Khim.*, 1984, **54**, 963.
38. S. Chitsaz, E. Iravani, B. Neumuller, *Z. Anorg. Allg. Chem.*, 2002, **628**, 2279.
39. B. M. Louie, S. J. Rettig, A. Storr, J. Trotter, *Can. J. Chem.*, 1985, **63**, 3019.
40. D. A. Cooper, S. T. Rettig, A. Storr, *Can. J. Chem.*, 1986, **64**, 566.
41. E. C. Onyiriuka, A. Storr, *Can. J. Chem.*, 1987, **65**, 1367.

42. A. Mar, S. J. Rettig, A. Storr, J. Trotter, *Can. J. Chem.*, 1988, **66**, 101.
43. H.-U. Schwering, E. Jungk, J. Weidlein, *J. Organomet. Chem.*, 1975, **91**, C4.
44. M. B. Power, W. M. Cleaver, A. W. Apblett, A. R. Barron, J. W. Ziller, *Polyhedron*, 1992, **11**, 477.
45. Y. Chi, T. Y. Chou, Y. J. Wang, S. F. Huang, A. J. Carty, L. Scoles, K. A. Udachin, S. M. Peng, G. H. Lee, *Organometallics*, 2004, **23**, 95.
46. E. Hecht, *Z. Anorg. Allg. Chem.*, 2000, **626**, 2223.
47. A. Willner, A. Hepp, N. W. Mitzel, *Dalton Trans.*, 20086832.
48. M. Veith, S. Faber, H. Wolfanger, V. Huch, *Chem. Berichte*, 1996, **129**, 381.
49. S. Chitsaz, B. Neumuller, *Organometallics*, 2001, **20**, 2338.
50. N. N. Chamazi, M. M. Heravi, B. Neumuller, *Z. Anorg. Allg. Chem.*, 2007, **633**, 2154.
51. M. Veith, S. Hill, V. Huch, *Eur. J. Inorg. Chem.*, 19991343.
52. J.-H. Ryou, R. Kanjolia, R. D. Dupuis, *Chemical Vapour Deposition, Precursors Processes and Application*, ed. A. C. Jones, M. L. Hitchman. 2009, Cambridge, RSC. Chapter 6.
53. N. Matsui, H. Katsuragi, *Manufacture of laminate piezoelectric devices*, 2001, (Minolta Camera Co., Ltd., Japan). Application: JP.
54. H. Kodokura, T. Ishii, *Process for purifying gallium alkoxide*, 2001, (Kabushiki Kaisha Kojundokagaku Kenkyusho, Japan). Application: US.
55. H. Funk, A. Paul, *Z. Anorg. Allg. Chem.*, 1964, **330**, 70.
56. R. Reinmann, A. Tanner, *Z. Naturforsch B*, 1965, **B 20**, 524.
57. J. G. Oliver, I. J. Worrall, *J. Chem. Soc. A*, 1970845.
58. M. Valet, D. M. Hoffman, *Chem. Mater.*, 2001, **13**, 2135.
59. S. Suh, D. M. Hoffman, *J. Am. Chem. Soc.*, 2000, **122**, 9396.
60. K. Folting, W. E. Streib, K. G. Caulton, O. Poncelet, L. G. Hubertpfalzgraf, *Polyhedron*, 1991, **10**, 1639.
61. L. Miinea, S. G. Suh, S. G. Bott, J. R. Liu, W. K. Chu, D. M. Hoffman, *J. Mater. Chem.*, 1999, **9**, 929.
62. J. Kane, H. P. Schweizer, W. Kern, *Thin Solid Films*, 1975, **29**, 155.
63. L. A. Ryabova, V. S. Salun, I. A. Serbinov, *Thin Solid Films*, 1982, **92**, 327.
64. T. Maruyama, K. Fukui, *J. Appl. Phys.*, 1991, **70**, 3848.
65. A. C. Wang, J. Y. Dai, J. Z. Cheng, M. P. Chudzik, T. J. Marks, R. P. H. Chang, C. R. Kannewurf, *Appl. Phys. Lett.*, 1998, **73**, 327.

66. S. Chatterjee, S. R. Bindal, R. C. Mehrotra, *J. Indian Chem. Soc.*, 1976, **53**, 867.
67. D. C. Bradley, H. Chudzynska, D. M. Frigo, M. B. Hursthouse, M. A. Mazid, *J. Chem. Soc.-Chem. Comm.*, 19881258.
68. R. Binions, C. J. Carmalt, I. P. Parkin, *Thin Solid Films*, 2004, **469-470**, 416.

Chapter 3

Gas Phase Electron Diffraction and Thermal Analysis of Group 13 Alkoxides

3.1. Introduction

Chemical vapour deposition (CVD) techniques are now widely employed for the deposition of thin films of materials because they offer the potential for good film uniformity and composition control, large area growth and excellent step coverage.¹ As was explored in the previous chapter, an important consideration when using the CVD method is the choice of precursor, which can affect a wide variety of issues including; the transparency, electrical properties, conformality and growth rate of the film.² However, information on the mechanisms of the CVD process, including how the precursors decompose, which species are present in the gas phase and the chemical reactions that are involved, is often limited.^{3,4}

The versatile nature of many metal alkoxides as convenient precursors to metal oxides *via* CVD processes is discussed extensively in the previous chapter and is largely recognised.⁵⁻¹⁰ These compounds can be stored indefinitely when kept in a dry

atmosphere, because they are intrinsically non-corrosive, and are easy to prepare and purify. Furthermore, metal alkoxides are ideal for use in aerosol-assisted (AA)CVD due to their solubilities in a wide range of organic solvents, and in low-pressure (LP)CVD as a result of their high volatilities.¹¹

This chapter describes, in part how to exploit the full potential of CVD, it is sometimes necessary to tailor the properties of the precursor in order to optimise process parameters such as evaporation temperature, deposition temperature, layer purity and uniformity. It has been reported previously that the replacement of simple alkoxide groups¹² by donor-functionalised alkoxides, such as dimethylamino ethoxide (dmae), can result in precursors with improved physical properties and enhanced CVD performance. For example, dmae provides an additional Lewis base site, which is able to form chelate rings and provide stabilisation to the metal centre. This thesis investigates the use of alkoxide precursors^{13,14} as described in Chapter 2 through to the deposition of gallium^{15,16} and indium¹⁷ oxide thin films *via* AACVD as described in Chapter 4. This chapter aims to elucidate what happens to the precursor before it is deposited as a thin film, *i.e.* the gas phase structure and decomposition characteristics.

Knowledge of the structures and natures of precursors in the gas phase should provide useful information regarding the decomposition processes central to CVD. However, despite the growing importance of gallium and indium oxides^{18,19} in gas sensing and transparent conducting oxide (TCO) applications, little is known about the gas-phase structures of the alkoxide precursors used to deposit the films. Moreover, given the large variety of metal oxides (including main group, lanthanide and transition metal elements) deposited from metal alkoxides incorporating donor-functionalised ligands, an understanding of gas-phase structures could lead to improvements in precursor design and film growth.²⁰

This chapter describes investigations into the suitability of a selection of the gallium and indium alkoxides, synthesised as described in Chapter 2 for CVD. Decomposition of the group 13 metal alkoxides was studied by thermogravimetric analysis (TGA) and differential scanning calorimetry (DSC). Following on from these studies, Chapter 4 will give examples of the deposition of thin films from some of the metal alkoxides, which has been achieved by AACVD.

3.1.1. Gas Phase Electron Diffraction

Traditionally, absorption and emission spectroscopy and diffraction techniques have been used when carrying out the structural determinations of compounds. With the structure of compounds commanding their chemical and physical properties these techniques have become vitally important to chemical research. In the solid state external constraints and packing forces can distort the chemical structure of a compound so it is often the case that the aforementioned methods of structural investigation are carried out in the gaseous phase. Gas phase electron diffraction (GED) and rotational spectroscopy are the two techniques that can be used to determine the molecular structures of gases. The shortfall of rotational spectroscopy is that it is only suitable for relatively small molecules, whereas GED can be considered the only experimental method for obtaining the gas-phase structures for larger molecules.

In recent years, chemists understanding of theoretical methods of structure determination has greatly improved. It is now acknowledged that quantum chemistry can usefully complement experimental data in the investigation of molecular geometry and that complete structures can be obtained by combining information from different sources. Conversely, accurate gas-phase structures are entirely necessary for the standardisation of some computational methods for isolated molecules. *Ab initio* molecular orbital theory and density functional theory are powerful computational tools that can be used to calculate any property of a molecule from first principles.

There are of course limitations to these theoretical methods of structural determination. One of the main factors that can limit *ab initio* calculations are the size of the molecules being studied and the speed and cost of suitable computer hardware. However, the widespread availability of parallel processors and access to the resources of the EPSRC-funded National Centre for Computational Chemistry Software have further extended the range of molecules that can be studied.

The gas phase molecular structures determined in this chapter were carried out in the laboratories of Edinburgh University. The Edinburgh diffraction group is one of only a handful worldwide, including one other in the UK, several in the USA and others in Norway, Russia Germany, Belgium and Japan. With GED being the principal technique

used by chemists to determine molecular structures of gases the facility is in high demand and diffractometers used from group to group have procedures which vary significantly. The following sections give an understanding to the performance of electron diffraction in Edinburgh.

3.1.1.1. Background

GED as a means of investigating structure was developed on the basis of two fundamental understandings. The double-slit experiment,²¹ performed by Thomas Young in 1801 showed that light possessed wave properties and, so could be diffracted giving rise to interference phenomena. Young established that when a wave of incident light encounters a narrow slit in a screen, the light diffracts to form a cylindrical wavefront. If this wave encounters a second screen with two parallel slits, further diffraction will occur. Two coherent wavefronts are produced and advance towards a third, solid screen where they combine showing an interference pattern of alternating light and dark areas, due to constructive and destructive interference, respectively.

The second theory necessary for the successful development of GED was developed by Louis de Broglie.²² Knowing that light behaved as a wave, de Broglie suggested that all moving particles have an associated wavelength. So a photon of light is both a wave and a particle, and so the same can be said for electrons. In 1927 Clinton Davisson and Lester Germer performed a crucial experiment, which demonstrated the diffraction of electrons by a nickel crystal.²³ Meanwhile George Thompson showed that a beam of electrons was diffracted when passing through a thin gold foil.²⁴

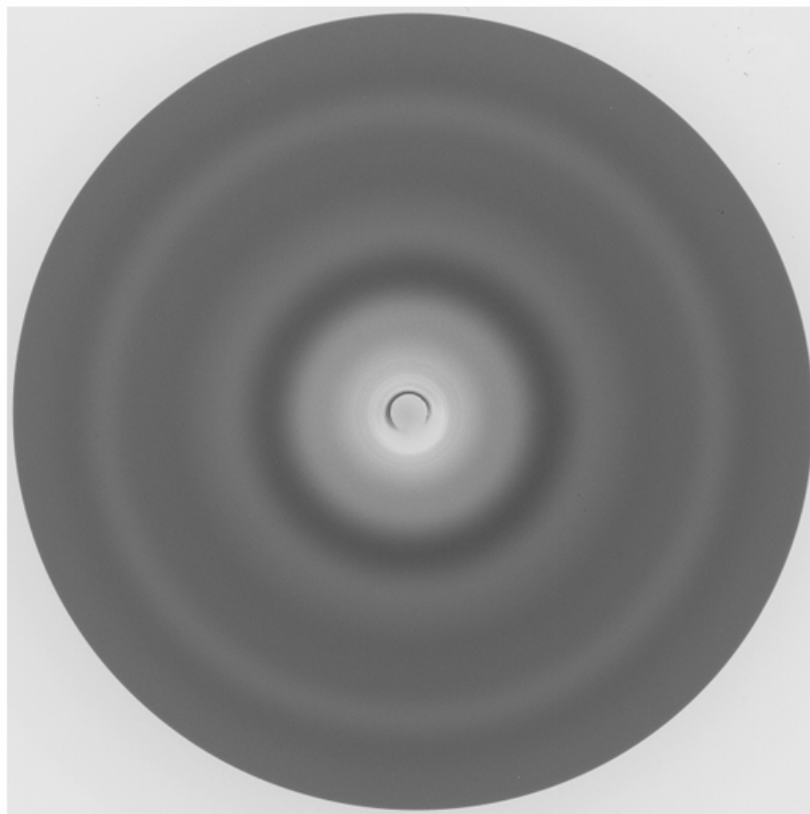


Fig. 3.1: Electron scattering data recorded on Kodak Electron Image film.

From these initial electron diffraction experiments, methods were developed for determination of molecular structure. It was shown that each pair of atoms in a molecule acted like a pair of slits and so diffract a beam of electrons directed at the molecule. The interference from these pairs caused light and dark areas to be recorded on a photographic film and since molecules in the gas phase are randomly orientated a pattern of concentric rings is observed (Fig. 3.1). Once the film has been developed, it can be assumed that the wavelength of the electrons is known, so the distance between pairs of atoms can be calculated from the pattern and consequently the molecular structure can be determined.

The initial structures to be determined *via* this technique were the rather simple structures of highly symmetrical molecules including cyclohexane, benzene, carbon tetrachloride and germanium tetrachloride.²⁵

3.1.1.2. Instrumentation

Essential requirements for an electron diffractometer include an electron gun, a method for focusing the electron beam, a nozzle to introduce the sample gas and a detector (Fig. 3.2). A beam of electrons is accelerated from a loop of hot tungsten wire across an accurately measured potential of approximately 40 kV. A series of magnetic lenses and apertures is then used to focus the narrow beam of electrons. The gaseous sample is introduced through a nozzle, perpendicular to the electron beam that intersects it. The diffracted electrons continue towards a photographic film, which acts as a detector, while the sample is condensed on a cold trap to prevent further interaction with the electron beam. The apparatus is typically evacuated to 10^{-6} Torr in order that the electrons do not encounter other species which may cause diffraction.²⁶

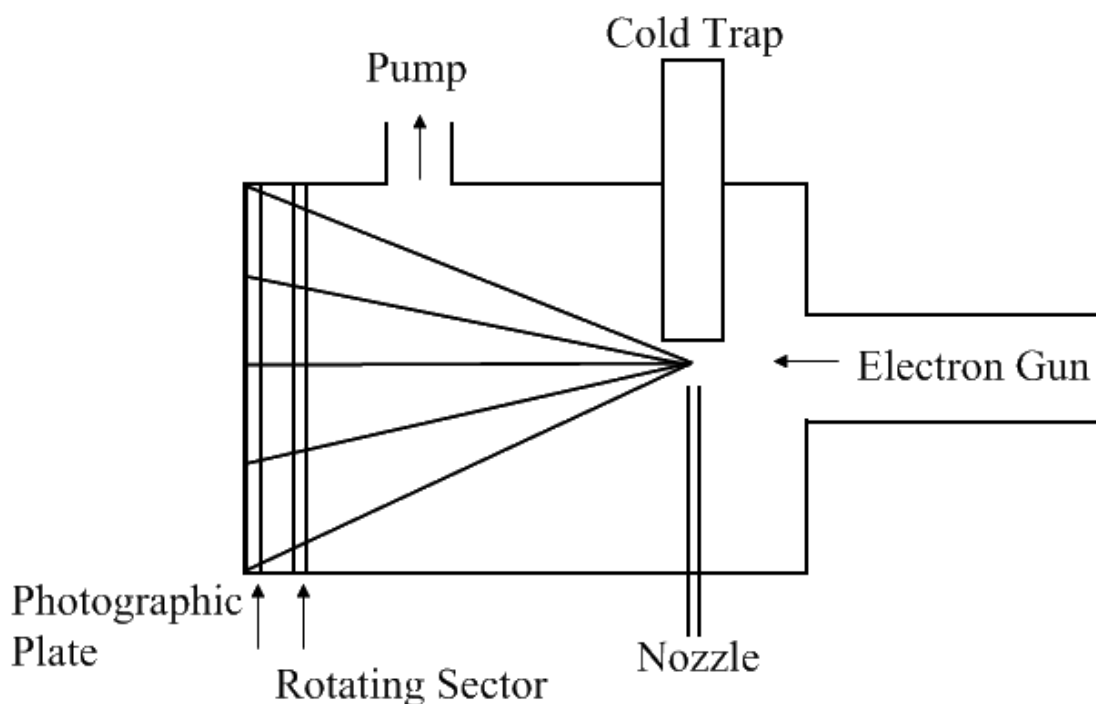


Fig. 3.2: Schematic diagram of a typical gas-phase electron diffraction apparatus²⁶

The range of intensities associated with the diffracted electrons is such that they cannot be recorded on a photographic plate, due to the intensity of scattered electrons decreasing steeply (approximately the 4th power of the scattering angle). To minimise this problem, a rotating sector²⁷ (Fig. 3.3) is positioned in front of the photographic film. Made from aluminium, the sector has an opening that increases in size (approximately proportional to r^4) on moving away from the centre of the plate. When this plate rotates rapidly, it acts to decrease the effective exposure time at scattering angles where the

intensities would normally be too strong to be recorded. Undiffracted electrons are collected by a metal cylinder, found at the centre of the sector, called a beam-stop.²⁶

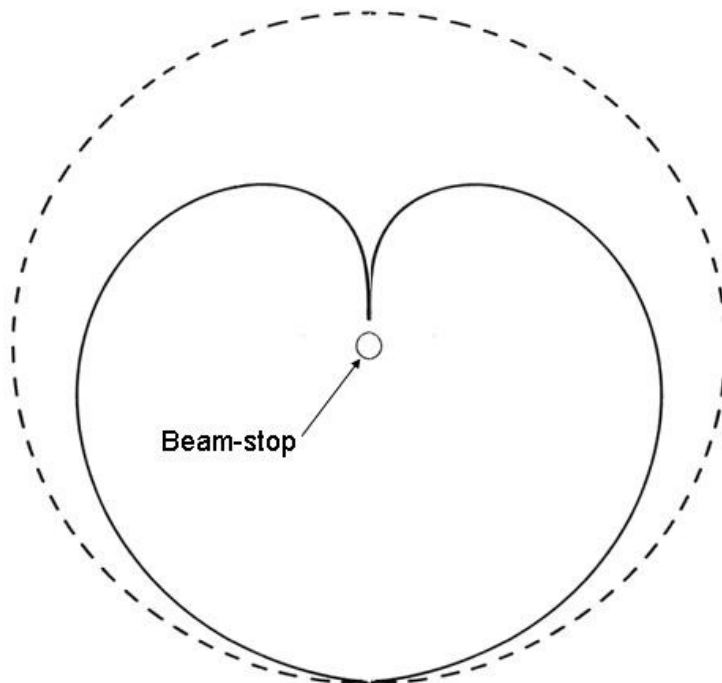


Fig. 3.3: Shape of rotating sector used in Edinburgh.²⁸

The scattering pattern of benzene, taken immediately after each sample is run is used as a reference to calculate the distances within the apparatus as well as the wavelength of the electrons. In all instances in this thesis experiment is performed twice, or three times, at different nozzle-to-film distances, to increase the range of scattering angles (Fig. 3.4) and therefore obtain more data for a more accurate structure determination.

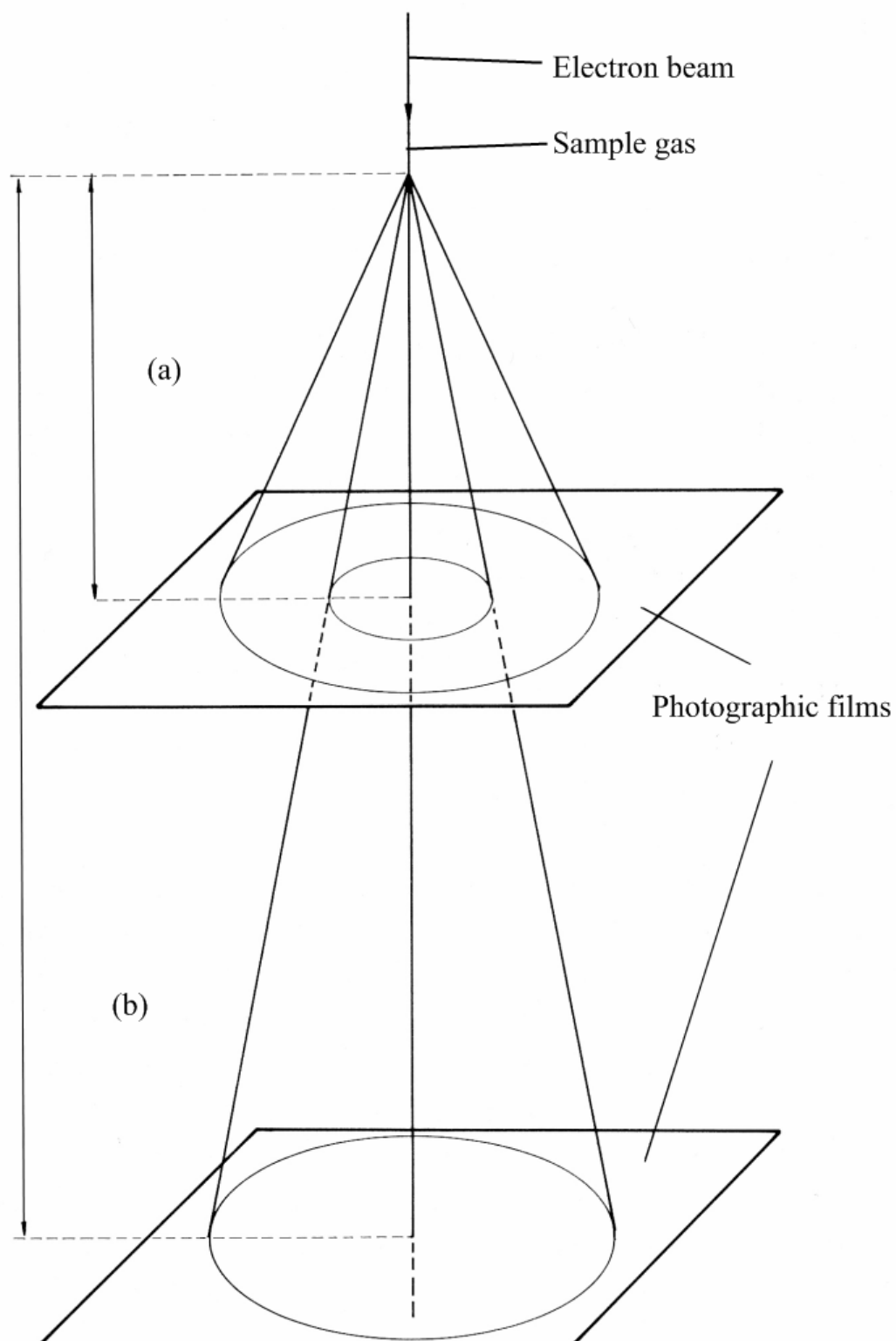


Fig. 3.4 Application of two nozzle-to-film distances, (a) short and (b) long.²⁸

3.1.1.3. Data analysis

Scattering intensities are recorded on photographic film, (as in Fig. 3.1) and are measured in Edinburgh using an Epson 1600 Pro flatbed scanner and converted to mean optical densities as a function of the scattering variable, s , using an established program.²⁹ The diffraction pattern recorded on the photographic film represents the overall scattering intensity. Three types of scattering are combined to give the total scattering (Eqn. 3.1).

$$I_{\text{total}} = I_{\text{atomic}} + I_{\text{molecular}} + I_{\text{background}} \quad (\text{Eqn. 3.1})$$

Atomic and background intensities have to be subtracted from the total to give the molecular intensity scattering curve in order to obtain the molecular structure. The atomic scattering is independent of the molecular structure and the scattering contribution from each of the atoms in the molecule can simply be subtracted. Even when the molecular-intensity scattering curve has been obtained, the values for the interatomic distances are not immediately obvious. A sine Fourier transformation must be performed to obtain a useful radial-distribution curve, which, in theory, shows a representation of each bonded and non-bonded distance in the molecule as the centre of a peak in the curve. It is from this radial-distribution curve that enough information about the bond lengths and angles can be extracted to determine the structure of a simple molecule.

3.1.1.4. Limitations of GED – and some solutions

Overlapping peaks occur in the radial distribution curve when interatomic distances are very similar. The correct distance associated with each atom pair is often impossible to obtain when this happens. If the distances cannot be correctly assigned then the structure cannot be accurately determined. This is one of the main limitations associated with the GED experiment, and is encountered in each radial-distribution curve displayed in this chapter.

Additionally light atoms scatter electrons less than heavy atoms and this can lead to poor definition of the positions of atoms such as hydrogen. When the positions of these

atoms is uncertain, it becomes impossible to obtain an accurate structure using GED alone. In which case other techniques can be used to help to solve the structure. The phase shift of an electron wave as it passes through an atomic field is another problem associated with GED. Attracted to the nucleus, the electron speeds up and its de Broglie wavelength is shortened. On leaving the field of the atom, the electron slows down to its original speed and wavelength. This becomes a problem when a molecule contains atoms with very different atomic numbers. As can be seen in Fig. 3.5, the heavier atom (B) causes a larger contraction of the electron wave than (A). This leads to beating in the molecular intensity curve, which shows up in the experimental radial distribution curve as a split peak corresponding to the bonded distance r_{A-B} . This effect is taken into account in the theoretical curves using complex (*i.e.* containing both a real and imaginary part) scattering factors to calculate the molecular scattering and therefore the radial-distribution curve.³⁰

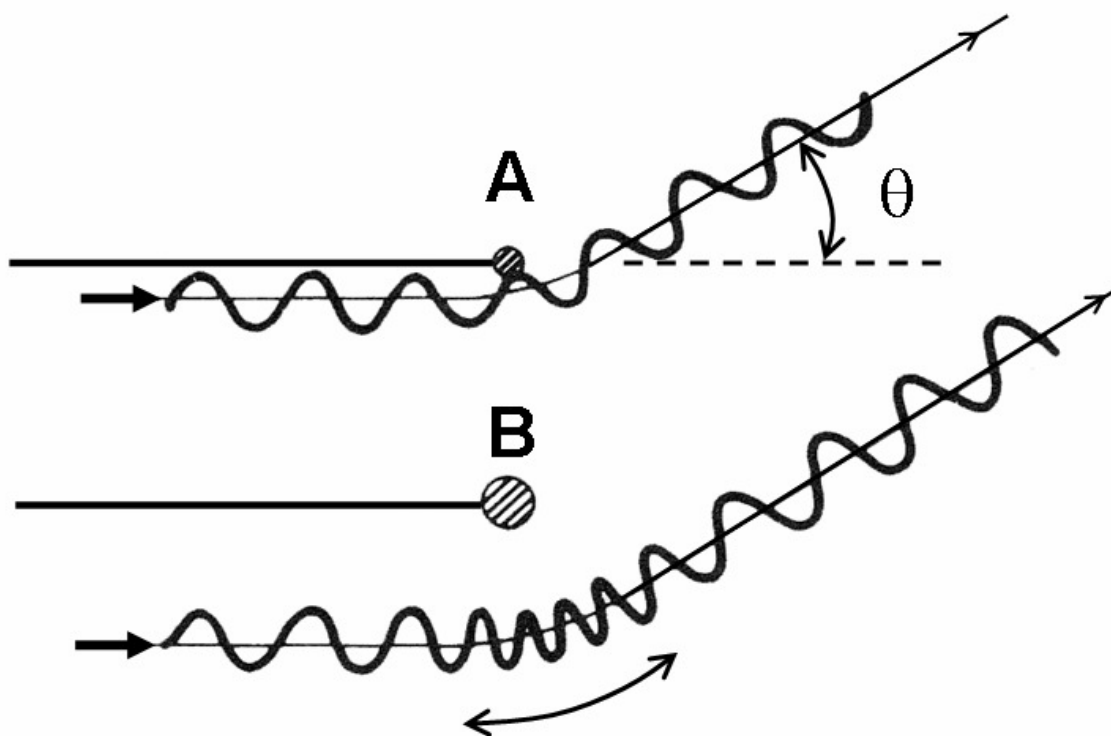


Fig. 3.5 The phase effect, caused by differences in wave contraction as the electron approaches a light atom (A) and heavy atom (B).³¹

Samples for GED may be solid, liquid or gas at ambient temperature and pressure but must have a suitable vapourisation rate (with heating if necessary) and vapour pressure

for significant diffraction to occur. In the lab at Edinburgh, recent developments have been made to the experimental procedure so that compounds that do not fit the criteria for vaporisation rate and vapour pressure can still be used.³² A small reservoir, heated by a flow of hot gas, was used in the collection of the data for the compounds in this chapter. This technique is much preferred to that used previously, where the heating was performed using heating tape, which was prone to giving hot spots.

The structure obtained by GED is vibrationally averaged which also causes problems. Each individual electron sees the molecule at a single instant in time and millions of electrons contribute to the total picture. For example, a linear, triatomic molecule vibrating (Fig. 3.6) spends its time bent (except for the instant when it is linear). So the distance between the two black atoms, on average, is less than twice the bond length between the black and white atoms. The two distances would imply that the molecule was bent, which would be wrong. A similar phenomenon is found for non-linear systems and is known as the shrinkage effect³³ and must be corrected for in the vibrational model.

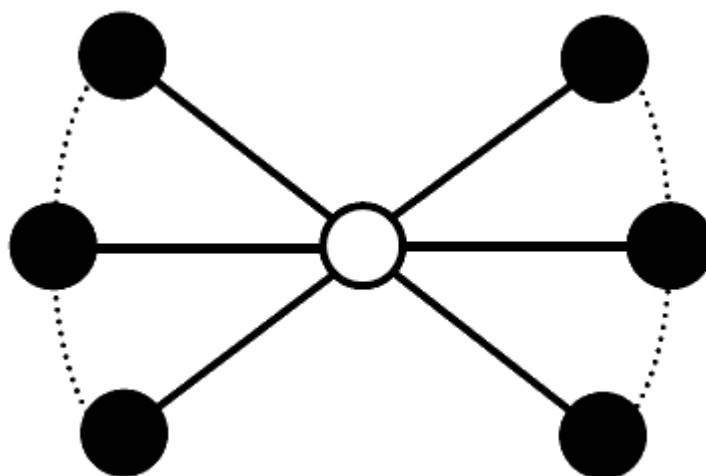


Fig. 3.6: Schematic diagram showing the vibration of a tri-atomic molecule.

This aforementioned shrinkage effect can be corrected using calculated force fields. The theoretical force constants are used to calculate either rectilinear or curvilinear corrections. Rectilinear corrections allow for perpendicular motions of the atoms (increasing the bond lengths when the atoms are not in the linear position). This is

intuitively wrong and so in this work curvilinear corrections are used throughout, modelling better the curved motion of the atoms. These corrections are calculated using the SHRINK program.^{34,35}

3.1.1.5. Experimental equilibrium structures

The vibrational correction calculated using the SHRINK programme is one of a number of corrections made to raw distances obtained from the GED experiment. These distances, r_a , are modified in order to produce an experimental equilibrium structure that is then independent of the method by which it was determined. The equilibrium structure of a molecule is the structure in a hypothetical vibrationless state at the minimum on the potential energy surface. The GED distances, a , are averaged over all vibrational motions and are the inverse of the inverse distance between a pair of atoms averaged over time, as shown in Equation 3.2. It is necessary to take the inverse because of the way that the distances are defined in the scattering equations.²⁶

$$r_a = \langle r^{-1} \rangle^{-1} \quad (\text{Eqn. 3.2})$$

The difference between the equilibrium distance and r_a has four terms. The first gives the average internuclear distance, r_g which allows for motion along the coordinate between two atoms. r_a and r_g are connected (Eqn. 3.3), where u is the root-mean-squared (RMS) amplitude of vibration (which can be calculated) and r_e is the equilibrium distance. Of course, r_e is not known and so r_a must be used as an approximation.

$$r_g = r_a + u^2 / r_e \quad (\text{Eqn. 3.3})$$

Eqn. 3.3 describes r_g at the temperature, T , of the experiment and should strictly be written r_g^T . To obtain a value for r_g at 0 K, the correction shown in Equation 3.4 is applied, (a is an anharmonicity constant used to allow for the anharmonicity of the potential well (Morse curve) and u is the RMS amplitude of vibration).

$$R_g^0 = r_g^T - \frac{3}{2} a(u_T - u_0)^2 \quad (\text{Eqn. 3.4})$$

For diatomic molecules, r_g^0 (the average internuclear distance at 0 K) is equal to another quantity, r_a^0 (the distance between average nuclear positions at 0 K). r_g^0 can be related to r_e by a further anharmonic correction (Eqn. 3.5).

$$r_e = r_g^0 - \frac{3}{2} a.u_0^2 \quad (\text{Eqn. 3.5})$$

As discussed in the previous section, when a molecule has three or more atoms it experiences a shrinkage effect, this alters non-bonded distances and $r_a^0 \neq r_g^0$. A perpendicular amplitude correction term, k , is calculated using SHRINK.^{35,36} The final term that is required to correct from r_a to r_e is an allowance for centrifugal distortion, δr . This is often negligible and has not been included in the corrections used during the refinements in this thesis. This entire correction (Eqn. 3.6) includes subscripts hn , and these denote the use of a harmonic force field calculation to obtain the corrections, with the vibrational motions treated at the n^{th} order approximation. In this work the distances reported are of the type r_{h1} , showing that the calculated harmonic force field has been used in conjunction with the SHRINK program to obtain corrections. As mentioned earlier, it was previously common to use rectilinear correction factors and these would be denoted r_{h0} .

$$r_{hn} = r_a + u_{hn}^2/r_e - \frac{3}{2} a u_{hn}^2 - k_{hn} - \delta r_{hn} \quad (\text{Eqn. 3.6})$$

3.1.1.6. *Ab initio* molecular orbital theory

In recent years the use of computational methods for structure determination has expanded exponentially. Due to rapid development, at relatively low cost, these theoretical techniques are being used more and more to complement experiment. Many techniques, including *ab initio* and semi-empirical methods, have been developed from an understanding of quantum mechanics. Geometries, thermodynamic properties, and bond energies can be derived from first principles alone using *Ab initio* molecular orbital theory. These calculations can be used alongside GED or other experimental results. They can also be used to obtain data for compounds that cannot be analysed by

known experimental methods. In theory, molecular geometries can be calculated exactly from an exact solution of the time-independent Schrödinger equation (Eqn. 3.7).

$$E\Psi = \hat{H}\Psi \quad (\text{Eqn. 3.7})$$

Where E is the total molecular energy, Ψ is the molecular wavefunction, and \hat{H} is the Hamiltonian operator.

As it is widely known, only simple one electron systems such as H and He^+ can be solved exactly. An approximate solution for the equation can be obtained for larger systems by simplifying both \hat{H} and Ψ .

3.1.1.7. Simplification of the Hamiltonian operator

There are several parts that make up the Hamiltonian operator, namely the kinetic energies of the nuclei and of the electrons in the molecule, and the potential energies associated with nuclear repulsion, electronic repulsion and nuclear–electronic attraction.

Born-Oppenheimer³⁷⁻³⁹ and adiabatic⁴⁰ approximations are employed to simplify the Hamiltonian. In order to make the nuclear and electronic wavefunctions separable the Born-Oppenheimer approximation assumes that the mass of the nuclei in a molecule is considered to be so much greater than the mass of the electrons that the nuclei can be said to be stationary in a field of moving electrons. Therefore the kinetic energy term for the nuclei can be equated to zero, and the value for the potential energy of the nuclear repulsion becomes constant. Additionally, so that only the terms of the Hamiltonian relating to the electrons are considered the adiabatic approximation, which neglects the coupling between electronic states caused by nuclear motion is utilized.

The electronic term in the Hamiltonian is replaced by the Hartree-Fock (HF) potential, where each electron is considered to move in a uniform field, generated by the other electrons present in the molecule. A series of single-electron Schrödinger equations can then be solved, generating a series of one-electron atomic orbitals. This method accounts for about 99% of the energy of the molecule. The deficit is due to the fact that electrons do not move in uniform fields. Fortunately there are ways to improve upon the HF method. Most take the HF wavefunction as their starting point and add in extra

terms to account for the effects of electron-electron repulsion. The Møller-Plesset (MP) perturbation series⁴¹ is one way of including the electron correlation effects, with the most commonly used one of these being the MP2 level of theory, which was used by Dr Derek Wann when elucidating the structures reported in this thesis in Edinburgh.

3.1.1.8. Simplification of the molecular wavefunction

The location of the nuclei and the electrons within a molecule is described by the wavefunction, Ψ . However, in order for the approximation of the Schrödinger equation to be solved this must be simplified. Using the Born-Oppenheimer approximation,^{37,39} the nuclei are imagined to be fixed in space and so only the region of space for the electronic motion (*i.e.* the atomic orbitals) need be considered. Gaussian-type orbitals (GTO) are used to approximate the atomic radial functions. Usually, as in this instance there is a distinct difference between the two functions (Fig. 3.7).

In order to represent the atomic radial functions accurately it is necessary to combine many GTOs with different weightings and coefficients. This basis set, or collection of GTOs are derived for each atom in a molecule. To allow for the maximum flexibility for electronic motion, ideally, the basis set would consist of an infinite number of functions. However, this is impossible in practice and so shortened series of GTOs are used. Basis sets are defined in terms of the number of GTOs describing each atomic orbital. A single- ζ basis set will allow one function to describe each occupied atomic orbital. A double- ζ basis set will have two functions for each orbital, and so on.

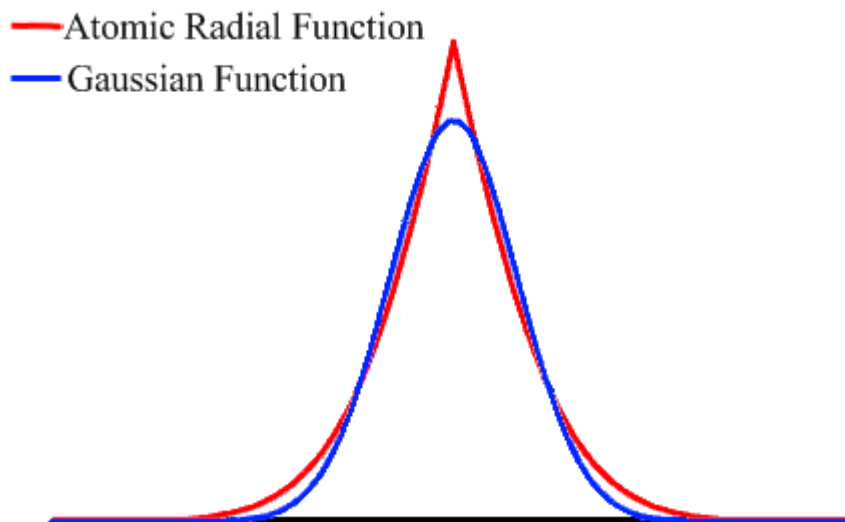


Fig. 3.7: Comparison of a Gaussian function with an atomic radial function.

With the simplification of the Hamiltonian operator, \hat{H} and the wavefunction, Ψ , the Schrödinger equation can be solved to an approximation. The approximation is dependent upon the degree of simplification of \hat{H} and Ψ .

3.1.1.9. Density functional theory

There is an alternative to the *ab initio* methods already discussed, namely density functional theory (DFT). In 1964 Hohenberg and Kohn showed that the ground-state energy of a system can be determined completely by its electron density.⁴² The energy is not calculated from the wavefunction, the $4N$ variables (atomic coordinates and spin for all N atoms) required for *ab initio* methods can be reduced to the three coordinates of the electron density. This is, therefore, independent of the number of electrons and requires much less computational effort. Where the time taken for *ab initio* calculations to complete can be prohibitive DFT methods are ideal for use with very large molecules. The only barrier to carrying out DFT calculations is that the functional relating the electron density to the energy of the electrons is unknown. The functionals available in the literature are developed by fitting parameters to known experimental data and then testing against large sets of reference atoms and molecules for reliability.²⁶

It was mentioned earlier that Hartree-Fock theory, while it calculates the electron exchange energy exactly, ignores electron correlation completely. The functionals used in pure DFT, however, work by approximating both electron exchange and electron correlation.

3.1.1.10. Structure refinement in practice

The GED process is concerned solely with gas phase structures, which are therefore free from intramolecular interactions, this is thus complementary to the *ab initio* and DFT calculations, which are also performed on isolated molecules, free from these constraints. The calculations are useful for providing extra data in a number of different ways. The theoretical relative energies of conformational isomers can give an indication of their abundance in an experimental sample.

A model in Fortran code to define the atomic coordinates of the proposed geometry is necessary to solve the structure from the minimal set of geometrical parameters. Bond lengths, bond angles, torsional angles and, where necessary, weightings of conformers are defined in the model and describes any local and overall symmetry the molecule possesses. The structure is then refined using a least-squares refinement program, allowing the parameters and amplitudes to vary until the best fit to the experimental data is obtained. Recently a new GED refinement program has been introduced in Edinburgh. The newly developed program, called ed@ed,⁴³ has improved upon its predecessors by incorporating a Windows interface.

The R_G factor, or the goodness of the fit (between the calculated and experimental data) should be under 10%, although the value depends on the scattering pattern for the molecule as well as the quality of the data and accuracy of the model. Another measure of the data fit is the difference curve between the experimental and theoretical data sets. When viewed together with the radial distribution curve it is possible to see where the data fit best, as is shown in this chapter.

3.1.2. Mechanistic studies in CVD

It would seem obvious that there is considerable advantage to be found in studying the reactions that take place during a CVD deposition, owing to the fact that this knowledge would provide an insight into the mechanisms at work during film deposition. It would follow that information attaining to the mechanisms at work laying down thin films would give a better understanding of the chemistry and so improvements upon the technique could be achieved. These could involve altering the reactors used or changing certain techniques, including precursor delivery to the reaction chamber, carrier gas flow rate, substrate type and temperature, or even to help the synthetic chemist to design better precursors in order to aid clean deposition and promote good quality film growth. However, there is little work in the literature to suggest that such studies have taken place. This section gives a brief overview of some of the mechanistic studies carried out in the past two decades on CVD of thin films.

3.1.2.1. Coherent anti-Stokes Raman scattering (CARS)

A non-invasive technique to access species concentrations at many points within a reactor was developed,⁴⁴ in a novel attempt to better understand the mechanisms at work in a CVD reaction chamber. It was instantly clear that spectroscopic methods would be well suited to this task but FTIR posed an immediate problem, with the addition of windows to the reactor, gas flows would be disturbed and movement of the sampling point would be near-on impossible. Near-infrared would render the reactor walls invisible but would have the disadvantage of giving an average concentration along the pathlength. A solution was Coherent anti-Stokes Raman scattering (CARS), which provides good sensitivity from a very small region within the reactor, while access is simplified by the coherent nature of the process which produces scattering in a tight, laser like beam. CARS was originally a technique used in combustion research, but was subsequently used to study mechanisms at work in CVD.

In initial experiments CARS was utilised to monitor the decomposition of GaMe₃ on the reactive internal surface of a protonated form of Zeolite Y under CVD conditions.⁴⁴ In this study the CARS data was able to detect increasing levels of methane with

increasing reaction time, which provided evidence for a facile room temperature decomposition of the GaMe₃ in the Zeolite.

Another study in the following year was able to provide new evidence to support a proposed mechanism for the decomposition in question.⁴⁵ In this report thin films of ZrO₂ were grown under kinetic control by decomposition of Zr(OⁱBu)₄ onto quartz substrates. In this instance the decomposition of the precursor was followed by *ex situ* infrared spectroscopy, allowing monitoring of the gas-phase products as a function of substrate temperature. The proposal of a possible mechanism for the decomposition reaction was in agreement with previous literature report.⁴⁵

In this study the reactor exhaust gases were analysed at different susceptor temperatures in order to identify the volatile reaction products with a view to elucidating the mechanism for the decomposition of the precursor. This was achieved by passing the exhaust through a cell placed between the spectrometer and the external detector. The experiments were carried out using a reactor well coated in the deposits from previous growth experiments. In the IR studies it was found to be necessary to keep the reactor at atmospheric pressure (of precursor and carrier gas) in order to produce a detectable signal from the precursor decomposition products at the IR detector.

It was deduced that a chain reaction is set up as the water formed initiates the hydrolysis of more alkoxide molecules, with the oxide alkoxide formed undergoing rapid disproportionation to the oxide and alkoxide. Strong OH stretching bands due to water were observed in the IR spectra at all substrate temperatures. However it is reported that these are caused by small fluctuations in humidity in the external gas environment which the IR beam passes through, leading to mis-cancellations between background and sample spectra. It is therefore impossible to ascertain whether water is detected as a decomposition product, and suggests that perhaps these techniques are not ideal for studying the mechanisms at work in CVD processes.

Later, the *in situ* monitoring of atmospheric pressure tin oxide CVD using CARS was reported⁴⁶ in an effort to investigate the mechanisms involved in the CVD of the thin films. A novel compact CARS experimental system was reported, in this instance operating with the use of a collinear sampling geometry constructed around a

Nd:YAG/dye laser combination. The system was able to sample gas phase species at specific points within the reactor, and was able to report concentrations of the major reaction product, methane, as a function of position within the reactor, it was also proposed that methyl radicals, which were believed to form via decomposition of the starting material could also be detected. This technique arguably is good for highly spatially selective investigation of precursor and product species distribution and could be used as a non-invasive technique for measuring temperature profiles, but the accuracy is likely to be severely limited without improvement in the instrument resolution.

Finally an *in situ* Fourier transform infrared spectroscopy gas phase study of vanadium (IV) oxide coating by APCVD was reported.³ Again the use of *in situ* FTIR successfully monitors the gas phase reactions during the formation of the thin film, as shown in other similar experiments⁴⁷, however whilst a mechanism for the decomposition of precursors is proposed it is also reported that while spectroscopic evidence for the formation of these species is presented, the mechanism proposed cannot be confirmed on the basis of these data alone.³

3.1.2.2. Density functional theory

A more recent report⁴⁸ described, computational methods to elucidate the decomposition reaction occurring when using dimethylaluminium hydride to deposit aluminium. Density functional theory (DFT) and the cluster model approach are employed to obtain the potential energies and structures of adsorbed molecules on the Al(111) surface. This study appears to be the first time experimental and computational values are compared, here the averaged bond strength is evaluated against the experimental value.

The report considers a variety of reactions occurring on the aluminium surface in Al-CVD including the adsorption of the precursor, surface reactions between the admolecules, the desorption of products and the growth of aluminium using the density-functional method. The calculations suggest a series of reactions initiated by the dissociative adsorption of the precursor into methylaluminium hydride and a methyl

group on the aluminium surface, it is proposed that this step is then quickly followed by dissociation of the methylaluminium hydride to methylaluminium.

3.1.3. Thermal Decomposition Studies

3.1.3.1. Background

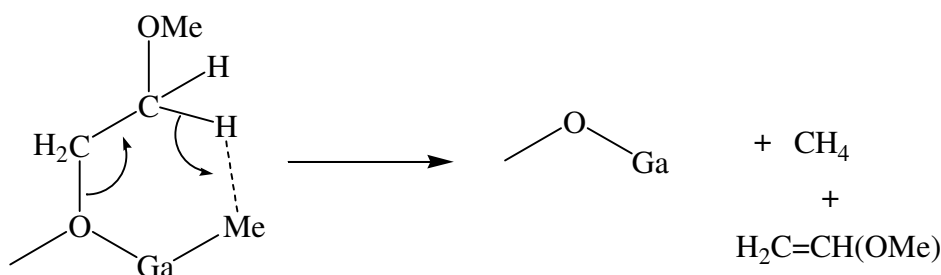
In this chapter thermogravimetric analysis (TGA) has been used to study the decomposition of some of the precursors previously discussed in Chapter 2. TGA can help to understand how a compound decomposes as it continuously records changes in the mass of a material whilst being heated. The atmosphere of the sample can be controlled, whether it be from changing the flow gas or sealing the sample in a pan. The total mass loss figure can be used to predict the decomposition pathway of the compound, and provide information about whether a precursor will be able to cleanly decompose to the required binary product. Take for example a gallium alkoxide compound, if the mass loss is consistent with the organic leaving groups surrounding the metal centre, it can be assumed this precursor will decompose to give pure Ga₂O₃. In addition to this, TGA has the ability to record decomposition steps, and where these are identified the prediction of a decomposition pathway results.

Another technique that is useful in determining whether a given complex will be a suitable CVD precursor is differential scanning calorimetry (DSC). In this method two pans, one loaded with sample and the other empty (acting as an inert reference) are simultaneously heated whilst the differences in heat flow into the two is recorded. DSC can give information concerning chemical or physical changes that are accompanied by a gain or loss of heat, as previously discussed a good CVD precursor will be capable of vaporization and must be able to travel across to the substrate without decomposing. Therefore a good precursor will exhibit a melting point at a temperature much lower than the onset of decomposition, allowing it to be thermally vaporized at a stable temperature. Also a necessary requirement of these compounds is that they will decompose to the required product (namely the thin film) at temperatures below 600°C, so that a glass substrate can be used in depositions.

It is important however to mention that this technique does not replicate a CVD experiment and therefore compounds which do not appear to be suitable precursors from these analytical results could still produce thin films.

3.1.3.2. Decomposition pathway

As shown below in Eqn. 3.8 a likely mechanism for the decomposition of typical group 13 alkoxides to the relevant binary product could involve γ -hydride elimination. In this instance the loss of an alkene, $\text{H}_2\text{C}=\text{CH}(\text{OMe})$, via γ -hydride elimination from a methylgallium alkoxide is depicted. If the alkoxide ligand is lost via γ -elimination the alkene $\text{H}_2\text{C}=\text{CH}(\text{OMe})$ would be eliminated. The γ -hydrogen could react with the Ga-Me group resulting in the elimination of methane.



(Eqn. 3.8)

3.2. Results and Discussion

Tailoring the properties of CVD precursors can help to exploit the full potential of CVD. It has been reported previously that the replacement of simple alkoxide groups¹² by donor-functionalised alkoxides, can result in precursors with improved physical properties and enhanced CVD performance as discussed in the last Chapter. It is proposed that knowledge of the structures of precursors in the gas phase could provide useful information regarding the decomposition processes central to CVD. In this chapter, the determination of the gas phase structure of selected CVD precursors is described and hence information on the possible chemical species present in the CVD process is reported. It is proposed that in light of the gas phase structures reported herein, improvements in precursor design and film growth is facilitated.

In addition to the GED studies, TGA studies were carried out on a selection of the compounds prepared as described in Chapter 2, to obtain information about decomposition pathways. The temperature at which the precursors decompose during the TGA studies provides information for the necessary conditions for any subsequent CVD reactions.

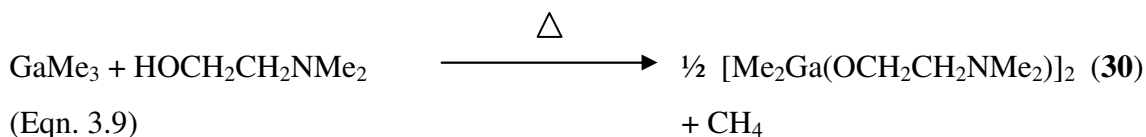
3.2.1. Gas Phase Electron Diffraction studies

This section describes the synthesis and gas phase structure of a range of gallium(III) mono(alkoxides) of the type, $[\text{Me}_2\text{Ga}(\text{OR})]_2$ ($\text{R} = \text{CH}_2\text{CH}_2\text{NMe}_2$ (**30**), $\text{CH}_2\text{CH}_2\text{OMe}$ (**31**), $t\text{Bu}$ (**32**)). Due to the computational nature of GED, the compounds investigated had to be relatively simple with small R groups. Thus, the computational models of the structures elucidated herein are relatively similar to one another, and are not complex, due to financial and time constraints. It is for this reason that mono- as opposed to bis- or tris- (alkoxides) were investigated, as larger structures, with multiple complex ligands would pose problems in modelling.

As with many gallium alkoxides, $[\text{Me}_2\text{Ga}(\text{OCH}_2\text{CH}_2\text{NMe}_2)]_2$ (**30**) and $[\text{Me}_2\text{Ga}(\text{OCH}_2\text{CH}_2\text{OMe})]_2$ (**31**) have been characterised previously in the crystalline phase using X-ray diffraction.^{49,50} The solid state structures of **30** and **31** have been shown to be dimeric with a planar centrosymmetric Ga_2O_2 ring. While the synthesis in this work focussed on the use of donor functionalised alkoxide ligands, in order to stabilise the group 13 metal centre and to avoid oligomerization, as a point of comparison the compound, $[\text{Me}_2\text{Ga}(\text{O}^t\text{Bu})]_2$ (**32**), was also investigated in the gas phase. Compound **32** is also dimeric in the solid state, with a planar centrosymmetric Ga_2O_2 ring. It is thought that **32** exists solely as a dimer because of the bulky tertiary butyl groups surrounding the metal centre, thus preventing further oligomerization.

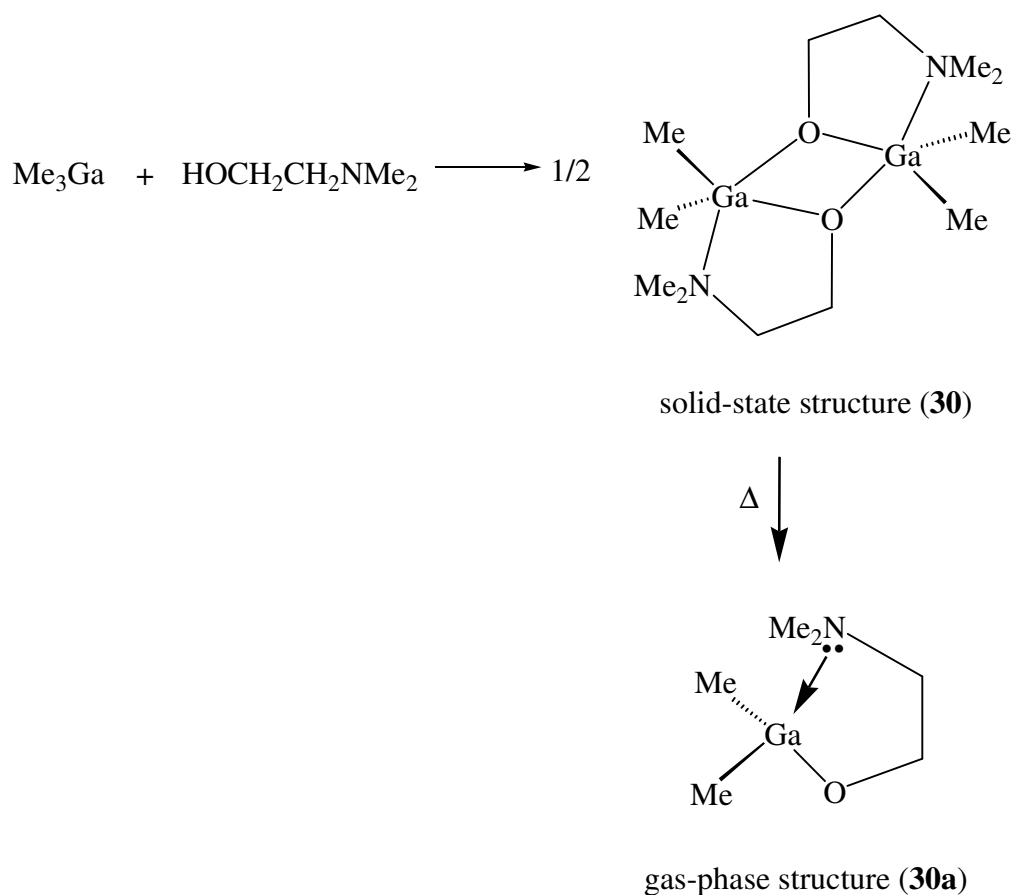
3.2.2. The reaction of GaMe_3 with $\text{HOCH}_2\text{CH}_2\text{NMe}_2$

The reaction of GaMe_3 with one equivalent of $\text{HOCH}_2\text{CH}_2\text{NMe}_2$ in toluene with stirring for 24 hours afforded the dimethylgallium mono(alkoxide) $[\text{Me}_2\text{Ga}(\text{OCH}_2\text{CH}_2\text{NMe}_2)]_2$ (**30**), as an oil. Analytical and spectroscopic data confirmed the formation of compound **30**.



The reaction shown in Eqn. 3.9 was successfully carried out, which is based on a modified previous report.⁴⁹ Peaks observed in the ¹H NMR spectrum at 3.49, 2.01 and 1.98 ppm can be assigned to hydrogen environments, OCH₂CH₂N, OCH₂CH₂N and NCH₃, respectively. These three peaks are in a 10:6 ratio with the singlet observed at 0.20 ppm assigned to the GaMe hydrogen environment, which is consistent with the formation of the mono(alkoxide) **30**. The peak observed at 0.20 ppm is a downfield shift from the starting material GaMe₃ (observed at 0.03 ppm). This downfield shift indicates the electron density being pulled away from the metal centre and thus the methyl group. Four peaks observed in the ¹³C{¹H}NMR spectrum of **30** at 5.2, 45.2, 59.1 and 61.7 ppm can be assigned to the carbon environments, GaMe, NMe, OCH₂CH₂N and OCH₂, respectively. In the IR spectrum of **30**, Ga₂O₂ ring modes are observed at 552 cm⁻¹, consistent with the dimeric structure in **30**. In the mass spectrum of **30**, taken in toluene, a molecular ion peak observed at (*m/z*) = 374 further supports the proposed dimeric nature of compound **30**.

The GED data was recorded and analysed at the University of Edinburgh. Initially, for compound **30** the GED data was compared with theoretical data representing both monomeric and dimeric species. It became obvious that the fit to the monomeric structure was far superior and so geometric models were written describing the structure, [Me₂Ga(OCH₂CH₂NMe₂)] (**30a**) in terms of bond lengths, bond angles and dihedral angles. Selected refinement parameters are shown in Table 3.1. The proposed route, from the synthesis of the dimeric structure, **30** to isolation of the gas phase monomer, **30a** is shown in Scheme 3.1.



Scheme 3.1: Preparation of $[\text{Me}_2\text{GaOCH}_2\text{CH}_2\text{NMe}_2]_2$ (30) and $[\text{Me}_2\text{Ga}(\text{OCH}_2\text{CH}_2\text{NMe}_2)]$ (30a).

Table 3.1: Selected GED-refined parameters (r_{h1}) for $[\text{Me}_2\text{GaOCH}_2\text{CH}_2\text{NMe}_2]$ (30a)^a

$r_{\text{Ga}-\text{O}(5)}$	190.6(4)	$\angle \text{O}(5)-\text{Ga}-\text{C}(1)$	115.3(8)
$r_{\text{Ga}-\text{C}(1)}$	200.6(2)	$\angle \text{O}(5)-\text{Ga}-\text{C}(2)$	112.8(8)
$r_{\text{Ga}-\text{C}(2)}$	200.6(2)	$\angle \text{Ga}-\text{O}(5)-\text{C}(6)$	116.2(12)
$r_{\text{O}(5)-\text{C}(6)}$	141.5(5)	$\angle \text{O}(5)-\text{C}(6)-\text{C}(7)$	110.9(9)
$r_{\text{C}(6)-\text{C}(7)}$	154.5(5)	$\angle \text{C}(6)-\text{C}(7)-\text{N}(21)$	109.7(9)
$r_{\text{C}(7)-\text{N}(21)}$	150.0(4)	$\angle \text{C}(7)-\text{N}(21)-\text{C}(3)$	110.7(7)
$r_{\text{N}(21)-\text{C}(3)}$	148.8(4)	$\angle \text{C}(7)-\text{N}(21)-\text{C}(22)$	110.3(7)
$r_{\text{N}(21)-\text{C}(22)}$	149.0(4)	$\phi_{\text{Ga}-\text{O}(5)-\text{C}(6)-\text{C}(7)}$	43.0(19)
$r_{\text{Ga}\cdots\text{N}(21)}$	233.2(11)	$\phi_{\text{O}(5)-\text{C}(6)-\text{C}(7)-\text{N}(21)}$	-48.1(25)

^a Distances (r) are in pm and angles (\angle) and dihedral angles (ϕ) are in degrees.

Ab initio molecular orbital calculations were performed for both the dimeric and monomeric forms of $[\text{Me}_2\text{Ga}(\text{OCH}_2\text{CH}_2\text{NMe}_2)]_n$ ($n = 1, 2$). All independent geometric parameters were refined by least-squares and restraints were applied, using the SARACEN method,⁵¹ to parameters that could otherwise not be refined. The calculations for the dimer indicated that in isolation it would have a structure generally similar to that seen in the crystalline state. The possibility of structures with both C_2 and C_i point-group symmetries were considered and it was estimated that the structure with C_2 symmetry would be lower in energy by approximately 2.8 kJ mol^{-1} . For the monomer, scans of the potential energy upon rotation about the O(5)–C(6) and C(6)–C(7) bonds (see Fig. 3.8 for atom numbering) were performed to investigate the presence, or otherwise, of different conformers. Only one structure representing a minimum on the potential-energy surface was identified (C_1 symmetry), in which the gallium and nitrogen atoms come close together to form a five-membered ring through dative bonding.

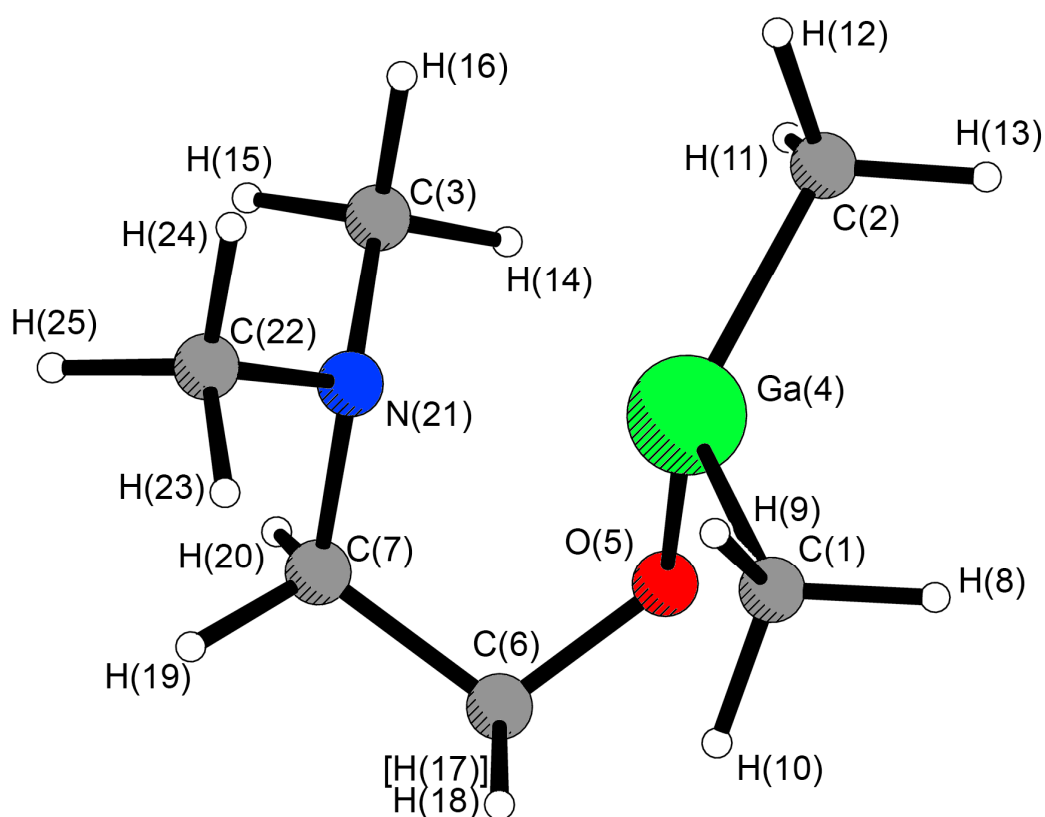


Fig. 3.8: Molecular structure of **30a** including the atom numbering scheme.

The relatively high volatility of **30** allowed a gas phase electron diffraction experiment to be performed by heating the sample to 398 K, with the nozzle heated to 415 K to prevent the sample recondensing. Analysis of the diffraction data revealed that the gaseous sample contained only the monomeric form **30a** with the geometry shown in Fig. 3.8. The fit of the theoretical model to the experimental data was good, with $R_G = 0.094$ ($R_D = 0.069$), and can be visualised using the radial-distribution curve in Fig. 3.9, which shows the experimental curve and the experimental-minus-theoretical difference curve. If there had been a proportion of the dimeric form of **30** present in the gas-phase sample there would have been evidence for interatomic interactions at distances longer than about 6 Å.

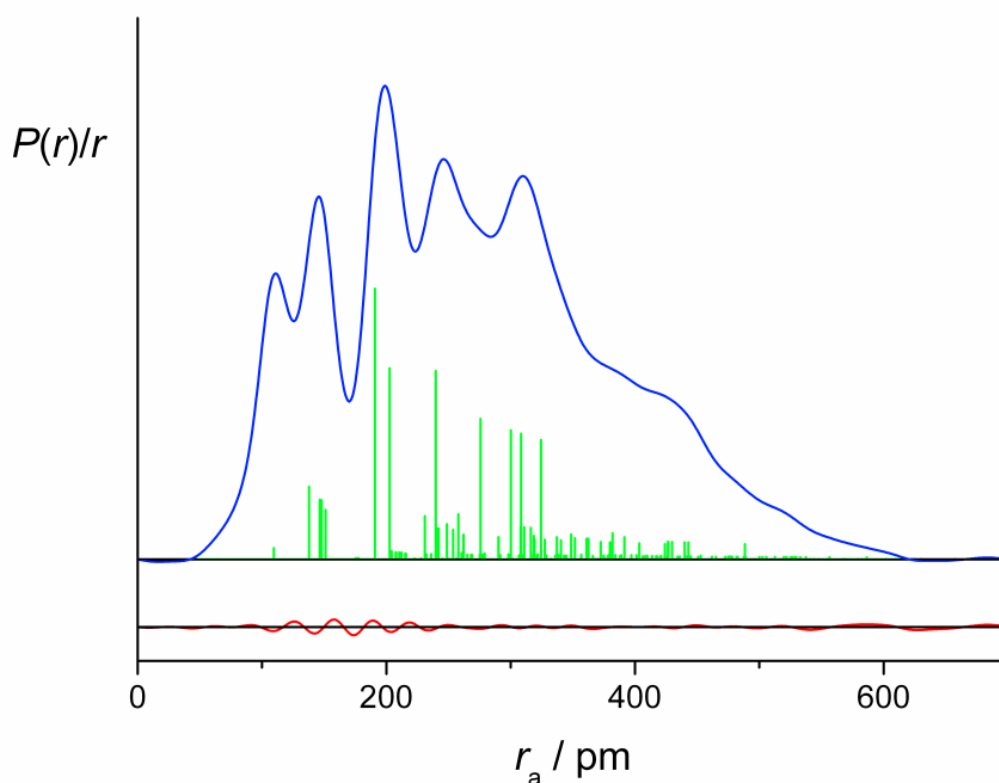


Fig. 3.9: Radial-distribution curve from the GED refinement of **30a** (Blue line shows experimental data, green sticks show model and red line shows difference).

Calculations were performed for the isolated monomer at HF/6-31G*, MP2(full)/6-31G* and MP2(full)/6-31G* levels. The optimised structures reveal that **30a** does not exhibit a particularly rigid structure. For example, calculated values for the Ga–O–C(6)–C(7) dihedral angle have a range of more than 12° and for the O–C(7)–C(6)–N

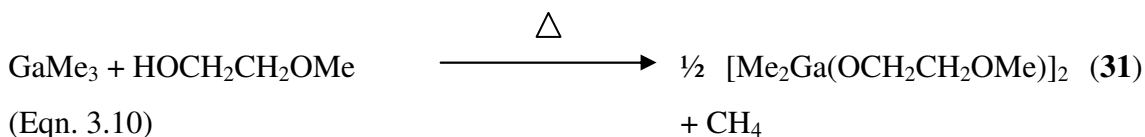
dihedral angle a range of 6°. Despite this, the highest level *ab initio* calculated structure of [Me₂GaOCH₂CH₂NMe₂] (**30a**) shows reasonably good agreement with the GED structure. Because the molecule has many degrees of flexibility, some of the experimental estimated standard deviations for the torsion angles are large, typically 2 – 3°.

The Ga atom in the gas-phase structure of **30a** is surrounded by two methyl groups as well as one oxygen and one nitrogen atom derived from the aminoalkoxide chelate. The Ga atom therefore has a distorted tetrahedral arrangement, with the N(21)···Ga–X angles in the range 81.6(10)–107.9(19)°. There is no indication of the formation of additional gallium-donor interactions (*i.e.* the presence of dimers) and hence the coordinative unsaturation of the Ga atom is satisfied by a dative interaction with the nitrogen atom in the gas phase.

The Ga···N distance in **30a** has been determined in the gas phase to be 2.332(11) Å. This can be compared to the solid-state structure, where the Ga···N bond distance was 2.471(4) Å.¹⁶ This is a relatively large difference even considering the fact that two different methods have been applied. However, it is not surprising that the bond distance would be shorter in monomeric **30a** compared to dimeric **30**. The Ga–O bond distance in **30a** in the gas phase is 1.906(4) Å, which is similar to the equatorial Ga–O bond length of 1.913(3) Å in the solid state, but shorter than the axial Ga–O bond distance of 2.078(3) Å. The average Ga–O bond length for tetrahedrally and octahedrally coordinated gallium atoms is 1.96 Å.^{13,16} For the dimeric structure **30**, the equatorial bonds would be expected to be shorter and axial ones longer based on hybridisation effects alone; this is indeed observed. The shorter Ga–O distance observed in gas phase **30a** is probably the result of monomer formation and the constraints of the chelating ring.⁵²

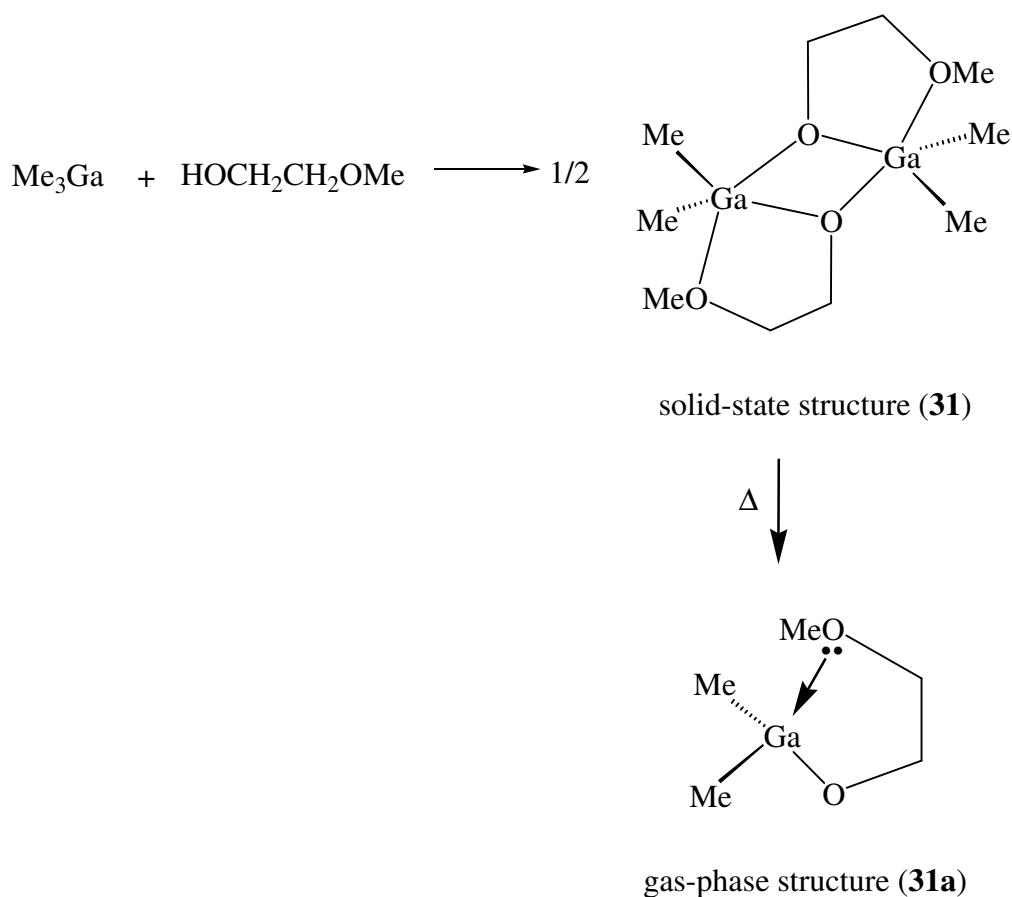
3.2.3. The reaction of GaMe₃ with HOCH₂CH₂OMe

The reaction of GaMe₃ with one equivalents of HOCH₂CH₂OMe in toluene with stirring for 24 hours afforded the dimethylgallium mono(alkoxide) [Me₂Ga(OCH₂CH₂OMe)]₂ (**31**), as a free flowing white powder. Analytical and spectroscopic data confirmed the formation of compound **31**.



The reaction shown in Eqn. 3.10 was successfully carried out, which is based on a modified previous report.⁵⁰ Peaks observed in the ¹H NMR spectrum at 3.79, 3.44 and 2.89 ppm can be assigned to hydrogen environments, OCH₂CH₂, OCH₂CH₂O and OCH₃, respectively. These peaks are in a 7:6 ratio with the singlet observed at 0.21 ppm assigned to the GaMe hydrogen environment, which is consistent with the formation of the mono(alkoxide) **31**. The peak observed at 0.21 ppm is a downfield shift from the starting material GaMe₃ (observed at 0.03 ppm). This downfield shift indicates the electron density being pulled away from the metal centre and thus the methyl group. Four peaks observed in the ¹³C{¹H}NMR spectrum of **31** at 5.1, 59.1, 62.9 and 72.8 ppm can be assigned to the carbon environments, GaMe, OMe, OCH₂CH₂O and OCH₂, respectively. In the IR spectrum of **31**, Ga₂O₂ ring modes are observed at 654 cm⁻¹, consistent with the dimeric structure of **31**. In the mass spectrum of **31**, taken in toluene, a molecular ion peak observed at (*m/z*) = 348 further supports the proposed dimeric nature of compound **31**.

As with compound **30** the GED data was recorded and analysed at the University of Edinburgh. Even with the prior knowledge that the analogous compound **30** was found to be monomeric in the gas phase, GED data was compared with theoretical data representing both monomeric and dimeric species. As with compound **30** the fit to the monomeric structure was far superior and so geometric models were written describing the structure, [Me₂Ga(OCH₂CH₂OMe)] (**31a**) in terms of bond lengths, bond angles and dihedral angles. Selected refinement parameters are shown in Table 3.2. The proposed route, from the synthesis of the dimeric structure, **31** to isolation of the gas phase monomer, **31a** is shown in Scheme 3.2.



Scheme 3.2: Preparation of $[\text{Me}_2\text{Ga}(\text{OCH}_2\text{CH}_2\text{OMe})]_2$ (31) and $[\text{Me}_2\text{Ga}(\text{OCH}_2\text{CH}_2\text{OMe})]$ (31a).

Table 3.2: Selected calculated parameters and GED-refined parameters for $[\text{Me}_2\text{GaOCH}_2\text{CH}_2\text{OMe}]$ (31a).^a

$r_{\text{Ga-O}(5)}$	186.5(10)	$\angle \text{O}(5)\text{-Ga-C}(1)$	112.2(19)
$r_{\text{Ga-C}(1)}$	197.1(6)	$\angle \text{O}(5)\text{-Ga-C}(2)$	108.9(20)
$r_{\text{Ga-C}(2)}$	197.1(6)	$\angle \text{Ga-O}(5)\text{-C}(6)$	114.3(9)
$r_{\text{O}(5)\text{-C}(6)}$	143.7(7)	$\angle \text{O}(5)\text{-C}(6)\text{-C}(7)$	108.4(11)
$r_{\text{C}(6)\text{-C}(7)}$	155.2(8)	$\angle \text{C}(6)\text{-C}(7)\text{-O}(21)$	104.4(11)
$r_{\text{C}(7)\text{-O}(21)}$	147.6(7)	$\angle \text{C}(7)\text{-O}(21)\text{-C}(3)$	112.3(12)
$r_{\text{O}(21)\text{-C}(3)}$	146.1(7)	$\phi_{\text{Ga-O}(5)\text{-C}(6)\text{-C}(7)}$	54.4(26)
$r_{\text{Ga}\cdots\text{O}(21)}$	216.0(20)	$\phi_{\text{O}(5)\text{-C}(6)\text{-C}(7)\text{-O}(21)}$	-36.3(38)

^a Distances (r) are in pm and angles (\angle) and dihedral angles (ϕ) are in degrees.

Ab initio molecular orbital calculations were performed for both the dimeric and monomeric forms of $[\text{Me}_2\text{Ga}(\text{OCH}_2\text{CH}_2\text{OMe})]_n$ ($n = 1, 2$). All independent geometric parameters were refined by least-squares and restraints were applied, using the SARACEN method,⁵¹ to parameters that could otherwise not be refined. As with compound **30** the calculations for the dimer indicated that in isolation it would have a structure similar to that in the solid state. The possibility of structures with both C_2 and C_i point-group symmetries were considered and it was estimated that the structure with C_2 symmetry would be lower in energy. Only one structure representing a minimum on the potential-energy surface was identified (C_1 symmetry), in which the gallium and oxygen atoms (O21) come close together to form a five-membered ring through dative bonding, just as in **30a** where the nitrogen atom exhibits a dative interaction with the gallium centre.

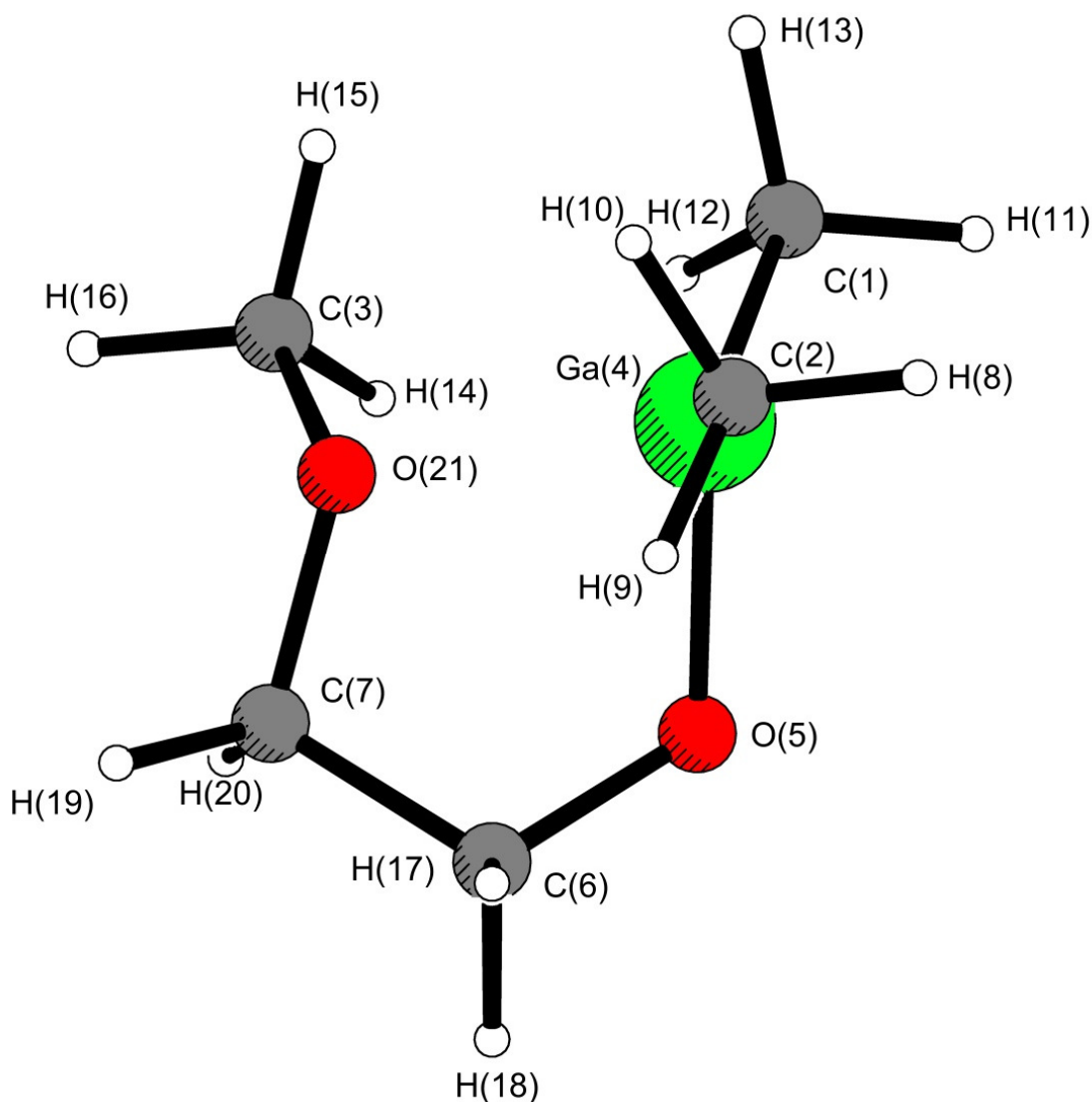


Fig. 3.10: Molecular structure of **31a** including the atom numbering scheme.

The relatively high volatility of **31** allowed a gas phase electron diffraction experiment to be performed by heating the sample to 398 K, with the nozzle heated to 393 K to prevent the sample recondensing. Analysis of the diffraction data revealed that the gaseous sample contained only the monomeric form **31a** with the geometry shown in Fig. 3.11. The fit of the theoretical model to the experimental data was good, with $R_G = 0.081$ ($R_D = 0.075$), and can be visualised using the radial-distribution curve in Fig. 3.12, which shows the experimental curve and the experimental-minus-theoretical difference curve. If there had been a proportion of the dimeric form of **31** present in the gas phase sample there would have been evidence for interatomic interactions at distances longer than about 6 Å.

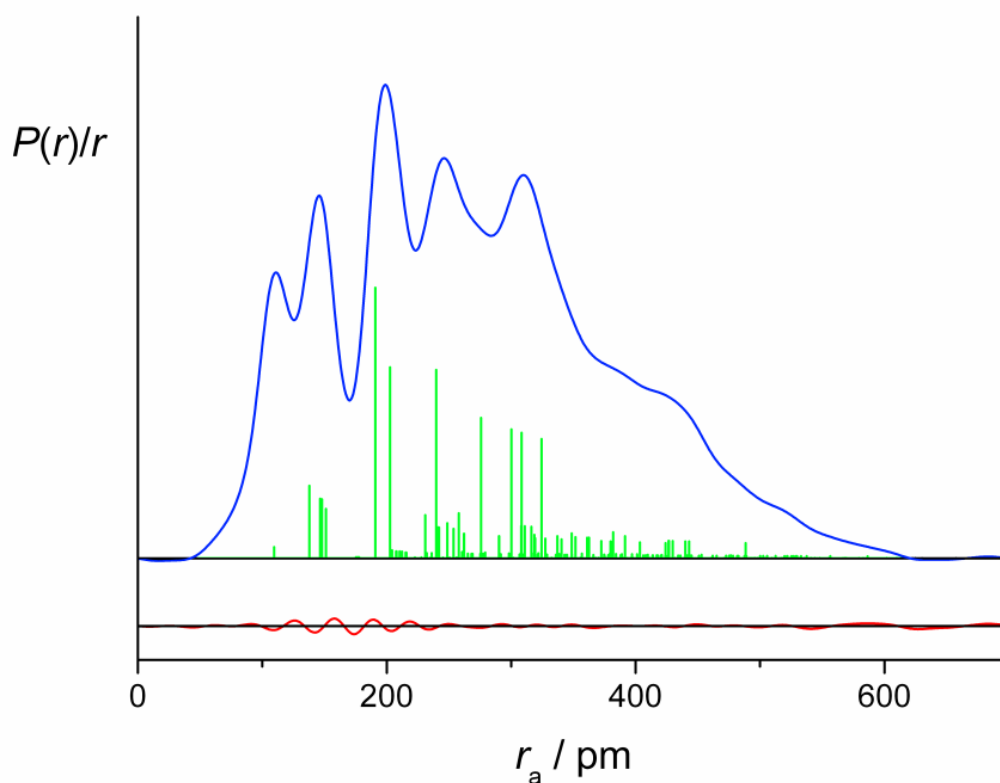


Fig. 3.11: Radial-distribution curve from the GED refinement of **31a**. (Blue line shows experimental data, green sticks show model and red line shows difference).

For the dimeric structure **31**, calculations for both C_2 and C_i point-group symmetries were performed. For the monomeric structures **31a**, scans of the potential energy were

performed by rotating about the Ga(1)O(5)C(6)C(7) and O(5)C(6)C(7)O(21) dihedral angles. For **31a**, as with **30a** only one minimum was identified.

For each of the molecules studied geometry optimisations were performed at the Hartree-Fock level with the 3-21G* basis set^{53,54} on all atoms followed by the 6-31G* basis set.⁵⁵ The optimised structures reveal that as with **30a**, compound **31a** does not exhibit a particularly rigid structure. For example, calculated values for the Ga(1)O(5)C(6)C(7) dihedral angle have a range of more than 10° and for the O(5)C(6)C(7)O(21) dihedral angle a range of 5°. Despite this, the highest level *ab initio* calculated structure of [Me₂Ga(OCH₂CH₂OMe)] (**31a**) shows agreement with the GED structure. Because the molecule has many degrees of flexibility, some of the experimental estimated standard deviations for the torsion angles are large, typically 2 – 3°.

The Ga atom in the gas phase structure of **31a** is surrounded by two methyl groups as well as two oxygen atoms, the first, O(5), from the direct bond with the alkoxide ligand and the second, O(21), derived from the alkoxide chelate. The Ga atom therefore has a distorted tetrahedral arrangement, with the O(21)···Ga–X angles in the range 81.5(3)–108.7(5)°. There is no indication of the formation of additional gallium-donor interactions (*i.e.* the presence of dimers) and hence the coordinative unsaturation of the Ga atom is satisfied by a dative interaction with the nitrogen atom in the gas phase.

The Ga···O distance in **31a** has been determined in the gas phase to be 2.160(20) Å. This can be compared to the solid-state structure, where the Ga···O bond distance was 2.624(6) Å.⁵⁶ This is a relatively large difference even considering the fact that two different methods have been applied. The Ga–O bond distance in **31a** in the gas phase is 1.865(10) Å, which is similar to the equatorial Ga–O bond length of 1.934(6) Å in the solid state, but shorter than the axial Ga–O bond distance of 2.624(6) Å. The average Ga–O bond length for tetrahedrally and octahedrally coordinated gallium atoms is 1.96 Å.^{13,16} For the dimeric structure **31**, the equatorial bonds would be expected to be shorter and axial ones longer based on hybridisation effects alone; this is indeed observed. The shorter Ga–O distance observed in gas phase **31a** is probably the result of monomer formation and the constraints of the chelating ring.⁵²

3.2.4. The reaction of GaMe₃ with HO^tBu

The reaction of GaMe₃ with one equivalent of HO^tBu in toluene with stirring for 24 hours afforded the dimethylgallium mono(alkoxide) [Me₂Ga(O^tBu)]₂ (**32**), as a free flowing white powder. Analytical and spectroscopic data confirmed the formation of compound **32**.



The reaction shown in Eqn. 3.11 was successfully carried out, which is based on a modified previous report for the synthesis of an analogous compound.⁵⁷ Peaks observed in the ¹H NMR spectrum at 1.12 and 0.01 ppm can be assigned to hydrogen environments, OC(CH₃)₃ and GaMe and are in a 9:6 ratio with each other, which is consistent with the formation of the mono(alkoxide) **32**. Three peaks observed in the ¹³C{¹H}NMR spectrum of **32** at 73.0, 32.3 and -1.35 ppm can be assigned to the carbon environments, C(CH₃)₃, C(CH₃)₃ and GaMe respectively. In the mass spectrum of **32**, taken in toluene, a molecular ion peak observed at (*m/z*) = 344 supports the proposed dimeric nature of compound **31**, which is further supported by peaks observed corresponding to fragments of the dimeric structure (287, 215, 172 and 157).

In sections 3.2.2-3.2.3 the gas phase structures, [Me₂Ga(OCH₂CH₂NMe₂)] (**30a**) and [Me₂Ga(OCH₂CH₂OMe)] (**31a**) have been determined and although both exist as dimeric species in their crystalline forms, they have been shown to exist solely as monomers in the gas phase. While the synthesis in this work focus on the use of donor functionalised alkoxide ligands, for comparison the gas phase structure of [Me₂Ga(O^tBu)]₂ (**32**), incorporating a monofunctional alkoxide, has been investigated. This was studied with a view to gaining an insight into superior stabilising effects of donor- over mono-functional ligands. Whilst the structure of [Me₂Ga(O^tBu)]₂ has not been reported using X-ray crystallographic techniques, it is reported it is also dimeric in the solid state, as well as analogous compounds, [^tBu₂Ga(O^tBu)]₂⁵⁷ and [H₂Ga(O^tBu)]₂,⁵⁸ whose crystal structures have been described previously. These compounds exhibit a planar centrosymmetric Ga₂O₂ ring at their centre, and are dimeric.

It is thought that **32** exists solely as a dimer because of the bulky tertiary butyl groups surrounding the metal centre, thus preventing further oligomerization

For **32** it was obvious from the GED data that a dimeric structure gave a much better fit. As the only minimum structure on the potential-energy surface was found to have C_{2h} symmetry, the model was written accordingly, describing the structure, $[\text{Me}_2\text{Ga}(\text{O}^t\text{Bu})]_2$ (**32**) in terms of bond lengths, bond angles and dihedral angles. Selected refinement parameters are shown in Table 3.3.

Table 3.3: Selected calculated parameters and GED-refined parameters for C_{2h} -symmetric $[\text{Me}_2\text{Ga}(\text{O}^t\text{Bu})]_2$ (**32**).^a

$r_{\text{Ga-O}}$	197.9(2)	$\angle \text{O-Ga-O}$	81.5(2)
$r_{\text{Ga-C}}$	196.5(3)	$\angle \text{O-C(5)-C(6)}$	108.0(5)
$r_{\text{C-O}}$	144.1(5)	$\angle \text{O-C(5)-C(7)}$	110.2(6)
$r_{\text{C(5)-C(6)}}$	153.9(3)	$\angle \text{C(31)-Ga-C(35)}$	122.2(16)
$r_{\text{C(5)-C(7)}}$	153.7(4)	$\phi \text{C(31)-Ga(4)-Ga(1)-O(3)}^b$	89.6(31)
$\angle \text{Ga-O-Ga}$	98.5(2)		

^a Distances (r) are in pm and angles (\angle) and dihedral angles (ϕ) are in degrees. ^b X is the mid-point of the $\text{Ga}\cdots\text{Ga}$ vector.

Ab initio molecular orbital calculations were performed for $[\text{Me}_2\text{Ga}(\text{O}^t\text{Bu})]_2$ (**32**). All independent geometric parameters were refined by least-squares and restraints were applied, using the SARACEN method,⁵¹ to parameters that could otherwise not be refined. As with compounds **30** – **31**, the calculations for the dimer indicated that in isolation it would have a structure similar to that in the solid state. Only one structure representing a minimum on the potential-energy surface was identified (C_{2h} symmetry), indicating that the compound remained a dimer in the gas phase (Fig. 3.13).

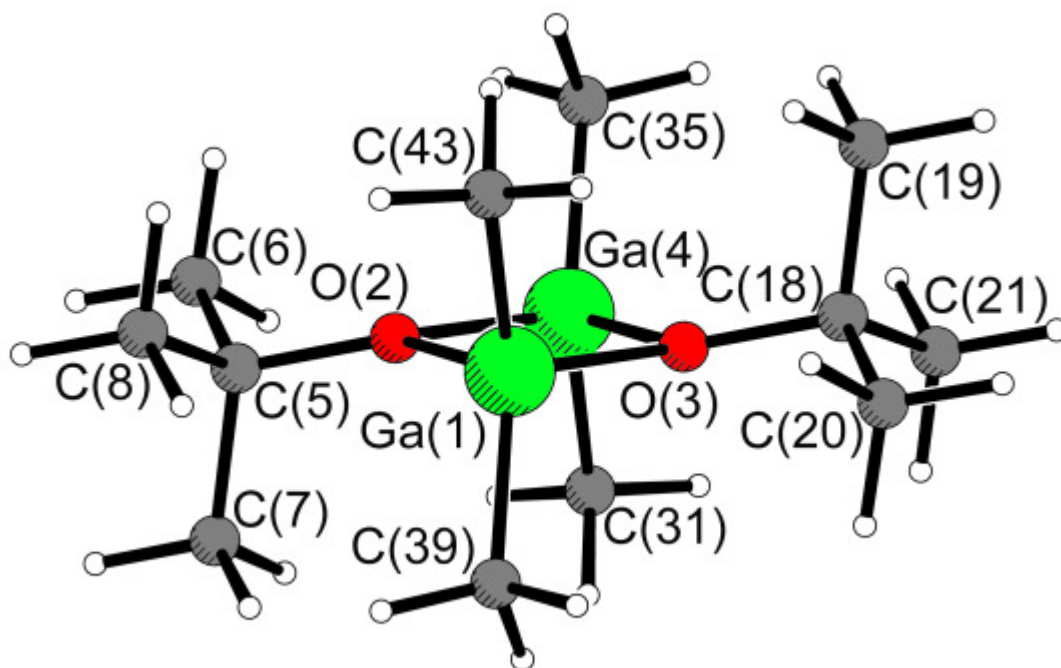


Fig. 3.12: Molecular structure of **32** including the atom numbering scheme.

The relatively high volatility of **32** allowed a gas-phase electron-diffraction experiment to be performed by heating the sample to 398 K, with the nozzle heated to 394 K to prevent the sample recondensing. Analysis of the diffraction data revealed that the gaseous sample contained only the dimeric form **32** with the geometry shown in Fig. 3.13. The fit of the theoretical model to the experimental data was good, with $R_G = 0.071$ ($R_D = 0.099$), and can be visualised using the radial-distribution curve in Fig. 3.14, which shows the experimental curve and the experimental-minus-theoretical difference curve. Based on the values of the final R factor, the fit for compound **32** is better than that of **30** or **31**, which both show higher R factors ($R_G = 0.094$, $R_G = 0.081$), so it is highly unlikely that there is a proportion of the monomeric form of **32** present in the gas-phase sample, as R values would certainly have been higher.

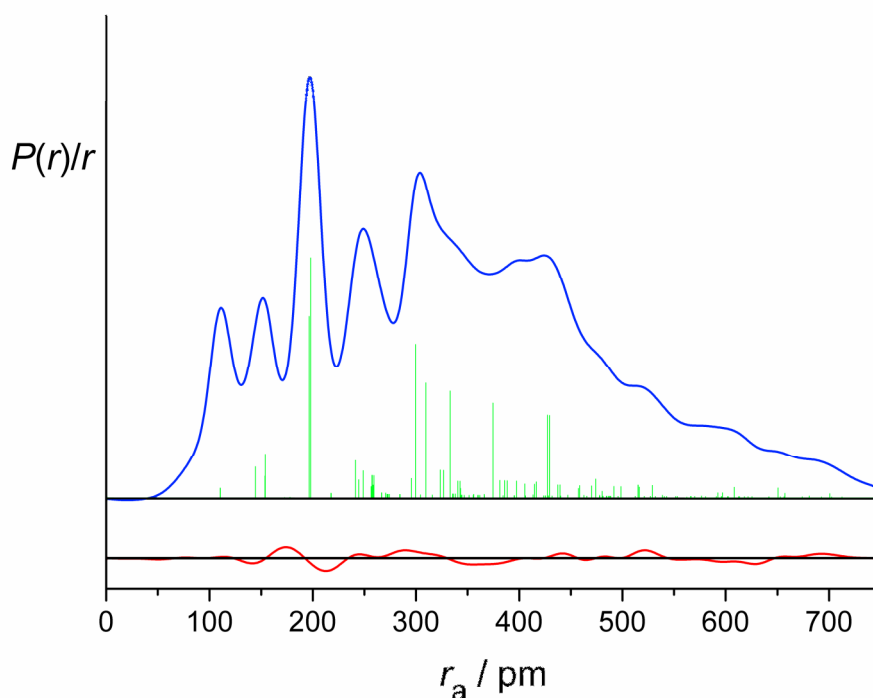


Fig. 3.13: Radial-distribution curve from the GED refinement of **32**. (Blue line shows experimental data, green sticks show model and red line shows difference).

Compound **32** is dimeric in the gas phase with the two gallium cations and two alkoxide oxygen anions forming a centrosymmetric, planar four-membered Ga_2O_2 ring that is common to this type of compound. Each monomeric unit is composed of one gallium cation, two methyl groups and a tertiary butyl alkoxide ligand. The inversion centre is located in the middle of the Ga_2O_2 ring.

Each gallium atom in **32** adopts a tetrahedral geometry. The bridging oxygen atoms of the Ga_2O_2 centrosymmetric ring make up two of the corners of the gallium centred tetrahedra, whilst the methyl terminal groups make up the remaining two.

Comparable bond lengths suggest that both methyl groups are tightly bound to both gallium centres ($\text{C}(39)\text{-Ga}(1)$ 1.965(3) Å and $\text{C}(43)\text{-Ga}(1)$ 1.950(5) Å). The average bond distance between Ga-O (1.979(2) Å) for the gas phase structure of **32**, reported here, is comparable to that of known solid state structures, the Ga-O bond distance in $[\text{H}_2\text{Ga}(\text{O}^t\text{Bu})]_2$ (1.905(9) Å),⁵⁸ and $[\text{tBu}_2\text{Ga}(\text{O}^t\text{Bu})]_2$ (1.990(2) Å).⁵⁷

The gallium centred tetrahedra are distorted, exhibiting bond angles which vary from the desired 109° seen in typical tetrahedra. The bond angles between methyl groups on the gallium centre have an average of $122.2(16)^\circ$, and the O(3)–Ga(1)–O(2) bond angle is reported to be $81.5(2)^\circ$, this large deviation from 109° is due to the steric constraints of in the Ga₂O₂ ring, as is often the case with compound of this type (*c.f.* compound **13**, in Chapter 2 which exhibits an internal O#1–Ga–O1 angle of $73.68(9)^\circ$). Bond angles are comparable with that of known compounds, [H₂Ga(O^tBu)]₂: C–Ga–C, $116.0(1)^\circ$, O–Ga–O, $78.6(5)^\circ$;⁵⁸ [tBu₂Ga(O^tBu)]₂: C–Ga–C, $115.1(3)^\circ$, O–Ga–O, $76.1(1)^\circ$.⁵⁷

Compound **32** is dimeric in the gas phase, providing experimental evidence for the driving force behind the ready dissociation of long-chain gallium alkoxides, despite the presence of strong oxygen-gallium bonds. Both **30a** and **31a** have structures in the gas phase that exhibit five-membered rings formed by a dative bond between Ga and N or O, respectively. In **32** there is no possibility of a monomer structure stabilised by the formation of such a dative bond.

3.2.5. Thermal decomposition analysis

This section describes the TGA and DSC carried out on a selection of compounds prepared as explained in Chapter 2 and section 3.2 of this chapter. Information regarding the decomposition pathway and the temperature range is discussed. The TGA and DSC results will also provide useful information concerning for the necessary conditions required for CVD of the precursors.

3.2.5.1. TGA analysis of [Me₂In(OCH(CH₃)CH₂OMe)]₂ (**4**)

The thermogravimetric analysis of [Me₂In(OCH(CH₃)CH₂OMe)]₂ (**4**) shows an overall mass loss of 49.2% (Fig. 3.15). The decomposition of **4** does not occur in clean, discrete stages but is continuous from the onset at *ca.* 150 °C throughout the temperature range studied and occurs in three stages. The first mass loss of 43.1% occurs at 200 °C, the second of 3.6% at 260 °C and finally the third mass loss of 2.5% at 380 °C. The overall mass loss of 49.2% is close to the 45.9% required for complete decomposition to In₂O₃ suggesting that this compound would make a good precursor and could deposit films at low temperatures (less than 400 °C). However, it should be noted that initially there is

an increase in mass loss (105%), this could be due to a buoyancy effect, which is can be initially observed and can be assigned to instrumentation error. Although the TGA process is carried out under nitrogen if any moisture was present this would also be observed as a weight gain on reaction with the precursor. The sharp endotherm at 46.2 °C in the DSC of $[\text{Me}_2\text{In}(\text{OCH}(\text{CH}_3)\text{CH}_2\text{OMe})]_2$ signifies a melting point. The broad exotherms observed at 240.3 and 360.5 °C could be an effect of the decomposition process. The decomposition of **4** begins at a higher temperature than the melting point suggesting that carry over of the intact molecule to the substrate could be successfully achieved. Hence, these results indicate that $[\text{Me}_2\text{In}(\text{OCH}(\text{CH}_3)\text{CH}_2\text{OMe})]_2$ would make a good CVD precursor. However, it should be noted that as the TGA does not occur in one clean stage, some contamination could be observed in the film deposited.

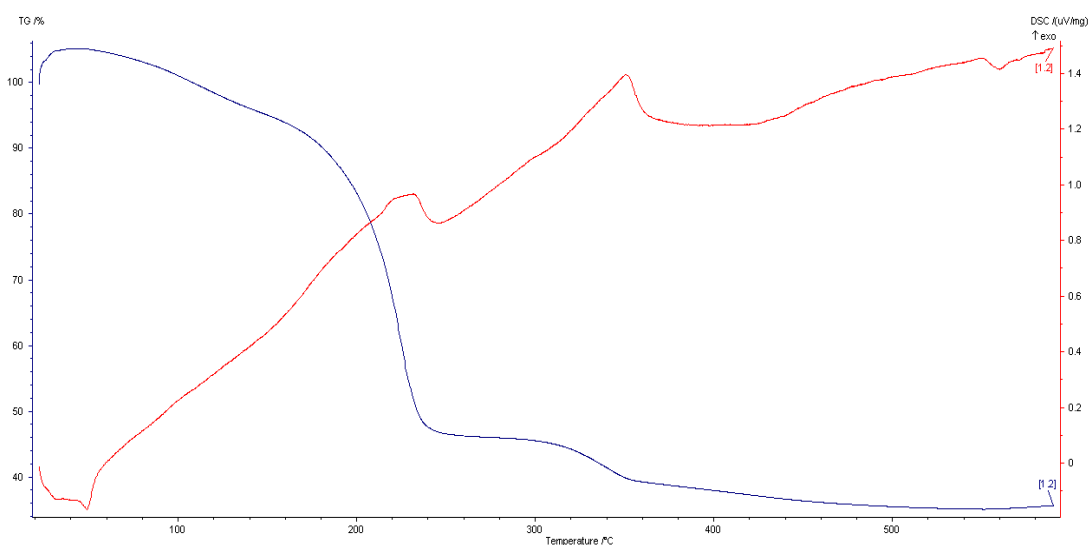


Fig 3.14: TGA of $[\text{Me}_2\text{In}(\text{OCH}(\text{CH}_3)\text{CH}_2\text{OMe})]_2$ (**4**)

3.2.5.2. TGA analysis of $[\text{Cl}(\text{Me})\text{Ga}(\text{OCH}_2\text{CH}_2\text{OMe})]_2$ (**14**)

The thermogravimetric analysis of $[\text{Cl}(\text{Me})\text{Ga}(\text{OCH}_2\text{CH}_2\text{OMe})]_2$ (**14**) shows an overall mass loss of 59.18% (Fig. 3.16). The decomposition of **14** does not occur in clean, discrete stages but is continuous from the onset at *ca.* 120 °C throughout the temperature range studied and occurs in two stages. The first mass loss of 59.18% occurs between 120–190 °C, which is consistent with the removal of the ligands, the second of 43.8% which begins at 200 °C is consistent with the remaining gallium and oxygen centre. The overall initial mass loss of 59.18% is close to the 56.18% required for complete decomposition to Ga_2O_3 , however the low temperature at which this

compound fully decomposes would suggest that compound would not make a good precursor at temperatures higher than 200 °C. The sharp endotherm at 81.2 °C in the DSC of $[\text{Cl}(\text{Me})\text{Ga}(\text{OCH}_2\text{CH}_2\text{OMe})]_2$ signifies a melting point. The broad exotherm observed between 120 and 200 °C could be an effect of the decomposition process. The decomposition of **14** begins at a higher temperature than the melting point suggesting that carry over of the intact molecule to the substrate could be successfully achieved. Hence, indicating that $[\text{Cl}(\text{Me})\text{Ga}(\text{OCH}_2\text{CH}_2\text{OMe})]_{22}$ would make a good CVD precursor, providing deposition temperatures are kept below 200 °C. However, it should be noted that as the TGA does not occur in one clean stage, some contamination could be observed in the film deposited.

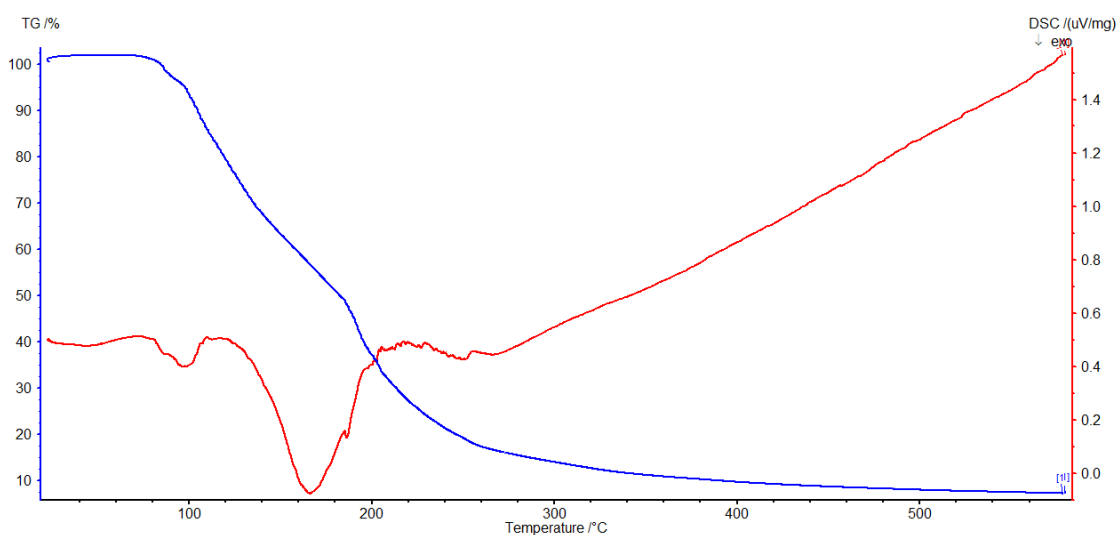


Fig 3.15: TGA/DSC of $[\text{Cl}(\text{Me})\text{Ga}(\text{OCH}_2\text{CH}_2\text{OMe})]_2$ (**14**)

3.2.5.3. TGA analysis of $[\text{Cl}(\text{Me})\text{In}(\text{OCH}_2\text{CH}_2\text{NMe}_2)]_2$ (**21**)

The thermogravimetric analysis of $[\text{Cl}(\text{Me})\text{In}(\text{OCH}_2\text{CH}_2\text{NMe}_2)]_2$ (**21**) shows an overall mass loss of 47.9% (Fig. 3.17). The decomposition of **21** does not occur in clean, discrete stages but is continuous from the onset at *ca.* 180 °C throughout the temperature range studied and occurs in two stages. The first mass loss of 13.2% occurs at 200 °C, and is consistent with the loss of the chloride ligand, the second of 34.7% at 230 °C is consistent with the loss of all alkoxide and aryl groups. The overall mass loss of 47.9% is consistent with loss of all ligands in **21** to leave the central indium and oxygen atoms. This compound would make a good precursor and could deposit films at low temperatures (less than 400 °C). In the DSC of $[\text{Cl}(\text{Me})\text{In}(\text{OCH}_2\text{CH}_2\text{NMe}_2)]_2$ broad exotherms observed shortly after the onset of decomposition at 156.3 °C onwards could

be an effect of the decomposition process, the compound is a liquid, hence no melting point is observed. Facile removal of the ligands in **21** in two gradual steps over temperature, indicate that $[\text{Cl}(\text{Me})\text{In}(\text{OCH}_2\text{CH}_2\text{NMe}_2)]_2$ would make a good CVD precursor. However, it should be noted that as the TGA does not occur in one clean stage and some contamination could be observed in the film deposited.

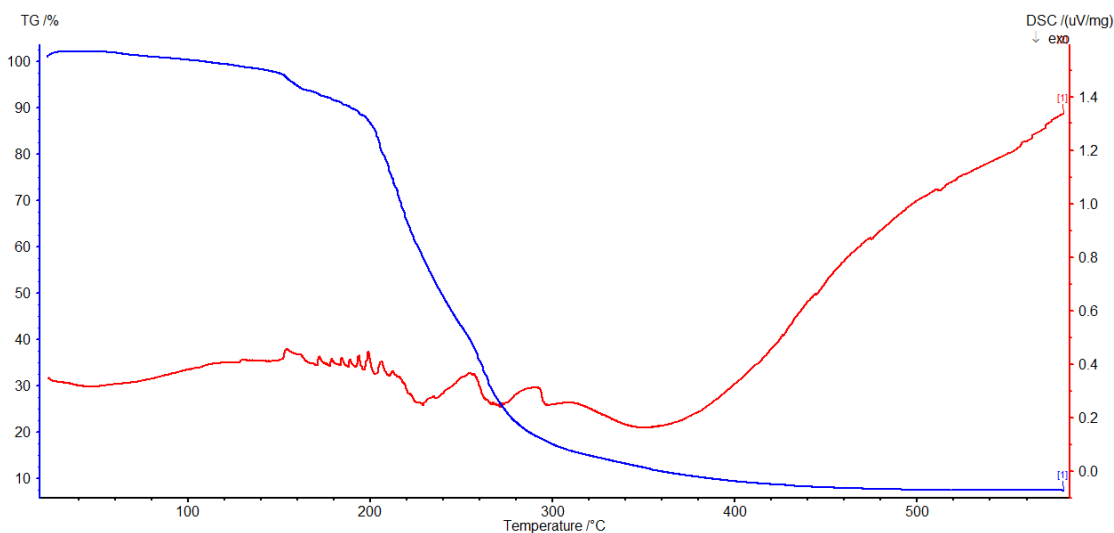


Fig 3.16: TGA/DSC of $[\text{Cl}(\text{Me})\text{In}(\text{OCH}_2\text{CH}_2\text{NMe}_2)]_2$ (**21**)

3.2.5.4. Thermal analysis of $[\text{Me}_2\text{Ga}(\text{OCH}_2\text{CH}_2\text{NMe}_2)]_2$ (**30**)

The decomposition properties of $[\text{Me}_2\text{Ga}(\text{OCH}_2\text{CH}_2\text{NMe}_2)]_2$ (**30**) was determined by TGA and the results are shown in Fig. 3.18. The decomposition of **30** shows a total weight loss of 99.2% below 300 °C, which is much higher than the expected weight loss of 54.5% if Ga_2O_3 was formed from **30**. This difference could be due to sublimation of the precursor. The observation of a steep weight loss (0-300 °C) followed by a more gradual loss of weight (300-580 °C) suggest that most of the decomposition occurs below 300 °C. The DSC of **30** shows a sharp endotherm at 30.9 °C, which corresponds to the melting point. The exotherms observed between 220–290 °C could be an effect of the decomposition process. The decomposition of **30** begins at a higher temperature than the melting point suggesting that carry over of the intact molecule to the substrate could be successfully achieved. This would suggest that $[\text{Me}_2\text{Ga}(\text{OCH}_2\text{CH}_2\text{NMe}_2)]_2$ would make a good CVD precursor. The fact that **30** appears to sublime readily is an excellent characteristic for use as a CVD precursor.

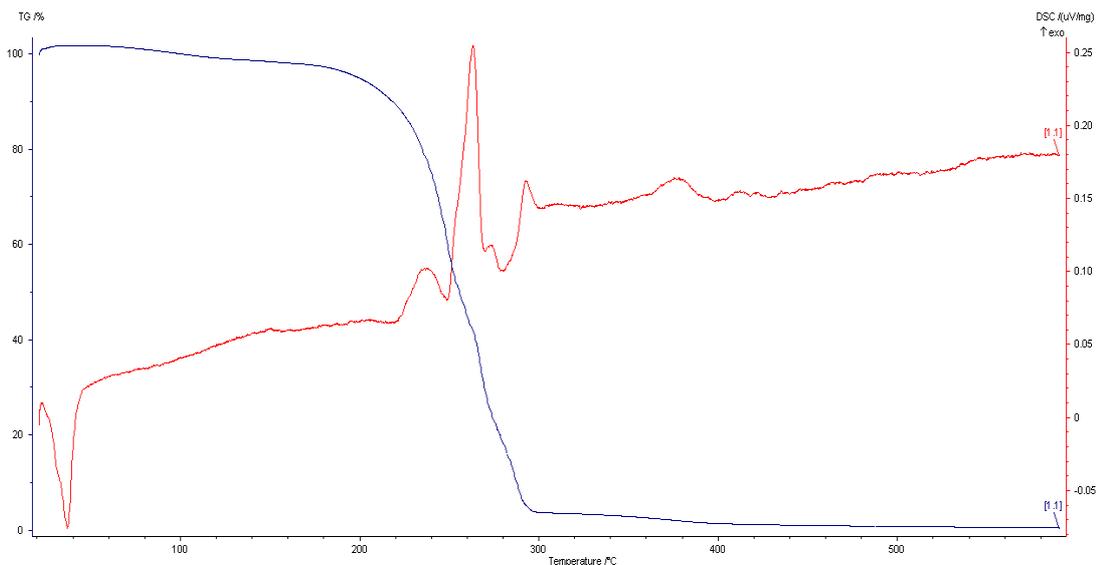


Fig 3.17: TGA/DSC for $[\text{Me}_2\text{Ga}(\text{OCH}_2\text{CH}_2\text{NMe}_2)]_2$ (**30**)

3.2.5.5. Thermal analysis of $[\text{Me}_2\text{Ga}(\text{OCH}_2\text{CH}_2\text{OMe})]_2$ (**31**)

The total mass loss of around 74.8% observed in the TGA of $[\text{Me}_2\text{Ga}(\text{OCH}_2\text{CH}_2\text{OMe})]_2$ (**31**) is significantly higher than the calculated mass loss of 51.15% for **31** to form Ga_2O_3 . A higher measured mass loss than that expected often indicates that sublimation has occurred. As shown in Fig. 3.19, the decomposition occurs in two stages. The mass change occurs in two steps, a steep weight loss of around 68.2% followed by a discrete mass loss of 4.6%. The second stage of mass loss corresponds well to a γ -hydride elimination of a methyl group, consistent with the production of methane. The DSC of **31** shows a sharp endotherm at 47.5 °C, which corresponds to the melting point. The exotherms at 208.6, 287.4 and 297.5 °C could be as a result of the decomposition process. The decomposition of this precursor also begins at a higher temperature than the melting point suggesting that carry over of the intact molecule to the substrate could be successfully achieved. This would suggest that $[\text{Me}_2\text{Ga}(\text{OCH}_2\text{CH}_2\text{OMe})]_2$ would make a good CVD precursor with little contamination in the film formed as the decomposition pathway, as shown by TGA, is clean.

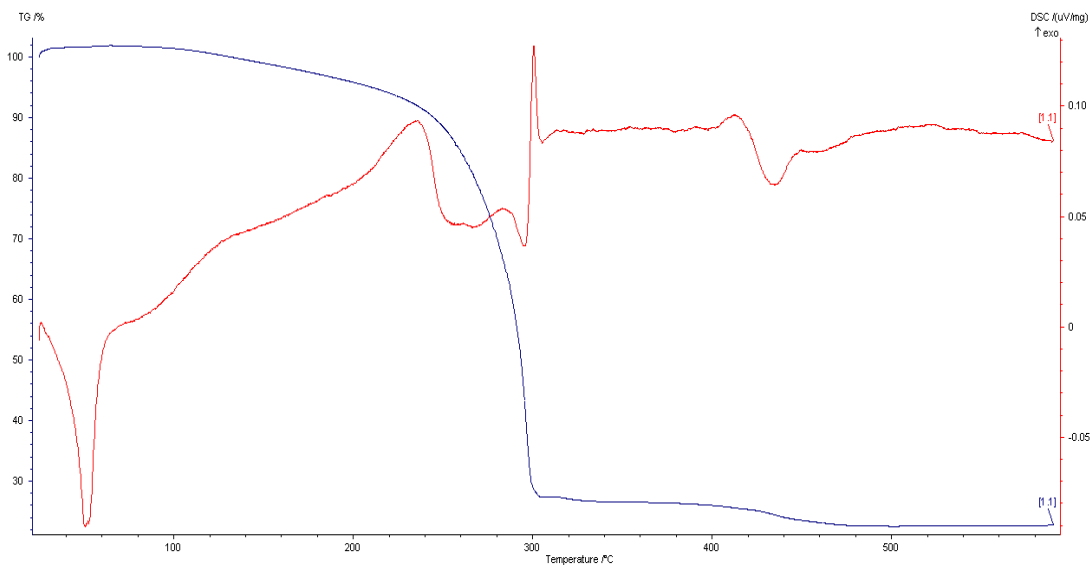


Fig 3.18: TGA/DSC for $[\text{Me}_2\text{Ga}(\text{OCH}_2\text{CH}_2\text{OMe})]_2$ (**31**)

3.2.5.6. Thermal analysis of $[\text{Me}_2\text{Ga}(\text{O}^t\text{Bu})]_2$ (**32**)

The total mass loss of around 98.98% observed in the TGA of $[\text{Me}_2\text{Ga}(\text{O}^t\text{Bu})]_2$ (**32**) is significantly higher than the calculated mass loss of 50.50% for **32** to form Ga_2O_3 . A higher measured mass loss than that expected often indicates that sublimation has occurred. As shown in Fig. 3.20, the decomposition occurs in three stages. The mass change occurs in three steps, a steep weight loss of around 53.86% followed by a mass loss of 17.42% and then 27.70%. The initial step is consistent with the loss of the ligands, leaving gallium and oxygen. The DSC of **32** shows a sharp endotherm at 59.1 °C, which corresponds to the melting point. The exotherms at 87.2 and 224.7 °C could be as a result of the decomposition process. The decomposition of this precursor also begins at a higher temperature than the melting point suggesting that carry over of the intact molecule to the substrate could be successfully achieved. This would suggest that $[\text{Me}_2\text{Ga}(\text{O}^t\text{Bu})]_2$ would make a good CVD precursor with little contamination in the film formed as the decomposition pathway, as shown by TGA, is clean.

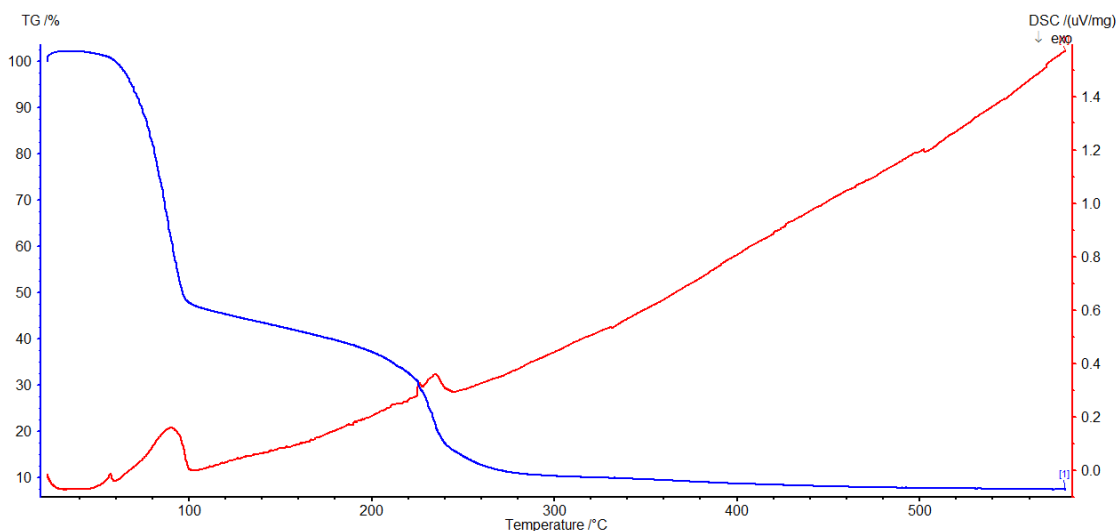


Fig 3.19: TGA/DSC for $[\text{Me}_2\text{Ga}(\text{O}^t\text{Bu})]_2$ (**32**).

3.3. Conclusions

The first full structural characterisation of the monomeric forms of **30** and **31** in the gas phase using a combined electron diffraction and computational approach has been described. The structure of $[\text{Me}_2\text{Ga}(\text{O}^t\text{Bu})]_2$, **32**, which retains its dimeric structure in the gas phase is also reported. This difference in behaviour gives us an insight into the driving force behind the transition from dimer to monomer for **30** and **31**.

Additionally the thermal decomposition of a selection of compounds has been studied using TGA and DSC. These techniques have shown the group 13 alkoxides have potential for use as precursors in the production of thin films *via* CVD. All of the compounds analysed, decompose to the desired binary material (M_2O_3), below 400 °C, so are viable as low temperature alternatives to many precursors reported.

Overall this work has shown that whilst compound **32** retains its dimeric structure in the gas phase, compounds **30** and **31** are monomeric in the gas phase. Therefore, although dialkylalkoxygallanes incorporating donor functionalised ligands generally adopt dimeric structures in the solid state, in the gas phase monomers are likely to be present. Monomers are expected to exhibit enhanced volatility in comparison to oligomeric complexes in which intermolecular solid-state interactions are likely to increase the

enthalpy of vaporisation. However, this work shows that the structure adopted in the solid state may differ from that in the gas phase and so compounds that appear unsuitable for CVD may in fact be feasible precursors. Overall, this study has provided information that can be used to aid the design of precursor molecules for a range of technologically important materials.

3.4. Experimental

3.4.1. General procedures

All manipulations were performed under a dry, oxygen-free dinitrogen atmosphere using standard Schlenk techniques or in an Mbraun glovebox. All solvents used were stored in alumina columns and dried with anhydrous engineering equipment, such as that the water concentration was 5 – 10 ppm. Chemicals were supplied by Multivalent or procured commercially from Aldrich and used without further purification, with the exception of alcohols which were further distilled and degassed and stored over molecular sieves. Analytical data were obtained at UCL. All ^1H and $^{13}\text{C}\{^1\text{H}\}$ NMR spectra were obtained on a Bruker AMX400 spectrometer, operating at 400.12 MHz. All spectra were recorded using C_6D_6 which was distilled over NaK/benzophenone and CDCl_3 which was dried and degassed over molecular sieves prior to use; ^1H and ^{13}C chemical shifts are reported relative to SiMe_4 (δ 0.00). All IR spectra were recorded using a Shimadzu FTIR-8200 spectrometer, operating in the region of 4000-400 cm^{-1} . The IR samples were prepared using Nujol. The mass spectra were obtained using a Micromass 70-SE spectrometer using Chemical Ionization (CI) with a methane carrier gas.

3.4.2. Physical Measurements

All ^1H and ^{13}C NMR spectra were obtained on a Bruker AMX300 and AMX400 spectrometer, operating at 299.87 MHz and 400.12 MHz respectively. All spectra were recorded using C_6D_6 and CD_2Cl_2 which were dried and degassed over molecular sieves prior to use; ^1H and ^{13}C chemical shifts are reported relative to SiMe_4 (δ 0.00). All IR spectra were recorded using a Shimadzu FTIR-8200 spectrometer, operating in the region of 4000-400 cm^{-1} . The IR samples were prepared using nujol. The mass spectra

were obtained using a Micromass 70-SE spectrometer using Chemical Ionisation (CI) with methane reagent gas. The Elemental Analysis (elemental analysis) was carried using Elemental Analyser (CE-440) (Exeter Analytical Inc). The instrument used for thermal analysis was the Netzsch Jupiter.

3.4.3. Synthesis of compounds

3.4.3.1. Synthesis of $[\text{Me}_2\text{Ga}(\text{OCH}_2\text{CH}_2\text{NMe}_2)]_2$ (30)

2-Dimethylaminoethanol (0.68 cm^3 , 6.73 mmol) was added dropwise to a solution of trimethyl gallium (0.7261 g, 6.37 mmol) in toluene (20 cm^3) at $-78 \text{ }^\circ\text{C}$, the reaction mixture was allowed to warm slowly to room temperature and stirred for a further 24 h. Removal of the solvent *in vacuo* afforded a colourless oil. The reaction flask was left at room temperature and X-ray quality crystals were obtained after several days (2.40 g, yield 82%). Anal. Calc. for $\text{C}_6\text{H}_{18}\text{NOGa}$: C, 38.5; H, 9.63; N, 7.48. Found: C, 38.38; H, 9.32; N, 7.13. ^1H NMR δ/ppm (C_6D_6): 0.20 (m, GaCH_3 , 6H), 1.98 (s, NCH_3 , 6H), 2.01 (t, $\text{OCH}_2\text{CH}_2\text{N}$, 2H), 3.49 (t, $\text{OCH}_2\text{CH}_2\text{N}$, 2H). $^{13}\text{C}\{^1\text{H}\}$ NMR δ/ppm (C_6D_6): 5.2 (GaCH_3), 45.2 (NCH_3), 59.1 ($\text{OCH}_2\text{CH}_2\text{N}$), 61.7 (OCH_2). IR (cm^{-1}): 2924 vs, 2789 w, 2719 w, 2700 w, 1666 s, 1420 m, 1356 m, 1273 s, 1233 w, 1187 m, 1165 w, 1036 m, 1000 m, 954 m, 932 m, 894 m, 786 m, 629 m, 552 m, 504 m, 430 m. Mass spec. (CI): (m/z) 374 ([M]), 359 ([M]–Me), 286 ([M]–($\text{OCH}_2\text{CH}_2\text{NMe}_2$)), 172 ($\text{MeGa}(\text{OCH}_2\text{CH}_2\text{NMe}_2)$), 99 (Me_2Ga).

3.4.3.2. Synthesis of $[\text{Me}_2\text{Ga}(\text{OCH}_2\text{CH}_2\text{OMe})]_2$ (31)

2-Methoxyethanol (0.51 cm^3 , 6.37 mmol), was added dropwise to a solution of trimethyl gallium (0.7230 g, 6.37 mmol) in toluene (20 cm^3) at $-78 \text{ }^\circ\text{C}$, the reaction mixture was allowed to warm slowly to room temperature and stirred for a further 24 h. Removal of the solvent *in vacuo* afforded a white free flowing powder (0.9201 g, yield 83%). Anal. Calc. for $\text{C}_{10}\text{H}_{26}\text{O}_4\text{Ga}_2$: C, 34.48; H, 7.47; N, 0.00 (%). Found: C, 34.21; H, 7.01; N 0.00 (%). ^1H NMR δ/ppm (C_6D_6): 0.21 (m, GaCH_3 , 6H), 2.89 (s, OCH_3 , 3H), 3.44 (t, $\text{OCH}_2\text{CH}_2\text{OCH}_3$, 2H), 3.79 (t, $\text{OCH}_2\text{CH}_2\text{OCH}_3$, 2H). $^{13}\text{C}\{^1\text{H}\}$ NMR δ/ppm (C_6D_6): 5.1 (GaCH_3), 59.1 (OCH_3), 62.91 ($\text{OCH}_2\text{CH}_2\text{OCH}_3$), 72.8 ($\text{OCH}_2\text{CH}_2\text{OCH}_3$). IR (cm^{-1}): 2935 s, 2865 m, 2726 m, 2373 m, 2152 m, 2046 m, 1975 m, 1568 s, 1456 s, 1418 m, 1394 m, 1362 m, 1261 s, 1237 s, 1198 s, 1127 s, 1081 s, 1025 s, 960 s, 908 s, 849 s, 801 vs, 654 vs. Mass spec. (CI): (m/z) 348 [M], 273 [M] – $\text{OCH}_2\text{CH}_2\text{OMe}$, 174 [M] – $\text{Me}_2\text{Ga}(\text{OCH}_2\text{CH}_2\text{OMe})$, 99 (Me_2Ga).

3.4.3.3. Synthesis of [Me₂Ga(O^tBu)]₂ (**32**)

Tertiary butanol (0.83 cm³, 8.77 mmol) was added dropwise to a solution of trimethyl gallium (1.0293 g, 8.77 mmol) in toluene (30 cm³) at -78°C. This was allowed to warm to room temperature, with stirring and stirred for 24 h. The solvent was reduced (*ca.* 20 cm³) *in vacuo* and the flask cooled overnight at 5°C, the precipitate was collected as a white solid (1.445 g, 95.8 % yield). Anal. Calc. for C₁₂H₃₀O₂Ga₂: C, 41.86; H, 8.72; N, 0.00 (%). Found: C, 41.56; H, 8.31; N 0.00 (%). ¹H NMR δ/ppm (C₆D₆): 1.12 (s, C(CH₃)₃, 9H), 0.01 (s, GaCH₃, 6H). ¹³C{¹H} NMR δ/ppm (C₆D₆): 73.0 (C(CH₃)₃), 32.3 (C(CH₃)₃), -1.35 (GaCH₃). Mass spec. (CI): (*m/z*) 344 [M], 287 [M] – C(CH₃)₃, 215 [M] – (CH₃)₃ – Me, 172 ½ [M], 157 [MeGaO^tBu], 84 MeGa, 57 [C(CH₃)₃].

3.4.4. GED experimental

All *ab initio* and DFT calculations were performed by Dr. Derek Wann at Edinburgh University.

3.4.4.1. Quantum chemical studies

All calculations were carried out using the resources provided by the NSCCS⁵⁹ running the Gaussian 03 suite of programs. Quantum chemical calculations were undertaken for both monomer and dimer species. It was anticipated that several possible conformers of each structure might exist. For the dimeric structures **30** and **31**, calculations for both C₂ and C_i point-group symmetries were performed. For each of the monomer structures **30a** and **31a**, scans of the potential energy were performed by rotating about the Ga(1)O(4)C(5)C(6) and O(4)C(5)C(6)N/O(7) dihedral angles. For both **30a** and **31a** only one minimum was identified, with the structure and atom numbering shown in Figure 1. For **32** geometry optimisation were started with the dimeric structure having C_s, C_i, C_{2h} and D_{2h} symmetries. The C_{2h} structure, which was the only potential minimum to be found.

For each of the molecules studied geometry optimisations were performed at the Hartree-Fock level with the 3-21G* basis set^{53,54} on all atoms followed by the 6-31G* basis set.⁵⁵ Frequency calculations were also performed at this level to ensure that the calculated structures represented minima on the potential-energy surface. Optimisations were then performed using MP2 theory⁴¹ to account for electron correlation. These MP2

calculations included all electrons in the valence shell and were carried out using the 6-311+G* basis set on all atoms.⁶⁰

The program SHRINK⁶¹ was used with harmonic force constants calculated at the B3LYP/6-311+G* level to produce a set of starting values for amplitudes of vibration and curvilinear distance corrections for use in each of the GED refinement undertaken.

Data were collected from samples of **30–32**, using the Edinburgh gas electron diffraction (GED) apparatus,⁶² using an accelerating voltage of 40 kV, resulting in an electron wavelength of approximately 6.0 pm. It is normal practice to record the scattering intensities on Kodak Electron Image films at two different nozzle-to-film distances to maximise the scattering angle through which data were collected. For **30** and **32** this was possible, but for **31** the increase in temperature that was required to volatilise the sample for the shorter nozzle-to-film distance caused the sample to degrade. For this reason only data collected at the longer nozzle-to-film distance are used.

The data collected for samples of each of **30–32** were scanned using an Epson Expression 1680 Pro flatbed scanner as described elsewhere.²⁹ The data-reduction processes and the least-squares refinements were carried out using the ed@ed v3.0 program⁴³ with the scattering factors of Ross *et al.*

3.4.4.2. Gas-phase electron diffraction

Data were collected for (**30–32**) using the Edinburgh gas-phase electron diffraction apparatus. An accelerating voltage of around 40 kV was used, representing an electron wavelength of approximately 6.0 pm. Scattering intensities were recorded on Kodak Electron Image films at nozzle-to-film distances of 94.89, 259.65 and 293.46 mm for (**30 – 32**). In both cases for all three sets of scattering intensity data were recorded with sample and nozzle temperatures held at 393 K.

The weighting points for the off-diagonal weight matrices, correlation parameters and scale factors for all camera distances for (**30–32**) are given in Table 1. Also included are the exact electron wavelengths as determined from the scattering patterns for benzene, which were recorded immediately after the patterns for the sample compounds. The

scattering intensities were measured using an Epson Expression 1600 Pro flatbed scanner and converted to mean optical densities as a function of the scattering variable, s . The data reduction and the least-squares refinement processes were carried out using the ed@ed program employing the scattering factors of Ross *et al.*

Table 3.4. Nozzle-to-film distances (mm), weighting functions (nm^{-1}), scale factors, correlation parameters and electron wavelengths (pm) used in the electron diffraction studies of (30–32).

	(30–32)	
Nozzle-to-film distance a	94.89	293.46
s	2	2
s_{min}	80	20
sw_1	100	40
sw_2	292	104
s_{max}	320	120
Scale factor b	0.798(22)	0.736(6)
Correlation parameter	0.444	0.436
Electron wavelength	6.020	6.020

a Determined by reference to the scattering pattern of benzene. b Values in parentheses are the estimated standard deviations.

3.5. References

1. A. C. Jones, *Chem. Soc. Rev.*, 1997, **26**, 101.
2. S. Basharat, C. J. Carmalt, *Elsevier Science Ltd.*, 20071.
3. D. Vernardou, M. E. Pemble, D. W. Sheel, *Thin Solid Films*, 2008, **516**, 4502.
4. R. J. Holdsworth, P. A. Martin, D. Raisbeck, J. Rivero, H. E. Sanders, D. Sheel, M. E. Pemble, *Chem. Vap. Deposition*, 2001, **7**, 39.
5. J. C. Michael, J. W. Peter, O. D. Hywel, C. J. Anthony, J. L. Timothy, O. B. Paul, W. C. Gary, *Chem. Vap. Deposition*, 1999, **5**, 9.
6. K. G. Caulton, L. G. Hubert-Pfalzgraf, *Chem. Rev.* , 2002, **90**, 969.
7. D. C. Bradley, *Polyhedron*, 1994, **13**, 1111.
8. R. C. Mehrotra, A. Singh, S. Sogani, *Chem. Rev.* , 2002, **94**, 1643.
9. C. D. Chandler, C. Roger, M. J. Hampden-Smith, *Chem. Rev.* , 2002, **93**, 1205.
10. M. Veith, S. Mathur, C. Mathur, *Polyhedron*, 1998, **17**, 1005.
11. S. Basharat, C. J. Carmalt, R. Binions, R. Palgrave, I. P. Parkin, *Dalton Trans.*, 2008591.
12. C. J. Carmalt, S. J. King, *Coord. Chem. Rev.*, 2006, **250**, 682.
13. S. Basharat, C. E. Knapp, C. J. Carmalt, S. A. Barnett, D. A. Tocher, *N. J. Chem.*, 2008, **32**, 1513.
14. S. Basharat, W. Betchley, C. J. Carmalt, S. Barnett, D. A. Tocher, H. O. Davies, *Organometallics*, 2007, **26**, 403.
15. S. Basharat, C. J. Carmalt, S. J. King, E. S. Peters, D. A. Tocher, *Dalton Trans.*, 20043475.
16. S. Basharat, C. J. Carmalt, R. Palgrave, S. A. Barnett, D. A. Tocher, H. O. Davies, *J. Organomet. Chem.*, 2008, **693**, 1787.
17. S. Basharat, C. J. Carmalt, S. A. Barnett, D. A. Tocher, H. O. Davies, *Inorg. Chem.*, 2007, **46**, 9473.
18. R. Binions, C. J. Carmalt, I. P. Parkin, K. F. E. Pratt, G. A. Shaw, *Chem. Mater.*, 2004, **16**, 2489.
19. R. Binions, C. J. Carmalt, I. P. Parkin, *Meas. Sci. Technol.*, 2007, **18**, 190.
20. L. G. Hubert-Pfalzgraf, *Coord. Chem. Rev.*, 1998, **178-180**, 967.
21. T. Young, *Philos. T. Roy. Soc.* , 1802, **92**, 12.
22. L. d. Broglie, *Philos. Mag. Ser. 6*, 1924, **47**, 446

23. C. Davisson, L. H. Germer, *Nature*, 1927, **119**, 558.
24. G. P. Thompson, *Nature*, 1927, **120**, 802.
25. H. Mark, R. Wierl, *Z. Elektrochem.*, 1930, **36**, 675.
26. D. Wann, *Ph.D Thesis*, 2005University of Edinburgh.
27. P. Debye, *Phys. Z.*, 1939, **40**, 404.
28. J. Tremmel, I. Hargittai, *VCH*, 1988.
29. H. Fleischer, D. A. Wann, S. L. Hinchley, K. B. Borisenko, J. R. Lewis, R. J. Mawhorter, H. E. Robertson, D. W. H. Rankin, *Dalton Trans.*, 20053221.
30. R. Glauber, V. Schomaker, *Phys. Rev.*, 1953, **89**, 667.
31. B. F. Johnston, *Ph.D Thesis*, 2002University of Edinburgh.
32. J. T. Schirlin, *Ph.D. Thesis*, 2004University of Edinburgh.
33. O. Bastiansen, M. Traetteberg, *Acta Crystallogr.*, 1960, **13**, 1108.
34. M. F. John, *J. Chem. Phys.*, 1962, **36**, 1106.
35. R. Stølevik, H. M. Seip, S. J. Cyvin, *Chem. Phys. Lett.*, 1972, **15**, 263.
36. V. A. Sipachev, *J. Mol. Struc.*, 1985, **121**, 143.
37. M. Born, J. R. Oppenheimer, *Ann. Phys. (Berlin)*, 1927, **84**, 457.
38. W. Kolos, L. Wolniewicz, *J. Chem. Phys.*, 1964, **41**, 3663.
39. B. T. Sutcliffe, *Adv. Quantum. Chem.*, 1997, **28**, 65.
40. N. C. Handy, A. M. Lee, *J. Chem. Phys.*, 1996, **252**, 425.
41. C. Moller, M. S. Plesset, *Phys. Rev.*, 1934, **46**, 618.
42. P. Hohenburg, W. Kohn, *Phys. Rev. Sect. B*, 1964, **136**, 864.
43. S. L. Hinchley, H. E. Robertson, K. B. Borisenko, A. R. Turner, B. F. Johnston, D. W. H. Rankin, M. Ahmadian, J. N. Jones, A. H. Cowley, *Dalton Trans.*, 20042469.
44. M. W. Anderson, G. K. Logothetis, M. E. Pemble, A. G. Taylor, N. C. Wallace, H. M. Yates, *Advan. Mater. Optics Electronics*, 1993, **2**, 313.
45. B. J. Gould, I. M. Povey, M. E. Pemble, W. R. Flavell, *J. Mater. Chem.*, 1994, **4**, 1815.
46. M. J. Davis, M. E. Pemble, *J. Phys.-Paris IV*, 1999, **9**, 49.
47. D. Vemardou, M. E. Pemble, D. W. Sheel, *Thin Solid Films*, 2007, **515**, 8768.
48. T. Nakajima, T. Tanaka, K. Yamashita, *Surf. Sci.*, 2000, **444**, 99.
49. S. J. Rettig, A. Storr, J. Trotter, *Can. J. Chem.*, 1975, **53**, 58.
50. H. Schumann, M. Frick, B. Heymer, F. Girgsdies, *J. Organomet. Chem.*, 1996, **512**, 117.

51. S. L. Hinchley, M. F. Haddow, D. W. H. Rankin, *Dalton Trans.*, 2004384.
52. Y. Chi, T. Y. Chou, Y. J. Wang, S. F. Huang, A. J. Carty, L. Scoles, K. A. Udachin, S. M. Peng, G. H. Lee, *Organometallics*, 2004, **23**, 95.
53. J. S. Binkley, J. A. Pope, W. J. Hehre, *J. Am. Chem. Soc.*, 1980, **102**, 939.
54. M. S. Gordon, J. S. Binkley, J. A. Pople, W. J. Pietro, W. J. Hehre, *J. Am. Chem. Soc.*, 1982, **104**, 2797.
55. W. J. Hehre, R. Ditchfield, J. A. Pople, *J. Chem. Phys.*, 1972, **56**, 2257.
56. H. Schumann, M. Frick, B. Heymer, F. Girgsdies, *J. Organomet. Chem.*, 1996, **512**, 117.
57. M. B. Power, W. M. Cleaver, A. W. Apblett, A. R. Barron, J. W. Ziller, *Polyhedron*, 1992, **11**, 477.
58. M. Veith, S. Faber, H. Wolfanger, V. Huch, *Chem. Berichte*, 1996, **129**, 381.
59. *National Service for Computational Chemistry Software (NSCCS)*. [cited; Available from: <http://www.nscs.ac.uk>].
60. R. Krishnan, J. S. Binkley, R. Seeger, J. A. Pople, *J. Chem. Phys.*, 1980, **72**, 650.
61. V. A. Sipachev, *J. Mol. Struct.*, 2001, **567-568**, 67.
62. C. M. Huntley, G. S. Laurenson, D. W. H. Rankin, *J. Chem. Soc., Dalton Trans.*, 1980954.

Chapter 4

Chemical Vapour Deposition of Metal Oxide Thin Films

4.1. Introduction

This chapter examines the aerosol assisted chemical vapour deposition (AACVD) of gallium oxide thin films using *in situ* methods incorporating precursors discussed in Chapter 2. Additionally the synthesis of indium gallium oxide and gallium zinc oxide thin films, using a variety of precursors is described. Chapter 3 described a study into the gas phase structures of CVD precursors, and this knowledge was used to optimise the AACVD variables leading to the final aim; deposition of thin films of group 13 oxide materials.

4.1.1. Chemical Vapour Deposition

A CVD process goes through a chemical reaction, which can consist of pyrolysis, oxidation, reduction and hydrolysis. Consequently, the reaction's thermodynamic and kinetic properties are driven by physical parameters. Therefore, temperature, pressure, reactant gas concentration and flow rate in the chamber have to be precisely set.

The principal difference between AACVD and other CVD techniques is the use of a liquid aerosol to transport the precursor to the substrate. This has the important effect of changing the precursor requirements: volatility is not necessary for AACVD precursors, meaning that precursors usually deemed unsuitable for conventional CVD, can be utilised and result in useful films with desirable properties.

In AACVD, the precursor can either be dissolved in a solvent, from which an aerosol is formed, or the precursor can be a liquid. Providing a compound can be dissolved in a suitable solvent there is no need to rely on the evaporation of the precursor, as is typical with other types of CVD, including atmospheric pressure CVD (APCVD) and the previously mentioned LPCVD. An aerosol can be generated from a solution or liquid precursor by ultrasonic atomisation as previously discussed in Chapter 1. Lifting the requirement for volatility opens up a large range of precursors for use in CVD that would otherwise be unsuitable. It is sometimes stated that in AACVD evaporation of the solvent occurs before chemical reaction of the dissolved precursors,¹ although it appears that no direct evidence of this has been reported. Certainly the evaporation to dryness of aerosol droplets occurs very rapidly. Their high surface area and the high temperatures found within the CVD reactor mean that droplet lifetimes can be of the order of milliseconds.²

Once in solution, the AACVD technique creates an aerosol mist of the precursor solution and so it can be transported through to the reaction chamber using a suitable carrier gas, upon entering the reactor the solvent evaporates in the high temperatures and the precursor is left in the gas phase to react, adsorb, nucleate and grow into the desired thin film.

AACVD is a cost effective process, the humidifier removes the need for high vacuums or temperatures which are used in conventional bubbler or vapourisation methods. Additionally, because the system is solution based, it follows that *in situ* reactions are possible, so that reactants can be mixed together before they enter the reactor without decomposition occurring. This eliminates the need for several starting 'pots' containing many volatile precursors and why the technique has come to be known as the 'one pot' approach.

4.1.2. Gallium indium oxide

It is often the case that the material used as the anode in OLED screen and other such technologies is a thin layer of indium tin oxide (ITO) or fluorinated tin oxide (FTO). There are a large number of other transparent conducting oxides known, for example tin oxide, indium oxide, zinc oxide and various combinations of these materials. However their properties, including low resistivity, good transparency, availability and also the ease with which it can be patterned are over shadowed in comparison to the performance of ITO.

Recently, multicomponent ternary and quaternary oxide wide band gap semiconductors have taken centre stage as new materials for transparent conducting films and as materials for thin film transistor (TFT) channel layers. The aforementioned transparent conducting oxides (TCOs), most notably ITO are largely used in photovoltaic technologies as well as being components of display technologies.³

Despite its extensive use, little is known about the chemical properties for use in LEDs. ITO has a large work function (4–5 eV) but in most polymers the highest occupied molecular orbital (HOMO) lies more than 5 eV below vacuum, suggesting that a transport organic layer be used to overcome this energy barrier. A solution to this problem, in terms of device lifetime polymer LEDs, incorporation of oxygen plasma treated anodes to give the best performance.⁴

The interest in TCOs over the past two decades has soared, partially due to their application in optoelectronic devices in photovoltaics, solar cells, optical waveguides, energy efficient windows and use in FPDs and OLED screens. TCO properties can be assigned to the basic relationships between their transparency, structure and composition and the atomic arrangements of the metal cations in both crystalline and amorphous oxide structures. There is a large amount of literature already developed on these properties, and how to improve on these to yield more efficient and effective TCO materials.

Reviews on TCOs cover a range of areas, including processing approaches and their electronic conductivity of these metal oxide systems, on the microscopic level. The

design of TCO materials with superior properties has, until recently not been largely explored when taking into account application of more rigorous scientific approaches.⁵⁻¹⁰ A recent review highlights new techniques for improving transmissivity in TCO's and similar conducting oxides *via* impedance matching and quantum mechanical tunnelling.¹¹

With a view to improve TCO film electrical, optical and chemical properties a number of studies have focused on combinations of In, Sn, Zn and Ga. Gallium indium oxide is the reported parent phase of a promising new TCO family.¹² An additional advantage gallium indium oxide has over ITO is its improved transmission in the blue-green region of the electromagnetic spectrum.¹³

There are few reports in the literature of the synthesis of phase pure gallium indium oxide¹⁴, and even less for the production of thin films of these materials. Solid solutions based on XRD data of $\text{In}_{2x}\text{Ga}_{2-2x}\text{O}_3$, where $x \leq 0.43$ results in indium substitution into the $\beta\text{-Ga}_2\text{O}_3$ lattice and $x \geq 0.95$ results in gallium substitution into the cubic In_2O_3 lattice. Any other In:Ga ratios have resulted in the presence of mixed phases.¹⁵ In an earlier study thin films of $\text{In}_x\text{Ga}_{2-x}\text{O}_3$ were reported to be amorphous, only adopting the $\beta\text{-Ga}_2\text{O}_3$ crystal structure. In this instance thin films were prepared by dc magnetron sputtering.¹⁶

More recently a study of the charge transport and transparency of heteroepitaxial metalorganic chemical vapour deposited gallium indium oxide films has been published.¹² It was shown here that the optical transmission window of these films were considerably broader than that of ITO, and the absolute transparency rival or exceeds that of the most transparent conductive oxides.

The use of AACVD processes is beneficial for a number of reasons including, simple *in situ* growth of highly adherent films, conformal coverage of a variety of substrates with straightforward control of atmospheric and deposition conditions. Here a highly efficient route to these thin film materials is used, using commercially available equipment. To the best of our knowledge, this work represents the first thin film growth of indium gallium oxide, *via* a novel aerosol assisted CVD route to $\text{In}_x\text{Ga}_{2-x}\text{O}_3$ from GaMe_3 , InMe_3 and $\text{HOCH}_2\text{CH}_2\text{OMe}$. Different and unique morphologies of films can

be obtained by AACVD due to the influence of the solvent on the deposition, which could potentially lead to improved properties. Furthermore thin films can be deposited under AACVD conditions at low temperatures and require only minimal amounts of precursor (0.1 g).

4.1.3. Gallium zinc oxide

It is a reasonable assertion that the three best known TCOs are indium tin oxide (ITO), fluorine doped tin oxide ($\text{SnO}_2:\text{F}$), and aluminium doped zinc oxide ($\text{ZnO}:\text{Al}$). However, with the ever increasing demands of technology the search for new TCOs with tailored properties for the specific task required of them is rapid.¹⁷ In recent years a number of excellent TCO alloys have been discovered, including $\text{In}_x\text{Ga}_{2-x}\text{O}_3$,¹³ Cd_2SnO_4 ,¹⁸ and $\text{In}_4\text{Sn}_3\text{O}_{12}$.¹⁹ Gallium–indium alloys have demonstrated excellent transmission in the infrared regime, and ZnGa_2O_4 itself has been identified as a UV-transparent TCO.^{20,21}

At the forefront of TCO research today lies multi-layered TCO film deposition²²⁻²⁵, and deposition of TCO films on flexible substrates.²⁶⁻²⁹ The aims of multi-layered films are to improve transmittance and to lower the resistivity. For deposition on plastic substrates, the key is to lower deposition temperatures, even as low as room temperature for such applications as touch panel, flexible TFT-LCDs and electronic devices.

In optoelectronic applications ITO is the most commonly used TCO exhibiting high transmittance in the visible region and having a resistivity close to $1 \times 10^{-4} \Omega\text{cm}$.^{8,30-32} For a variety of reasons, not least because of the scarcity of indium, ZnO-based materials have recently attracted much interest as a promising alternative to ITO. Zinc oxide is a transparent and wide band gap ($\sim 3.36 \text{ eV}$) semiconducting material that has been extensively studied with application in piezoelectric, pyroelectric and optoelectronic devices, with a high excitation binding energy of $\sim 60 \text{ meV}$.³³⁻³⁵

The intrinsic oxygen defects and Zn interstitials enable good electrical conductivity of ZnO thin films. Non-doped zinc oxide usually presents a high resistivity due to a low carrier concentration. However the conductivity of ZnO can be further improved by doping with several elements such as As, In, Ga, Fe, Sb, Al and Li, with potential

application as ultraviolet lasers, light emitting devices, TCOs and thin film transistors (TFTs).³⁶⁻³⁹

There are reports in the literature of the excellent suitability of gallium as an *n*-type dopant to zinc oxide because of its good lattice match with ZnO lattice; the bond lengths of Ga–O and Zn–O are 1.92 Å and 1.97 Å, respectively.⁴⁰ Also the Ga atom replaces the zinc ions and acts as substitutional impurity, releasing a free electron in the conduction band at room temperature. Gallium- or aluminium-doped ZnO (GZO or AZO) films, as aforementioned, have potential as a transparent electrode to replace ITO thin film for optoelectronic and electronic devices, such as flat panel displays,⁴¹ solar cells⁴² and light emitting diodes,⁴³⁻⁴⁶ as they can be grown as a transparent single crystal thin film and have a wide band gap (3.76 eV).^{47,48} Zinc–gallate thin films phase have been synthesized to date primarily by sputtering,²⁰ laser ablation,^{21,49} and sol–gel techniques.⁵⁰ It is more commonly found that aluminium is used as a dopant in works related to zinc oxide, however aluminium presents a very high reactivity leading to oxidation during film growth, which may become a problem. Gallium is less reactive and more resistant to oxidation compared to aluminium.^{40,51} Recently, it was demonstrated that doping with gallium led to films both with low resistivity and a high transmittance in the visible region.⁵² Several techniques have been used including rf magnetron sputtering, evaporation, magnetron sputtering, sol–gel, plasma assisted molecular beam epitaxy, among others.⁵³ However, most of these techniques need to use moderate temperatures to obtain low values of resistivity.

Upon doping with gallium, the free electron density is increased, as an *n*-type dopant gallium is presumed to replace zinc atoms. Upon introducing a small amount of Ga, it is ionized as a Ga³⁺ and replaces Zn²⁺. The atomic radii of zinc (1.225 Å) and gallium (1.225 Å) are the same and gallium can be easily substituted for zinc without much lattice distortion. The electronegativity of gallium (1.13) and zinc (0.99) are also close as compared to other impurities. So the localization of conduction electrons by gallium is also small. Hence, the carrier concentration initially increases with doping. But at higher Ga concentration, free electron density decreases because increasing dopant atom produces some kind of neutral defects, which do not contribute to conductivity. The mobility is also highest for 2 atomic % doped sample.⁵⁴

Physical vapour deposition (PVD) techniques, such as sputtering⁵⁵ or pulsed laser deposition⁵⁶ are most commonly used to deposit aluminium doped ZnO, and many works are focused on intrinsic zinc oxide for structural applications⁵⁷ and more recently for UV emission.⁵⁸ So as a final motivation for this work, the novel use of AACVD to deposit thin films is utilized, with the use of gallium as a dopant as opposed to aluminium, as there are reports of some of the best conducting zinc oxide films being gallium doped produced by other variants of chemical vapour deposition.^{24,59}

4.2. Results and discussion

Based on TGA data collected in the previous chapter, a selection of precursors developed in Chapter 2 were used in the attempted deposition of group 13 oxide thin films. These experiments were carried out under a range of conditions, however no films were deposited. The lack of film growth can be attributed to the small amount of precursor used (< 0.5g), as a direct result of the low yields in the synthesis of said precursors (Chapter 2). Based on the success of previously reported depositions of thin films of metal oxides, where *in situ* reactions were used,⁶⁰ a variety of reactions were successfully devised and are reported herein.

Routes towards the deposition of thin films of Ga₂O₃, In_xGa_{2-x}O₃ and GaZnO by AACVD were carried out. Films were deposited by an *in situ* reaction of metal alkyl species with excess donor functionalised alcohol, as described in the following sections. It is proposed that reactions in the bubbler cause the synthesis of viable precursors, for use in deposition of the desired binary products. When using this *in situ* route the films were deposited from the reaction mixture, without isolating the product. The precursors were left to react for 30 minutes in all instances, prior to the deposition run.

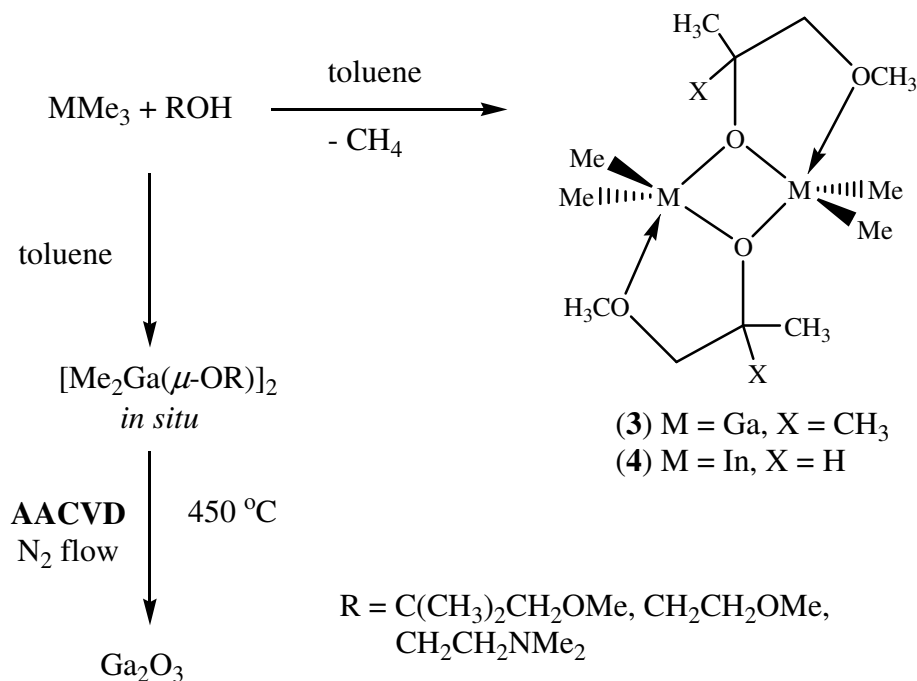
4.2.1. Gallium oxide films

In the AACVD process, the reaction between the reagents GaMe₃ and ROH takes place *in situ* and an excess of alcohol is used to ensure the resulting metal oxide film is not oxygen deficient.⁶¹⁻⁶³ It has been previously reported that the use of diorganoalkoxogallanes as precursors in LPCVD results in oxygen deficient gallium oxide thin films on glass.^{61,63} In order to better understand the *in situ* reactions taking

place in the AACVD bubbler, the reaction of GaMe_3 with excess ROH has been studied *via* a solution-based reflux and the resulting compounds analyzed as already discussed in Chapter 2 (Scheme 4.1).

Brown coloured films were deposited on glass from the AACVD reaction of GaMe_3 and ROH ($\text{R} = \text{CH}_2\text{CH}_2\text{NMe}_2$, $\text{C}(\text{CH}_3)_2\text{CH}_2\text{OMe}$, $\text{CH}_2\text{CH}_2\text{OMe}$) at $450\text{ }^\circ\text{C}$ (Scheme 4.1). The reaction of GaMe_3 and excess ROH in toluene was assumed to generate *in situ* diorganoalkoxogallanes, such as $[\text{Me}_2\text{Ga}(\mu\text{-OR})_2]$, similar to compounds **3** and **4** discussed in Chapter 2. Deposition was observed on both the top plate and the substrate, which is consistent with the precursor decomposing on the substrate and the reactive species desorbing from the surface. During the reaction the top plate was measured to be $50\text{--}75\text{ }^\circ\text{C}$ lower in temperature than the substrate. The films deposited were uniform and covered the substrate completely. The films were adherent to the substrate, passing the Scotch tape test but readily scratched by a brass or stainless steel stylus. The gallium oxide films were characterized using a range of techniques as described below.

Scheme 4.1: Proposed route to gallium oxide thin films.



4.2.1.1. Energy dispersive X-ray analysis

The composition of the film was determined by energy dispersive X-ray analysis (EDXA) measurements. EDXA confirmed the presence of gallium, oxygen and carbon, however breakthrough to the underlying glass substrate was observed, so gallium to oxygen ratios could not be deduced.

4.2.1.2. Wavelength dispersive X-ray analysis

The composition of the film was further determined by wavelength dispersive analysis of X-rays (WDX) measurements. WDX analysis showed the as-deposited films had a Ga : O ratio close to the expected 1 : 1.5 for Ga₂O₃. Deviations from the Ga₂O₃ stoichiometry occurred (1 : 1.3) with the formation of thinner films, which resulted in breakthrough to the underlying glass inhibiting accurate compositional analysis.

4.2.1.3. Scanning electron microscopy

The film morphology was studied using SEM, which indicated that deposition occurred *via* an island growth mechanism with particles of size *ca.* 1 μm in diameter (Fig. 4.1).

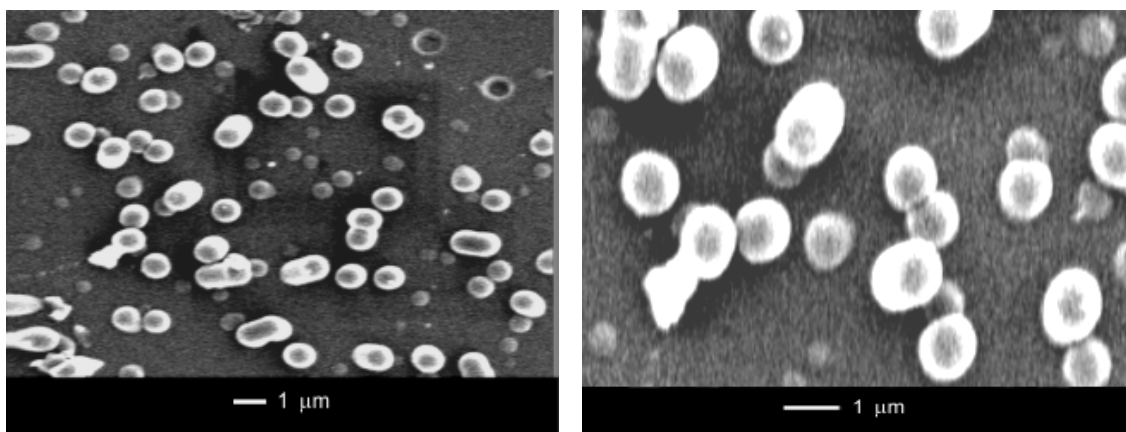


Fig 4.1: SEM images the film produced from the AACVD of GaMe₃ and HOCH₂CH₂OMe at 450 °C in toluene.

4.2.1.4. X-ray Photoelectron Spectroscopy

The XPS of the Ga 2p peaks of a film deposited at 450°C *via* the *in situ* route using GaMe₃ and excess HOCH₂CH₂NMe₂ shows one distinct gallium environment at the surface (Fig. 4.2). The peaks at 1115.102 and 1140.957 eV correspond to the Ga 2p_{3/2}

and $2p_{1/2}$ peaks of Ga_2O_3 , respectively and are in a 1:2 ratio with each other, which fit with peaks previously reported.

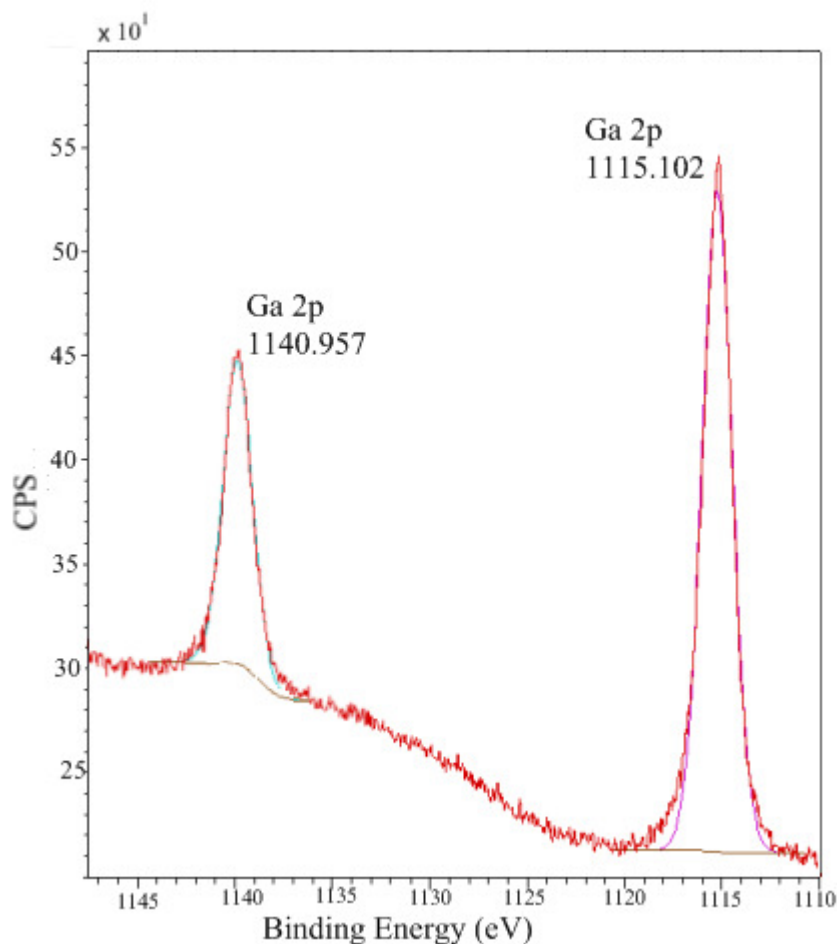


Fig 4.2: XPS of Ga 2p peaks for a film deposited at 450°C by AACVD from the *in situ* reaction of GaMe_3 and excess $\text{HOCH}_2\text{CH}_2\text{NMe}_2$ in toluene.

X-ray photoelectron spectroscopy (XPS) of selected gallium oxide films show binding energy shifts of 1115.102 eV for Ga $2p_{3/2}$ and 530.511 eV for O 1s. These values are in close agreement with binding energy shifts for Ga_2O_3 previously reported from XPS of 1116.9 eV for Ga $2p_{3/2}$ and 529.8 – 531.3 eV for O 1s.^{63,64} No evidence for nitrogen (for films grown from $\text{HOCH}_2\text{CH}_2\text{NMe}_2$) contamination was seen to the detection limits of the instrument, however some surface contamination from carbon was observed.

4.2.1.5. X-ray Powder Diffraction

The films deposited by AACVD were amorphous to X-rays at all deposition temperatures. This is an effect of the low deposition temperatures used. X-ray

diffraction patterns for the films indicated that they were amorphous, as expected for the deposition of gallium oxide at these temperatures (< 700 °C).⁶⁴

4.2.1.6. Summary

The successful formation of Ga₂O₃ thin films from the *in situ* AACVD reaction of GaMe₃ and ROH indicates that there is no need to prepare, isolate and purify a single-source precursor. This has been shown previously for AACVD reactions of GaEt₃ and ROH to afford films of Ga₂O₃ and the AACVD of InMe₃ and ROH resulting in the formation of films of In₂O₃ (R = donor functionalized ligand).⁶⁰⁻⁶²

4.2.2. Gallium indium oxide films

The AACVD reaction of GaMe₃, InMe₃ and the donor functionalised alcohol HOCH₂CH₂OMe on glass and quartz substrates was studied at 350–450 °C. For each system, deposition was observed on both the substrate and top plate.

At all deposition temperatures the films showed excellent film coverage, were transparent with a slightly brown tinge and were strongly adherent (passed scotch tape test but were scratched off with a steel stylus) although thermoforetic effects were observed at higher temperatures (> 450 °C), indicated by delamination at the front of the reactor on the substrate. Films are insoluble in common organic solvents, and were quickly decomposed in nitric acid. Films of uniform thickness were grown across the full length of the substrate. EDXA and WDX results show that in all cases, all areas of the films had the same composition.

Four-point probe measurements suggest that the films are conductive at room temperature.

Table 4.1: Deposition conditions and analysis of the films grown from the AACVD of GaMe₃, InMe₃ and ROH (R = CH₂CH₂OMe) in toluene.

Precursors	<i>T</i> [°C]	<i>T</i> annealed [°C]	EDXA	WDX
GaMe ₃ , InMe ₃ , ROH	350	-	InGa _{1.33}	In _{0.77} Ga _{1.23} O _{2.44}
GaMe ₃ , InMe ₃ , ROH	350	550	InGa _{1.04}	In _{0.98} Ga _{1.02} O _{2.87}
GaMe ₃ , InMe ₃ , ROH	400	550	InGa _{0.82}	-
GaMe ₃ , InMe ₃ , ROH	450	1000	InGa _{0.55}	In _{1.4} Ga _{0.58} O _{3.42}
GaMe ₃ , InMe ₃ , ROH	450	1000	InGa _{0.44}	In _{1.39} Ga _{0.61} O _{0.12}

4.2.2.1. Energy dispersive X-ray analysis

EDXA confirmed the presence of gallium, indium and oxygen, in the thin films produced, however breakthrough to the underlying glass substrate was observed, so metal to oxygen ratios could not be deduced. No carbon was detected in EDXA experiments so carbon contamination levels as a direct result of the precursors used are suitably low (< 5%).

Films deposited at 400 °C showed the best coverage of the substrate, with a complete conformal coating. Table 4.1 shows the deposition conditions and analysis of the films grown. Films grown at 400 °C and annealed at 550 °C were too thin to analyse by WDX, breakthrough to the substrate silica was seen so no metal to oxygen (M : O) ratio could be obtained and so no compositional formula. However, from EDXA the metal to metal (M : M) ratio was shown to be 1 : 0.82, which is comparable to the M : M ratios in films deposited at different temperatures.

4.2.2.2. Wavelength dispersive X-ray analysis

The composition of the films was further determined by WDX measurements. WDX analysis showed the as-deposited films had a M : O ratio close to the expected 1 : 1.5 for Ga₂O₃. Deviations from the Ga₂O₃ stoichiometry occurred (1 : 1.7) with the formation of thinner films, which resulted in breakthrough to the underlying glass inhibiting accurate compositional analysis.

The thin films deposited on quartz at 450°C and annealed at 1000°C have the same composition ($\text{In}_{1.4}\text{Ga}_{0.6}\text{O}_{3.1}$). It would seem that the films before annealing have varied composition, although the M : O ratio does not vary far from 1:1.5, making it likely that a mixed phase of gallium oxide and indium oxide was not formed, but more likely a strained indium gallium oxide framework. Annealing at 1000°C in air seems to stabilize the framework as well as crystallise the films.

4.2.2.3. Scanning electron microscopy

The film morphology was studied using SEM, which indicated that deposition occurred *via* an island growth mechanism (Fig. 4.3–4.4). After annealing at 1000 °C overnight, crystallite regions are observed of size *ca.* 200 nm in diameter (Fig. 4.5). Interestingly films that were annealed for 1 hour at 1000°C showed a morphology somewhere between amorphous and crystalline, exhibiting sharpened edges with no distinct crystallite regions (Fig. 4.6).

Pre-annealed films had a brown tint, a direct result of carbon contamination in the films. Films were amorphous pre-anneal (Fig. 4.3–4.4), meaning composition could not be determined by XRD. Films were annealed at temperatures as low as 550 °C, and this step helped to remove any excess carbon (EDXA analysis shows films contained less than 5% carbon after annealing). As expected these lower temperature anneals did not crystallise the films, analogous Ga_2O_3 films are not crystalline until after 650 °C and so higher temperatures were needed to crystallise the films for XRD analysis.

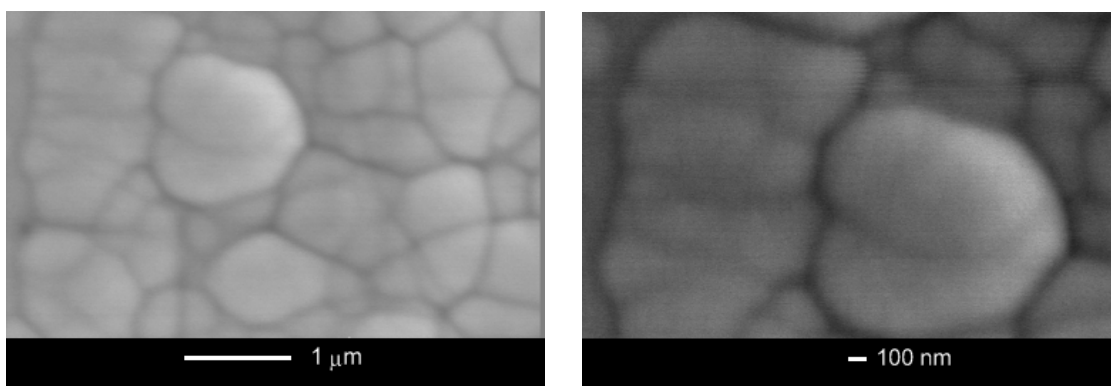


Fig. 4.3: SEM images of InGaO film on glass, deposition carried out at 350°C, before annealing.

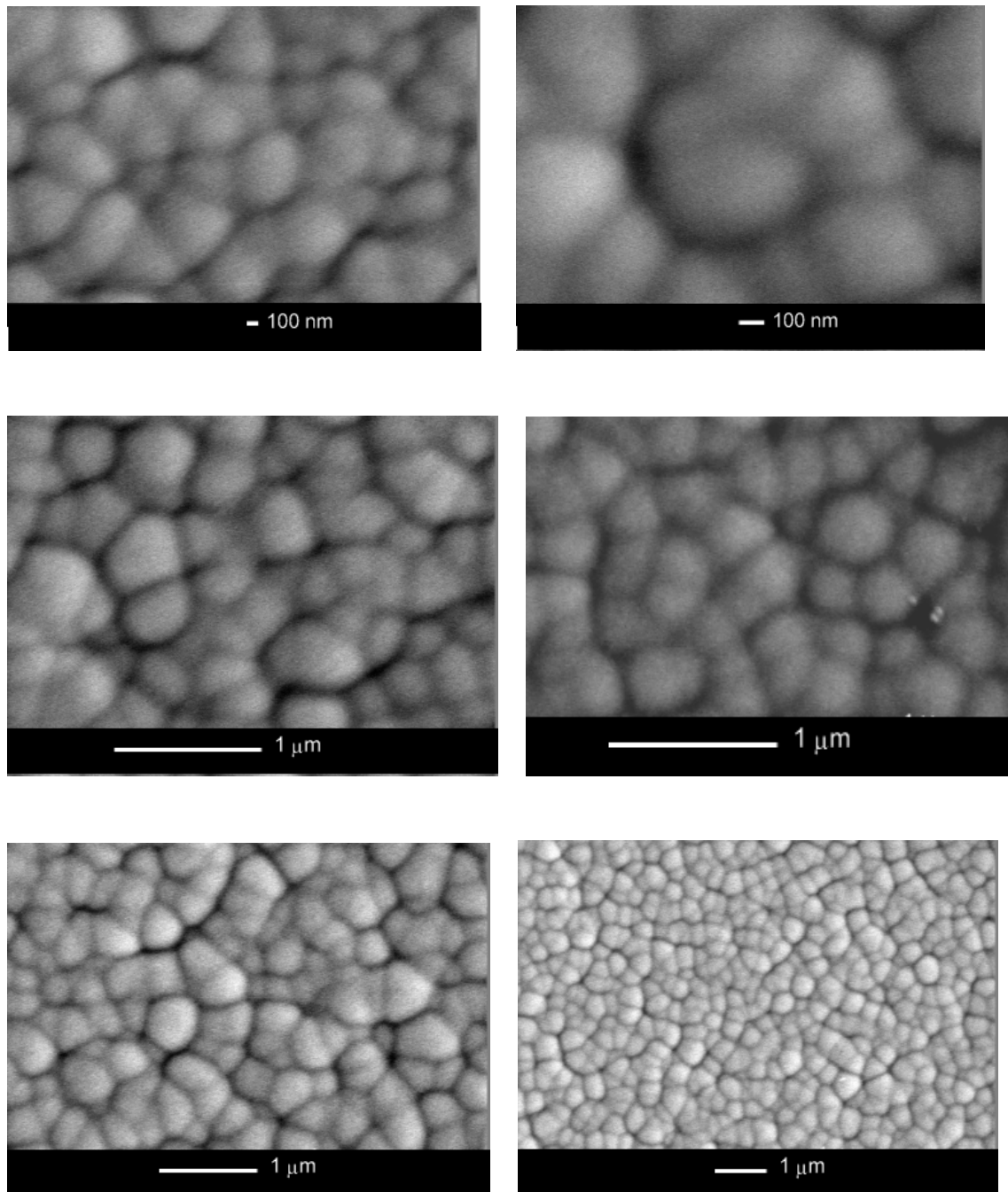


Fig 4.4: SEM images of InGaO film on glass, deposition carried out at 450 °C, films were annealed at 550 °C.

Films pre- and post- anneal were analysed *via* a variety of techniques, and the SEM images can give us information about the growth mechanisms at work. Films deposited at 350 °C (Fig. 4.3) are not changed at the surface after annealing to remove carbon at

550 °C (Fig 4.4), showing individual clusters that have grown and agglomerated, displaying an island growth mechanism.

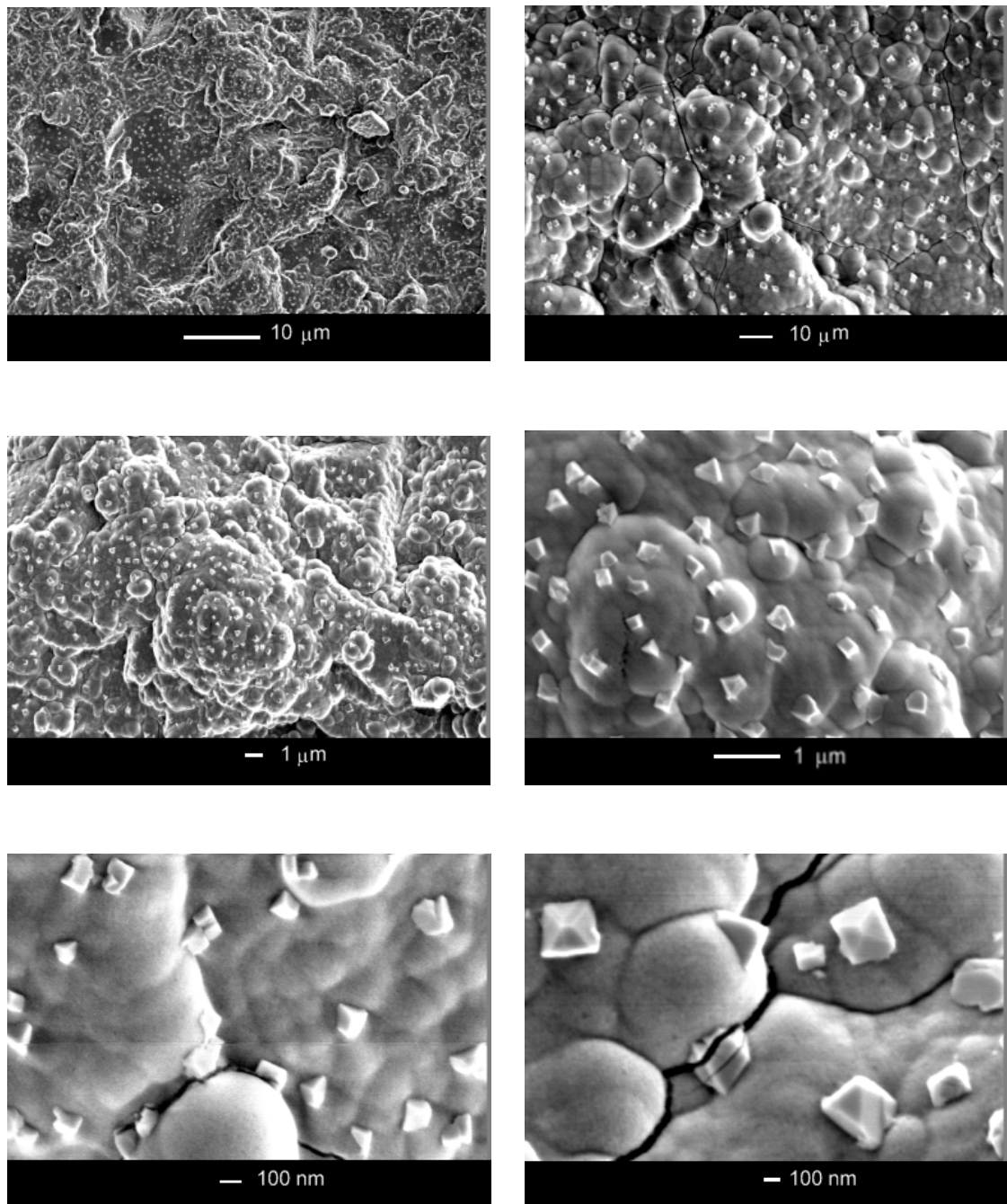


Fig. 4.5: SEM images of InGaO film on quartz, deposition carried out at 450 °C, annealed overnight at 1000 °C.

SEM images of mixed indium gallium oxide thin films on quartz and annealed at 1000 °C overnight clearly indicate the growth of crystals from the amorphous substrate (Fig.

4.5). At higher magnification the amorphous regions of the film are comparable to pre annealed films (Fig. 4.3–4.4). The films deposited at 450 °C and annealed at 1000 °C shows a regular crystallite array, and lower magnification a consistent thin film coating is apparent (Fig. 4.5). At higher magnification the individual crystallites can be observed as being evenly distributed and of the same shape, the edges of which are in the region of 100–200 nm in length. Area and spot analysis of amorphous and crystallite regions of the film by EDXA have shown that the film composition is consistent throughout.

Films annealed at 1000 °C for one hour give poor scattering patterns in XRD so were not suitable for further analysis. Whilst SEM images show the morphology to be different to that of films deposited at 350 °C, a regular crystallite array is however is not observed (Fig 4.6).

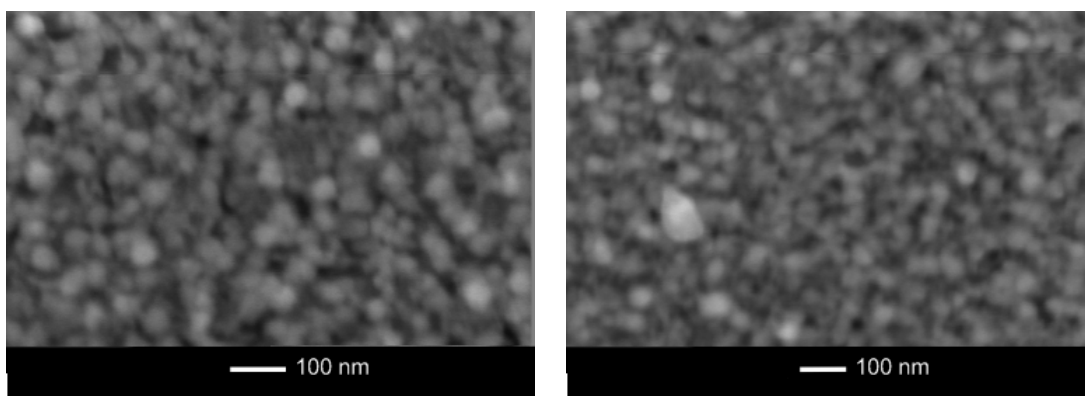


Fig 4.6: SEM images of InGaO film on quartz, deposition carried out at 450 °C, annealed for 1 hour at 1000°C.

4.2.2.4. X-ray Photoelectron Spectroscopy

The XPS of the In 3d peaks of a film deposited at 450°C *via* the *in situ* route using GaMe₃, InMe₃ and excess HOCH₂CH₂OMe shows one distinct indium environment at the surface (Fig. 4.7). The peaks at 445.289 and 452.880 eV correspond to the In 3d_{5/2} 3d_{3/2} peaks of In₂O₃, respectively and are in a 1 : 1.5 ratio with each other, which fit with peaks previously reported.⁶⁵

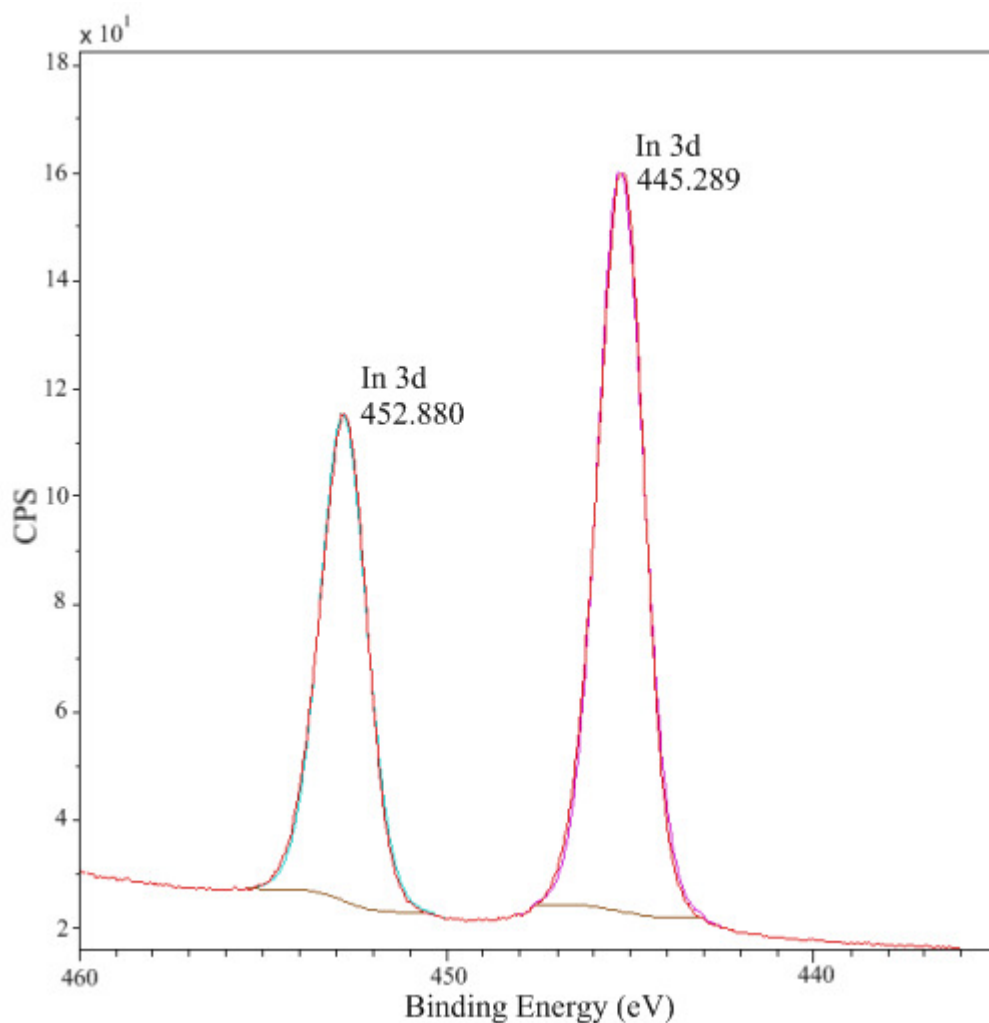


Fig. 4.7: XPS of In 3d peaks for a film deposited at 450 °C by AACVD from the *in situ* reaction of GaMe₃, InMe₃ and excess HOCH₂CH₂OMe in toluene.

The Ga 2p peaks for the same film show that only one gallium environment is present in the film with peaks at 1145.157 and 1118.251 eV, corresponding to Ga 2p_{1/2} and 2p_{3/2}, respectively (Fig. 4.8), with peaks in a 1 : 2 ratio with each other which is consistent with literature reports for Ga₂O₃ peaks.⁶⁶

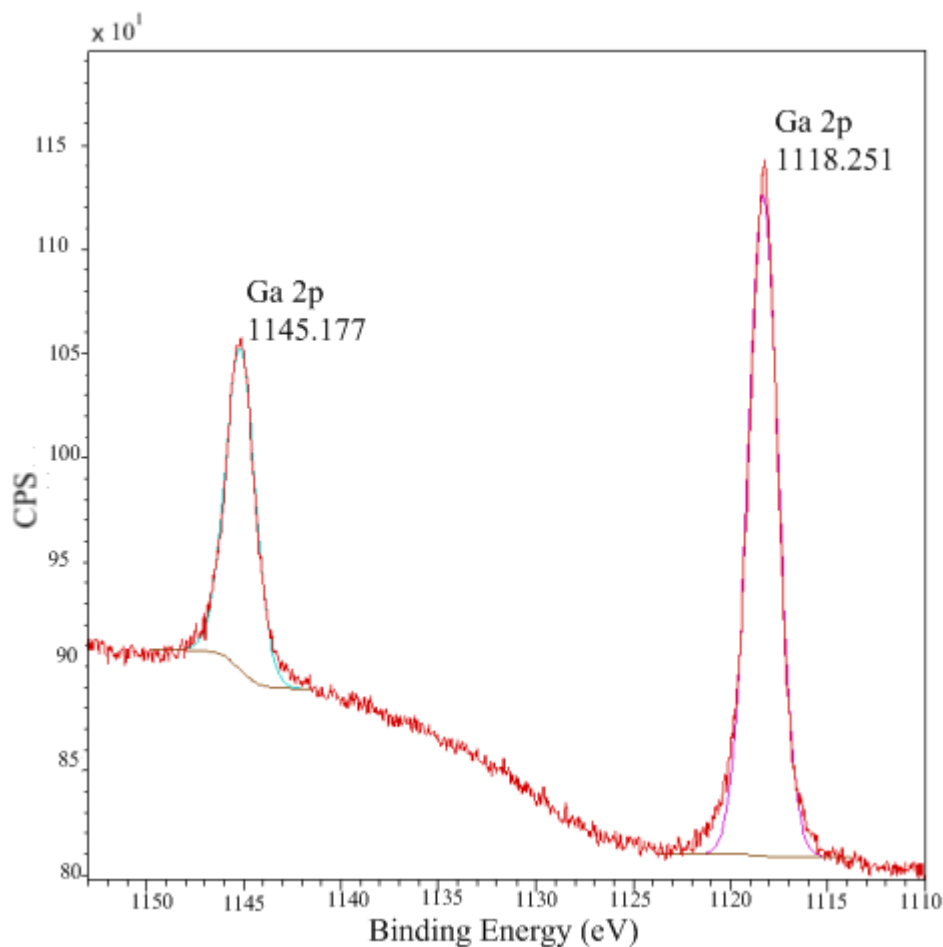


Fig. 4.8: XPS of Ga 2p peaks for a film deposited at 450 °C by AACVD from the *in situ* reaction of GaMe₃, InMe₃ and excess HOCH₂CH₂OMe in toluene.

The O 1s peaks (Fig 4.9) of the same sample can be deconvoluted into two components: two Gauss-Lorentz peaks with the same FWHM of 1.7 eV for both the peaks. This is similar to reported XPS investigations on In₂O₃ samples.⁶⁵ The observed O 1s peak at 530.829 eV can be assigned to the lattice oxygen in crystalline In₂O₃, and O 1s peak at 532.709 eV to adsorbed OH groups on the surface. It is proposed here that with the presence of only one oxygen environment, within the sample, the compound adopts a distorted In₂O₃ lattice with some indium atoms replaced by gallium atoms within the framework, consistent with XPS results showing only one oxygen environment, along with indium and gallium peaks corresponding to In₂O₃ and Ga₂O₃ environments.

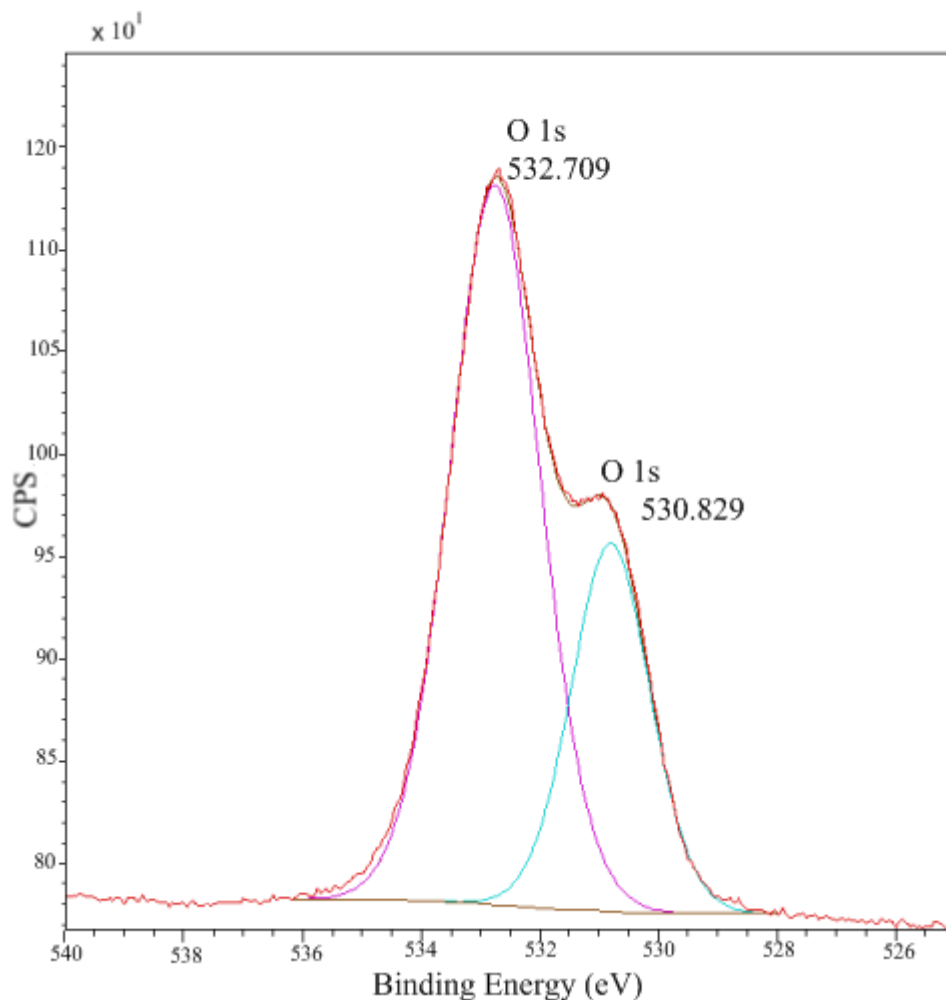


Fig 4.9: XPS of O 1s peaks for a film deposited at 450°C by AACVD from the *in situ* reaction of GaMe₃, InMe₃ and excess HOCH₂CH₂OMe in toluene.

The XPS survey scan for the same film shows that the film formed is predominantly a mixed indium gallium oxide material (Fig 4.10). A peak observed for the C 1s environment indicated the presence of carbon at the surface of the film. The donor functionalised alcohol, HOCH₂CH₂OMe used in the reaction is responsible for the carbon impurity, however it is likely that carbon contamination is low (< 5 atom%). No impurities other than carbon were detected.

The O : Ga and O : In ratios, calculated using sensitivity factors determined from the empirical peak area and then corrected for the systems transmission function, were found to give a total metal to oxygen ratio of 1 : 1.3. This is slightly lower than the expected 1 : 1.5 metal to oxygen ratio expected, however, this is an acceptable limit of accuracy in regards to this technique.

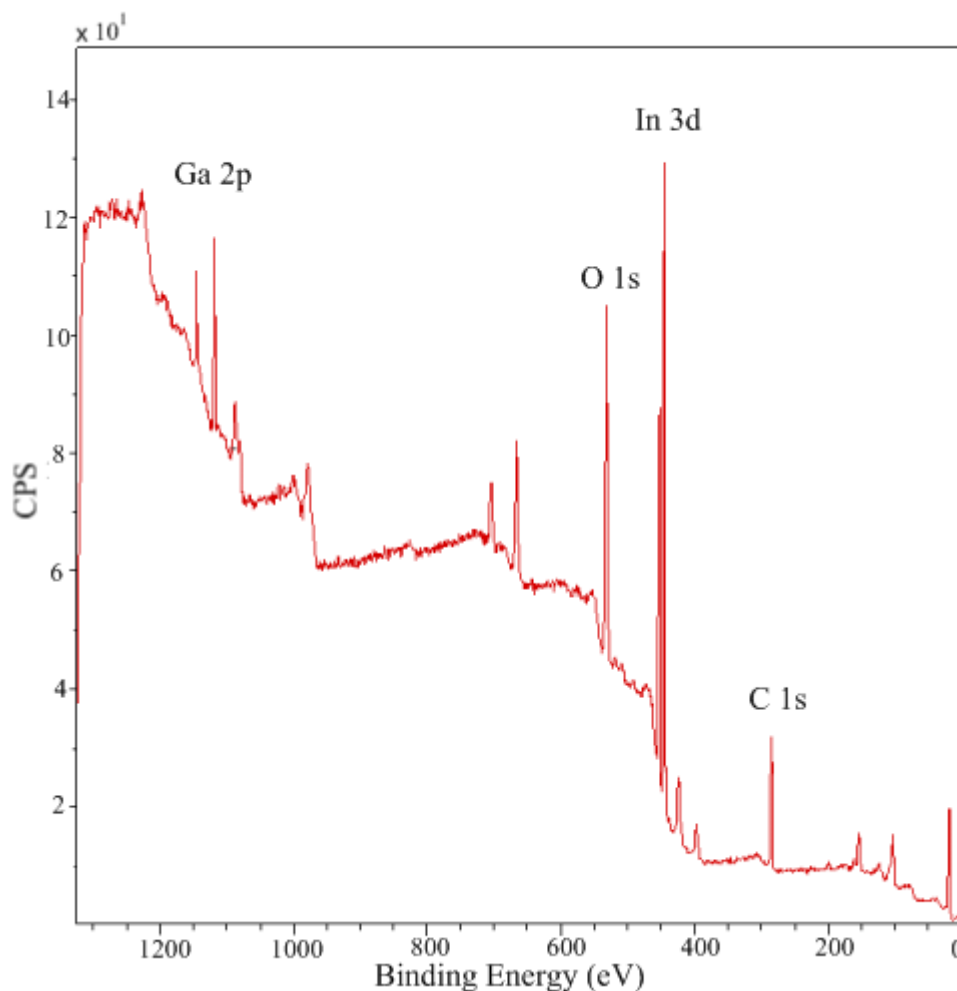


Fig. 4.10: XPS of all regions for a thin film deposited at 450 °C by AACVD from the *in situ* reaction of GaMe₃, InMe₃ and excess HOCH₂CH₂OMe in toluene. (Peaks with lower intensity are the other orbitals of gallium and indium).

4.2.2.5. X-ray Powder Diffraction

The films deposited by AACVD were amorphous to X-rays at all deposition temperatures. This is an effect of the low deposition temperatures used, as reported thin films of gallium oxide are not crystalline below 650 °C.⁶⁷ Films deposited at 450 °C were annealed at 1000 °C overnight and were found to be crystalline (Fig 4.5).

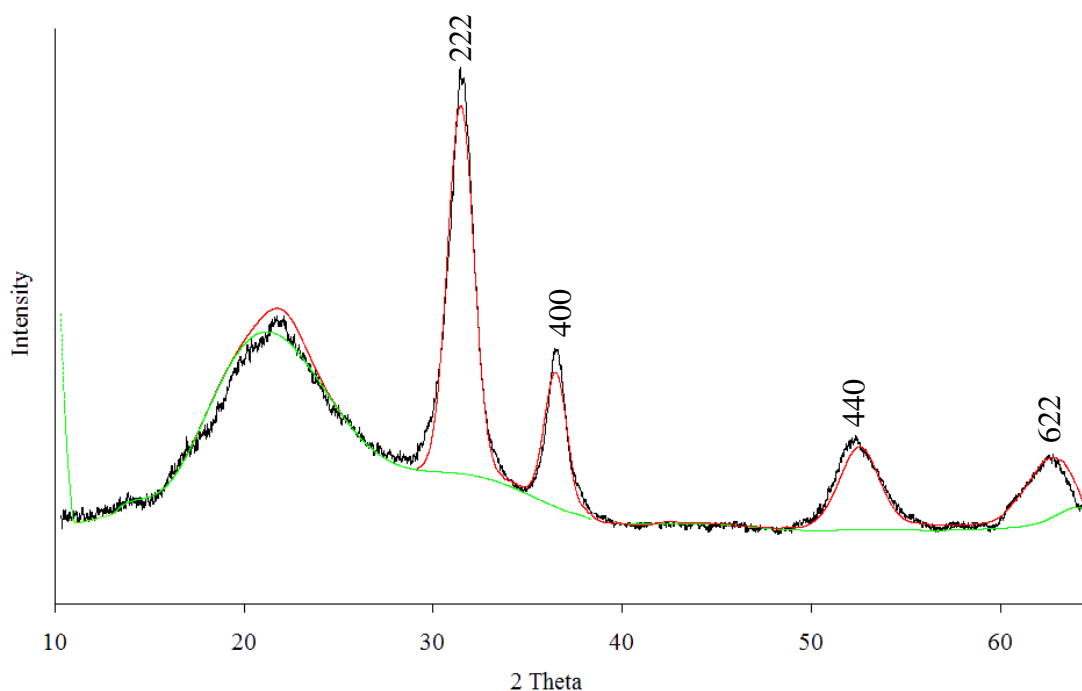


Fig.4.11: XRD pattern for film deposited on quartz and annealed at 1000 °C. The black line is the experimental data, the red line shows the model, the green line shows the background.

X-ray powder diffraction patterns varied little between films, but in all instances peaks were observed to be unusually wide. Whilst wider peaks is a consequence of low angle XRD, it is possible that the wide peaks observed here are in fact multiple peaks indicative of mixtures of similar phases of the material, however XPS, XRD, EDXA and WDX data do not give evidence to support this, suggesting that only one phase is present.

The lattice parameter of the material was deduced *via* Rietveld refinement to be 9.84 Å. The model was initially based on an indium oxide framework, with a starting indium oxide lattice parameter of 10.12 Å. The significant change in lattice parameter observed after refinement is indicative of a unit cell contraction which is consistent with the hypothesis that indium sites in the indium oxide framework have been substituted with gallium atoms. No peaks are observed for gallium oxide in the XRD pattern (Fig. 4.11) and so XRD is consistent with XPS analysis that a gallium doped indium oxide material is present.

4.2.2.6. Atomic Force Microscope Images

Images taken of the thin films of gallium indium oxide were able to give a root mean squared (RMS) roughness. This is a measure of the surface roughness/smoothness of a material, which is the root mean square average of the "peaks and valleys" of the AFM scanned surface. RMS roughness is an important factor to be taken into consideration if films are to be used in microelectronic application, for example. Typical RMS roughness values in industrial application are below 100 nm.⁴

Films were found to have a variety of RMS roughness values, and whilst some samples had suitably low RMS roughness (94.2 nm) many others exhibited roughness which exceeded 200 nm (Fig 4.12).

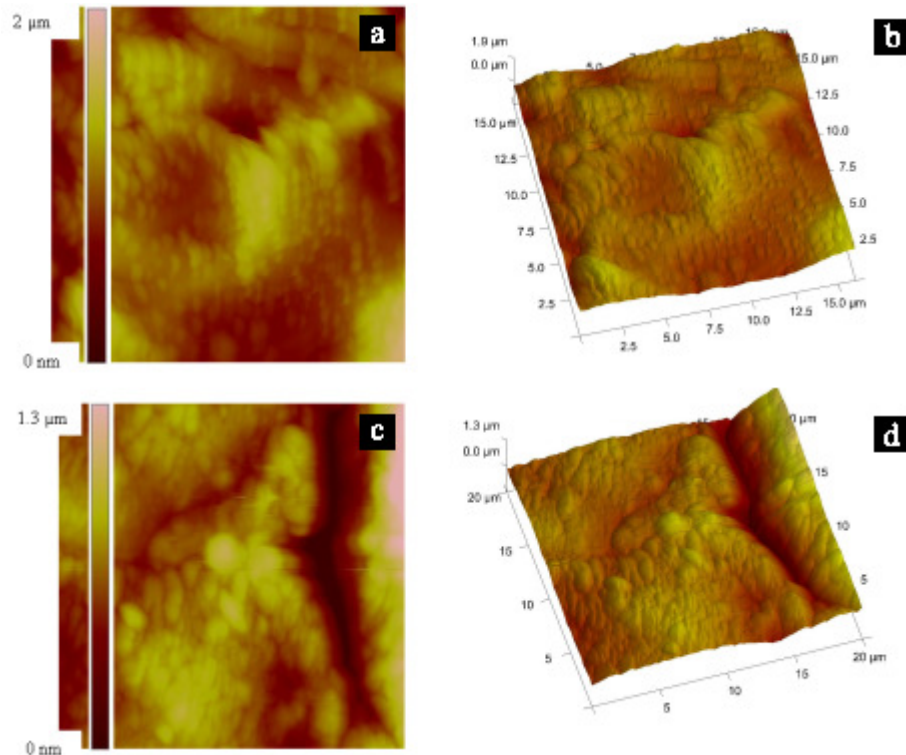


Fig 4.12: a) 16 μm Field size AFM image (magnified image of the previous image, indicated by the blue square) RMS Roughness = 203 nm b) 3D image of same area. c) Another 20 μm Field size AFM image RMS Roughness = 224 nm. d) 3D image of the same area.

4.2.2.7. Kelvin Probe measurement

The mixed indium gallium oxide thin films reported herein may be used as transparent conductive oxides in photovoltaic cells, it is favourable for the TCO to have a large work function. This significantly enhances the hole injection properties at anode/emitter interface since the barrier height between the interface is reduced, this in turn reduces the operating voltage of devices and thus improves its efficiency.

In collaboration with the Physics department at UCL, a Kelvin probe measurement was used to estimate the work function of the gallium indium oxide thin films. The work function was measured to be 4.6 eV. This is consistent with reports of indium gallium oxide in the literature (4–5 eV)¹² and is comparable with ITO (4.5–5 eV).⁴

4.2.2.8. Summary

EDXA and WDX analysis showed thin films deposited on quartz at 450°C and annealed at 1000°C have the same composition ($\text{In}_{1.4}\text{Ga}_{0.6}\text{O}_{3.1}$), the as-deposited films had a M : O ratio close to the expected 1 : 1.5 for Ga_2O_3 . SEM images, reveal that films deposited at 350 °C (Fig. 4.3) are not changed at the surface after annealing to remove carbon at 550 °C (Fig 4.4), showing individual clusters that have grown and agglomerated, displaying an island growth mechanism. SEM images of films annealed overnight at 1000 °C are crystalline, and individual crystallites can be observed as being evenly distributed and of the same shape. Area and spot analysis of amorphous and crystallite regions of the film by EDXA have shown that the film composition is consistent throughout.

The XPS survey scan for the film annealed at 1000 °C shows that the film formed is predominantly a mixed indium gallium oxide material (Fig 4.10). The O : Ga and O : In ratios, calculated using sensitivity factors determined from the empirical peak area and then corrected for the systems transmission function, were found to give a total metal to oxygen ratio of 1 : 1.3. Analysis of the XRD pattern of the films annealed at 1000 °C *via* Rietveld refinement found the lattice parameter to be 9.84 Å. The significant change in lattice parameter observed after refinement is indicative of a unit cell contraction which is consistent with the hypothesis that indium sites in the indium oxide framework have been substituted with gallium atoms.

AFM techniques showed films to have a variety of RMS roughness values, and whilst some samples had a desirable RMS roughness of less than 100 nm, many had higher RMS roughness. In addition, a Kelvin probe measurement found the work function of the film be 4.6 eV (literature value, 4–5 eV)¹² and is comparable with ITO (4.5–5 eV).⁴

The successful formation of gallium indium oxide thin films from the *in situ* AACVD reaction of InMe₃, GaMe₃ and ROH indicates that there is no need to prepare, isolate and purify a single-source precursor. This has been shown previously for AACVD reactions of GaEt₃ and ROH to afford films of Ga₂O₃ and the AACVD of InMe₃ and ROH resulting in the formation of films of In₂O₃ (R = donor functionalized ligand),⁶⁰ but never before for the synthesis of mixed gallium indium oxide thin films *via* AACVD.

4.2.3. Gallium zinc oxides

The AACVD reaction of GaMe₃, ZnEt₂ and the donor functionalised alcohol HOCH₂CH₂OMe on glass and quartz substrates was studied between 350–550 °C. For each system, deposition was observed on both the substrate and top plate.

At all deposition temperatures the films showed excellent film coverage, were transparent and were strongly adherent (passed scotch tape test but could be scratched off with a steel scapel), however films in all instances were found to be extremely thin, which was often problematic in analysis. Films are insoluble in common organic solvents, and were quickly decomposed in nitric acid. Films of uniform thickness were grown across the full length of the substrate. EDXA and WDX results show that in all cases, different surface features of the films had differing composition, as is discussed herein. Additionally four-point probe measurements suggest that the films are not conductive at room temperature.

Table 4.2: Deposition conditions and analysis of the films grown from the AACVD of GaMe₃, ZnEt₂ and ROH (R = CH₂CH₂OMe) in toluene.

Precursors	<i>T</i> [°C]	<i>T</i> annealed [°C]	Surface	EDXA
GaMe ₃ , ZnEt ₂ , ROH	350	1000	Film	Zn _{1.38} Ga
GaMe ₃ , ZnEt ₂ , ROH	450	1000	Film	ZnGa _{2.65}
GaMe ₃ , ZnEt ₂ , ROH	450	1000	Feature	ZnGa _{2.61}
GaMe ₃ , ZnEt ₂ , ROH	550	1000	Film	ZnGa _{2.90}
GaMe ₃ , ZnEt ₂ , ROH	550	1000	Feature	ZnGa _{3.03}

4.2.3.1. Energy dispersive X-ray analysis

The composition of the films was determined by energy dispersive X-ray analysis (EDXA). EDXA confirmed the presence of gallium, zinc and oxygen, however breakthrough to the underlying glass substrate was observed in all instances as films were so thin so metal to oxygen ratio could not be deduced. No carbon was detected in EDXA experiments so carbon contamination levels as a direct result of the precursors used are suitably low (< 5%).

Films deposited at 450 °C showed the best coverage of the substrate, with a complete conformal coating. Table 4.2 shows the deposition conditions and analysis of the films grown. Films grown at 350 °C and annealed at 1000 °C were the only instance where the zinc content was higher than the gallium, with a Zn to Ga ratio of 1.38 : 1, however, coverage of the substrate was poor. Films grown at 450 °C and annealed at 1000 °C are consistent with XPS results (Section 4.2.3.4) and XRD analysis (Section 4.2.3.5), they showed a Zn to Ga ratio of 1 : 2.65, which was consistent in all areas of the film and only varied slightly on features (Fig. 4.14) found on the film (1 : 2.61). Films grown at 550 °C and annealed at 1000 °C showed the lowest Zn content, with ratios of Zn to Ga being at their highest. In all areas of the film the Zn to Ga ratio was 1 : 2.90, which only differed slightly in surface features observed, where the Zn to Ga ratio was 1 : 3.03.

The increase in the zinc to gallium ratio with increase in substrate temperature can be assigned to the volatility of the precursors utilized. ZnEt₂ is a very pyrophoric liquid,

GaMe_3 is also pyrophoric but less so when compared directly with ZnEt_2 . So it is proposed that at the lower deposition temperatures (350°C) zinc has more time to adhere to the substrate before being removed in the gas flow through the exhaust. Depositions carried out at the higher end of the temperature scale (550°C) have the lowest zinc content, so arguably much of the ZnEt_2 is lost in exhaust before it can travel to the surface to react, accounting for the lower amount of the element in the films. Films deposited at 450°C have a 1 : 2.6 zinc to gallium ratio, as well as the best conformal coverage of substrates so are used in all further analysis.

4.2.3.2. Wavelength dispersive X-ray analysis

As a direct result of the low thickness of the films, WDX analysis was not possible. Despite the use of a lower energy electron beam breakthrough to substrate silica was still observed, making any oxygen content recorded considerably higher because of the substrate silica present.

The breakthrough to the substrate silica meant that no metal to oxygen (M :O) ratio could be obtained and so no compositional formula, however from EDXA the metal to metal (M : M) ratio is reported.

4.2.3.3. Scanning electron microscopy

The film morphology was studied using SEM, which indicated that deposition occurred *via* an island growth mechanism (Fig. 4.16). In all instances films were very thin, smooth and relatively featureless, in all SEM images, features on the film were found and included in images to give a better idea of how smooth the rest of the film was. All films were annealed at 1000°C overnight, in order to crystallize the material for XRD analysis. Interestingly this had no effect on the morphology of the films, although it is proposed this is a direct result of the films thickness.

Unlike most films prepared *via* AACVD pre-annealed films did not exhibit a brown tint, indicative of carbon contamination in the films, suggesting that this approach to thin films limits carbon contamination. Films were amorphous pre-anneal meaning composition could not be determined by XRD. Films were annealed 1000°C , this step

removes any excess carbon (EDXA analysis shows films contained less than 5% carbon after annealing).

At all deposition temperatures films are smooth, transparent, and have no detectable carbon content. The films are featureless, but after scanning large areas of the films at fairly low magnification ($\times 900$) a few surface defects can be found (Fig. 4.14–4.15), but these small areas only help to highlight the smooth nature of the film. At higher magnification ($\times 6000$), the feature of the film is more clearly observed, is crystalline (Fig. 4.14, right) and SEM results show this to have similar composition to the rest of the film. It is proposed that these features are a direct result of cracks forming in the underlying film being used as nucleation points for further film growth.

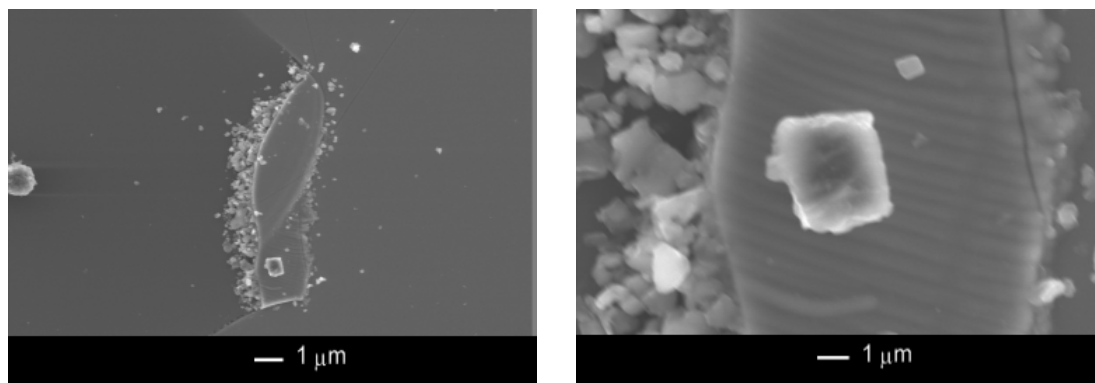


Fig 4.13: SEM images of zinc gallium oxide film on quartz, deposition carried out at 550 °C, annealed overnight at 1000 °C.

SEM images of mixed gallium zinc oxide thin films on quartz at 450 °C and annealed at 1000 °C overnight (Fig. 4.15) are identical in morphology to those deposited at 550 °C. The films are featureless, but again after scanning large areas of the films surface defects can be found. At higher magnification ($\times 9000$), the feature of the film is more clearly observed, is crystallite (Fig. 4.15, top left, bottom right) and SEM results show this to have similar composition to the rest of the film.

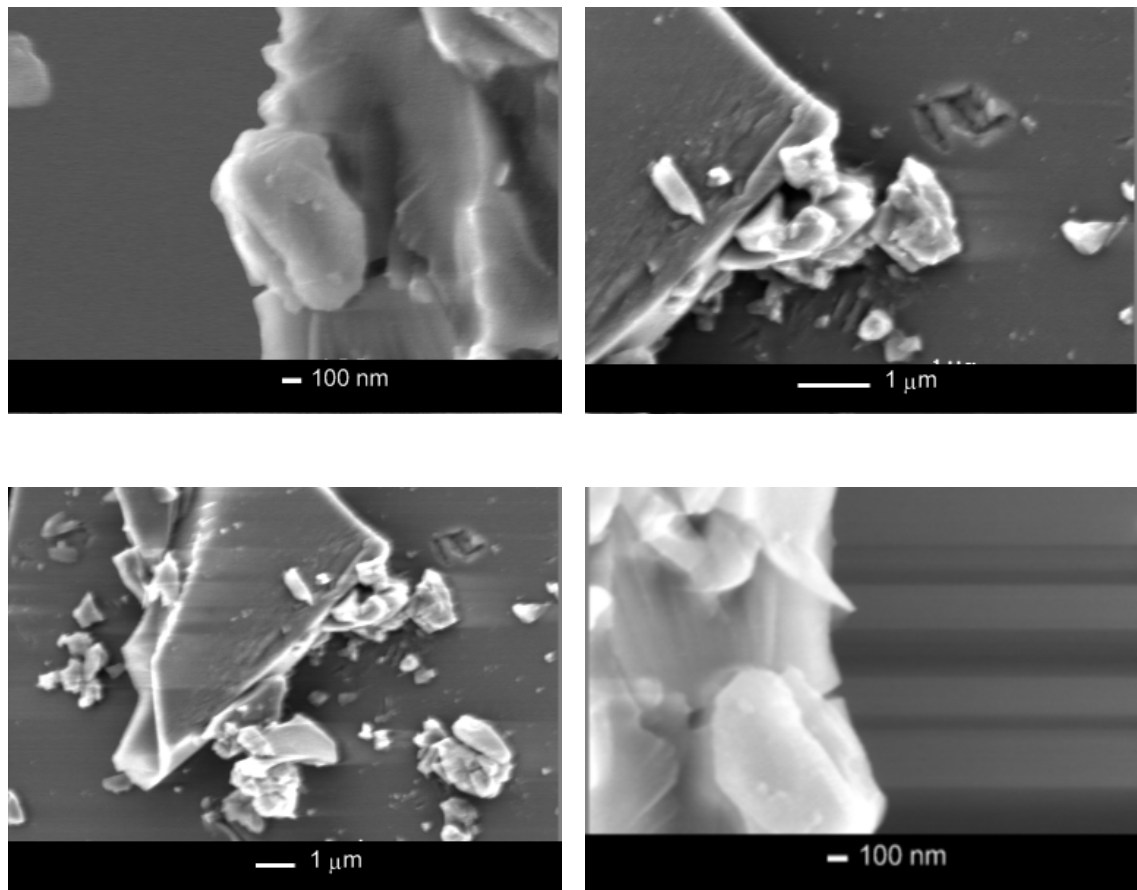


Fig 4.14: SEM images of zinc gallium oxide film on quartz, deposition carried out at 450°C, annealed overnight at 1000°C.

In thicker films analysed, surface defects were found to be larger in area, on closer inspection of these films (Fig. 4.16) crystallite growth is evident as a direct result of annealing. At lower magnification ($\times 6000$), islands of film are evident (Fig. 4.16, left), whilst at higher magnification ($\times 40000$) the microstructure is clearly crystalline, showing individual clusters that have grown and agglomerated as islands of the material, indicative of the island growth mechanism of the material (Fig. 4.16, right).

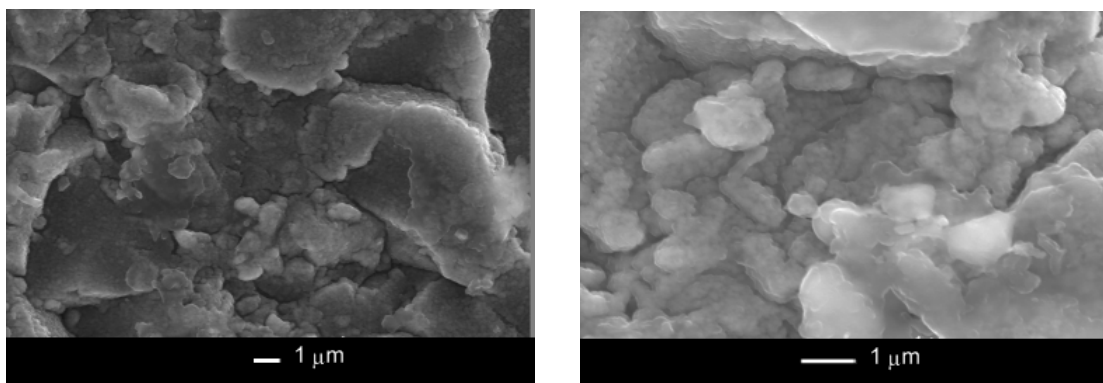


Fig. 4.15: SEM images of features on a zinc gallium oxide film on quartz, deposition carried out at 450 °C, annealed overnight at 1000 °C.

4.2.3.4. X-ray Photoelectron Spectroscopy

The XPS of the Ga 2p peaks of a film deposited at 450 °C *via* the *in situ* route using GaMe₃, ZnEt₂ and excess HOCH₂CH₂OMe shows two gallium environments at the surface (Fig. 4.17). The peaks at 1143.952 and 1117.121 eV correspond to Ga 2p_{1/2} and 2p_{3/2}, respectively, with peaks in a 1 : 2 ratio with each other, which is consistent with literature reports for Ga₂O₃ peaks.⁶⁶ The second, much smaller environment at 1136.261 and 1109.491 eV correspond to Ga 2p_{1/2} and 2p_{3/2}, respectively, again with peaks in a 1 : 2 ratio with each other. The presence of two gallium environments is thought to be indicative of mixed phase in the material.

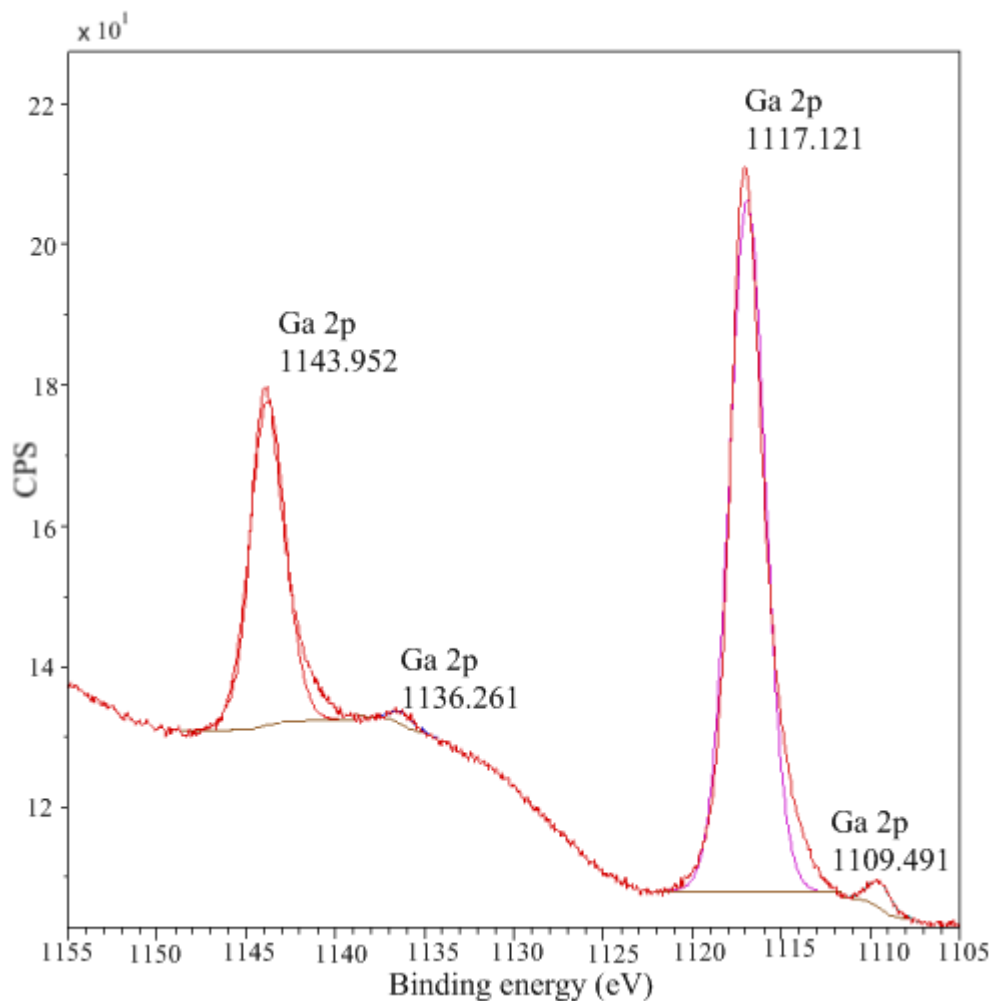


Fig 4.16: XPS of Ga 2p peaks for a film deposited at 450 °C by AACVD from the *in situ* reaction of GaMe₃, ZnEt₂ and excess HOCH₂CH₂OMe in toluene.

The XPS of the Zn 2p peaks of a film deposited at 450 °C shows two zinc environments at the surface (Fig. 4.18). The peaks at 1043.762 and 1020.685 eV correspond to Zn 2p_{1/2} and 2p_{3/2}, respectively, with peaks in a 1 : 2 ratio with each other which is consistent with literature reports for ZnO peaks.⁶⁸ The second, much smaller environment at 1036.934 and 1013.612 eV correspond to Zn 2p_{1/2} and 2p_{3/2}, respectively, again with peaks in a 1 : 2 ratio with each other. The presence of two zinc environments is thought to be indicative of mixed phase in the material.

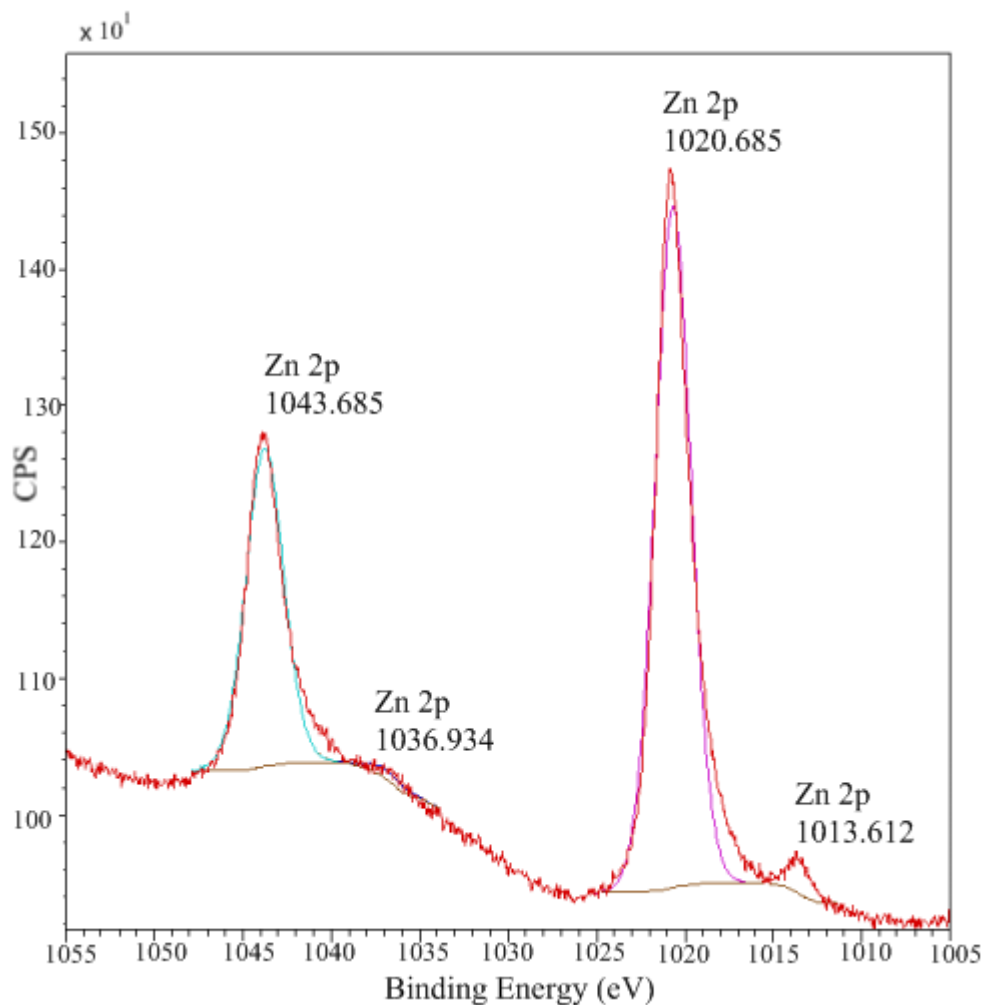


Fig 4.17: XPS of Zn 2p peaks for a film deposited at 450 °C by AACVD from the *in situ* reaction of GaMe₃, ZnEt₂ and excess HOCH₂CH₂OMe in toluene.

The Ga 2p_{3/2} peak located at 1117.121 eV is in good agreement with other reported values⁶⁶ which is evidence that gallium ions exist as Ga³⁺ into the ZnO matrix. It is proposed that Ga³⁺ ions are incorporated into the Zn²⁺ sites due to their radii similarity, leading to a substitutional doping.

The two peaks at 1143.952 and 1117.121 eV are ascribed to the electronic states Ga 2p_{1/2} and 2p_{3/2} respectively, whose energy gap is consistent with the value for the element, 26.84 eV.⁶⁹ The appearance of Ga element peaks in Ga-doped ZnO samples indicates that Ga element has been doped into the ZnO lattice successfully.

The O1s peak in the XPS data can be fitted by a Gaussian distribution, centred at 530.174 eV, which is attributed to the O²⁻ ions in the ZnO lattice.⁷⁰ The intensity of this

peak shows the amount of oxygen atoms in the wurtzite structure of the hexagonal Zn^{2+} array. Gallium atoms have been doped into the ZnO lattice by substituting zinc ions or occupying the position of Zn vacancies. The O 1s peak observed at 523.093 eV with considerably lower intensity can be assigned to the related O^{2-} ions in the oxygen deficient regions within the matrix of ZnO,⁷⁰ whose intensity partly represents the variation in the concentration of oxygen vacancies, in this instance the ZnO is highly doped with gallium ions so the intensity of this peak is particularly low.

The XPS survey scan for the same film shows that the film formed is predominantly a mixed gallium zinc oxide material (Fig 4.19). A peak observed for the C 1s environment indicated presence of carbon at the surface of the film. The donor functionalised alcohol, $\text{HOCH}_2\text{CH}_2\text{OMe}$ used in the reaction is responsible for the carbon impurity, however it is likely that carbon contamination is low (< 5 atom%). No impurities other than carbon were detected.

The O : Ga and O : Zn ratios, calculated using sensitivity factors determined from the empirical peak area and then corrected for the systems transmission function, were found to give a total metal to oxygen ratio of 1 : 4, whilst the zinc to gallium ratio was found to be in agreement with EDXA analysis with a ratio of 1 : 2.

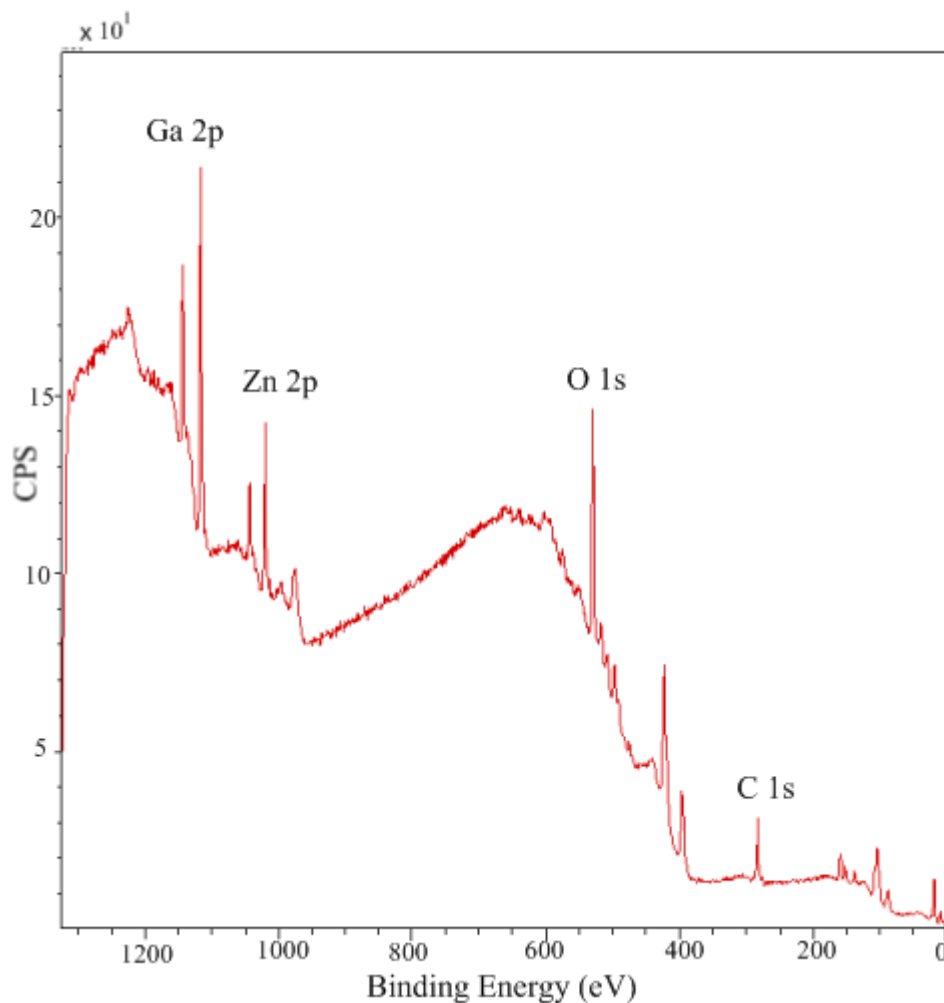


Fig 4.18: XPS of all regions for a thin film deposited at 450 °C by AACVD from the *in situ* reaction of GaMe₃, ZnEt₂ and excess HOCH₂CH₂OMe in toluene.

4.2.3.5. X-ray Powder Diffraction

The films deposited by AACVD were amorphous to X-rays at all deposition temperatures. This is an effect of the low deposition temperatures used, as reported thin films of gallium oxide are not crystalline below 650 °C.⁶⁷ Films deposited at 450 °C were annealed at 1000 °C overnight and were found to be crystalline thereafter. In addition, X-ray powder diffraction patterns varied little between films.

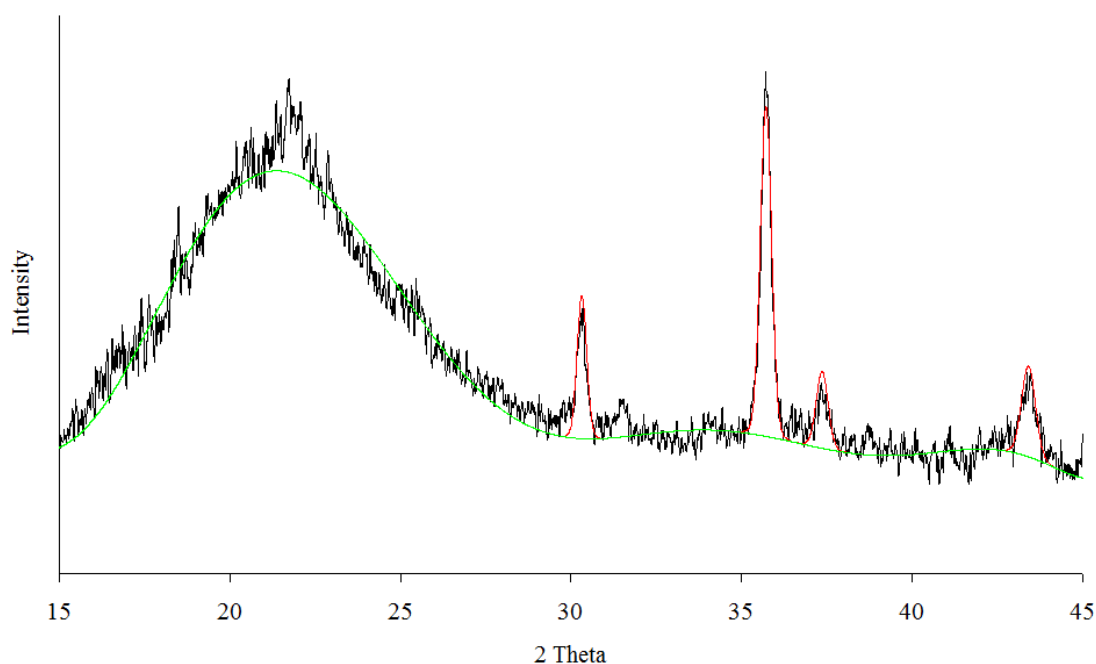


Fig 2.19: XRD pattern for film deposited on quartz and annealed at 1000 °C. The black line is the experimental data, the red line shows the model, the green line shows the background.

The lattice parameter of the material was deduced *via* a la Bail refinement to be 8.238 Å. The model was initially based on a previously reported gallium doped zinc oxide framework, with a starting zinc oxide lattice parameter of 8.330 Å.⁶⁸ The shift in lattice parameter observed after refinement is indicative of a unit cell expansion which is consistent with the hypothesis that zinc sites in the zinc oxide framework have been doped with gallium atoms. No peaks are observed for separate phases of gallium oxide or zinc oxide in the XRD pattern (Fig. 4.20), and so XRD is consistent with XPS analysis that a gallium doped zinc oxide material is present.

Whilst differing slightly to the reported material, the lattice parameter expected to be similar to that of zinc doped gallium oxide (8.331 Å cf 8.330 Å), the calculated unit cell parameter of 8.331 Å is significantly larger than that of gallium oxide (8.238 Å) which is justified accordingly when comparing the larger ionic radius of zinc in the 2⁺ state (0.74 for Zn²⁺, 0.62 for Ga³⁺). Additionally, both zinc and gallium are *d*¹⁰ species and so are isoelectronic.

4.2.3.6. Summary

EDXA analysis of films grown at 450 °C and annealed at 1000 °C showed a Zn to Ga ratio of 1 : 2.65, which was consistent in all areas of the film and only varied slightly on features (Fig. 4.14) found on the film (1 : 2.61). Films grown at 550 °C and annealed at 1000 °C showed the lowest Zn content, with ratios of Zn to Ga being at their highest. In all areas of the film the Zn to Ga ratio was 1 : 2.90, which only differed slightly in surface features observed, where the Zn to Ga ratio was 1 : 3.03. This increase in the zinc to gallium ratio with increase in substrate temperature can be assigned to the volatility of the precursors utilized. Depositions carried out at the higher end of the temperature scale (550 °C) have the lowest zinc content, so arguably much of the ZnEt₂ is lost in exhaust before it can travel to the surface to react, accounting for the lower amount of the element in the films. Films deposited at 450 °C have a 1 : 2.6 zinc to gallium ratio, as well as the best conformal coverage of substrates so are used in all further analysis.

SEM images indicated that deposition occurred *via* an island growth mechanism (Fig. 4.16). In all instances films were very thin, smooth and relatively featureless. All films were annealed at 1000 °C overnight, in order to crystallize the material for XRD analysis. At lower magnification (×6000), islands of film are evident (Fig. 4.16), whilst at higher magnification (×40000) the microstructure is clearly crystalline, showing individual clusters that have grown and agglomerated as islands of the material, indicative of the island growth mechanism of the material (Fig. 4.16.). The XPS survey scan for the same film shows that the film formed is predominantly a mixed gallium zinc oxide material (Fig 4.19).

Additionally, analysis of the XRD pattern of the films *via* a Le Bail refinement calculated the lattice parameter of the material to be 8.238 Å. The shift in lattice parameter observed after refinement is indicative of a unit cell expansion which is consistent with the hypothesis that zinc sites in the zinc oxide framework have been doped with gallium atoms.

The successful formation of gallium doped zinc oxide thin films from the *in situ* AACVD reaction of ZnEt₂, GaMe₃ and ROH indicates that there is no need to prepare,

isolate and purify a single-source precursor. This has been shown previously for AACVD reactions of GaEt₃ and ROH to afford films of Ga₂O₃ and the AACVD of InMe₃ and ROH resulting in the formation of films of In₂O₃ (R = donor functionalized ligand),⁶⁰ but never before for the synthesis of mixed gallium zinc oxide thin films *via* AACVD.

4.3. Conclusions

The AACVD of GaMe₃ and ROH (R = C(CH₃)₂CH₂OMe, CH₂CH₂OMe, CH₂CH₂NMe₂) resulted in the formation of Ga₂O₃ films on glass. Gallium oxide films have now been grown *via* AACVD using the gallium precursors, GaMe₃, GaEt₃ and [Ga(NMe₂)₃]₂ and indium oxide using InMe₃.^{14,15,18}

Transparent electrically conductive gallium indium oxide films have been grown for the first time *via* AACVD using Me₃In, Me₃Ga and HOCH₂CH₂OMe under AACVD conditions. Furthermore the *in situ* reaction of the reagents eliminates the need for the synthesis, isolation and purification of a single-source metal alkoxide precursor. Rietveld refinement can assign XRD patterns to a cubic homogeneously Ga-substituted In₂O₃ structure.

The AACVD of ZnEt₂, GaMe₃ and HOCH₂CH₂OMe resulted in the formation of gallium doped zinc oxide films on glass. As with all results reported herein the *in situ* reaction of the reagents eliminates the need for the synthesis, isolation and purification of a single-source metal alkoxide precursor. A Le Bail refinement of the XRD data confirms the synthesis of gallium doped zinc oxide, with comparable lattice parameter with literature reports.⁶⁸ This is the first reported instance of deposition of thin films of gallium doped zinc oxide *via* AACVD to date.

4.4. Experimental

Caution: It should be noted that GaMe₃ and InMe₃ are highly pyrophoric substances which ignite spontaneously in air and the CVD of these chemicals can potentially be highly toxic and corrosive. All experiments should be conducted in a fumehood.

Following the deposition films are air and moisture stable and are safe to handle as any reactive species leave via the reactor exhaust during the AACVD process.

4.4.1. General procedures – synthesis.

All manipulations were performed under a dry, oxygen-free dinitrogen atmosphere using standard Schlenk techniques or in an Mbraun Unilab glovebox. All solvents used were stored in alumina columns and dried with anhydrous engineering equipment, such that the water concentration was 5–10 ppm. GaMe₃ and InMe₃ were supplied by SAFC Hitech. All other reagents were procured commercially from Aldrich, were distilled, degassed by three freeze-pump-thaw cycles and stored over 4 Å molecular sieves.

4.4.2. General procedures – AACVD.

All AACVD experiments were conducted on 150 mm × 45 mm × 3 mm pieces of glass using a horizontal bed cold wall CVD reactor (Fig. 4.1).

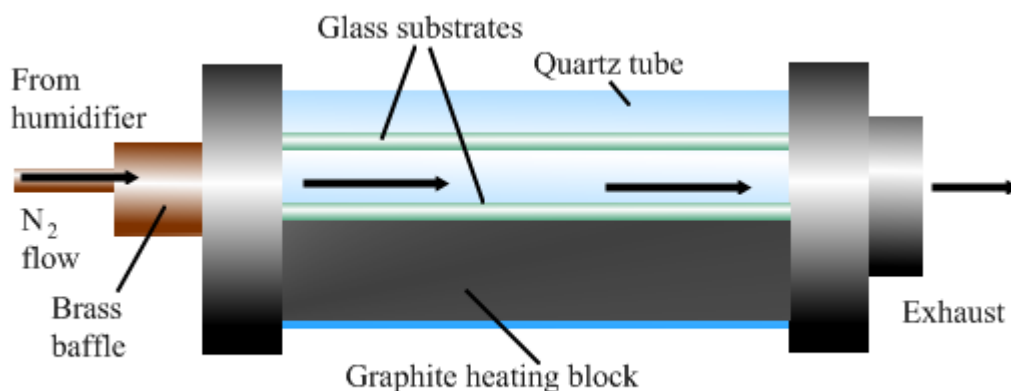


Fig 4.20: AACVD apparatus, the deposition chamber.

The glass substrates were cleaned prior to use by washing, initially with acetone, and then with propan-2-ol, substrates were then dried at 150 °C in an oven to reduce moisture levels. The graphite heating block contains a Whatman cartridge heater, controlled using a Pt-Rh thermocouple. The bottom glass substrate sits directly on top of the graphite heating block, whilst the top plate is suspended directly above, with no direct heating. Temperature gradient measurements have shown there to be a temperature difference of 50 – 70 °C between the two plates.

The precursor solution was transported in all cases reported within this thesis to the flat-bottomed Schlenk flask, which combined with a bypass valve is used as a bubbler for the precursor solutions. The bypass has a two way valve enabling gas flow to be diverted away from the bubbler. The flask, once loaded can be placed over a piezoelectric device to obtain a mist of the precursor solution. Nitrogen gas was passed through the mist and carried through the reactor, over the substrate glass. In several instances a 20mm × 10 mm × 1 mm piece of quartz was placed on the bottom substrate to enable further annealing after the deposition had occurred. The gas flow rate was 1 L min⁻¹, regulated by a calibrated flow meter, and the exhaust fumes from the reactor were vented into a fume cupboard.

The reactor consisted of an open ended quartz cylindrical tube, 60 mm in diameter and 160 mm in length. Within the tube were supports for a top plate and a carbon block containing a heating element and two thermocouples. Each end of the quartz tube was capped with a removable stainless steel end plate. Gas may enter through one of the plates via brass manifold, and leave at the opposite end via an exhaust port. The substrate was placed on the carbon block, and a top plate was placed parallel to the substrate and 10 mm above it.

Both the substrate and top plate were 150 x 45 x 4 mm sheets of SiO₂ coated float glass cut from larger sheets supplied by Pilkington Glass Plc, which were cleaned using acetone and propan-2-ol and then dried in air prior to use. The substrate was placed on top of the carbon heating block at room temperature. The reactor was then sealed and heated to the desired temperature. Only the substrate was directly heated, hence the reactor is known as a cold wall reactor.

The precursor solution was contained within a glass vessel with a thinned base, which allowed more rapid aerosol generation. A Vicks ultrasonic humidifier was used to generate the aerosol mist. The piezoelectric device contained within the humidifier functioned at 20 kHz. Nitrogen gas, supplied by BOC, was passed through a flow meter and into the precursor flask, driving the aerosol mist to the reactor through PTFE tubing. The aerosol mist passed through the brass manifold, designed to generate a uniform flow of gas across the width of the reactor, and entered the reactor between the

substrate and the top plate. The exhaust was vented into a fume cupboard. The gas flow was continued until all the precursor mix had passed through the reactor, typically taking 30 to 90 minutes depending on the gas flow rate. Films were cooled to room temperature in situ under a flow of N_2 , and after cooling were handled and stored in air. The brass manifold was routinely cleaned in an ultrasonic bath and by rinsing with organic solvents. This was necessary to avoid blockages.

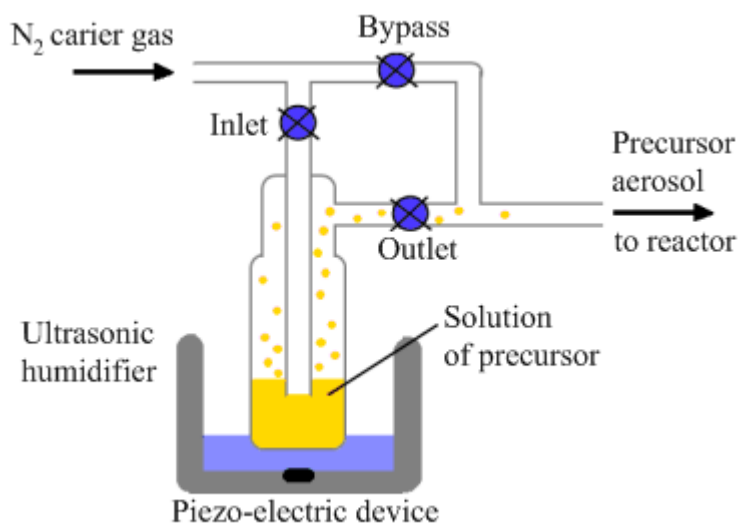


Fig 4.21: AACVD apparatus, the humidifier and bypass valve.

Depositions were carried out under dinitrogen (99.99% from BOC). Precursors were placed in an AACVD glass bubbler and an aerosol mist was created using a piezo electric device. The solvent mist was transported in a flow of cold nitrogen from the bubbler in an 8-mm gauge pipe to a horizontal bed, cold-wall reactor (internal dimensions 15 cm x 5 cm) fitted with a graphite block containing a Whatman cartridge heater, used to heat the glass substrate. The temperature of the substrate was monitored by a Pt-Rh thermocouple. Depositions were carried out by heating the horizontal bed reactor to the required temperature before diverting the nitrogen line through the aerosol and hence to the reactor. The glass substrate was SiO_2 , pre-coated (*ca* 50 nm thick SiO_2 barrier layer) standard float glass (Pilkington, UK) 15 cm x 4 cm x 0.3 cm. A sheet of polished quartz (4 cm x 1.5 cm x 0.1 cm) was placed on the substrate 2 cm from the front of the reactor to enable a subsequent annealing step at 1000 °C. A top plate was suspended 0.5 cm above the glass substrate to ensure a laminar flow. The substrates

were well cleaned prior to use, to remove surface grease. Two-way taps were used to divert the nitrogen carrier gas through the bubbler and the aerosol was carried into the reactor in a stream of nitrogen gas through a brass baffle to obtain a laminar flow. The total time for the deposition process was in the region of 2-3 hours. At the end of the deposition the nitrogen flow through the aerosol was diverted and only nitrogen passed over the substrate. The glass substrate was allowed to cool with the graphite block to less than 100 °C before it was removed. Coated substrates were handled and stored in air. Large pieces of glass (*ca.* 4 cm x 2 cm) were used for X-ray powder diffraction. The coated glass substrate was cut into *ca.* 1 cm x 1 cm squares for subsequent analysis by scanning electron microscopy (SEM), wavelength dispersive analysis of X-rays (WDX) and energy dispersive analysis of X-rays (EDX).

The mixed metal oxide film was generated *in situ* from the reaction of various metal alkyl precursors with excess HOCH₂CH₂OMe in toluene. HOCH₂CH₂OMe was procured from Aldrich and was further distilled, degassed and stored in a Young's tap flask over molecular sieves. Excess alcohol was used in order to minimise the risk of producing partially oxidised films. The reagents and solvent were individually cooled to -78 °C before mixing (due to the pyrophoric nature of metal alkyl species) and mixed in an inert atmosphere using standard Schlenk techniques. Reagents were left to stir for *ca.* 30 minutes prior to deposition. Depositions were carried out in toluene at a flow rate of 1.0 Lmin⁻¹ over a range of substrate temperatures (350 – 550 °C). Deposition times for each experiment differed. After the deposition the bubbler was closed and the substrate allowed to cool under flow of nitrogen. Quartz sheets were further annealed overnight at 1000 °C.

XRD patterns were measured on a Siemens D5000 diffractometer using monochromated Cu K α_1 radiation (K α_1 = 1.5406 Å). The diffractometer used glancing incident radiation (1.5 °). The samples were indexed using the GSAS programme and refined *via* the Rietveld method and were compared to database standards. EDAX was obtained on a Philips XL30ESEM instrument, and SEM on a JEOL 6301 instrument. UV-vis-NIR spectra were recorded in the range 190-1100 nm using a Helios double beam instrument. Reflectance and transmission spectra were recorded between 300 nm and 2300 nm by a Zeiss miniature spectrometer. Reflectance measurements were standardized relative to a rhodium mirror, and transmission relative to air.

4.4.2.1. AACVD reaction of GaMe₃ and HOCH₂CH₂OMe

HOCH₂CH₂OMe (0.0042 cm³, 5.26 mmol) was added dropwise to an AACVD bubbler containing a solution of GaMe₃ (0.55 g, 4.38 mmol) in toluene (20 cm³) at -78 °C. The reaction mixture was warmed to room temperature and allowed to react for 30 minutes prior to deposition.

The same procedure was used for the AACVD reaction of GaMe₃ and HOCH(CH₃)CH₂OMe and the AACVD reaction of GaMe₃ and HOCH₂CH₂NMe₂.

4.4.2.2. AACVD reaction of InMe₃, GaMe₃ and HOCH₂CH₂OMe

InMe₃ (1.3897 g, 8.7 mmol) and GaMe₃ (1.0094 g, 8.8 mmol) were cooled to -78 °C and each dissolved in pre-cooled toluene (*ca.* 15 cm³) at -78 °C. These were added dropwise to an AACVD flask along with the dropwise addition of HOCH₂CH₂OMe (6.2 cm³, 0.052 mol), this was allowed to sit for *ca.* 30 min before the deposition was started.

The same procedure was used for the AACVD reaction of InMe₃, GaMe₃ and HOCH₂CH₂OMe at deposition temperatures ranging from 350–450 °C.

4.4.2.3. AACVD reaction of GaMe₃, ZnEt₂ and HOCH₂CH₂OMe

ZnEt₂ (0.9601 g, 1.02 mmol) and GaMe₃ (0.1523 g, 1.33 mmol) were cooled to -78 °C and each dissolved in pre-cooled toluene (*ca.* 15 cm³) at -78 °C. These were added dropwise to an AACVD flask along with the dropwise addition of HOCH₂CH₂OMe (0.71 cm³, 6.01 mmol), this was allowed to sit for *ca.* 30 min before the deposition was started.

The same procedure was used for the AACVD reaction of GaMe₃, ZnEt₂ and HOCH₂CH₂OMe at deposition temperatures ranging from 350–450 °C.

4.5. References

1. X. H. Hou, K. L. Choy, *Chem. Vap. Deposition*, 2006, **12**, 583.
2. T. T. Kodas, M. J. Hampden-Smith, *The Chemistry of Metal CVD*. 1994, New York, VCH.
3. D. S. Ginley, C. Bright, *MRS Bull.*, 2000, **25**, 15.
4. J.-S. Kim, F. Cacialli, R. Friend, *Thin Solid Films*, 2003, **445**, 358.
5. T. J. Coutts, *Renew. Sust. Energ. Rev.*, 1999, **3**, 77.
6. T. J. Y. Coutts, D. L., Li, X., *Materials Research Society symposia proceedings* **623**, 2000.
7. A. J. P. Freeman, K. R.; Mason, T. O.; Chang, R. P. H.; Marks, T. J., *MRS Bull.*, 2000, **25**, 45.
8. C. G. Granqvist, A. Hultåker, *Thin Solid Films*, 2002, **411**, 1.
9. H. Hosono, H. Ohta, M. Orita, K. Ueda, M. Hirano, *Vacuum*, 2002, **66**, 419.
10. J. H. Hwang, D. D. Edwards, D. R. Kammler, T. O. Mason, *Solid State Ionics*, 2000, **129**, 135.
11. G. J. Exarhos, X. D. Zhou, *Thin Solid Films*, 2007, **515**, 7025.
12. A. C. Wang, N. L. Edleman, J. R. Babcock, T. J. Marks, M. A. Lane, P. R. Brazis, C. R. Kannewurf, *J. Mater. Res.*, 2002, **17**, 3155.
13. R. J. Cava, J. M. Phillips, J. Kwo, G. A. Thomas, R. B. Vandover, S. A. Carter, J. J. Krajewski, W. F. Peck, J. H. Marshall, D. H. Rapkine, *Appl. Phys. Lett.*, 1994, **64**, 2071.
14. J. Wang, Q. Yang, *Dalton Trans.*, 20086060.
15. D. D. Edwards, *J. Am. Ceram. Soc.*, 1997, **80**, 253.
16. T. Minami, Y. Takeda, T. Kakumu, S. Takata, I. Fukuda, *J. Vac. Sci. Technol. A*, 1997, **15**, 958.
17. T. Minami, *Mat. Res. Bull.*, 2000, **25**, 38.
18. T. J. Coutts, X. Wu, W. P. Mulligan, J. M. Webb, *J. Electron. Mater.*, 1996, **25**, 935.
19. T. Minami, Y. Takeda, S. Takata, T. Kakumu, *Thin Solid Films*, 1997, **308-309**, 13.
20. T. Omata, N. Ueda, K. Ueda, H. Kawazoe, *Appl. Phys. Lett.*, 1994, **64**, 1077.
21. Y. E. Lee, D. P. Norton, J. D. Budai, Y. Wei, *J. Appl. Phys.*, 2001, **90**, 3863.

22. E. J. J. Martin, M. Yan, M. Lane, J. Ireland, C. R. Kannewurf, R. P. H. Chang, *Thin Solid Films*, 2004, **461**, 309.
23. D. R. Sahu, S. Y. Lin, J. L. Huang, *Sol. Energ. Mater. Solar Cells*, 2007, **91**, 851.
24. J. J. Robbins, J. Esteban, C. Fry, C. A. Wolden, *J. Electrochem. Soc.*, 2003, **150**, 693.
25. M. Sawada, M. Higuchi, S. Kondo, H. Saka, *Jpn. J. Appl. Phys.*, 2001, **40**, 3332.
26. E. Fortunato, A. Goncalves, A. Marques, A. Viana, H. Aguas, L. Pereira, I. Ferreira, P. Vilarinho, R. Martins, *Surf. Coat. Tech.*, 2004, **180**, 20.
27. E. Fortunato, P. Nunes, D. Costa, D. Brida, I. Ferreira, R. Martins, *Vacuum*, 2002, **64**, 233.
28. X. Hao, J. Ma, D. Zhang, T. Yang, H. Ma, Y. Yang, C. Cheng, J. Huang, *Appl. Surf. Sci.*, 2001, **183**, 137.
29. C. S. Moon, Y. M. Chung, W. S. Jung, J. G. Han, *Surf. Coat. Tech.*, 2007, **201**, 287.
30. H. Ohta, K. Kawamura, M. Orita, M. Hirano, N. Sarukura, H. Hosono, *Appl. Phys. Lett.*, 2000, **77**, 475.
31. H. Ohta, M. Orita, M. Hirano, H. Hosono, *J. Appl. Phys.*, 2002, **91**, 3547.
32. T. Minami, *Semicond. Sci. Technol.*, 2005, **20**, S35.
33. Y. J. Li, Y. W. Kwon, M. Jones, Y. W. Heo, J. Zhou, S. C. Luo, P. H. Holloway, E. Douglas, D. P. Norton, Z. Park, S. Li, *Semicond. Sci. Technol.*, 2005, **20**, 720.
34. R. L. Hoffman, B. J. Norris, J. F. Wagner, *Appl. Phys. Lett.*, 2003, **82**, 733.
35. K. Nomura, H. Ohta, A. Takagi, T. Kamiya, M. Hirano, H. Hosono, *Nature*, 2004, **432**, 488.
36. C. Bundesmann, N. Ashkenov, M. Schubert, D. Spemann, T. Butz, E. M. Kaidashev, M. Lorenz, M. Grundmann, *Appl. Phys. Lett.*, 2003, **83**, 1974.
37. E. Egerton, A. K. Sood, R. Singh, Y. R. Puri, R. F. Davis, J. Pierce, D. C. Look, T. Steiner, *J. Electron. Mater.*, 2005, **34**, 949.
38. J. Hu, R. G. Gordon, *Sol. Cells*, 1991, **30**, 437.
39. B. H. Choi, H. B. Im, J. S. Song, K. H. Yoon, *Thin Solid Films*, 1990, **193**, 712.
40. H. J. Ko, Y. F. Chen, S. K. Hong, H. Wensch, T. Yao, *Appl. Phys. Lett.*, 2000, **77**, 3761.
41. R. Street, *Technology and Applications of Amorphous Silicon*. 2000, New York, Springer.

42. C. G. Granqvist, *Sol. Energ. Mater. Solar Cells*, 2007, **91**, 1529.
43. Y. R. Ryu, W. J. Kim, H. W. White, *J. Cryst. Growth*, 2000, **219**, 419.
44. F. Zhuge, L. P. Zhu, Z. Z. Ye, D. W. Ma, J. G. Lu, J. Y. Huang, F. Z. Wang, Z. G. Ji, S. B. Zhang, *Appl. Phys. Lett.*, 2005, **87**, 092103.
45. J. G. Lu, Z. Z. Ye, L. Wang, B. H. Zhao, J. Y. Huang, *Chin. Phys. Lett.*, 2002, **19**, 1494.
46. J. G. Lu, Z. Z. Ye, F. Zhuge, Y. J. Zeng, B. H. Zhao, L. P. Zhu, *Appl. Phys. Lett.*, 2004, **85**, 3134.
47. S. Yoshida, A. Tsukazaki, A. Ohtomo, M. Kawasaki, *Appl. Phys. Lett.*, 2004, **85**, 759.
48. G. A. Hirata, J. McKittrick, T. Cheeks, J. M. Siqueiros, J. A. Diaz, O. Contreras, O. A. Lopez, *Thin Solid Films*, 1996, **288**, 29.
49. S. S. Yi, I. W. Kim, H. L. Park, J. S. Bae, B. K. Moon, J. H. Jeong, *J. Cryst. Growth*, 2003, **247**, 213.
50. H. Naito, S. Fujihara, T. Kimura, *J. Sol-Gel Sci. Technol.*, 2003, **26**, 997.
51. R. G. Gordon, *MRS Bull.*, 2000, **25**, 52.
52. V. Assuncao, E. Fortunato, A. Marques, H. Aguas, I. Ferreira, M. E. V. Costa, *Thin Solid Films*, 2003, **427**, 401.
53. H. L. Hartnagel, A. L. Dawar, A. K. Jain, C. Jagadish, *Semiconducting Transparent Thin Films*. 1995, Bristol, Institute of Physics Publ. 110.
54. V. Fathollahi, M. M. Amini, *Mater. Lett.*, 2001, **50**, 235.
55. T. Minami, H. Nanto, S. S. S. Takata, *Thin Solid Films*, 1984, **111**, 167.
56. M. Hiramatsu, K. Imaeda, N. Horio, M. Nawata, *J. Vac. Sci. Technol. A*, 1998, **16**, 669.
57. J. H. Hu, R. G. Gordon, *J. Appl. Phys.*, 1992, **72**, 5381.
58. Y. Li, G. S. Tompa, S. Liang, C. Gorla, Y. Lu, J. Doyle, *J. Vac. Sci. Technol. A*, 1997, **15**, 1063.
59. R. Groenen, J. Löffler, P. M. Sommeling, J. L. Linden, E. A. G. Hamers, R. E. I. Schropp, M. C. M. v. d. Sansen, *Thin Solid Films*, 2001, **392**, 226.
60. S. Basharat, C. J. Carmalt, S. A. Barnett, D. A. Tocher, H. O. Davies, *Inorg. Chem.*, 2007, **46**, 9473.
61. S. Basharat, C. J. Carmalt, R. Palgrave, S. A. Barnett, D. A. Tocher, H. O. Davies, *J. Organomet. Chem.*, 2008, **693**, 1787.

62. S. Basharat, C. J. Carmalt, R. Binions, R. Palgrave, I. P. Parkin, *Dalton Trans.*, 2008591.
63. S. Basharat, C. J. Carmalt, S. J. King, E. S. Peters, D. A. Tocher, *Dalton Trans.*, 20043475.
64. R. Binions, C. J. Carmalt, I. P. Parkin, K. F. E. Pratt, G. A. Shaw, *Chem. Mater.*, 2004, **16**, 2489.
65. S. Suh, D. M. Hoffman, *J. Am. Chem. Soc.*, 2000, **122**, 9396.
66. Y. Chi, T. Y. Chou, Y. J. Wang, S. F. Huang, A. J. Carty, L. Scoles, K. A. Udachin, S. M. Peng, G. H. Lee, *Organometallics*, 2004, **23**, 95.
67. S. Basharat, C. J. Carmalt, R. Binions, R. Palgrave, I. P. Parkin, *Dalton Trans.*, 2008591.
68. A. d. S. Goncalves, M. R. Davolos, N. Masaki, S. Yanagida, A. Morandeira, J. R. Durrant, J. N. Freitas, A. F. Nogueira, *Dalton Trans.*, 20081487.
69. J. F. Moulder, W. F. Sticks, P. E. Sobol, K. D. Bomben, *Handbook of X-ray Photoelectron Spectroscopy*. 1995, USA, Physical Electronics Inc.
70. H. H. Wang, S. Baek, J. J. Song, J. Lee, S. W. Lim, *Nanotechnology*, 2008, **19**.

Chapter 5

Summary

This work is concerned with the synthesis of precursors to group 13 mixed metal oxide thin films, investigations into the mechanisms at work during their decomposition *via* various techniques including gas phase electron diffraction (GED), and the subsequent CVD using these precursors.

5.1. Chapter 2

This chapter describes the synthesis and characterization of a range of gallium and indium alkoxides. These compounds were prepared for application as single source precursors for the CVD of gallium and indium oxide thin films as discussed in Chapter 4. The group 13 monoalkoxometallanes of the type $[\text{Me}_2\text{M}(\text{OR}')_2]$ were synthesised by the reaction of Me_3Ga or Me_3In with $\text{R}'\text{OH}$ ($\text{M} = \text{Ga}$, $\text{R}' = \text{OCH}_2\text{CH}_2\text{OMe}$, $\text{OCH}_2\text{CH}_2\text{NMe}_2$, $\text{OC}(\text{CH}_3)_2\text{CH}_2\text{OMe}$, $\text{OCH}(\text{CF}_3)_2$ (**1–3**, **5**); $\text{M} = \text{In}$, $\text{R}' = \text{OCH}(\text{CH}_3)\text{CH}_2\text{OMe}$ (**4**) in toluene.

Additionally compounds of the type $[\text{Ga}(\text{OR}')_n\text{Cl}_{3-n}]$ were synthesised directly from the reaction of $\text{R}'\text{OH}$ with $[\text{Ga}(\text{NMe}_2)_n\text{Cl}_{3-n}]$ ($n = 1$ (**6**); 2 (**7**)) ($n = 1$, $\text{R}' = \text{OC}(\text{CH}_3)_2\text{CH}_2\text{OMe}$ (**8**); $n = 2$, $\text{R}' = \text{OCH}(\text{CH}_3)\text{CH}_2\text{NMe}_2$ (**9**), $\text{OCH}_2\text{CH}_2\text{NMe}_2$ (**10**)).

With a view to further enhancing the properties of these group 13 alkoxide precursors a series of protonolysis and alcoholysis steps were devised and carried out to synthesise a wide range of group 13 compounds of the type $[\text{Me}_x(\text{Cl})_{2-(x+z)}\text{M}\{\text{N}(\text{SiMe}_3)_2\}_{1-y}(\text{OR}')_y(\text{OR})_z]_2$ ($\text{M} = \text{Ga}$ (**11** – **19**); $\text{M} = \text{In}$ (**20** – **27**)) incorporating a variety of donor functionalised alkoxide ligands ($\text{R}' = \text{OCH}_2\text{CH}_2\text{OMe}$, $\text{OCH}_2\text{CH}_2\text{NMe}_2$, $\text{OCH}(\text{CH}_3)\text{CH}_2\text{OMe}$, $\text{OC}(\text{CH}_3)_2\text{CH}_2\text{NMe}_2$, ...) and a simple alkoxide ligand ($\text{R} = \text{O}^i\text{Bu}$) to act as precursors to group 13 oxide thin films. The variety in size of ligands surrounding the metal centre further enhances solubility, lowers the temperature of vapourization and enables facile decomposition; all of which are desired properties for CVD.

Finally the synthesis of homoleptic group 13 tris(alkoxide) $[\text{Ga}(\text{O}^i\text{Pr})_3]$ (**28**) and cluster compound $[(\text{InO}^i\text{Pr})_5(\mu_2\text{-O}^i\text{Pr})_4(\mu_3\text{-O}^i\text{Pr})_4(\mu_5\text{-O})]$ (**29a**) was achieved by reaction of MCl_3 with three equivalents of $\text{Ba}(\text{O}^i\text{Pr})_2$ as characterized by spectroscopic data.

5.2. Chapter 3

Chapter 3 describes the synthesis and structures of the dimethylalkoxygallanes $[\text{Me}_2\text{GaOCH}_2\text{CH}_2\text{NMe}_2]_2$ (**30**) and $[\text{Me}_2\text{GaOCH}_2\text{CH}_2\text{OMe}]_2$ (**31**) from studying the vapour produced upon heating, *via* gas-phase electron diffraction and *ab initio* molecular orbital calculations. Only the monomeric forms $[\text{Me}_2\text{GaOCH}_2\text{CH}_2\text{NMe}_2]$ (**30a**), $[\text{Me}_2\text{GaOCH}_2\text{CH}_2\text{OMe}]$ (**31a**) are observed in the vapour, with the nitrogen (**30**) and oxygen (**31**) atoms respectively, forming a dative bond with the metal centre.

Interestingly this work has shown that whilst compound **32**, $[\text{Me}_2\text{Ga}(\text{O}^i\text{Bu})]_2$ retains its dimeric structure in the gas phase, compounds **30** and **31** are monomeric in the gas phase. Therefore, although dialkylalkoxygallanes incorporating donor functionalised ligands generally adopt dimeric structures in the solid state, in the gas phase monomers are likely to be present. Monomers are expected to exhibit enhanced volatility in comparison to oligomeric complexes in which intermolecular solid-state interactions are

likely to increase the enthalpy of vapourisation. However, this work shows that the structure adopted in the solid state may differ from that in the gas phase and so compounds that appear unsuitable for CVD may in fact be feasible precursors. Overall, this study has provided information that can be used to aid the design of precursor molecules for a range of technologically important materials.

Additionally the thermal decomposition of a selection of compounds has been studied using TGA and DSC. These techniques have shown the group 13 alkoxides have potential for use as precursors in the production of thin films *via* CVD. All of the compounds analysed, decompose to the desired binary material (M_2O_3), below 400 °C, so are viable as low temperature alternatives to many precursors reported.

5.3. Chapter 4

This chapter describes a selection of the gallium and indium alkoxides, synthesised as described in Chapter 2, for CVD, it also explores the synthesis of mixed metal oxide thin films. The deposition of thin films from the metal alkoxides is achieved by AACVD.

The AACVD of $GaMe_3$ and ROH (R = $C(CH_3)_2CH_2OMe$, CH_2CH_2OMe , $CH_2CH_2NMe_2$) resulted in the formation of Ga_2O_3 films on glass. Gallium oxide films have now been grown via AACVD using a variety of group 13 precursors. Films are not oxygen deficient and little carbon contamination was observed, this is attributed to being as a direct result of precursor design.

Transparent electrically conductive gallium indium oxide films have been grown for the first time *via* AACVD using Me_3In , Me_3Ga and $HOCH_2CH_2OMe$ under AACVD conditions. Furthermore the *in situ* reaction of the reagents eliminates the need for the synthesis, isolation and purification of a single-source metal alkoxide precursor. Rietveld refinement can assign XRD patterns to a cubic homogeneously Ga-substituted In_2O_3 structure.

The AACVD of $ZnEt_2$, $GaMe_3$ and $HOCH_2CH_2OMe$ resulted in the formation of gallium doped zinc oxide films on glass. As with all results reported herein the *in situ*

reaction of the reagents eliminates the need for the synthesis, isolation and purification of a single-source metal alkoxide precursor. A Le Bail refinement of the XRD data confirms the synthesis of gallium doped zinc oxide, with comparable lattice parameter with literature reports. This is the first reported instance of deposition of thin films of gallium doped zinc oxide *via* AACVD to date.

5.4. Summary

A wide variety of group 13 alkoxides have been synthesised and characterised in this thesis. Significant findings in Chapter 2 support previous investigations showing the reaction of $[MR_3]$ with excess of a donor functionalised alcohol does not yield a group 13 bis(alkoxide). In addition compounds of the type $[Ga(OR')_nCl_{3-n}]$ (**8-10**) were synthesised using direct routes from precursors (**6, 7**) also synthesised, as well as a wide variety of novel group 13 precursors ($M = Ga$ (**11 – 19**); $M = In$ (**20 – 27**)) incorporating a mixture of ligands leading to enhanced properties, desirable for CVD. Additionally, the synthesis of homoleptic group 13 tris(alkoxides) **28** and **29a** *via* a novel barium chloride elimination route is reported as characterized by spectroscopic data.

Many of these compounds have been characterised by a variety of techniques including X-ray crystallography, which show that compounds of the form $[X_2M(OR')]_2$ ($X = Cl, Et, Me$) are dimeric in the solid state whilst compounds of the type $[XM(OR')]_2$ ($X = Cl, Et, Me$) are monomeric in the solid state.

GED has elucidated the structures of $[Me_2GaOCH_2CH_2NMe_2]_2$ (**30**) and $[Me_2GaOCH_2CH_2OMe]_2$ (**31**) in the gas-phase as the monomeric forms: $[Me_2GaOCH_2CH_2NMe_2]$ (**31a**), $[Me_2GaOCH_2CH_2OMe]$ (**32a**), and the dimeric gas phase structure of $[Me_2GaO^tBu]_2$ (**32**). Overall, this study has provided information that can be used to aid the design of precursor molecules for a range of technologically important materials.

Lastly Chapter 4 shows the synthesis of smooth transparent electrically conductive mixed metal oxide films, grown for the first time *via* AACVD using a variety of volatile precursors, including Et_2Zn , Me_3In , Me_3Ga and $HOCH_2CH_2OMe$ under AACVD

conditions. Furthermore the *in situ* reaction of the reagents eliminates the need for the synthesis, isolation and purification of a single-source mixed metal alkoxide precursor. Rietveld refinement has been utilized to assign the XRD patterns to a cubic homogeneously Ga-substituted In_2O_3 structure and a gallium doped zinc oxide material.

Appendices

A.1 List of Publications

1. C. J. Carmalt, C. E. Knapp, S. E. Potts. *Molecular design of precursors for the CVD of metal oxides and nitrides*. Abstracts of Papers, 237th ACS National Meeting, Salt Lake City, UT, United States, March 22-26, 2009 (2009).
2. C. E. Knapp, C. J. Carmalt, L. Pemberton, D. Pugh, P. F. McMillan, S. A. Barnett; D. A. Tocher. *Synthesis, AACVD and X-ray crystallographic structures of group 13 monoalkoxometallanes*. Main Group Chemistry. (2009), in press
3. C. E. Knapp, C. J. Carmalt, P. F. McMillan, D. A. Wann, H. E. Robertson, D. W. H. Rankin. *Dimethylalkoxygallane incorporating a donor-functionalised alkoxide: the monomeric gas-phase structure*. Dalton Trans. (2008), 48, 6880-6882.
4. S. Basharat, C. E. Knapp, C. J. Carmalt, S. A. Barnett, D. A. Tocher. *Synthesis and structures of gallium alkoxides*. New J. Chem. (2008), 32, 1513-1518.
5. C. J. Carmalt, C. E. Knapp, P. F. McMillan. *Group 13 amides and alkoxides: Synthesis, reactivity and thermal decomposition*. Abstracts of Papers, 234th ACS National Meeting, Boston, MA, United States, August 19-23, (2007).
6. D. A. Wann, C. E. Knapp, J. T. Schirlin, H. E. Robertson, S. L. Masters, C. J. Carmalt, D. W. H. Rankin. *The monomeric structures $Me_2GaOCH_2CH_2NMe_2$ and $Me_2GaOCH_2CH_2OMe$ and the dimeric structure $[Me_2GaO^iBu]_2$ by gas-phase electron diffraction*. J. Am. Chem. Soc. (2009), in preparation.
7. C. E. Knapp, C. J. Carmalt, Y. S. Shin, F. Cacialli, P. F. McMillan. *AACVD of a novel gallium doped indium oxide semiconducting phase*. J. Mater. Chem. (2009), in preparation.
8. C. E. Knapp, C. J. Carmalt, P. F. McMillan. *AACVD of gallium zinc oxide films*. Chem. Mater. (2009), in preparation.

A.2 Crystal data for [Me₂Ga(OC(CH₃)₂CH₂OMe)]₂ (**3**)

Chemical formula	C ₇ H ₁₇ GaO ₂	
Formula weight	202.93	
Temperature	150(2) K	
Radiation, wavelength	MoK α , 0.71073 Å	
Crystal system, space group	Monoclinic, P2 ₁ n	
Unit cell parameters	$a = 10.4812(12)$ Å	$\alpha = 90^\circ$
	$b = 8.6035(10)$ Å	$\beta = 95.252(2)^\circ$
	$c = 10.8725(13)$ Å	$\gamma = 90^\circ$
Cell volume	976.3(2) Å ³	
Z	4	
Calculated density	1.381 g/cm ³	
Absorption coefficient	2.768 mm ⁻¹	
F(000)	424	
Crystal colour and size	Colourless, 0.96 × 0.22 × 0.16 mm ³	
Reflections for cell refinement	4107 (θ range 2.584 to 28.124°)	
Data collection method	Bruker SMART APEX diffractometer ω rotation with narrow frames	
θ range for data collection	2.58 to 28.19°	
Index ranges	$h -13$ to 13, $k -11$ to 11, $l -14$ to 14	
Completeness to $\theta = 26.00^\circ$	98.6 %	
Intensity decay	None	
Reflections collected	8528	
Independent reflections	2439 ($R_{\text{int}} = 0.0366$)	
Reflections with $F^2 > 2\sigma$	2039	
Absorption correction	semi-empirical from equivalents	
Min. and max. transmission	0.5037 and 1.0000	
Structure solution	direct methods	
Refinement method	Full-matrix least-squares on F^2	
Weighting parameters a, b	0.0362, 0.2767	

Data / restraints / parameters	2283 / 0 / 96
Final R indices [$F^2 > 2\sigma$]	R1 = 0.0247, wR2 = 0.0635
R indices (all data)	R1 = 0.0288, wR2 = 0.0650
Goodness-of-fit on F^2	1.042
Largest and mean shift/su	0.002 and 0.000
Largest diff. peak and hole	0.533 and $-0.430 \text{ e } \text{\AA}^{-3}$

Atomic coordinates and equivalent isotropic displacement parameters (\AA^2) for compound **3**. U_{eq} is defined as one third of the trace of the orthogonalized U^{ij} tensor.

	<i>x</i>	<i>y</i>	<i>z</i>	U_{eq}
Ga1	0.524407(17)	0.32544(2)	0.523124(16)	0.01952(8)
O1	0.61288(11)	0.51195(13)	0.47979(10)	0.0203(2)
C1	0.7192(2)	0.4849(3)	0.29210(18)	0.0346(4)
C2	0.73495(16)	0.5188(2)	0.43093(16)	0.0229(3)
C3	0.79361(19)	0.6794(2)	0.4562(2)	0.0297(4)
C4	0.82123(17)	0.3981(2)	0.49805(19)	0.0288(4)
O2	0.75995(13)	0.25116(15)	0.48187(13)	0.0312(3)
C5	0.8350(2)	0.1284(3)	0.5382(2)	0.0439(5)
C6	0.5675(2)	0.2701(2)	0.69754(17)	0.0321(4)
C7	0.4722(2)	0.1861(2)	0.38491(19)	0.0310(4)

Bond lengths [\AA] and angles [$^\circ$] for compound **3**.

Ga1–O1	1.9331(11)	Ga1–C7	1.9605(19)
Ga1–C6	1.9672(18)	Ga1–O1#1	2.0051(11)

Ga1-O2	2.6282(14)	O1-C2	1.431(2)
O1-Ga1#1	2.0051(11)	C1-C2	1.531(3)
C1-H1A	0.9800	C1-H1B	0.9800
C1-H1C	0.9800	C2-C4	1.519(2)
C2-C3	1.527(2)	C3-H3A	0.9800
C3-H3B	0.9800	C3-H3C	0.9800
C4-O2	1.422(2)	C4-H4A	0.9900
C4-H4B	0.9900	O2-C5	1.421(2)
C5-H5A	0.9800	C5-H5B	0.9800
C5-H5C	0.9800	C6-H6A	0.9800
C6-H6B	0.9800	C6-H6C	0.9800
C7-H7A	0.9800	C7-H7B	0.9800
C7-H7C	0.9800		
O1-Ga1-C7	115.29(7)	O1-Ga1-C6	111.28(7)
C7-Ga1-C6	127.90(9)	O1-Ga1-O1#1	77.09(5)
C7-Ga1-O1#1	105.37(7)	C6-Ga1-O1#1	106.56(7)
O1-Ga1-O2	71.41(5)	C7-Ga1-O2	85.47(7)
C6-Ga1-O2	88.25(7)	O1#1-Ga1-O2	148.31(4)
C2-O1-Ga1	126.14(10)	C2-O1-Ga1#1	129.07(10)
Ga1-O1-Ga1#1	102.91(5)	C2-C1-H1A	109.5
C2-C1-H1B	109.5	H1A-C1-H1B	109.5
C2-C1-H1C	109.5	H1A-C1-H1C	109.5
H1B-C1-H1C	109.5	O1-C2-C4	107.87(14)

O1-C2-C3	109.22(14)	C4-C2-C3	108.64(14)
O1-C2-C1	109.81(14)	C4-C2-C1	110.42(15)
C3-C2-C1	110.81(16)	C2-C3-H3A	109.5
C2-C3-H3B	109.5	H3A-C3-H3B	109.5
C2-C3-H3C	109.5	H3A-C3-H3C	109.5
H3B-C3-H3C	109.5	O2-C4-C2	107.82(14)
O2-C4-H4A	110.1	C2-C4-H4A	110.1
O2-C4-H4B	110.1	C2-C4-H4B	110.1
H4A-C4-H4B	108.5	C5-O2-C4	112.43(15)
C5-O2-Ga1	126.77(13)	C4-O2-Ga1	100.57(10)
O2-C5-H5A	109.5	O2-C5-H5B	109.5
H5A-C5-H5B	109.5	O2-C5-H5C	109.5
H5A-C5-H5C	109.5	H5B-C5-H5C	109.5
Ga1-C6-H6A	109.5	Ga1-C6-H6B	109.5
H6A-C6-H6B	109.5	Ga1-C6-H6C	109.5
H6A-C6-H6C	109.5	H6B-C6-H6C	109.5
Ga1-C7-H7A	109.5	Ga1-C7-H7B	109.5
H7A-C7-H7B	109.5	Ga1-C7-H7C	109.5
H7A-C7-H7C	109.5	H7B-C7-H7C	109.5
O1-Ga1-C7	115.29(7)	O1-Ga1-C6	111.28(7)
C7-Ga1-C6	127.90(9)	O1-Ga1-O1#1	77.09(5)
C7-Ga1-O1#1	105.37(7)	C6-Ga1-O1#1	106.56(7)
O1-Ga1-O2	71.41(5)	C7-Ga1-O2	85.47(7)

C6–Ga1–O2	88.25(7)	O1#1–Ga1–O2	148.31(4)
C2–O1–Ga1	126.14(10)	C2–O1–Ga1#1	129.07(10)
Ga1–O1–Ga1#1	102.91(5)	C2–C1–H1A	109.5
C2–C1–H1B	109.5	H1A–C1–H1B	109.5
C2–C1–H1C	109.5	H1A–C1–H1C	109.5

Symmetry operations for equivalent atoms

#1 $-x+1, -y+1, -z+1$

Anisotropic displacement parameters (\AA^2) for compound **3**. The anisotropic displacement factor exponent takes the form: $-2\pi^2[h^2a^*U^{11} + \dots + 2hka^*b^*U^{12}]$

	U^{11}	U^{22}	U^{33}	U^{23}	U^{13}	U^{12}
Ga1	0.02534(13)	0.01449(11)	0.01855(12)	0.00034(6)	0.00103(8)	-0.00126(7)
O1	0.0218(6)	0.0169(6)	0.0229(6)	0.0003(4)	0.0051(4)	-0.0009(4)
C1	0.0349(10)	0.0440(12)	0.0261(9)	-0.0050(8)	0.0101(7)	-0.0009(9)
C2	0.0212(8)	0.0234(9)	0.0246(8)	-0.0009(7)	0.0049(6)	-0.0027(7)
C3	0.0271(10)	0.0251(10)	0.0370(11)	0.0038(7)	0.0037(8)	-0.0065(7)
C4	0.0239(9)	0.0240(10)	0.0382(11)	-0.0022(8)	0.0006(8)	-0.0010(7)
O2	0.0285(7)	0.0201(7)	0.0441(8)	-0.0015(6)	-0.0018(6)	0.0010(5)
C5	0.0447(13)	0.0260(10)	0.0590(15)	-0.0007(10)	-0.0058(11)	0.0093(9)
C6	0.0411(11)	0.0304(10)	0.0244(9)	0.0061(8)	0.0013(8)	0.0028(8)
C7	0.0354(11)	0.0247(10)	0.0325(10)	-0.0088(7)	0.0001(8)	-0.0025(7)

A.3 Crystal data for [Me₂In(OCH(CH₃)CH₂OMe)]₂ (**4**)

Empirical formula	C ₁₂ H ₃₀ In ₂ O ₄
Formula weight	468.00
Temperature	150(2) K
Wavelength	0.71073 Å
Crystal system	Monoclinic
Space group	P21/c
Unit cell dimensions	$a = 7.158(3) \text{ \AA}$ $\alpha = 90^\circ$. $b = 8.173(3) \text{ \AA}$ $\beta = 97.831(6)^\circ$. $c = 16.048(6) \text{ \AA}$ $\gamma = 90^\circ$.
Volume	930.1(6) Å ³
Z	2
Density (calculated)	1.671 Mg/m ³
Absorption coefficient	2.483 mm ⁻¹
F(000)	464
Crystal size	0.20 × 0.10 × 0.02 mm ³
Theta range for data collection	2.80 to 28.29°.
Index ranges	-9 ≤ h ≤ 9, -10 ≤ k ≤ 10, -20 ≤ l ≤ 20
Reflections collected	7650
Independent reflections	2210 [R(int) = 0.0409]
Completeness to theta = 28.29°	95.6 %
Absorption correction	Semi-empirical from equivalents
Max. and min. transmission	0.9520 and 0.6365
Refinement method	Full-matrix least-squares on F ²
Data / restraints / parameters	2210 / 0 / 86
Goodness-of-fit on F ²	1.143
Final R indices [I > 2σ(I)]	R1 = 0.0507, wR2 = 0.1203
R indices (all data)	R1 = 0.0634, wR2 = 0.1254
Largest diff. peak and hole	1.796 and -1.388 e.Å ⁻³

Atomic coordinates ($\times 10^4$) and equivalent isotropic displacement parameters ($\text{\AA}^2 \times 10^3$) for compound **4**. $U(\text{eq})$ is defined as one third of the trace of the orthogonalized U^{ij} tensor.

	<i>x</i>	<i>y</i>	<i>z</i>	$U(\text{eq})$
C(1)	6726(10)	1989(9)	3632(5)	39(2)
C(2)	1861(11)	-250(11)	3450(5)	46(2)
C(3)	1596(11)	4375(9)	3540(4)	39(2)
C(4)	2383(9)	3689(8)	4984(4)	28(1)
C(5)	3836(11)	2826(9)	5578(4)	40(2)
C(6)	3296(11)	2789(9)	6461(4)	39(2)
O(1)	4193(6)	1267(5)	5289(3)	26(1)
O(2)	2882(7)	3613(6)	4164(3)	37(1)
In(1)	4398(1)	777(1)	4015(1)	28(1)

Bond lengths [Å] and angles [°] for compound **4**

C(1)-In(1)	2.102(7)	In(1)-C(1)-H(1C)	109.5
C(1)-H(1A)	0.9800	H(1A)-C(1)-H(1C)	109.5
C(1)-H(1B)	0.9800	H(1B)-C(1)-H(1C)	109.5
C(1)-H(1C)	0.9800	In(1)-C(2)-H(2A)	109.5
C(2)-In(1)	2.092(8)	In(1)-C(2)-H(2B)	109.5
C(2)-H(2A)	0.9800	H(2A)-C(2)-H(2B)	109.5
C(2)-H(2B)	0.9800	In(1)-C(2)-H(2C)	109.5
C(2)-H(2C)	0.9800	H(2A)-C(2)-H(2C)	109.5
C(3)-O(2)	1.410(8)	H(2B)-C(2)-H(2C)	109.5
C(3)-H(3A)	0.9800	O(2)-C(3)-H(3A)	109.5
C(3)-H(3B)	0.9800	O(2)-C(3)-H(3B)	109.5
C(3)-H(3C)	0.9800	H(3A)-C(3)-H(3B)	109.5
C(4)-O(2)	1.412(8)	O(2)-C(3)-H(3C)	109.5
C(4)-C(5)	1.490(10)	H(3A)-C(3)-H(3C)	109.5
C(4)-H(4A)	0.9900	H(3B)-C(3)-H(3C)	109.5
C(4)-H(4B)	0.9900	O(2)-C(4)-C(5)	109.4(5)
C(5)-O(1)	1.392(8)	O(2)-C(4)-H(4A)	109.8
C(5)-C(6)	1.519(9)	C(5)-C(4)-H(4A)	109.8
C(5)-H(5)	1.0000	O(2)-C(4)-H(4B)	109.8
C(6)-H(6A)	0.9800	C(5)-C(4)-H(4B)	109.8
C(6)-H(6B)	0.9800	H(4A)-C(4)-H(4B)	108.2
C(6)-H(6C)	0.9800	O(1)-C(5)-C(4)	111.4(6)
O(1)-In(1)	2.107(4)	O(1)-C(5)-C(6)	112.0(6)
O(1)-In(1)#1	2.179(4)	C(4)-C(5)-C(6)	111.2(6)
O(2)-In(1)	2.584(5)	O(1)-C(5)-H(5)	107.3
In(1)-O(1)#1	2.179(4)	C(4)-C(5)-H(5)	107.3
In(1)-C(1)-H(1A)	109.5	C(6)-C(5)-H(5)	107.3
In(1)-C(1)-H(1B)	109.5	C(5)-C(6)-H(6A)	109.5
H(1A)-C(1)-H(1B)	109.5	C(5)-C(6)-H(6B)	109.5

H(6A)-C(6)-H(6B)	109.5	C(2)-In(1)-C(1)	137.6(3)
C(5)-C(6)-H(6C)	109.5	C(2)-In(1)-O(1)	109.0(3)
H(6A)-C(6)-H(6C)	109.5	C(1)-In(1)-O(1)	110.9(2)
H(6B)-C(6)-H(6C)	109.5	C(2)-In(1)-O(1)#1	103.2(3)
C(5)-O(1)-In(1)	122.5(4)	C(1)-In(1)-O(1)#1	100.5(2)
C(5)-O(1)-In(1)#1	128.6(4)	O(1)-In(1)-O(1)#1	74.77(17)
In(1)-O(1)-In(1)#1	105.23(17)	C(2)-In(1)-O(2)	92.8(3)
C(3)-O(2)-C(4)	114.8(5)	C(1)-In(1)-O(2)	87.9(2)
C(3)-O(2)-In(1)	125.0(4)	O(1)-In(1)-O(2)	69.79(15)
C(4)-O(2)-In(1)	106.8(4)	O(1)#1-In(1)-O(2)	144.23(15)

Symmetry transformations used to generate equivalent atoms:

#1 -x+1,-y,-z+1

Anisotropic displacement parameters ($\text{\AA}^2 \times 10^3$) for compound **4**. The anisotropic displacement factor exponent takes the form: $-2\pi^2 [h^2 a^{*2} U^{11} + \dots + 2 h k a^* b^* U^{12}]$

	U11	U22	U33	U23	U13	U12
C(1)	38(4)	41(4)	38(4)	-3(3)	10(3)	-5(3)
C(2)	43(4)	49(4)	46(4)	-10(4)	4(4)	-2(4)
C(3)	44(4)	41(4)	31(4)	15(3)	2(3)	10(3)
C(4)	32(3)	22(3)	32(3)	1(2)	10(3)	2(2)
C(5)	53(4)	35(4)	32(4)	-4(3)	11(3)	8(3)
C(6)	57(5)	37(4)	25(3)	-2(3)	9(3)	16(3)
O(1)	40(2)	21(2)	19(2)	2(2)	5(2)	10(2)
O(2)	48(3)	35(3)	29(2)	3(2)	6(2)	17(2)
In(1)	29(1)	29(1)	27(1)	-2(1)	4(1)	1(1)

A.4 Crystal data for $[\text{Cl}_2\text{Ga}(\text{OCH}_2\text{CH}_2\text{NMe}_2)]_2$ (**13**)

Empirical formula	C ₈ H ₂₀ Cl ₄ Ga ₂ N ₂ O ₂	
Formula weight	457.50	
Temperature	150(2) K	
Wavelength	0.71073 Å	
Crystal system	Monoclinic	
Space group	P2 ₁ /n	
Unit cell dimensions	$a = 6.9853(13)$ Å	$\alpha = 90^\circ$.
	$b = 10.2533(18)$ Å	$\beta = 91.840(3)^\circ$.
	$c = 11.877(2)$ Å	$\gamma = 90^\circ$.
Volume	850.2(3) Å ³	
Z	2	
Density (calculated)	1.787 Mg/m ³	
Absorption coefficient	3.792 mm ⁻¹	
F(000)	456	
Crystal size	0.20 × 0.20 × 0.10 mm ³	
Theta range for data collection	2.62 to 28.23°.	
Index ranges	-9 ≤ h ≤ 9, -13 ≤ k ≤ 13, -15 ≤ l ≤ 15	
Reflections collected	7044	
Independent reflections	2027 [R(int) = 0.0268]	
Completeness to theta = 28.23°	96.3 %	
Absorption correction	Semi-empirical from equivalents	
Max. and min. transmission	0.6860 and 0.4890	
Refinement method	Full-matrix least-squares on F ²	
Data / restraints / parameters	2027 / 0 / 84	
Goodness-of-fit on F ²	1.069	
Final R indices [I > 2σ(I)]	R1 = 0.0312, wR2 = 0.0837	
R indices (all data)	R1 = 0.0359, wR2 = 0.0860	
Largest diff. peak and hole	0.593 and -0.671 e.Å ⁻³	

Table 2. Atomic coordinates ($\times 10^4$) and equivalent isotropic displacement parameters ($\text{\AA}^2 \times 10^3$) for compound **13**. $U(\text{eq})$ is defined as one third of the trace of the orthogonalized U^{ij} tensor.

	x	y	z	$U(\text{eq})$
C(1)	2882(4)	9444(3)	6311(2)	27(1)
C(2)	3818(4)	8297(3)	5749(3)	32(1)
C(3)	3165(6)	6436(3)	4528(4)	54(1)
C(4)	1334(6)	6754(4)	6198(3)	55(1)
N(1)	2312(3)	7420(2)	5275(2)	28(1)
O(1)	1337(3)	9829(2)	5589(2)	42(1)
Cl(1)	-1812(1)	7223(1)	4114(1)	39(1)
Cl(2)	1920(2)	9093(1)	2869(1)	55(1)
Ga(1)	444(1)	8698(1)	4397(1)	26(1)

Table 3. Bond lengths [Å] and angles [°] for compound **13**.

C(1)-O(1)	1.413(3)	C(1)-C(2)-H(2B)	109.8
C(1)-C(2)	1.511(4)	H(2A)-C(2)-H(2B)	108.3
C(1)-H(1A)	0.9900	N(1)-C(3)-H(3A)	109.5
C(1)-H(1B)	0.9900	N(1)-C(3)-H(3B)	109.5
C(2)-N(1)	1.481(4)	H(3A)-C(3)-H(3B)	109.5
C(2)-H(2A)	0.9900	N(1)-C(3)-H(3C)	109.5
C(2)-H(2B)	0.9900	H(3A)-C(3)-H(3C)	109.5
C(3)-N(1)	1.481(4)	H(3B)-C(3)-H(3C)	109.5
C(3)-H(3A)	0.9800	N(1)-C(4)-H(4A)	109.5
C(3)-H(3B)	0.9800	N(1)-C(4)-H(4B)	109.5
C(3)-H(3C)	0.9800	H(4A)-C(4)-H(4B)	109.5
C(4)-N(1)	1.478(4)	N(1)-C(4)-H(4C)	109.5
C(4)-H(4A)	0.9800	H(4A)-C(4)-H(4C)	109.5
C(4)-H(4B)	0.9800	H(4B)-C(4)-H(4C)	109.5
C(4)-H(4C)	0.9800	C(4)-N(1)-C(3)	109.5(3)
N(1)-Ga(1)	2.103(2)	C(4)-N(1)-C(2)	109.8(2)
O(1)-Ga(1)	1.9195(19)	C(3)-N(1)-C(2)	110.3(2)
O(1)-Ga(1)#1	1.9571(19)	C(4)-N(1)-Ga(1)	111.2(2)
Cl(1)-Ga(1)	2.2017(8)	C(3)-N(1)-Ga(1)	112.5(2)
Cl(2)-Ga(1)	2.1533(9)	C(2)-N(1)-Ga(1)	103.41(16)
Ga(1)-O(1)#1	1.9571(19)	C(1)-O(1)-Ga(1)	120.17(16)
O(1)-C(1)-C(2)	106.4(2)	C(1)-O(1)-Ga(1)#1	133.15(16)
O(1)-C(1)-H(1A)	110.4	Ga(1)-O(1)-Ga(1)#1	106.32(9)
C(2)-C(1)-H(1A)	110.4	O(1)-Ga(1)-O(1)#1	73.68(9)
O(1)-C(1)-H(1B)	110.4	O(1)-Ga(1)-N(1)	80.13(9)
C(2)-C(1)-H(1B)	110.4	O(1)#1-Ga(1)-N(1)	149.46(9)
H(1A)-C(1)-H(1B)	108.6	O(1)-Ga(1)-Cl(2)	110.80(8)
N(1)-C(2)-C(1)	109.2(2)	O(1)#1-Ga(1)-Cl(2)	100.59(8)
N(1)-C(2)-H(2A)	109.8	N(1)-Ga(1)-Cl(2)	103.22(7)
C(1)-C(2)-H(2A)	109.8	O(1)-Ga(1)-Cl(1)	137.84(8)
N(1)-C(2)-H(2B)	109.8	O(1)#1-Ga(1)-Cl(1)	94.55(7)

N(1)-Ga(1)-Cl(1) 94.43(7) Cl(2)-Ga(1)-Cl(1) 111.13(4)

Symmetry transformations used to generate equivalent atoms: #1 -x,-y+2,-z+1

Table 4. Anisotropic displacement parameters ($\text{\AA}^2 \times 10^3$) for compound **13**. The anisotropic displacement factor exponent takes the form: $-2\pi^2 [h^2 a^{*2} U^{11} + \dots + 2 h k a^* b^* U^{12}]$

	U ¹¹	U ²²	U ³³	U ²³	U ¹³	U ¹²
C(1)	30(1)	25(1)	26(1)	2(1)	-9(1)	3(1)
C(2)	25(1)	26(1)	43(2)	-1(1)	-8(1)	4(1)
C(3)	53(2)	33(2)	77(3)	-22(2)	-15(2)	21(2)
C(4)	81(3)	42(2)	41(2)	19(2)	-14(2)	-29(2)
N(1)	32(1)	19(1)	32(1)	2(1)	-4(1)	3(1)
O(1)	51(1)	30(1)	42(1)	-20(1)	-30(1)	21(1)
Cl(1)	33(1)	39(1)	46(1)	-10(1)	-3(1)	-6(1)
Cl(2)	65(1)	66(1)	35(1)	13(1)	1(1)	-20(1)
Ga(1)	32(1)	18(1)	25(1)	-5(1)	-9(1)	5(1)

A.5 Crystal data for [Me{Cl}Ga(O^tBu)]₂ (**17**)

Empirical formula	C ₁₀ H ₂₄ Cl ₂ Ga ₂ O ₂
Formula weight	386.63
Temperature	150(2) K
Wavelength	0.71073 Å
Crystal system	Monoclinic
Space group	P2 ₁ /n
Unit cell dimensions	$a = 7.0602(6)$ Å $\alpha = 90^\circ$. $b = 15.1857(13)$ Å $\beta = 99.4220(10)^\circ$. $c = 8.1299(7)$ Å $\gamma = 90^\circ$.
Volume	859.88(13) Å ³
Z	2
Density (calculated)	1.493 Mg/m ³
Absorption coefficient	3.431 mm ⁻¹
F(000)	392
Crystal size	0.10 × 0.10 × 0.10 mm ³
Theta range for data collection	2.87 to 28.29°.
Index ranges	-9 ≤ h ≤ 9, -20 ≤ k ≤ 20, -10 ≤ l ≤ 10
Reflections collected	7075
Independent reflections	2020 [R(int) = 0.0235]
Completeness to theta = 28.29°	94.5 %
Absorption correction	Semi-empirical from equivalents
Max. and min. transmission	0.7109 and 0.7109
Refinement method	Full-matrix least-squares on F ²
Data / restraints / parameters	2020 / 0 / 77
Goodness-of-fit on F ²	1.120
Final R indices [I > 2σ(I)]	R1 = 0.0356, wR2 = 0.0720
R indices (all data)	R1 = 0.0415, wR2 = 0.0750
Largest diff. peak and hole	0.674 and -0.646 e.Å ⁻³

Table 2. Atomic coordinates ($\times 10^4$) and equivalent isotropic displacement parameters ($\text{\AA}^2 \times 10^3$) for compound **17**. $U(\text{eq})$ is defined as one third of the trace of the orthogonalized U^{ij} tensor.

	x	y	z	$U(\text{eq})$
C(1)	2862(5)	4716(3)	8260(4)	39(1)
C(2)	1258(5)	3480(2)	3895(4)	29(1)
C(3)	569(7)	2720(2)	4840(6)	51(1)
C(4)	3426(6)	3554(3)	4224(6)	49(1)
C(5)	548(7)	3402(3)	2045(5)	52(1)
O(1)	446(3)	4286(1)	4475(2)	25(1)
Cl(1)	-1996(1)	4061(1)	7566(1)	37(1)
Ga(1)	475(1)	4676(1)	6721(1)	23(1)

Table 3. Bond lengths [Å] and angles [°] for compound **17**.

C(1)-Ga(1)	1.928(3)	C(2)-C(3)-H(3A)	109.5
C(1)-H(1A)	0.9800	C(2)-C(3)-H(3B)	109.5
C(1)-H(1B)	0.9800	H(3A)-C(3)-H(3B)	109.5
C(1)-H(1C)	0.9800	C(2)-C(3)-H(3C)	109.5
C(2)-O(1)	1.463(4)	H(3A)-C(3)-H(3C)	109.5
C(2)-C(5)	1.510(5)	H(3B)-C(3)-H(3C)	109.5
C(2)-C(3)	1.510(5)	C(2)-C(4)-H(4A)	109.5
C(2)-C(4)	1.514(5)	C(2)-C(4)-H(4B)	109.5
C(3)-H(3A)	0.9800	H(4A)-C(4)-H(4B)	109.5
C(3)-H(3B)	0.9800	C(2)-C(4)-H(4C)	109.5
C(3)-H(3C)	0.9800	H(4A)-C(4)-H(4C)	109.5
C(4)-H(4A)	0.9800	H(4B)-C(4)-H(4C)	109.5
C(4)-H(4B)	0.9800	C(2)-C(5)-H(5A)	109.5
C(4)-H(4C)	0.9800	C(2)-C(5)-H(5B)	109.5
C(5)-H(5A)	0.9800	H(5A)-C(5)-H(5B)	109.5
C(5)-H(5B)	0.9800	C(2)-C(5)-H(5C)	109.5
C(5)-H(5C)	0.9800	H(5A)-C(5)-H(5C)	109.5
O(1)-Ga(1)#1	1.909(2)	H(5B)-C(5)-H(5C)	109.5
O(1)-Ga(1)	1.916(2)	C(2)-O(1)-Ga(1)#1	130.21(18)
Cl(1)-Ga(1)	2.1856(9)	C(2)-O(1)-Ga(1)	128.46(18)
Ga(1)-O(1)#1	1.909(2)	Ga(1)#1-O(1)-Ga(1)	100.40(9)
Ga(1)-Ga(1)#1	2.9388(7)	O(1)#1-Ga(1)-O(1)	79.60(9)
Ga(1)-C(1)-H(1A)	109.5	O(1)#1-Ga(1)-C(1)	119.53(14)
Ga(1)-C(1)-H(1B)	109.5	O(1)-Ga(1)-C(1)	119.98(13)
H(1A)-C(1)-H(1B)	109.5	O(1)#1-Ga(1)-Cl(1)	106.85(7)
Ga(1)-C(1)-H(1C)	109.5	O(1)-Ga(1)-Cl(1)	106.44(7)
H(1A)-C(1)-H(1C)	109.5	C(1)-Ga(1)-Cl(1)	117.86(12)
H(1B)-C(1)-H(1C)	109.5	O(1)#1-Ga(1)-Ga(1)#1	39.89(6)
O(1)-C(2)-C(5)	107.6(3)	O(1)-Ga(1)-Ga(1)#1	39.72(6)
O(1)-C(2)-C(3)	107.4(3)	C(1)-Ga(1)-Ga(1)#1	130.24(12)
C(5)-C(2)-C(3)	111.4(3)	Cl(1)-Ga(1)-Ga(1)#1	111.90(3)
O(1)-C(2)-C(4)	108.6(3)		
C(5)-C(2)-C(4)	110.1(3)		
C(3)-C(2)-C(4)	111.6(3)		

Table 4. Anisotropic displacement parameters ($\text{\AA}^2 \times 10^3$) for compound **17**. The anisotropic displacement factor exponent takes the form: $-2\pi^2 [h^2 a^{*2} U^{11} + \dots + 2 h k a^* b^* U^{12}]$

	U ¹¹	U ²²	U ³³	U ²³	U ¹³	U ¹²
C(1)	30(2)	57(2)	28(2)	-4(2)	-1(1)	5(2)
C(2)	37(2)	22(2)	28(2)	-4(1)	7(1)	4(1)
C(3)	68(3)	25(2)	66(3)	-2(2)	30(2)	6(2)
C(4)	38(2)	45(2)	65(3)	-10(2)	12(2)	6(2)
C(5)	74(3)	47(2)	34(2)	-16(2)	2(2)	15(2)
O(1)	33(1)	21(1)	20(1)	-2(1)	7(1)	5(1)
Cl(1)	39(1)	38(1)	39(1)	4(1)	16(1)	-7(1)
Ga(1)	25(1)	24(1)	20(1)	1(1)	4(1)	0(1)

A.6 Crystal data for [MeGa(OCH₂CH₂NMe₂)₂] (18)

Empirical formula	C ₁₁ H ₂₇ Ga N ₂ O ₂	
Formula weight	289.07	
Temperature	150(2) K	
Wavelength	0.71073 Å	
Crystal system	Triclinic	
Space group	P-1	
Unit cell dimensions	$a = 7.863(2)$ Å	$\alpha = 99.218(4)^\circ$.
	$b = 8.040(2)$ Å	$\beta = 92.963(5)^\circ$.
	$c = 12.054(4)$ Å	$\gamma = 102.620(4)^\circ$.
Volume	731.0(4) Å ³	
Z	2	
Density (calculated)	1.313 Mg/m ³	
Absorption coefficient	1.873 mm ⁻¹	
F(000)	308	
Crystal size	0.40 x 0.15 x 0.15 mm ³	
Theta range for data collection	2.64 to 28.29°.	
Index ranges	-10 ≤ h ≤ 10, -10 ≤ k ≤ 10, -15 ≤ l ≤ 16	
Reflections collected	6259	
Independent reflections	3319 [R(int) = 0.0219]	
Completeness to theta = 25.00°	96.8 %	
Absorption correction	Semi-empirical from equivalents	
Max. and min. transmission	0.7664 and 0.5212	
Refinement method	Full-matrix least-squares on F ²	
Data / restraints / parameters	3319 / 0 / 153	
Goodness-of-fit on F ²	1.095	
Final R indices [I > 2σ(I)]	R1 = 0.0342, wR2 = 0.0897	
R indices (all data)	R1 = 0.0397, wR2 = 0.0951	
Largest diff. peak and hole	0.687 and -0.542 e.Å ⁻³	

Table 2. Atomic coordinates ($\times 10^4$) and equivalent isotropic displacement parameters ($\text{\AA}^2 \times 10^3$) for compound **18**. $U(\text{eq})$ is defined as one third of the trace of the orthogonalized U^{ij} tensor.

	x	y	z	$U(\text{eq})$
C(1)	6196(3)	3229(3)	2327(2)	22(1)
C(2)	2751(3)	7952(3)	4779(2)	32(1)
C(3)	3181(3)	6211(3)	4352(2)	23(1)
C(4)	1723(3)	5087(3)	3499(2)	25(1)
C(5)	2518(3)	2369(3)	3635(2)	28(1)
C(6)	1114(3)	2732(3)	1892(2)	30(1)
C(7)	3044(3)	8278(4)	796(2)	34(1)
C(8)	4456(3)	7275(3)	959(2)	24(1)
C(9)	5927(3)	8376(3)	1811(2)	25(1)
C(10)	8080(3)	6727(3)	1253(2)	29(1)
C(11)	8219(3)	8170(3)	3177(2)	31(1)
N(1)	2331(2)	3618(2)	2888(2)	23(1)
N(2)	7042(2)	7269(2)	2176(2)	23(1)
O(1)	4791(2)	6467(2)	3875(1)	24(1)
O(2)	3718(2)	5718(2)	1315(1)	24(1)
Ga(1)	4921(1)	5115(1)	2497(1)	19(1)

Table 3. Bond lengths [Å] and angles [°] for compound **18**.

C(1)-Ga(1)	1.983(2)	C(10)-H(10B)	0.9800
C(1)-H(1A)	0.9800	C(10)-H(10C)	0.9800
C(1)-H(1B)	0.9800	C(11)-N(2)	1.466(3)
C(1)-H(1C)	0.9800	C(11)-H(11A)	0.9800
C(2)-C(3)	1.527(3)	C(11)-H(11B)	0.9800
C(2)-H(2A)	0.9800	C(11)-H(11C)	0.9800
C(2)-H(2B)	0.9800	N(1)-Ga(1)	2.2424(19)
C(2)-H(2C)	0.9800	N(2)-Ga(1)	2.2250(19)
C(3)-O(1)	1.406(3)	O(1)-Ga(1)	1.8538(16)
C(3)-C(4)	1.522(3)	O(2)-Ga(1)	1.8554(16)
C(3)-H(3)	1.0000	Ga(1)-C(1)-H(1A)	109.5
C(4)-N(1)	1.473(3)	Ga(1)-C(1)-H(1B)	109.5
C(4)-H(4A)	0.9900	H(1A)-C(1)-H(1B)	109.5
C(4)-H(4B)	0.9900	Ga(1)-C(1)-H(1C)	109.5
C(5)-N(1)	1.477(3)	H(1A)-C(1)-H(1C)	109.5
C(5)-H(5A)	0.9800	H(1B)-C(1)-H(1C)	109.5
C(5)-H(5B)	0.9800	C(3)-C(2)-H(2A)	109.5
C(5)-H(5C)	0.9800	C(3)-C(2)-H(2B)	109.5
C(6)-N(1)	1.474(3)	H(2A)-C(2)-H(2B)	109.5
C(6)-H(6A)	0.9800	C(3)-C(2)-H(2C)	109.5
C(6)-H(6B)	0.9800	H(2A)-C(2)-H(2C)	109.5
C(6)-H(6C)	0.9800	H(2B)-C(2)-H(2C)	109.5
C(7)-C(8)	1.530(3)	O(1)-C(3)-C(4)	110.84(18)
C(7)-H(7A)	0.9800	O(1)-C(3)-C(2)	110.18(19)
C(7)-H(7B)	0.9800	C(4)-C(3)-C(2)	110.3(2)
C(7)-H(7C)	0.9800	O(1)-C(3)-H(3)	108.5
C(8)-O(2)	1.404(3)	C(4)-C(3)-H(3)	108.5
C(8)-C(9)	1.522(3)	C(2)-C(3)-H(3)	108.5
C(8)-H(8)	1.0000	N(1)-C(4)-C(3)	109.70(19)
C(9)-N(2)	1.477(3)	N(1)-C(4)-H(4A)	109.7
C(9)-H(9A)	0.9900	C(3)-C(4)-H(4A)	109.7
C(9)-H(9B)	0.9900	N(1)-C(4)-H(4B)	109.7
C(10)-N(2)	1.479(3)	C(3)-C(4)-H(4B)	109.7
C(10)-H(10A)	0.9800	H(4A)-C(4)-H(4B)	108.2

N(1)-C(5)-H(5A)	109.5	N(2)-C(11)-H(11A)	109.5
N(1)-C(5)-H(5B)	109.5	N(2)-C(11)-H(11B)	109.5
H(5A)-C(5)-H(5B)	109.5	H(11A)-C(11)-H(11B)	109.5
N(1)-C(5)-H(5C)	109.5	N(2)-C(11)-H(11C)	109.5
H(5A)-C(5)-H(5C)	109.5	H(11A)-C(11)-H(11C)	109.5
H(5B)-C(5)-H(5C)	109.5	H(11B)-C(11)-H(11C)	109.5
N(1)-C(6)-H(6A)	109.5	C(4)-N(1)-C(6)	111.00(19)
N(1)-C(6)-H(6B)	109.5	C(4)-N(1)-C(5)	110.76(19)
H(6A)-C(6)-H(6B)	109.5	C(6)-N(1)-C(5)	109.58(19)
N(1)-C(6)-H(6C)	109.5	C(4)-N(1)-Ga(1)	97.68(13)
H(6A)-C(6)-H(6C)	109.5	C(6)-N(1)-Ga(1)	114.88(15)
H(6B)-C(6)-H(6C)	109.5	C(5)-N(1)-Ga(1)	112.46(14)
C(8)-C(7)-H(7A)	109.5	C(11)-N(2)-C(9)	111.20(19)
C(8)-C(7)-H(7B)	109.5	C(11)-N(2)-C(10)	109.63(19)
H(7A)-C(7)-H(7B)	109.5	C(9)-N(2)-C(10)	110.37(19)
C(8)-C(7)-H(7C)	109.5	C(11)-N(2)-Ga(1)	114.29(15)
H(7A)-C(7)-H(7C)	109.5	C(9)-N(2)-Ga(1)	97.95(13)
H(7B)-C(7)-H(7C)	109.5	C(10)-N(2)-Ga(1)	112.93(14)
O(2)-C(8)-C(9)	110.83(18)	C(3)-O(1)-Ga(1)	117.99(13)
O(2)-C(8)-C(7)	109.84(19)	C(8)-O(2)-Ga(1)	117.64(13)
C(9)-C(8)-C(7)	110.0(2)	O(1)-Ga(1)-O(2)	112.46(7)
O(2)-C(8)-H(8)	108.7	O(1)-Ga(1)-C(1)	123.18(8)
C(9)-C(8)-H(8)	108.7	O(2)-Ga(1)-C(1)	124.36(8)
C(7)-C(8)-H(8)	108.7	O(1)-Ga(1)-N(2)	87.60(7)
N(2)-C(9)-C(8)	109.37(18)	O(2)-Ga(1)-N(2)	82.71(7)
N(2)-C(9)-H(9A)	109.8	C(1)-Ga(1)-N(2)	99.13(8)
C(8)-C(9)-H(9A)	109.8	O(1)-Ga(1)-N(1)	82.34(7)
N(2)-C(9)-H(9B)	109.8	O(2)-Ga(1)-N(1)	87.22(7)
C(8)-C(9)-H(9B)	109.8	C(1)-Ga(1)-N(1)	99.02(8)
H(9A)-C(9)-H(9B)	108.2	N(2)-Ga(1)-N(1)	161.85(7)
N(2)-C(10)-H(10A)	109.5		
N(2)-C(10)-H(10B)	109.5		
H(10A)-C(10)-H(10B)	109.5		
N(2)-C(10)-H(10C)	109.5		
H(10A)-C(10)-H(10C)	109.5		
H(10B)-C(10)-H(10C)	109.5		

Table 4. Anisotropic displacement parameters ($\text{\AA}^2 \times 10^3$) for compound **18**. The anisotropic displacement factor exponent takes the form: $-2\pi^2 [h^2 a^{*2} U^{11} + \dots + 2 h k a^* b^* U^{12}]$

	U ¹¹	U ²²	U ³³	U ²³	U ¹³	U ¹²
C(1)	25(1)	19(1)	25(1)	5(1)	6(1)	12(1)
C(2)	32(1)	27(1)	35(1)	0(1)	7(1)	9(1)
C(3)	25(1)	25(1)	22(1)	4(1)	6(1)	7(1)
C(4)	22(1)	28(1)	28(1)	4(1)	5(1)	7(1)
C(5)	31(1)	23(1)	31(1)	10(1)	2(1)	1(1)
C(6)	28(1)	28(1)	29(1)	0(1)	-2(1)	2(1)
C(7)	31(1)	38(2)	38(2)	16(1)	2(1)	15(1)
C(8)	25(1)	26(1)	23(1)	7(1)	3(1)	8(1)
C(9)	24(1)	21(1)	29(1)	6(1)	4(1)	3(1)
C(10)	23(1)	35(1)	27(1)	2(1)	6(1)	6(1)
C(11)	26(1)	32(1)	29(1)	0(1)	-2(1)	0(1)
N(1)	24(1)	21(1)	23(1)	4(1)	1(1)	5(1)
N(2)	20(1)	23(1)	23(1)	1(1)	1(1)	4(1)
O(1)	22(1)	27(1)	20(1)	-1(1)	1(1)	5(1)
O(2)	24(1)	23(1)	22(1)	6(1)	-4(1)	2(1)
Ga(1)	20(1)	19(1)	18(1)	2(1)	0(1)	6(1)

A.7 Crystal data for [(Ga(Me){Cl}{N(SiMe₃)₂)}](μ₂-OCH₂CH₂NMe₂)(Ga){Me}{Cl}] (**19**)

Empirical formula	C ₁₂ H ₃₄ Cl ₂ Ga ₂ N ₂ O Si ₂	
Formula weight	488.93	
Temperature	120(2) K	
Wavelength	0.71073 Å	
Crystal system	Trigonal	
Space group	R3c	
Unit cell dimensions	$a = 41.8983(16)$ Å	$\alpha = 90^\circ$.
	$b = 41.8983(16)$ Å	$\beta = 90^\circ$.
	$c = 7.1970(4)$ Å	$\gamma = 120^\circ$.
Volume	10941.4(8) Å ³	
Z	18	
Density (calculated)	1.336 Mg/m ³	
Absorption coefficient	2.535 mm ⁻¹	
F(000)	4536	
Crystal size	0.46 x 0.03 x 0.01 mm ³	
Theta range for data collection	2.92 to 27.61°.	
Index ranges	-54 ≤ h ≤ 54, -49 ≤ k ≤ 53, -9 ≤ l ≤ 7	
Reflections collected	32747	
Independent reflections	2833 [R(int) = 0.1385]	
Completeness to theta = 27.61°	99.6 %	
Absorption correction	Semi-empirical from equivalents	
Max. and min. transmission	0.9751 and 0.3885	
Refinement method	Full-matrix least-squares on F ²	
Data / restraints / parameters	2833 / 1 / 195	
Goodness-of-fit on F ²	1.132	
Final R indices [I > 2σ(I)]	R1 = 0.0855, wR2 = 0.1559	
R indices (all data)	R1 = 0.1065, wR2 = 0.1645	
Absolute structure parameter	0.47(6)	
Largest diff. peak and hole	0.976 and -0.535 e.Å ⁻³	

Table 2. Atomic coordinates ($\times 10^4$) and equivalent isotropic displacement parameters ($\text{\AA}^2 \times 10^3$) for compound **19**. $U(\text{eq})$ is defined as one third of the trace of the orthogonalized U^{ij} tensor.

	x	y	z	$U(\text{eq})$
C(1)	95(3)	6290(3)	7379(18)	28(2)
C(2)	806(4)	6002(4)	10370(19)	38(3)
C(3)	453(4)	5679(4)	11030(20)	40(3)
C(4)	131(4)	6019(5)	11810(20)	50(4)
C(5)	-215(4)	5389(4)	10800(30)	59(4)
C(6)	1125(3)	5875(3)	5494(19)	28(2)
C(7)	2089(4)	6658(5)	5240(20)	58(4)
C(8)	2402(4)	7058(5)	8780(30)	65(5)
C(9)	1929(5)	6236(4)	8890(30)	74(6)
C(10)	1848(4)	7489(4)	7570(30)	70(6)
C(11)	1763(5)	7145(5)	11440(20)	68(5)
C(12)	1110(4)	6993(4)	9240(30)	51(4)
O(1)	758(2)	6115(2)	8557(13)	32(2)
Cl(1)	93(1)	5459(1)	6206(6)	48(1)
Cl(2)	906(1)	6546(1)	4833(6)	50(1)
Ga(1)	257(1)	5943(1)	7913(2)	33(1)
Ga(2)	1168(1)	6326(1)	6769(2)	39(1)
N(1)	137(3)	5741(3)	10548(17)	41(3)
N(2)	1585(2)	6689(3)	7977(17)	32(2)
Si(1)	1981(1)	6661(1)	7741(8)	43(1)
Si(2)	1579(1)	7062(1)	9017(7)	40(1)

Table 3. Bond lengths [\AA] and angles [$^\circ$] for compound **19**.

C(1)-Ga(1)	1.929(11)	C(9)-H(9C)	0.9800
C(1)-H(1A)	0.9800	C(10)-Si(2)	1.881(15)
C(1)-H(1B)	0.9800	C(10)-H(10A)	0.9800
C(1)-H(1C)	0.9800	C(10)-H(10B)	0.9800
C(2)-O(1)	1.435(16)	C(10)-H(10C)	0.9800
C(2)-C(3)	1.497(19)	C(11)-Si(2)	1.870(17)
C(2)-H(2A)	0.9900	C(11)-H(11A)	0.9800
C(2)-H(2B)	0.9900	C(11)-H(11B)	0.9800
C(3)-N(1)	1.512(17)	C(11)-H(11C)	0.9800
C(3)-H(3A)	0.9900	C(12)-Si(2)	1.845(14)
C(3)-H(3B)	0.9900	C(12)-H(12A)	0.9800
C(4)-N(1)	1.488(18)	C(12)-H(12B)	0.9800
C(4)-H(4A)	0.9800	C(12)-H(12C)	0.9800
C(4)-H(4B)	0.9800	O(1)-Ga(1)	1.904(8)
C(4)-H(4C)	0.9800	O(1)-Ga(2)	1.966(9)
C(5)-N(1)	1.488(18)	Cl(1)-Ga(1)	2.165(4)
C(5)-H(5A)	0.9800	Cl(2)-Ga(2)	2.236(4)
C(5)-H(5B)	0.9800	Ga(1)-N(1)	2.033(12)
C(5)-H(5C)	0.9800	Ga(2)-N(2)	1.860(10)
C(6)-Ga(2)	2.027(11)	N(2)-Si(1)	1.730(10)
C(6)-H(6A)	0.9800	N(2)-Si(2)	1.745(11)
C(6)-H(6B)	0.9800	Ga(1)-C(1)-H(1A)	109.5
C(6)-H(6C)	0.9800	Ga(1)-C(1)-H(1B)	109.5
C(7)-Si(1)	1.859(17)	H(1A)-C(1)-H(1B)	109.5
C(7)-H(7A)	0.9800	Ga(1)-C(1)-H(1C)	109.5
C(7)-H(7B)	0.9800	H(1A)-C(1)-H(1C)	109.5
C(7)-H(7C)	0.9800	H(1B)-C(1)-H(1C)	109.5
C(8)-Si(1)	1.872(16)	O(1)-C(2)-C(3)	110.5(10)
C(8)-H(8A)	0.9800	O(1)-C(2)-H(2A)	109.6
C(8)-H(8B)	0.9800	C(3)-C(2)-H(2A)	109.6
C(8)-H(8C)	0.9800	O(1)-C(2)-H(2B)	109.6
C(9)-Si(1)	1.870(15)	C(3)-C(2)-H(2B)	109.6
C(9)-H(9A)	0.9800	H(2A)-C(2)-H(2B)	108.1
C(9)-H(9B)	0.9800	C(2)-C(3)-N(1)	108.9(11)

C(2)-C(3)-H(3A)	109.9	Si(1)-C(9)-H(9B)	109.5
N(1)-C(3)-H(3A)	109.9	H(9A)-C(9)-H(9B)	109.5
C(2)-C(3)-H(3B)	109.9	Si(1)-C(9)-H(9C)	109.5
N(1)-C(3)-H(3B)	109.9	H(9A)-C(9)-H(9C)	109.5
H(3A)-C(3)-H(3B)	108.3	H(9B)-C(9)-H(9C)	109.5
N(1)-C(4)-H(4A)	109.5	Si(2)-C(10)-H(10A)	109.5
N(1)-C(4)-H(4B)	109.5	Si(2)-C(10)-H(10B)	109.5
H(4A)-C(4)-H(4B)	109.5	H(10A)-C(10)-H(10B)	109.5
N(1)-C(4)-H(4C)	109.5	Si(2)-C(10)-H(10C)	109.5
H(4A)-C(4)-H(4C)	109.5	H(10A)-C(10)-H(10C)	109.5
H(4B)-C(4)-H(4C)	109.5	H(10B)-C(10)-H(10C)	109.5
N(1)-C(5)-H(5A)	109.5	Si(2)-C(11)-H(11A)	109.5
N(1)-C(5)-H(5B)	109.5	Si(2)-C(11)-H(11B)	109.5
H(5A)-C(5)-H(5B)	109.5	H(11A)-C(11)-H(11B)	109.5
N(1)-C(5)-H(5C)	109.5	Si(2)-C(11)-H(11C)	109.5
H(5A)-C(5)-H(5C)	109.5	H(11A)-C(11)-H(11C)	109.5
H(5B)-C(5)-H(5C)	109.5	H(11B)-C(11)-H(11C)	109.5
Ga(2)-C(6)-H(6A)	109.5	Si(2)-C(12)-H(12A)	109.5
Ga(2)-C(6)-H(6B)	109.5	Si(2)-C(12)-H(12B)	109.5
H(6A)-C(6)-H(6B)	109.5	H(12A)-C(12)-H(12B)	109.5
Ga(2)-C(6)-H(6C)	109.5	Si(2)-C(12)-H(12C)	109.5
H(6A)-C(6)-H(6C)	109.5	H(12A)-C(12)-H(12C)	109.5
H(6B)-C(6)-H(6C)	109.5	H(12B)-C(12)-H(12C)	109.5
Si(1)-C(7)-H(7A)	109.5	C(2)-O(1)-Ga(1)	113.9(7)
Si(1)-C(7)-H(7B)	109.5	C(2)-O(1)-Ga(2)	120.6(7)
H(7A)-C(7)-H(7B)	109.5	Ga(1)-O(1)-Ga(2)	124.1(5)
Si(1)-C(7)-H(7C)	109.5	O(1)-Ga(1)-C(1)	120.0(4)
H(7A)-C(7)-H(7C)	109.5	O(1)-Ga(1)-N(1)	85.9(4)
H(7B)-C(7)-H(7C)	109.5	C(1)-Ga(1)-N(1)	113.0(5)
Si(1)-C(8)-H(8A)	109.5	O(1)-Ga(1)-Cl(1)	105.5(3)
Si(1)-C(8)-H(8B)	109.5	C(1)-Ga(1)-Cl(1)	121.7(4)
H(8A)-C(8)-H(8B)	109.5	N(1)-Ga(1)-Cl(1)	104.1(3)
Si(1)-C(8)-H(8C)	109.5	N(2)-Ga(2)-O(1)	108.3(5)
H(8A)-C(8)-H(8C)	109.5	N(2)-Ga(2)-C(6)	125.6(4)
H(8B)-C(8)-H(8C)	109.5	O(1)-Ga(2)-C(6)	103.0(4)
Si(1)-C(9)-H(9A)	109.5	N(2)-Ga(2)-Cl(2)	114.1(4)

O(1)-Ga(2)-Cl(2)	95.5(3)	N(2)-Si(1)-C(9)	111.1(7)
C(6)-Ga(2)-Cl(2)	105.6(4)	C(7)-Si(1)-C(9)	109.6(9)
C(5)-N(1)-C(4)	107.6(12)	N(2)-Si(1)-C(8)	114.2(7)
C(5)-N(1)-C(3)	108.7(12)	C(7)-Si(1)-C(8)	105.7(9)
C(4)-N(1)-C(3)	110.7(11)	C(9)-Si(1)-C(8)	106.2(9)
C(5)-N(1)-Ga(1)	116.3(10)	N(2)-Si(2)-C(12)	112.8(6)
C(4)-N(1)-Ga(1)	110.2(9)	N(2)-Si(2)-C(11)	112.3(7)
C(3)-N(1)-Ga(1)	103.3(8)	C(12)-Si(2)-C(11)	104.8(8)
Si(1)-N(2)-Si(2)	123.1(6)	N(2)-Si(2)-C(10)	110.2(8)
Si(1)-N(2)-Ga(2)	116.2(6)	C(12)-Si(2)-C(10)	106.2(8)
Si(2)-N(2)-Ga(2)	120.2(5)	C(11)-Si(2)-C(10)	110.2(10)
N(2)-Si(1)-C(7)	109.8(7)		

Table 4. Anisotropic displacement parameters ($\text{\AA}^2 \times 10^3$) for compound **19**. The anisotropic displacement factor exponent takes the form: $-2\pi^2 [h^2 a^{*2} U^{11} + \dots + 2 h k a^* b^* U^{12}]$

	U ¹¹	U ²²	U ³³	U ²³	U ¹³	U ¹²
C(1)	14(4)	20(4)	50(5)	-11(4)	-1(3)	9(3)
C(2)	30(7)	46(8)	40(7)	0(6)	-6(6)	20(6)
C(3)	44(8)	40(7)	37(7)	6(6)	-12(6)	21(6)
C(4)	54(9)	65(10)	39(8)	-11(7)	2(7)	35(8)
C(5)	41(9)	44(9)	71(11)	17(8)	6(8)	5(7)
C(6)	14(4)	20(4)	50(5)	-11(4)	-1(3)	9(3)
C(7)	41(9)	59(10)	81(12)	-7(9)	9(8)	30(8)
C(8)	20(7)	52(10)	116(16)	0(10)	-6(8)	14(7)
C(9)	68(12)	46(10)	118(17)	31(10)	20(11)	37(9)
C(10)	30(8)	35(8)	132(18)	38(10)	13(9)	7(7)
C(11)	69(12)	80(13)	63(11)	-23(10)	-18(9)	42(11)
C(12)	34(8)	38(7)	78(11)	-14(7)	0(8)	15(7)
O(1)	16(4)	37(5)	39(5)	-1(4)	3(3)	10(4)
Cl(1)	43(2)	42(2)	56(2)	-9(2)	-3(2)	20(2)
Cl(2)	41(2)	61(2)	42(2)	2(2)	-5(2)	21(2)
Ga(1)	31(1)	35(1)	37(1)	-3(1)	-3(1)	20(1)
Ga(2)	28(1)	36(1)	44(1)	-6(1)	0(1)	10(1)
N(1)	32(6)	41(6)	49(7)	-3(5)	7(5)	17(5)
N(2)	14(4)	26(5)	48(6)	-11(4)	-5(5)	3(4)
Si(1)	25(2)	35(2)	67(3)	6(2)	-1(2)	14(2)
Si(2)	26(2)	28(2)	62(3)	-2(2)	0(2)	9(2)

A.8 Crystal data for [Me{Cl}In(OCH(CH₃)CH₂OMe)]₂ (**22**)

Chemical formula	C ₁₀ H ₂₄ Cl ₂ In ₂ O ₄	
Formula weight	508.83	
Temperature	150(2) K	
Radiation, wavelength	MoK α , 0.71073 Å	
Crystal system, space group	Monoclinic, P2 ₁ /c	
Unit cell parameters	$a = 9.168(4)$ Å	$\alpha = 90^\circ$
	$b = 13.586(6)$ Å	$\beta = 109.114(7)^\circ$
	$c = 7.819(3)$ Å	$\gamma = 90^\circ$
Cell volume	920.2(7) Å ³	
Z	2	
Calculated density	1.836 g/cm ³	
Absorption coefficient μ	2.798 mm ⁻¹	
F(000)	496	
Crystal colour and size	Colourless, 0.27 × 0.14 × 0.07 mm ³	
Reflections for cell refinement	2096 (θ range 2.789 to 26.671°)	
Data collection method	Bruker SMART APEX diffractometer ω rotation with narrow frames	
θ range for data collection	3.00 to 28.34°	
Index ranges	h -12 to 11, k -16 to 17, l -10 to 8	
Completeness to $\theta = 26.00^\circ$	97.8 %	
Intensity decay	None	
Reflections collected	5565	
Independent reflections	2223 ($R_{\text{int}} = 0.0378$)	
Reflections with $F^2 > 2\sigma$	1837	
Absorption correction	semi-empirical from equivalents	
Min. and max. transmission	0.6884 and 1.0000	
Structure solution	direct methods	
Refinement method	Full-matrix least-squares on F^2	
Weighting parameters a, b	0.0302, 0.8408	
Data / restraints / parameters	2126 / 0 / 85	
Final R indices [$F^2 > 2\sigma$]	R1 = 0.0327, wR2 = 0.0722	

R indices (all data)	R1 = 0.0403, wR2 = 0.0748
Goodness-of-fit on F ²	1.063
Largest and mean shift/su	0.001 and 0.000
Largest diff. peak and hole	0.894 and -0.726 e Å ⁻³

Table 2. Atomic coordinates and equivalent isotropic displacement parameters (Å²) for compound **22**. U_{eq} is defined as one third of the trace of the orthogonalized U^{ij} tensor.

	<i>x</i>	<i>y</i>	<i>z</i>	U _{eq}
In1	0.80979(3)	0.022466(18)	0.96875(3)	0.02615(10)
O1	0.9572(3)	-0.0504(2)	0.8524(4)	0.0329(6)
C1	1.0089(5)	-0.1572(4)	0.6320(6)	0.0463(11)
C2	0.9000(5)	-0.0862(4)	0.6746(6)	0.0460(11)
C3	0.7423(4)	-0.1286(3)	0.6388(6)	0.0394(10)
O2	0.6523(3)	-0.0606(2)	0.7000(4)	0.0375(6)
C4	0.5021(5)	-0.0964(4)	0.6836(7)	0.0474(11)
C5	0.6885(5)	0.1583(3)	0.8931(6)	0.0410(10)
Cl1	0.74082(13)	-0.09540(8)	1.15533(15)	0.0438(3)

Table 4. Bond lengths [\AA] and angles [$^\circ$] for compound **22**.

In1–O1	2.106(3)	In1–C5	2.135(4)
In1–O1#1	2.170(3)	In1–Cl1	2.3867(12)
In1–O2	2.406(3)	O1–C2	1.403(5)
O1–In1#1	2.170(3)	C1–C2	1.502(6)
C1–H1A	0.9800	C1–H1B	0.9800
C1–H1C	0.9800	C2–C3	1.495(6)
C2–H2A	1.0000	C3–O2	1.422(5)
C3–H3A	0.9900	C3–H3B	0.9900
O2–C4	1.426(5)	C4–H4A	0.9800
C4–H4B	0.9800	C4–H4C	0.9800
C5–H5A	0.9800	C5–H5B	0.9800
C5–H5C	0.9800		
O1–In1–C5	129.48(16)	O1–In1–O1#1	74.03(11)
C5–In1–O1#1	109.94(14)	O1–In1–Cl1	106.53(9)
C5–In1–Cl1	122.06(13)	O1#1–In1–Cl1	97.20(9)
O1–In1–O2	71.88(10)	C5–In1–O2	93.10(14)
O1#1–In1–O2	145.87(9)	Cl1–In1–O2	90.91(8)
C2–O1–In1	120.5(2)	C2–O1–In1#1	132.0(2)
In1–O1–In1#1	105.97(11)	C2–C1–H1A	109.5
C2–C1–H1B	109.5	H1A–C1–H1B	109.5
C2–C1–H1C	109.5	H1A–C1–H1C	109.5
H1B–C1–H1C	109.5	O1–C2–C3	110.1(4)
O1–C2–C1	112.5(4)	C3–C2–C1	112.6(4)
O1–C2–H2A	107.1	C3–C2–H2A	107.1
C1–C2–H2A	107.1	O2–C3–C2	108.6(3)
O2–C3–H3A	110.0	C2–C3–H3A	110.0
O2–C3–H3B	110.0	C2–C3–H3B	110.0
H3A–C3–H3B	108.3	C3–O2–C4	113.5(3)
C3–O2–In1	110.5(2)	C4–O2–In1	121.6(3)
O2–C4–H4A	109.5	O2–C4–H4B	109.5
H4A–C4–H4B	109.5	O2–C4–H4C	109.5

H4A–C4–H4C	109.5	H4B–C4–H4C	109.5
In1–C5–H5A	109.5	In1–C5–H5B	109.5
H5A–C5–H5B	109.5	In1–C5–H5C	109.5
H5A–C5–H5C	109.5	H5B–C5–H5C	109.5

Symmetry operations for equivalent atoms: #1 $-x+2, -y, -z+2$

Table 5. Anisotropic displacement parameters (\AA^2) for compound **22**. The anisotropic displacement factor exponent takes the form: $-2\pi^2[h^2a^*{}^2U^{11} + \dots + 2hka^*b^*U^{12}]$

	U^{11}	U^{22}	U^{33}	U^{23}	U^{13}	U^{12}
In1	0.02220(14)	0.02565(15)	0.03192(16)	-0.00242(1)	0.01067(11)	0.00118(1)
O1	0.0211(12)	0.0419(15)	0.0346(14)	-0.0143(12)	0.0078(11)	0.0004(11)
C1	0.040(2)	0.054(3)	0.045(3)	-0.020(2)	0.013(2)	0.004(2)
C2	0.037(2)	0.058(3)	0.044(3)	-0.015(2)	0.015(2)	0.000(2)
C3	0.033(2)	0.039(2)	0.043(2)	-0.0154(18)	0.0074(18)	-0.0029(17)
O2	0.0276(14)	0.0407(15)	0.0437(16)	-0.0134(13)	0.0111(12)	-0.0042(12)
C4	0.027(2)	0.056(3)	0.055(3)	-0.012(2)	0.009(2)	-0.0100(19)
C5	0.034(2)	0.027(2)	0.057(3)	0.0041(18)	0.008(2)	0.0050(16)
Cl1	0.0519(6)	0.0382(5)	0.0472(6)	0.0084(4)	0.0243(5)	-0.0009(5)

A.9 Supplementary data for all gas phase electron diffraction experiments.

Table S1 Nozzle-to-film distances / mm, weighting functions / nm⁻¹, scale factors, correlation parameters and electron wavelengths / pm used in the electron diffraction studies of Me₂GaOCH₂CH₂NMe₂ (**30a**), Me₂GaOCH₂CH₂OMe (**31a**), and [Me₂GaO^tBu]₂ (**32**).

	30a		31a	32	
Nozzle-to-film distance ^a	93.39	254.54	255.93	195.93	255.45
Δs	4	2	2	2	1
s _{min}	100	20	20	80	20
sw ₁	120	40	40	100	40
sw ₂	276	120	129	172	120
s _{max}	300	130	150	200	140
Scale factor ^b	0.900(38)	1.292(37)	1.309(81)	0.521(15)	0.749(9)
Correlation parameter	0.334	0.344	0.477	0.362	0.479
Electron wavelength	6.18	6.18	6.18	6.18	6.18

^a Determined by reference to the scattering pattern of benzene. ^b Values in parentheses are the estimated standard deviations.

GED model for Me₂GaOCH₂CH₂NMe₂ (**30a**)

A model for use in the GED refinement was written to describe the geometric structure of **1a** in terms of bond lengths, bond angles and dihedral angles. Wherever parameters were judged from *ab initio* calculations to be closely correlated (for instance very similar distances, which would lie under a single broad peak in the radial distribution curve) an average value was refined along with corresponding differences.

Table S2 shows the parameters required to describe **1a**, including eight distance parameters, 12 angles and 6 dihedral angles. As well as the C–H bonded distance (*p*₁), for which a mean value was used, there were two distinct groups of distance parameters. The Ga–C and Ga–O distances were sufficiently close in value that it made sense to define them as the average and the corresponding difference (*p*₂₋₃). Similarly the C–O, C–C and C–N distances were calculated to lie close enough to one another that the following average and difference parameters were used:

$$p_4 = [rO(4)–C(5) + rC(5)–C(6) + rC(6)–N(7) + rN(7)–C(8) + rN(7)–C(9)] / 5$$

$$p_5 = rO(4)–C(5) - \{[rC(5)–C(6) + rC(6)–N(7) + rN(7)–C(8) + rN(7)–C(9)] / 4\}$$

$$p_6 = rC(5)–C(6) - \{[rC(6)–N(7) + rN(7)–C(8) + rN(7)–C(9)] / 3\}$$

$$p_7 = rC(6)–N(7) - \{[rN(7)–C(8) + rN(7)–C(9)] / 2\}$$

$$p_8 = r_{\text{N}(7)\text{-C}(8)} - r_{\text{N}(7)\text{-C}(9)}$$

For the angles defined in the model, a single Ga–C–H angle (p_9) was used, justified by the fact that the calculations showed that the spread of these angles was less than 1° . As no other bond angle was used to define them the GaCH₃ groups were therefore constrained to have C_{3v} symmetry. The O–Ga–C_{Me} angles were predicted to be different and so the average of the two values and the difference between them were used as parameters (p_{10-11}). Other angles that were defined in the model, but that required no special consideration, were Ga–O–C(5), O–C(5)–C(6), H(51)–C(5)–H(52), H(61)–C(6)–H(62) and C(5)–C(6)–N (p_{12-16}). A point X, defined as the midpoint of H(51)···H(52) was used and X–C(5)–C(6) was included as a parameter (p_{17}). As the calculations suggested that there were two different C(6)–N–C angles, these were once again described as the average and difference (p_{18-19}). The use of a single N–C–H angle, justified by the small spread of angles predicted by the calculations, meant that the NCH₃ groups were constrained to have C_{3v} symmetry (p_{20}). Six dihedral angles were defined for use in the model: C(2)–Ga–O–C(5), C(3)–Ga–O–C(5), Ga–O–C(5)–C(6), O–C(5)–C(6)–N, C(5)–C(6)–N–C(9) and C(5)–C(6)–N–C(8) (p_{21-26}).

Table S2 Calculated starting values [r_e ; MP2(full)/6-311+G*] and refined parameters (r_{h1}) from the GED refinement of Me₂GaOCH₂CH₂NMe₂ (**30a**).^a

Parameters	r_{h1}	R_e	Restraint
<i>Independent</i>			
p_1 r_{C-H} mean	108.4(2)	109.5	—
p_2 $r_{Ga-C/Ga-O}$ average	197.3(2)	194.1	—
p_3 $r_{Ga-C/Ga-O}$ difference	10.0(4)	9.5	9.5(5)
p_4 $r_{C-O/C-C/C-N}$ average	148.8(3)	147.1	—
p_5 $r_{C-O/C-C/C-N}$ difference 1	-9.0(5)	-9.3	-9.3(5)
p_6 $r_{C-O/C-C/C-N}$ difference 2	5.2(5)	5.2	5.2(5)
p_7 $r_{C-O/C-C/C-N}$ difference 3	1.1(5)	1.2	1.2(5)
p_8 $r_{C-O/C-C/C-N}$ difference 4	0.2(5)	0.2	0.2(5)
p_9 $\angle Ga-C-H$ mean	110.8(9)	111.5	111.5(10)
p_{10} $\angle O-Ga-C_{Me}$ average	114.0(8)	113.6	113.6(9)
p_{11} $\angle O-Ga-C_{Me}$ difference	2.5(5)	2.5	2.5(5)
p_{12} $\angle Ga-O-C(5)$	116.2(12)	112.5	—
p_{13} $\angle O-C(5)-C(6)$	110.9(9)	109.6	109.6(12)
p_{14} $\angle H(51)-C(5)-H(52)$	106.7(11)	106.6	106.6(10)
p_{15} $\angle H(61)-C(6)-H(62)$	108.9(11)	108.7	108.7(10)
p_{16} $\angle C(5)-C(6)-N$	109.7(9)	109.2	109.2(10)
p_{17} $\angle X-C(5)-C(6)$	127.1(11)	127.2	127.2(10)
p_{18} $\angle C(6)-N-C_{Me}$ average	110.5(7)	110.8	110.8(10)
p_{19} $\angle C(6)-N-C_{Me}$ difference	0.4(3)	0.4	0.4(3)
p_{20} $\angle N-C(6)-H$ mean	109.8(11)	110.0	110.0(10)
p_{21} $\phi C(2)-Ga-O-C(5)$	86.5(15)	91.1	91.1(20)
p_{22} $\phi C(3)-Ga-O-C(5)$	-117.3(15)	-119.9	-119.9(20)
p_{23} $\phi Ga-O-C(5)-C(6)$	43.0(19)	39.4	—
p_{24} $\phi O-C(5)-C(6)-N$	-48.1(25)	-52.9	—
p_{25} $\phi C(5)-C(6)-N-C(9)$	-81.5(21)	-81.1	—
p_{26} $\phi C(5)-C(6)-N-C(8)$	144.8(20)	157.6	—
<i>Dependent</i>			
p_{27} $r_{Ga-C(2)}$	200.6(2)	197.5	—
p_{28} $r_{Ga-C(3)}$	200.6(2)	197.2	—
p_{29} $r_{Ga-O(4)}$	190.6(4)	187.8	—
p_{30} $r_{O(4)-C(5)}$	141.5(5)	139.7	—
p_{31} $r_{C(5)-C(6)}$	154.5(5)	152.9	—
p_{32} $r_{C(6)-N}$	150.0(4)	148.5	—
p_{33} $r_{N-C(8)}$	148.8(4)	147.2	—
p_{34} $r_{N-C(9)}$	149.0(4)	147.4	—
p_{35} $\angle O-Ga-C(2)$	115.3(8)	114.8	—
p_{36} $\angle O-Ga-C(3)$	112.8(8)	112.3	—
p_{37} $\angle C(6)-N-C(8)$	110.7(7)	111.0	—
p_{38} $\angle C(6)-N-C(9)$	110.3(7)	110.6	—
p_{39} $r_{Ga\cdots N}$	233.2(11)	216.8	—

^a Distances (r) are in pm, angles (\angle) and dihedral angles (ϕ) are in degrees.

GED model for Me₂GaOCH₂CH₂OMe (31a)

A couple of adaptations were required to the model of **1a** to make it suitable to describing the geometry of **2a**. Most notably, there was more asymmetry in the methyl groups attached to Ga than was the case in **1a**, because there is only one methyl group on the opposite side of the molecule.

Despite the asymmetry in the methyl groups, it was still decided to use a mean C–H distance (p_1). A mean Ga–C distance was also employed (p_2), as was Ga–O (p_3). There are four C–O and C–C distances that will lie under a single peak in the radial-distribution curve, and these were defined as an average of the four, and three corresponding differences (p_{4-7}) as follows:

For the methyl group centred on C(3), only a single mean Ga–C–H angle was used (p_8), and the group was assumed to have C_3 symmetry. For the methyl group centred on C(2), however, there was significant asymmetry and so three separate Ga–C(2)–H angles were defined using an average value and two differences (p_{21-23}), as follows:

Two H–C(2)–H angles were required to finish the definition of this methyl group (p_{24-25}). Two separate O–Ga–C_{Me} angles were used, defined as the average value and the difference between the two (p_{9-10}). The Ga–O–C(5) and O–C(5)–C(6) angles were also defined (p_{11-12}), as were two H–C–H angles, one for each of the CH₂ groups (p_{13-14}). A point X was defined as lying mid-way between H(51) and H(52). This dummy atom was used to define the X–C(5)–C(6) angle (p_{16}).

The methyl group attached to O(7) was positioned using $\angle C(6)–O(7)–C(8)$ (p_{17}) and, as this methyl group was noticeably asymmetric, three O(7)–C(8)–H angles were defined as the average of all three and two differences as follows:

The asymmetry of this methyl group attached to O(7) was accounted for by using two H–C(8)–H angles (p_{26-27}). Five self-explanatory dihedral angles were used to describe the remainder of the heavy-atom structure (p_{28-32}). Three dihedral angles were used to account for the torsions of the methyl groups (p_{33-35}).

Table S3 Calculated starting values [r_e ; MP2(full)/6-311+G*] and refined parameters (r_{hl}) from the GED refinement of Me₂GaOCH₂CH₂OMe (**31a**).^a

Parameters	r_{hl}	r_e	Restraint
<i>Independent</i>			
p_1 rC–H mean	109.9(7)	109.3	109.3(10)
p_2 rGa–C mean	197.1(6)	196.5	196.5(10)
p_3 rGa–O	186.5(11)	186.6	186.6(10)
p_4 rC–O/C–C average	148.1(6)	144.7	144.7(10)
p_5 rC–O/C–C difference 1	9.4(6)	9.7	9.7(5)
p_6 rC–O/C–C difference 2	2.7(6)	2.9	2.9(5)
p_7 rC–O/C–C difference 3	–2.4(6)	–2.7	–2.7(5)
p_8 ∠Ga–C–H mean	109.6(24)	111.3	111.3(20)
p_9 ∠O–Ga–C _{Me} average	110.4(19)	114.3	114.3(20)
p_{10} ∠O–Ga–C _{Me} difference	3.3(10)	3.1	3.1(8)
p_{11} ∠Ga–O–C(5)	114.3(9)	111.4	—
p_{12} ∠O–C(5)–C(6)	108.4(11)	109.4	—
p_{13} ∠H(51)–C(5)–H(52)	107.2(25)	107.5	107.5(20)
p_{14} ∠H(61)–C(6)–H(62)	108.9(25)	110.2	110.2(20)
p_{15} ∠C(5)–C(6)–O	104.4(11)	105.7	—
p_{16} ∠X–C(5)–C(6)	130.1(25)	130.2	130.2(20)
p_{17} ∠C(6)–O–C _{Me}	112.3(12)	113.5	113.5(10)
p_{18} ∠O–C(8)–H average	109.5(25)	109.2	109.2(20)
p_{19} ∠O–C(8)–H difference 1	–3.3(11)	–3.0	–3.0(9)
p_{20} ∠O–C(8)–H difference 2	–1.0(11)	–0.8	–0.8(9)
p_{21} ∠Ga–C(2)–H average	109.7(23)	111.4	111.4(20)
p_{22} ∠Ga–C(2)–H difference 1	–2.1(8)	–2.1	–2.1(6)
p_{23} ∠Ga–C(2)–H difference 2	–1.8(8)	–1.7	–1.7(6)
p_{24} ∠H(9)–C(2)–H(10)	108.5(25)	108.5	108.5(20)
p_{25} ∠H(9)–C(2)–H(11)	107.4(25)	107.1	107.1(20)
p_{26} ∠H(81)–C(8)–H(83)	109.5(25)	109.8	109.8(20)
p_{27} ∠H(82)–C(8)–H(83)	109.3(25)	109.7	109.7(20)
p_{28} ϕ C(2)–Ga–O(4)–C(5)	65.9(28)	73.9	73.9(50)
p_{29} ϕ C(3)–Ga–O(4)–C(5)	–132.0(33)	–126.0	–126.0(50)
p_{30} ϕ Ga–O(4)–C(5)–C(6)	54.4(26)	50.2	—
p_{31} ϕ O(4)–C(5)–C(6)–O(7)	–36.4(28)	–54.1	—
p_{32} ϕ C(5)–C(6)–O(7)–C(8)	133.5(28)	168.9	168.9(50)
p_{33} ϕ H(83)–C(8)–O(7)–C(6)	177.1(63)	179.4	179.4(50)
p_{34} ϕ H(22)–C(2)–Ga–O(4)	145.4(63)	144.2	144.2(50)
p_{35} ϕ H(32)–C(3)–Ga–O(4)	–165.1(63)	–165.7	–165.7(50)
<i>Dependent</i>			
p_{36} rO(4)–C(5)	143.7(7)	140.0	—
p_{37} rC(5)–C(6)	155.2(8)	152.0	—
p_{38} rC(6)–O(7)	147.6(7)	144.2	—
p_{39} rO(7)–C(8)	146.1(7)	142.7	—
p_{40} ∠O–Ga–C(2)	112.2(20)	115.8	—
p_{41} ∠O–Ga–C(3)	108.9(20)	112.7	—
p_{42} rGa···O(7)	216.0(20)	218.3	—

^a Distances (r) are in pm, angles (\angle) and dihedral angles (ϕ) are in degrees.

GED model for [Me₂GaO^tBu]₂ (32)

The C_{2h} -symmetric structure of **3** was described using six distance parameters, 12 angles and two dihedral angles. Two symmetrically unique C–C distances and one C–O distance were combined as follows:

There was one unique Ga–O and one unique Ga–C distance and these were represented as the average of the two values and the difference between them (p_{4-5}). As calculations showed a very small spread of C–H distances a single mean value was used in the refinement (p_6).

As the O–^tBu group has C_s symmetry, two different O–C–C angles are required and these were defined as the average of all three angles and some difference between the two different ones as follows:

The C(6)–C(5)–C(7) angle (p_9) was also needed to define the *tert*-Bu group.

The elevation of the *tert*-butyl group out of the Ga₂O₂ plane was defined by the O–O–C angle (p_{10}). A single mean CCH angle was used for all the methyl groups forming the *tert*-butyl group (p_{11}). For the methyl groups attached to Ga, three different Ga–C–H angles were defined using the average of all three and two differences (p_{12-14}) as follows:

In this case two H–C–H angles were also defined (p_{15-16}). The final angles required in the model were C(31)–Ga(4)–C(35) and O(2)–Ga(1)–O(3) (p_{17-18}). Two dihedral angles were included, one to allow the methyl groups attached to Ga to lie out of the plane that is perpendicular to the Ga₂O₂ plane (p_{19}), and one to allow those methyl groups to rotate (p_{20}).

Table S4 Calculated starting values [r_e ; MP2(full)/6-311+G*] and refined parameters (r_{h1}) from the GED refinement of $[\text{Me}_2\text{GaO}^t\text{Bu}]_2$, **32**.^a

Parameters	r_{h1}	r_e	Restraint
<i>Independent</i>			
p_1 $r_{\text{C-C/O}}$ average	151.5(2)		
p_2 $r_{\text{C-C/O}}$ difference 1	-9.4(5)		
p_3 $r_{\text{C-C/O}}$ difference 2	0.3(5)		
p_4 $r_{\text{Ga-O/Ga-C}}$ average	197.2(1)		
p_5 $r_{\text{Ga-O/Ga-C}}$ difference	1.4(5)		
p_6 $r_{\text{C-H}}$ mean	110.4(3)		
p_7 $\angle\text{O-C-C}$ average	108.7(5)		
p_8 $\angle\text{O-C-C}$ difference	2.3(5)		
p_9 $\angle\text{C(6)-C(5)-C(7)}$	108.2(8)		
p_{10} $\angle\text{O-O-C}$	168.4(17)		
p_{11} $\angle\text{C-C-H}$ mean	110.5(9)		
p_{12} $\angle\text{Ga-C-H}$ average	112.0(8)		
p_{13} $\angle\text{Ga-C-H}$ difference 1	1.5(5)		
p_{14} $\angle\text{Ga-C-H}$ difference 2	-0.1(5)		
p_{15} $\angle\text{H(33)-C(31)-H(34)}$	108.3(10)		
p_{16} $\angle\text{H(32)-C(31)-H(34)}$	108.0(10)		
p_{17} $\angle\text{C(31)-Ga(4)-C(35)}$	122.2(16)		
p_{18} $\angle\text{O(2)-Ga(1)-O(3)}$	81.5(3)		
p_{19} $\phi_{\text{C-Ga-Ga-O}}$	89.6(31)		
p_{20} $\phi_{\text{H-C-Ga-Ga}}$	5.4(21)		
<i>Dependent</i>			
p_{21} $r_{\text{Ga-O}}$	197.9(2)		—
p_{22} $r_{\text{Ga-C}}$	196.5(3)		—
p_{23} $r_{\text{C-O}}$	144.5(5)		—
p_{24} $r_{\text{C(5)-C(6)}}$	154.0(3)		—
p_{25} $r_{\text{C(5)-C(7)}}$	153.7(4)		—
p_{26} $\angle\text{O-C(5)-C(6)}$	108.0(5)		—
p_{27} $\angle\text{O-C(5)-C(7)}$	110.2(7)		—

^a Distances (r) are in pm, angles (\angle) and dihedral angles (ϕ) are in degrees.

Table S5 Interatomic distances (r_a / pm), refined and calculated amplitudes of vibration (u_{hl} / pm) and distance corrections (k_{hl}) for the SARACEN-restrained GED structure of $\text{Me}_2\text{GaOCH}_2\text{CH}_2\text{NMe}_2$ (**30a**).^a

	Atom pair	r_a	$u_{\text{hl}}(\text{exp.})^b$	k_{hl}	$u_{\text{hl}}(\text{calc.})$	Restraint
u_{11}	C(3)–H(33)	108.4(2)	7.0(tied to u_1)	0.4	7.5	–
u_{10}	C(2)–H(21)	108.4(2)	7.0(tied to u_1)	0.4	7.5	–
u_9	C(3)–H(31)	108.4(2)	7.0(tied to u_1)	0.4	7.5	–
u_6	C(2)–H(23)	108.4(2)	7.0(tied to u_1)	0.4	7.5	–
u_{15}	C(2)–H(22)	108.4(2)	7.1(tied to u_1)	0.4	7.5	–
u_{13}	C(3)–H(32)	108.4(2)	7.0(tied to u_1)	0.4	7.5	–
u_7	C(8)–H(82)	108.4(2)	7.0(tied to u_1)	0.4	7.5	–
u_8	C(9)–H(93)	108.4(2)	7.0(tied to u_1)	0.4	7.5	–
u_3	C(9)–H(92)	108.4(2)	6.9(tied to u_1)	0.4	7.4	–
u_2	C(8)–H(81)	108.4(2)	6.9(tied to u_1)	0.4	7.4	–
u_1	C(9)–H(91)	108.4(2)	6.9(5)	0.4	7.4	–
u_4	C(8)–H(83)	108.4(2)	7.0(tied to u_1)	0.4	7.4	–
u_{12}	C(6)–H(61)	108.4(2)	7.0(tied to u_1)	0.4	7.5	–
u_{14}	C(5)–H(51)	108.4(2)	7.1(tied to u_1)	0.4	7.6	–
u_5	C(6)–H(62)	108.4(2)	7.0(tied to u_1)	0.4	7.5	–
u_{16}	C(5)–H(52)	108.4(2)	7.1(tied to u_1)	0.5	7.6	–
u_{17}	O(4)–C(5)	141.1(5)	5.6(4)	-0.2	4.5	–
u_{18}	C(8)–N(7)	148.7(4)	5.9(tied to u_{17})	0.1	4.8	–
u_{19}	N(7)–C(9)	148.9(4)	6.0(tied to u_{17})	0.1	4.8	–
u_{20}	C(6)–N(7)	150.2(4)	6.1(tied to u_{17})	0.4	4.9	–
u_{21}	C(5)–C(6)	154.4(5)	6.3(tied to u_{17})	0.2	5.1	–
u_{24}	H(51)...H(52)	173.6(13)	11.8(fixed)	0.3	11.8	–
u_{26}	H(21)...H(23)	174.5(12)	12.1(fixed)	-0.3	12.1	–
u_{29}	H(22)...H(23)	174.5(12)	12.1(fixed)	-0.3	12.1	–
u_{23}	H(21)...H(22)	174.5(12)	12.1(fixed)	-0.3	12.1	–
u_{30}	H(31)...H(32)	174.5(12)	12.1(fixed)	-0.3	12.1	–
u_{22}	H(31)...H(33)	174.5(12)	12.1(fixed)	-0.3	12.1	–
u_{25}	H(32)...H(33)	174.5(12)	12.1(fixed)	-0.2	12.1	–
u_{28}	H(81)...H(83)	174.9(12)	11.9(fixed)	0.1	11.9	–
u_{33}	H(82)...H(83)	174.9(12)	11.9(fixed)	0.1	11.9	–
u_{34}	H(81)...H(82)	174.9(12)	11.8(fixed)	0.1	11.8	–
u_{35}	H(92)...H(93)	175.5(9)	11.9(fixed)	0.1	11.9	–
u_{32}	H(91)...H(93)	175.5(9)	11.8(fixed)	0.1	11.8	–
u_{31}	H(61)...H(62)	175.9(13)	11.9(fixed)	0.2	11.9	–
u_{27}	H(91)...H(92)	176.0(13)	11.9(fixed)	0.0	11.9	–
u_{36}	Ga(1)–O(4)	190.3(4)	4.5(4)	-0.2	5.0	5.0(5)
u_{38}	C(3)–Ga(1)	200.7(2)	5.0(tied to u_{36})	0.1	5.6	–
u_{37}	C(2)–Ga(1)	200.7(2)	5.0(tied to u_{36})	0.1	5.6	–
u_{40}	O(4)...H(52)	204.9(7)	8.7(tied to u_{36})	-0.2	9.7	–
u_{39}	O(4)...H(51)	205.1(7)	8.7(tied to u_{36})	0.0	9.6	–
u_{41}	H(62)...N(7)	211.0(11)	9.0(tied to u_{36})	0.1	10.0	–
u_{48}	H(61)...N(7)	211.4(11)	9.0(tied to u_{36})	0.5	10.0	–
u_{43}	N(7)...H(92)	211.4(14)	9.0(tied to u_{36})	-0.1	10.0	–
u_{45}	N(7)...H(91)	211.4(14)	9.0(tied to u_{36})	-0.1	10.0	–
u_{42}	H(83)...N(7)	212.5(11)	9.0(tied to u_{36})	-0.1	10.0	–
u_{44}	H(81)...N(7)	212.5(11)	9.0(tied to u_{36})	-0.1	10.0	–

u_{47}	H(82)...N(7)	212.5(11)	8.9(tied to u_{36})	-0.1	9.9	—
u_{46}	N(7)...H(93)	212.7(11)	9.0(tied to u_{36})	-0.1	9.9	—
u_{52}	C(6)...H(52)	216.5(7)	9.4(tied to u_{36})	0.2	10.4	—
u_{49}	C(6)...H(51)	216.6(7)	9.5(tied to u_{36})	0.3	10.5	—
u_{50}	C(5)...H(62)	217.2(9)	9.6(tied to u_{36})	0.0	10.6	—
u_{53}	C(5)...H(61)	217.5(9)	9.5(tied to u_{36})	0.3	10.5	—
u_{82}	H(31)...H(81)	226.9(99)	46.1(fixed)	9.7	46.1	—
u_{55}	H(62)...H(81)	232.3(29)	20.9(fixed)	3.3	20.9	—
u_{51}	Ga(1)...N(7)	233.2(11)	8.3(7)	0.3	7.7	7.7(8)
u_{54}	H(52)...H(91)	234.2(65)	24.9(fixed)	6.4	24.9	—
u_{60}	H(61)...H(93)	234.2(32)	23.0(fixed)	3.3	23.0	—
u_{56}	O(4)...C(6)	242.4(14)	7.2(tied to u_{51})	-1.2	6.7	—
u_{64}	H(51)...H(52)	242.4(20)	17.6(fixed)	0.9	17.6	—
u_{57}	H(51)...H(62)	244.3(21)	16.8(fixed)	0.7	16.8	—
u_{66}	C(8)...H(62)	244.9(27)	15.3(tied to u_{51})	0.8	14.2	—
u_{61}	C(6)...C(9)	245.3(11)	7.5(tied to u_{51})	0.1	7.0	—
u_{62}	C(8)...C(6)	246.0(11)	7.6(tied to u_{51})	0.5	7.1	—
u_{65}	C(5)...N(7)	248.2(14)	6.7(tied to u_{51})	-0.5	6.3	—
u_{70}	H(61)...C(9)	252.0(26)	16.9(tied to u_{51})	0.7	15.7	—
u_{81}	H(23)...H(91)	252.8(85)	41.3(fixed)	12.8	41.3	—
u_{58}	C(8)...C(9)	256.4(21)	7.4(tied to u_{51})	0.1	6.9	—
u_{59}	H(83)...H(92)	256.7(46)	22.4(fixed)	2.9	22.4	—
u_{67}	H(51)...H(61)	257.6(19)	15.9(fixed)	0.9	15.9	—
u_{97}	H(82)...H(62)	258.3(42)	25.4(fixed)	0.1	25.4	—
u_{73}	Ga(1)...H(31)	258.6(12)	13.9(tied to u_{51})	-0.4	13.0	—
u_{72}	Ga(1)...H(32)	258.7(12)	13.9(tied to u_{51})	-0.3	12.9	—
u_{74}	Ga(1)...H(23)	258.7(12)	13.9(tied to u_{51})	-0.3	12.9	—
u_{69}	Ga(1)...H(33)	258.7(12)	14.0(tied to u_{51})	-0.3	13.1	—
u_{68}	Ga(1)...H(21)	258.7(12)	14.0(tied to u_{51})	-0.2	13.1	—
u_{71}	Ga(1)...H(22)	258.8(12)	14.0(tied to u_{51})	-0.2	13.1	—
u_{94}	H(32)...H(81)	265.4(110)	51.3(fixed)	8.5	51.3	—
u_{80}	C(6)...H(91)	267.7(21)	18.8(tied to u_{89})	0.0	15.5	—
u_{86}	C(6)...H(93)	269.6(20)	19.0(tied to u_{89})	0.5	15.7	—
u_{88}	C(6)...H(82)	270.2(20)	20.0(tied to u_{89})	0.6	16.5	—
u_{79}	C(6)...H(81)	270.6(20)	18.3(tied to u_{89})	0.7	15.1	—
u_{110}	H(32)...H(83)	271.2(68)	52.0(fixed)	10.2	52.0	—
u_{99}	C(3)...H(81)	272.3(101)	33.8(tied to u_{89})	5.7	27.9	—
u_{96}	H(61)...H(91)	273.6(37)	27.1(fixed)	-0.7	27.1	—
u_{90}	H(22)...H(92)	275.6(59)	54.3(fixed)	9.8	54.3	—
u_{85}	O(4)...N(7)	276.1(27)	10.1(tied to u_{89})	-2.2	8.4	—
u_{84}	O(4)...H(62)	276.5(32)	21.3(tied to u_{89})	-1.7	17.6	—
u_{75}	C(8)...H(92)	276.7(34)	16.9(tied to u_{89})	0.4	15.7	—
u_{76}	H(83)...C(9)	278.2(29)	16.8(tied to u_{89})	0.2	15.6	—
u_{89}	Ga(1)...C(5)	280.6(17)	8.7(6)	-2.3	7.2	7.2(7)
u_{95}	H(52)...N(7)	282.0(27)	18.2(tied to u_{89})	-0.6	15.0	—
u_{87}	C(5)...H(91)	283.2(50)	19.0(tied to u_{89})	1.9	20.8	—
u_{63}	H(82)...H(93)	287.2(40)	23.5(fixed)	2.7	23.5	—
u_{83}	H(82)...H(61)	287.6(29)	23.9(fixed)	3.3	23.9	—
u_{78}	C(8)...H(93)	290.9(25)	19.5(tied to u_{89})	0.2	16.1	—
u_{77}	H(82)...C(9)	291.0(25)	19.1(tied to u_{89})	0.3	15.7	—

u_{117}	C(2)...H(91)	291.9(82)	36.8(tied to u_{89})	1.5	30.3	—
u_{98}	H(52)...C(9)	295.6(53)	18.1(tied to u_{106})	1.4	19.8	—
u_{91}	C(8)...H(61)	297.8(17)	13.8(tied to u_{106})	1.2	15.1	—
u_{146}	H(22)...H(91)	299.5(76)	55.6(fixed)	-2.4	55.6	—
u_{107}	Ga(1)...H(91)	301.6(84)	18.6(tied to u_{106})	0.3	20.4	—
u_{92}	Ga(1)...C(6)	303.7(27)	7.9(tied to u_{106})	-0.6	8.7	—
u_{105}	H(52)...H(62)	304.2(10)	12.2(fixed)	-1.0	12.2	—
u_{101}	Ga(1)...C(9)	306.3(58)	9.7(tied to u_{106})	0.0	10.6	—
u_{121}	C(8)...H(32)	306.6(67)	39.1(tied to u_{106})	6.3	42.9	—
u_{136}	C(8)...H(31)	307.4(73)	36.3(tied to u_{106})	2.9	39.8	—
u_{106}	C(8)...Ga(1)	312.9(39)	9.8(8)	0.3	10.8	—
u_{120}	Ga(1)...H(52)	313.2(30)	21.4(tied to u_{106})	-4.0	23.5	—
u_{108}	C(5)...C(9)	313.9(35)	12.2(tied to u_{106})	-0.3	13.4	—
u_{113}	Ga(1)...H(92)	314.3(80)	17.3(tied to u_{106})	0.6	18.9	—
u_{93}	H(23)...H(92)	318.1(66)	50.0(fixed)	8.2	50.0	—
u_{171}	H(23)...H(52)	318.4(62)	65.4(fixed)	2.7	65.4	—
u_{100}	H(82)...H(92)	319.4(34)	26.0(fixed)	-0.5	26.0	—
u_{102}	C(2)...H(92)	319.5(59)	25.8(tied to u_{106})	5.1	28.2	—
u_{103}	H(83)...H(93)	320.6(32)	26.1(fixed)	-0.9	26.1	—
u_{141}	C(3)...H(83)	320.8(58)	31.9(tied to u_{106})	1.8	35.0	—
u_{111}	H(23)...C(9)	323.1(64)	33.5(tied to u_{106})	7.7	36.6	—
u_{135}	C(3)...C(8)	323.6(60)	18.6(tied to u_{106})	2.0	20.3	—
u_{114}	Ga(1)...H(92)	323.8(73)	17.1(tied to u_{106})	0.6	18.7	—
u_{118}	C(3)...O(4)	324.9(16)	11.3(tied to u_{106})	-0.7	12.4	—
u_{169}	H(31)...H(83)	325.8(82)	49.9(fixed)	-1.4	49.9	—
u_{139}	H(22)...C(9)	326.7(51)	43.8(tied to u_{106})	2.4	47.9	—
u_{112}	O(4)...H(91)	327.8(79)	35.4(tied to u_{106})	-0.5	38.7	—
u_{128}	O(4)...H(31)	328.9(27)	24.3(tied to u_{106})	1.7	26.7	—
u_{119}	C(2)...O(4)	329.7(16)	11.1(tied to u_{106})	-0.4	12.2	—
u_{116}	Ga(1)...H(83)	331.0(29)	18.4(tied to u_{106})	0.8	20.1	—
u_{122}	C(3)...N(7)	333.8(36)	12.6(tied to u_{106})	-0.1	13.8	—
u_{123}	O(4)...H(61)	334.2(12)	8.9(tied to u_{106})	-1.8	9.8	—
u_{124}	H(62)...C(9)	334.2(15)	9.3(tied to u_{106})	-1.0	10.1	—
u_{134}	O(4)...H(23)	336.0(27)	25.0(tied to u_{106})	2.6	27.4	—
u_{125}	H(52)...H(93)	336.4(61)	33.5(fixed)	1.1	33.5	—
u_{130}	C(2)...C(9)	336.7(53)	17.6(tied to u_{106})	1.8	19.3	—
u_{131}	C(6)...H(92)	338.5(12)	9.0(tied to u_{106})	-1.1	9.9	—
u_{137}	H(31)...N(7)	339.5(54)	29.2(fixed)	2.0	29.2	—
u_{132}	C(6)...H(83)	339.7(11)	9.1(tied to u_{106})	-0.9	10.0	—
u_{133}	H(51)...N(7)	341.0(13)	9.0(tied to u_{106})	-1.0	9.9	—
u_{115}	H(81)...H(61)	342.2(22)	23.1(fixed)	0.3	23.1	—
u_{109}	Ga(1)...H(62)	344.2(52)	17.8(tied to u_{106})	-0.7	19.5	—
u_{127}	C(8)...H(91)	344.9(18)	9.0(tied to u_{106})	-1.2	9.8	—
u_{104}	H(31)...H(62)	345.3(78)	57.2(fixed)	9.3	57.2	—
u_{126}	H(81)...C(9)	345.9(14)	9.0(tied to u_{106})	-1.2	9.8	—
u_{149}	H(32)...N(7)	348.5(41)	28.5(tied to u_{106})	0.9	31.2	—
u_{142}	H(83)...H(62)	349.4(25)	15.6(fixed)	-1.0	15.6	—
u_{129}	C(2)...N(7)	350.6(42)	11.9(tied to u_{106})	-0.3	13.0	—
u_{150}	H(62)...H(93)	353.8(29)	17.4(fixed)	-0.9	17.4	—
u_{153}	H(61)...H(92)	354.1(24)	16.4(fixed)	-1.0	16.4	—

u_{140}	C(2)...C(3)	358.1(21)	11.4(tied to u_{106})	-0.2	12.5	—
u_{138}	O(4)...C(9)	358.9(55)	22.1(tied to u_{106})	-2.9	24.3	—
u_{147}	C(5)...H(93)	360.3(40)	22.1(tied to u_{106})	-0.8	24.2	—
u_{144}	H(23)...N(7)	364.5(57)	25.0(tied to u_{106})	1.7	27.4	—
u_{148}	H(22)...N(7)	365.2(52)	30.5(tied to u_{106})	1.3	33.4	—
u_{180}	O(4)...H(81)	368.6(41)	23.2(tied to u_{106})	-3.8	25.4	—
u_{200}	C(2)...H(52)	368.7(48)	46.8(tied to u_{106})	-6.2	51.3	—
u_{151}	O(4)...H(33)	370.4(20)	26.7(tied to u_{106})	-0.6	29.2	—
u_{162}	H(62)...H(91)	370.5(21)	15.9(fixed)	-1.7	15.9	—
u_{152}	H(81)...H(92)	370.7(31)	16.5(fixed)	-1.3	16.5	—
u_{167}	C(8)...C(5)	370.7(11)	6.9(tied to u_{106})	-1.2	7.5	—
u_{154}	H(83)...H(91)	371.6(27)	16.5(fixed)	-1.4	16.5	—
u_{181}	H(33)...H(81)	371.8(99)	30.2(fixed)	-1.3	30.2	—
u_{159}	Ga(1)...H(51)	372.7(13)	11.1(tied to u_{106})	-4.0	12.2	—
u_{185}	C(5)...H(23)	374.7(45)	35.5(tied to u_{106})	0.7	38.9	—
u_{161}	O(4)...H(21)	375.2(20)	27.0(tied to u_{106})	-0.6	29.6	—
u_{166}	H(51)...H(91)	379.4(48)	20.8(fixed)	-0.2	20.8	—
u_{176}	C(5)...H(81)	380.5(31)	14.6(tied to u_{106})	-1.1	16.0	—
u_{177}	C(8)...O(4)	381.4(16)	11.0(tied to u_{106})	-4.2	12.1	—
u_{158}	H(22)...H(32)	382.7(60)	42.4(fixed)	9.1	42.4	—
u_{163}	C(2)...H(32)	383.7(36)	24.9(tied to u_{106})	1.5	27.3	—
u_{165}	C(3)...H(22)	383.7(36)	26.5(tied to u_{106})	1.4	29.0	—
u_{156}	C(6)...H(31)	384.5(44)	38.8(tied to u_{106})	4.6	42.5	—
u_{172}	H(52)...H(92)	385.6(52)	21.9(fixed)	-1.3	21.9	—
u_{168}	C(2)...H(33)	387.0(28)	24.5(tied to u_{106})	1.0	26.9	—
u_{164}	C(3)...H(21)	387.3(28)	24.4(tied to u_{106})	1.6	26.7	—
u_{157}	H(82)...H(91)	387.5(23)	16.9(fixed)	-1.5	16.9	—
u_{170}	H(83)...H(61)	388.1(16)	16.5(fixed)	-0.6	16.5	—
u_{155}	H(81)...H(93)	388.2(24)	17.0(fixed)	-1.5	17.0	—
u_{198}	H(21)...H(91)	390.2(83)	33.3(fixed)	-5.3	33.3	—
u_{160}	H(21)...H(33)	390.5(45)	39.5(fixed)	8.9	39.5	—
u_{143}	C(3)...H(62)	393.2(71)	43.9(fixed)	0.2	43.9	—
u_{193}	C(2)...C(5)	395.1(30)	24.0(fixed)	-4.7	24.0	—
u_{209}	H(31)...H(82)	396.6(84)	41.9(fixed)	1.6	41.9	—
u_{173}	Ga(1)...H(61)	397.1(20)	10.6(fixed)	-1.5	10.6	—
u_{178}	C(5)...H(92)	404.3(32)	14.5(fixed)	-2.0	14.5	—
u_{207}	H(32)...H(82)	404.5(76)	45.5(fixed)	3.6	45.5	—
u_{174}	C(3)...C(6)	405.4(36)	27.3(fixed)	-1.2	27.3	—
u_{179}	Ga(1)...H(93)	406.4(48)	12.4(fixed)	-1.6	12.4	—
u_{194}	O(4)...H(32)	406.7(15)	14.5(fixed)	-5.1	14.5	—
u_{145}	H(22)...H(83)	409.8(92)	49.6(fixed)	12.6	49.6	—
u_{197}	O(4)...H(22)	410.0(15)	15.2(fixed)	-5.3	15.2	—
u_{186}	H(51)...C(9)	411.0(31)	13.5(fixed)	-1.3	13.5	—
u_{183}	Ga(1)...H(82)	412.1(35)	12.3(fixed)	-1.4	12.3	—
u_{184}	C(5)...H(31)	412.8(27)	35.2(fixed)	1.4	35.2	—
u_{188}	H(22)...H(33)	414.9(40)	46.0(fixed)	-1.1	46.0	—
u_{182}	H(21)...H(32)	415.3(41)	44.9(fixed)	0.3	44.9	—
u_{195}	H(23)...H(93)	416.2(76)	38.8(fixed)	6.0	38.8	—
u_{196}	H(62)...H(92)	416.3(19)	13.2(fixed)	-1.7	13.2	—
u_{201}	C(5)...H(82)	417.1(18)	15.1(fixed)	-1.3	15.1	—

u_{187}	H(21)...H(92)	417.3(58)	30.9(fixed)	-3.2	30.9	—
u_{227}	H(33)...H(83)	418.0(57)	38.3(fixed)	-4.1	38.3	—
u_{199}	H(81)...H(91)	420.7(17)	13.0(fixed)	-2.1	13.0	—
u_{230}	H(32)...H(92)	421.1(100)	41.3(fixed)	2.8	41.3	—
u_{192}	C(3)...C(5)	421.2(16)	19.6(fixed)	-3.7	19.6	—
u_{203}	C(8)...H(52)	423.5(21)	14.1(fixed)	-1.7	14.1	—
u_{190}	O(4)...H(92)	423.7(59)	25.1(fixed)	-3.7	25.1	—
u_{221}	C(3)...H(82)	425.0(69)	21.8(fixed)	-0.4	21.8	—
u_{224}	C(8)...H(33)	425.4(59)	22.0(fixed)	-4.6	22.0	—
u_{220}	H(22)...H(93)	426.5(60)	50.3(fixed)	1.4	50.3	—
u_{205}	H(33)...N(7)	428.5(32)	15.4(fixed)	-5.1	15.4	—
u_{218}	C(6)...H(23)	432.0(54)	29.2(fixed)	0.2	29.2	—
u_{204}	O(4)...H(93)	433.9(49)	27.8(fixed)	-4.7	27.8	—
u_{259}	H(22)...H(52)	434.2(50)	55.4(fixed)	-11.1	55.4	—
u_{250}	H(21)...H(52)	434.2(48)	60.3(fixed)	-11.2	60.3	—
u_{175}	C(2)...H(83)	434.7(70)	32.0(fixed)	2.7	32.0	—
u_{189}	H(32)...H(62)	435.0(73)	53.0(fixed)	-3.0	53.0	—
u_{214}	H(21)...C(9)	437.1(53)	21.2(fixed)	-5.7	21.2	—
u_{208}	C(2)...C(6)	438.0(41)	13.9(fixed)	-3.1	13.9	—
u_{211}	C(3)...H(23)	439.2(17)	13.7(fixed)	-4.9	13.7	—
u_{210}	C(2)...H(31)	439.6(17)	13.6(fixed)	-4.5	13.6	—
u_{217}	C(2)...H(93)	440.2(61)	21.1(fixed)	-0.1	21.1	—
u_{232}	C(3)...H(92)	440.4(89)	24.8(fixed)	-1.5	24.8	—
u_{206}	H(21)...N(7)	442.2(35)	14.5(fixed)	-5.8	14.5	—
u_{228}	C(3)...C(9)	442.3(64)	13.4(fixed)	-2.1	13.4	—
u_{219}	H(51)...H(93)	442.8(39)	24.2(fixed)	-0.8	24.2	—
u_{191}	C(8)...H(22)	443.3(79)	40.1(fixed)	5.6	40.1	—
u_{222}	O(4)...H(83)	443.6(20)	16.5(fixed)	-4.8	16.5	—
u_{243}	H(32)...C(9)	443.8(71)	31.7(fixed)	-0.2	31.7	—
u_{226}	H(81)...H(51)	444.5(41)	19.9(fixed)	-0.2	19.9	—
u_{215}	C(6)...H(32)	445.7(40)	37.3(fixed)	-3.3	37.3	—
u_{202}	C(2)...C(8)	447.1(65)	20.2(fixed)	-0.1	20.2	—
u_{223}	C(8)...H(51)	448.2(21)	12.1(fixed)	-1.0	12.1	—
u_{225}	C(5)...H(83)	450.6(14)	11.6(fixed)	-2.4	11.6	—
u_{236}	H(81)...H(52)	454.1(29)	17.8(fixed)	-2.8	17.8	—
u_{239}	O(4)...H(82)	455.5(17)	14.7(fixed)	-5.7	14.7	—
u_{246}	C(5)...H(21)	459.8(31)	35.3(fixed)	-8.4	35.3	—
u_{255}	C(5)...H(22)	462.7(32)	29.1(fixed)	-8.7	29.1	—
u_{216}	H(31)...H(51)	465.9(44)	54.6(fixed)	2.2	54.6	—
u_{263}	H(23)...H(51)	466.2(45)	41.0(fixed)	-3.7	41.0	—
u_{229}	H(82)...H(52)	466.9(24)	19.9(fixed)	-1.0	19.9	—
u_{240}	H(23)...H(32)	469.7(37)	26.6(fixed)	-5.2	26.6	—
u_{248}	H(31)...C(9)	469.8(68)	26.8(fixed)	-2.1	26.8	—
u_{237}	H(22)...H(31)	470.3(37)	27.7(fixed)	-4.5	27.7	—
u_{253}	C(3)...H(91)	472.5(78)	19.1(fixed)	-3.1	19.1	—
u_{241}	H(23)...H(33)	473.6(29)	26.3(fixed)	-5.3	26.3	—
u_{238}	H(21)...H(31)	474.4(29)	25.7(fixed)	-4.6	25.7	—
u_{247}	C(6)...H(22)	477.3(47)	29.3(fixed)	-4.2	29.3	—
u_{213}	H(33)...H(62)	478.0(71)	50.3(fixed)	-5.6	50.3	—
u_{212}	H(23)...H(83)	479.9(77)	45.2(fixed)	-0.9	45.2	—

u_{235}	C(2)...H(81)	480.0(94)	25.0(fixed)	-1.7	25.0	—
u_{264}	H(23)...H(61)	481.6(64)	38.4(fixed)	-0.1	38.4	—
u_{231}	C(8)...H(23)	481.6(68)	33.4(fixed)	-1.5	33.4	—
u_{251}	H(82)...H(51)	481.9(26)	20.1(fixed)	-0.5	20.1	—
u_{244}	C(5)...H(33)	483.5(18)	32.8(fixed)	-7.3	32.8	—
u_{265}	H(31)...H(92)	483.6(91)	31.0(fixed)	-3.9	31.0	—
u_{258}	C(3)...H(52)	484.7(21)	15.4(fixed)	-7.2	15.4	—
u_{234}	H(31)...H(61)	485.2(50)	47.5(fixed)	3.2	47.5	—
u_{257}	C(5)...H(32)	487.3(21)	23.7(fixed)	-7.4	23.7	—
u_{233}	H(22)...H(81)	488.9(107)	41.3(fixed)	3.0	41.3	—
u_{275}	H(32)...H(91)	490.3(80)	28.7(fixed)	-3.2	28.7	—
u_{242}	C(3)...H(51)	490.6(29)	38.1(fixed)	-5.2	38.1	—
u_{245}	C(6)...H(33)	491.0(33)	33.0(fixed)	-6.6	33.0	—
u_{256}	H(83)...H(52)	491.5(31)	18.4(fixed)	-2.8	18.4	—
u_{267}	C(2)...H(51)	491.9(28)	22.0(fixed)	-8.2	22.0	—
u_{261}	H(31)...H(52)	493.5(25)	29.2(fixed)	-3.8	29.2	—
u_{270}	C(2)...H(61)	503.9(45)	21.4(fixed)	-4.4	21.4	—
u_{262}	H(51)...H(92)	506.1(28)	15.2(fixed)	-3.4	15.2	—
u_{254}	C(3)...H(61)	506.4(35)	29.3(fixed)	-2.6	29.3	—
u_{276}	H(31)...H(91)	508.2(76)	28.4(fixed)	-2.7	28.4	—
u_{252}	C(2)...H(62)	508.4(52)	16.3(fixed)	-4.0	16.3	—
u_{273}	H(23)...H(31)	510.1(23)	16.9(fixed)	-7.6	16.9	—
u_{249}	H(21)...H(83)	515.6(66)	37.6(fixed)	-3.3	37.6	—
u_{269}	H(23)...H(62)	516.3(55)	24.7(fixed)	-3.1	24.7	—
u_{272}	C(6)...H(21)	520.9(37)	19.2(fixed)	-7.9	19.2	—
u_{283}	H(33)...H(92)	523.9(86)	29.4(fixed)	-6.0	29.4	—
u_{271}	H(23)...H(81)	525.5(89)	31.2(fixed)	-4.6	31.2	—
u_{289}	H(33)...H(82)	526.0(70)	23.5(fixed)	-7.7	23.5	—
u_{286}	H(32)...H(93)	528.0(64)	36.9(fixed)	-1.7	36.9	—
u_{282}	H(33)...C(9)	529.6(62)	15.9(fixed)	-7.0	15.9	—
u_{260}	H(22)...H(82)	530.7(64)	44.5(fixed)	3.9	44.5	—
u_{281}	C(3)...H(93)	531.0(52)	16.5(fixed)	-3.8	16.5	—
u_{268}	C(8)...H(21)	531.5(61)	23.4(fixed)	-5.8	23.4	—
u_{290}	H(22)...H(61)	534.4(50)	37.5(fixed)	-5.4	37.5	—
u_{279}	H(32)...H(61)	537.2(42)	41.3(fixed)	-4.3	41.3	—
u_{280}	H(83)...H(51)	537.3(19)	14.1(fixed)	-3.0	14.1	—
u_{266}	C(2)...H(82)	538.8(52)	22.2(fixed)	-1.6	22.2	—
u_{285}	H(21)...H(93)	540.2(62)	23.2(fixed)	-8.2	23.2	—
u_{295}	H(32)...H(52)	543.5(34)	23.5(fixed)	-10.2	23.5	—
u_{274}	H(33)...H(51)	544.3(30)	52.5(fixed)	-9.5	52.5	—
u_{287}	H(33)...H(52)	544.5(23)	27.6(fixed)	-10.9	27.6	—
u_{288}	H(31)...H(93)	546.0(61)	31.9(fixed)	-2.8	31.9	—
u_{294}	H(21)...H(51)	547.5(29)	35.9(fixed)	-11.7	35.9	—
u_{293}	H(33)...H(91)	548.2(83)	23.6(fixed)	-6.7	23.6	—
u_{277}	H(22)...H(62)	548.4(61)	29.2(fixed)	-4.4	29.2	—
u_{284}	H(21)...H(81)	552.1(96)	29.5(fixed)	-5.8	29.5	—
u_{278}	H(23)...H(82)	562.2(59)	37.3(fixed)	-1.7	37.3	—
u_{291}	H(32)...H(51)	564.1(29)	38.5(fixed)	-10.2	38.5	—
u_{297}	H(22)...H(51)	564.5(30)	26.0(fixed)	-12.8	26.0	—
u_{292}	H(21)...H(62)	584.6(50)	21.6(fixed)	-7.8	21.6	—

u_{298}	H(21)...H(61)	592.3(42)	24.9(fixed)	-10.6	24.9	—
u_{296}	H(33)...H(61)	594.0(32)	34.3(fixed)	-9.1	34.3	—
u_{300}	H(33)...H(93)	622.4(50)	17.9(fixed)	-10.0	17.9	—
u_{299}	H(21)...H(82)	627.2(49)	24.2(fixed)	-8.5	24.2	—

^a Estimated standard deviations, as obtained in the least squares refinement, are given in parentheses. ^b Amplitudes not refined were fixed at the values obtained using the force field calculated at the B3LYP/6-311+G* level.

Table S6 Interatomic distances (r_a / pm), refined and calculated amplitudes of vibration (u_{h1} / pm) and distance corrections (k_{h1}) for the SARACEN-restrained GED structure of Me₂GaOCH₂CH₂OMe (**31a**).

	Atom pair	r_a	$u_{h1}(\text{exp.})^b$	k_{h1}	$u_{h1}(\text{calc.})$	Restraint
u_8	C(1)-H(9)	109.6(7)	8.2(tied to u_1)	0.4	7.8	–
u_{12}	C(1)-H(10)	109.6(7)	8.1(tied to u_1)	0.4	7.8	–
u_6	C(1)-H(11)	109.7(7)	8.1(tied to u_1)	0.4	7.7	–
u_9	C(2)-H(14)	109.7(7)	8.0(tied to u_1)	0.4	7.6	–
u_7	C(2)-H(12)	109.7(7)	8.0(tied to u_1)	0.4	7.6	–
u_{11}	C(2)-H(13)	109.7(7)	8.0(tied to u_1)	0.4	7.6	–
u_1	C(3)-H(17)	109.7(7)	7.8(7)	0.4	7.4	–
u_3	C(3)-H(15)	109.7(7)	7.8(tied to u_1)	0.4	7.5	–
u_2	C(3)-H(16)	109.7(7)	7.8(tied to u_1)	0.4	7.4	–
u_4	C(8)-H(20)	109.7(7)	7.8(tied to u_1)	0.4	7.5	–
u_{10}	C(7)-H(18)	109.8(7)	7.9(tied to u_1)	0.4	7.5	–
u_5	C(8)-H(21)	109.8(7)	7.8(tied to u_1)	0.4	7.5	–
u_{13}	C(7)-H(19)	109.8(7)	8.0(tied to u_1)	0.5	7.6	–
u_{14}	O(6)-C(7)	143.6(7)	4.2(5)	0.0	4.5	–
u_{15}	C(3)-O(4)	146.1(7)	4.3(tied to u_{14})	0.1	4.6	–
u_{16}	O(4)-C(8)	147.7(7)	4.5(tied to u_{14})	0.2	4.8	–
u_{17}	C(7)-C(8)	155.2(8)	4.7(tied to u_{14})	0.1	5.0	–
u_{73}	H(12)...H(15)	172.8(31)	72.5(fixed)	14.0	72.5	–
u_{18}	H(13)...H(14)	175.7(31)	12.3(fixed)	-0.5	12.3	–
u_{23}	H(18)...H(19)	176.2(31)	11.8(fixed)	0.2	11.8	–
u_{24}	H(12)...H(13)	177.0(31)	12.2(fixed)	-0.6	12.2	–
u_{22}	H(10)...H(11)	177.7(30)	12.3(fixed)	-0.7	12.3	–
u_{21}	H(9)...H(11)	177.8(30)	12.4(fixed)	-0.7	12.4	–
u_{19}	H(9)...H(10)	177.8(30)	12.5(fixed)	-0.6	12.5	–
u_{28}	H(20)...H(21)	178.2(31)	11.8(fixed)	0.2	11.8	–
u_{25}	H(15)...H(17)	178.6(31)	11.8(fixed)	0.1	11.8	–
u_{26}	H(16)...H(17)	178.8(31)	11.8(fixed)	0.1	11.8	–
u_{27}	H(15)...H(16)	178.8(92)	11.8(fixed)	0.1	11.8	–
u_{20}	H(12)...H(14)	180.4(87)	12.3(fixed)	-0.6	12.3	–
u_{29}	Ga(5)-O(6)	186.4(11)	5.7(6)	0.1	4.9	–
u_{31}	C(2)-Ga(5)	197.0(6)	6.4(tied to u_{29})	0.2	5.5	–
u_{30}	C(1)-Ga(5)	197.0(6)	6.4(tied to u_{29})	0.2	5.5	–
u_{38}	O(4)...H(15)	206.6(35)	11.3(tied to u_{29})	-0.1	9.7	–
u_{37}	O(6)...H(19)	208.2(13)	11.2(tied to u_{29})	-0.2	9.6	–
u_{33}	O(6)...H(18)	208.5(13)	11.3(tied to u_{29})	0.1	9.7	–
u_{32}	O(4)...H(17)	210.1(33)	11.4(tied to u_{29})	-0.1	9.8	–
u_{34}	O(4)...H(21)	211.0(22)	11.3(tied to u_{29})	-0.2	9.7	–
u_{35}	O(4)...H(16)	211.3(33)	11.3(tied to u_{29})	-0.1	9.7	–
u_{36}	O(4)...H(20)	211.4(22)	11.4(tied to u_{29})	0.2	9.8	–
u_{39}	O(4)...Ga(5)	215.9(20)	9.4(tied to u_{29})	0.2	8.0	–
u_{40}	C(8)...H(19)	218.3(14)	12.1(tied to u_{29})	-0.1	10.4	–
u_{41}	C(8)...H(18)	218.4(14)	12.2(tied to u_{29})	0.0	10.4	–
u_{112}	H(12)...H(17)	218.9(31)	68.8(fixed)	-1.3	68.8	–
u_{42}	C(7)...H(21)	220.4(20)	12.3(tied to u_{29})	-0.1	10.5	–
u_{43}	C(7)...H(20)	220.5(20)	12.2(tied to u_{29})	0.0	10.4	–
u_{50}	H(15)...H(21)	237.8(11)	26.9(fixed)	4.5	26.9	–

<i>u</i> ₄₄	O(4)...C(7)	238.9(20)	5.3(tied to <i>u</i> ₅₄)	-0.2	6.4	—
<i>u</i> ₄₇	H(19)...H(20)	240.9(32)	16.8(fixed)	0.1	16.8	—
<i>u</i> ₄₅	O(6)...C(8)	242.2(17)	5.3(tied to <i>u</i> ₅₄)	-0.2	6.4	—
<i>u</i> ₆₇	H(16)...H(21)	242.6(11)	28.9(fixed)	-1.3	28.9	—
<i>u</i> ₁₀₁	C(3)...H(12)	242.7(22)	48.7(tied to <i>u</i> ₅₄)	4.8	58.8	—
<i>u</i> ₄₈	H(18)...H(21)	243.1(36)	16.8(fixed)	0.2	16.8	—
<i>u</i> ₅₉	C(3)...H(21)	243.5(42)	13.8(tied to <i>u</i> ₅₄)	0.5	16.7	—
<i>u</i> ₄₆	C(3)...C(8)	243.6(19)	6.0(tied to <i>u</i> ₅₄)	-0.2	7.2	—
<i>u</i> ₅₄	O(4)...O(6)	251.9(31)	6.5(7)	-0.8	7.8	—
<i>u</i> ₇₆	H(13)...H(17)	253.5(19)	63.0(fixed)	16.5	63.0	—
<i>u</i> ₅₁	Ga(5)...H(14)	253.9(34)	11.1(tied to <i>u</i> ₅₄)	0.3	13.4	—
<i>u</i> ₅₇	Ga(5)...H(12)	255.3(33)	11.0(tied to <i>u</i> ₅₄)	0.0	13.2	—
<i>u</i> ₅₆	Ga(5)...H(11)	255.5(33)	11.0(tied to <i>u</i> ₅₄)	0.1	13.2	—
<i>u</i> ₅₃	Ga(5)...H(9)	255.6(33)	11.3(tied to <i>u</i> ₅₄)	0.3	13.6	—
<i>u</i> ₅₅	Ga(5)...H(10)	255.7(33)	11.0(tied to <i>u</i> ₅₄)	0.3	13.3	—
<i>u</i> ₅₈	Ga(5)...H(13)	257.9(33)	10.8(tied to <i>u</i> ₅₄)	0.1	13.1	—
<i>u</i> ₇₂	H(11)...H(19)	265.1(115)	52.4(fixed)	19.2	52.4	—
<i>u</i> ₆₀	C(8)...H(16)	266.8(60)	13.9(tied to <i>u</i> ₅₄)	-0.3	16.8	—
<i>u</i> ₉₁	C(2)...H(15)	267.2(149)	39.8(tied to <i>u</i> ₅₄)	3.8	48.1	—
<i>u</i> ₉₆	C(2)...H(17)	267.6(191)	31.1(tied to <i>u</i> ₅₄)	2.1	37.6	—
<i>u</i> ₆₄	C(8)...H(15)	268.7(65)	14.9(tied to <i>u</i> ₅₄)	0.8	18.0	—
<i>u</i> ₅₂	H(18)...H(20)	271.0(31)	15.5(fixed)	0.2	15.5	—
<i>u</i> ₆₅	Ga(5)...C(7)	277.4(18)	5.1(7)	-0.8	7.0	—
<i>u</i> ₆₂	O(4)...H(19)	284.2(38)	11.2(tied to <i>u</i> ₆₅)	-0.2	15.3	—
<i>u</i> ₆₃	O(6)...H(21)	288.7(40)	11.2(tied to <i>u</i> ₆₅)	-0.1	15.3	—
<i>u</i> ₁₀₃	C(2)...C(3)	296.8(106)	20.6(tied to <i>u</i> ₆₅)	0.5	28.1	—
<i>u</i> ₇₁	C(3)...Ga(5)	297.1(24)	9.1(tied to <i>u</i> ₆₅)	-0.2	12.4	—
<i>u</i> ₈₈	H(13)...H(15)	300.6(182)	83.6(fixed)	6.4	83.6	—
<i>u</i> ₄₉	H(16)...H(20)	301.6(73)	24.0(fixed)	2.7	24.0	—
<i>u</i> ₇₀	Ga(5)...H(19)	301.9(43)	12.8(tied to <i>u</i> ₆₅)	-1.6	17.5	—
<i>u</i> ₈₆	O(4)...H(12)	302.4(132)	28.4(tied to <i>u</i> ₆₅)	5.0	38.8	—
<i>u</i> ₆₆	Ga(5)...C(8)	306.3(21)	5.7(tied to <i>u</i> ₆₅)	-0.3	7.7	—
<i>u</i> ₇₄	Ga(5)...H(17)	306.8(76)	14.5(tied to <i>u</i> ₆₅)	1.9	19.8	—
<i>u</i> ₆₁	C(3)...H(20)	306.9(39)	11.2(tied to <i>u</i> ₆₅)	-0.1	15.3	—
<i>u</i> ₆₈	H(19)...H(21)	307.1(23)	12.2(fixed)	-1.0	12.2	—
<i>u</i> ₉₃	Ga(5)...H(15)	307.4(106)	20.0(tied to <i>u</i> ₆₅)	0.0	27.4	—
<i>u</i> ₇₈	C(2)...O(4)	311.3(87)	11.4(tied to <i>u</i> ₆₅)	-0.8	15.5	—
<i>u</i> ₇₇	C(2)...O(6)	311.5(39)	8.8(tied to <i>u</i> ₆₅)	-0.2	12.0	—
<i>u</i> ₇₉	C(1)...O(6)	317.0(37)	8.6(tied to <i>u</i> ₆₅)	-0.9	11.8	—
<i>u</i> ₁₀₄	C(1)...H(19)	318.7(86)	35.4(fixed)	-2.3	35.4	—
<i>u</i> ₉₇	C(3)...H(13)	319.6(123)	45.7(tied to <i>u</i> ₆₅)	6.7	62.4	—
<i>u</i> ₈₉	O(6)...H(11)	320.8(76)	31.1(fixed)	6.6	31.1	—
<i>u</i> ₁₃₄	O(6)...H(15)	321.0(82)	23.9(fixed)	-1.3	23.9	—
<i>u</i> ₈₅	O(6)...H(12)	323.8(75)	30.6(fixed)	6.7	30.6	—
<i>u</i> ₇₅	C(1)...O(4)	331.7(61)	11.5(tied to <i>u</i> ₆₅)	0.0	15.7	—
<i>u</i> ₈₁	O(4)...H(18)	332.2(22)	9.6(fixed)	-0.9	9.6	—
<i>u</i> ₁₀₅	C(7)...H(11)	333.2(92)	38.0(fixed)	12.3	38.0	—
<i>u</i> ₈₄	O(6)...H(20)	334.3(20)	9.6(fixed)	-1.0	9.6	—
<i>u</i> ₈₃	C(8)...H(17)	336.7(28)	10.1(fixed)	-2.1	10.1	—
<i>u</i> ₁₆₃	H(12)...H(16)	337.2(197)	59.6(fixed)	1.1	59.6	—

u_{102}	O(6)...H(14)	340.3(79)	38.7(fixed)	-0.2	38.7	—
u_{152}	H(14)...H(15)	340.5(184)	51.5(fixed)	-12.0	51.5	—
u_{92}	O(4)...H(10)	344.5(106)	47.3(fixed)	1.9	47.3	—
u_{120}	C(3)...O(6)	344.9(36)	10.6(fixed)	-2.2	10.6	—
u_{80}	O(4)...H(11)	346.4(113)	41.2(fixed)	6.9	41.2	—
u_{95}	O(4)...H(13)	348.0(101)	44.2(fixed)	0.5	44.2	—
u_{100}	H(17)...H(21)	349.4(43)	17.6(fixed)	-2.1	17.6	—
u_{69}	H(15)...H(20)	352.6(78)	27.9(fixed)	-1.0	27.9	—
u_{127}	C(7)...H(15)	354.1(60)	16.6(fixed)	-1.3	16.6	—
u_{106}	C(3)...C(7)	354.7(20)	7.1(fixed)	-1.7	7.1	—
u_{115}	C(1)...C(7)	361.3(55)	20.5(fixed)	-2.3	20.5	—
u_{156}	H(14)...H(17)	361.9(200)	42.8(fixed)	-11.3	42.8	—
u_{108}	O(6)...H(9)	363.4(75)	38.4(fixed)	-1.1	38.4	—
u_{94}	C(1)...C(2)	364.2(33)	12.2(fixed)	-0.4	12.2	—
u_{82}	Ga(5)...H(21)	370.8(45)	17.9(fixed)	-0.2	17.9	—
u_{107}	Ga(5)...H(18)	374.1(18)	9.7(fixed)	-1.6	9.7	—
u_{147}	H(10)...H(19)	376.3(117)	55.0(fixed)	-13.5	55.0	—
u_{142}	H(9)...H(19)	377.6(117)	59.4(fixed)	-11.3	59.4	—
u_{113}	Ga(5)...H(20)	384.8(34)	10.9(fixed)	-1.6	10.9	—
u_{168}	C(3)...H(14)	386.7(128)	31.1(fixed)	-13.6	31.1	—
u_{109}	C(1)...H(13)	390.6(82)	30.0(fixed)	5.1	30.0	—
u_{99}	H(17)...H(20)	392.5(53)	17.3(fixed)	-2.8	17.3	—
u_{132}	O(6)...H(10)	392.7(49)	18.5(fixed)	-9.5	18.5	—
u_{129}	C(8)...H(11)	393.0(104)	37.0(fixed)	9.0	37.0	—
u_{116}	C(2)...H(9)	394.0(66)	34.8(fixed)	1.7	34.8	—
u_{125}	Ga(5)...H(16)	395.7(25)	13.5(fixed)	-3.4	13.5	—
u_{138}	O(4)...H(14)	396.3(82)	19.1(fixed)	-10.8	19.1	—
u_{130}	O(6)...H(13)	396.9(41)	17.7(fixed)	-8.3	17.7	—
u_{90}	H(12)...H(21)	397.1(80)	53.3(fixed)	18.6	53.3	—
u_{110}	C(2)...H(10)	397.5(87)	31.6(fixed)	5.5	31.6	—
u_{114}	C(8)...H(12)	398.0(66)	40.2(fixed)	11.4	40.2	—
u_{169}	C(2)...H(16)	399.3(106)	28.6(fixed)	-4.2	28.6	—
u_{117}	C(1)...H(14)	402.2(81)	33.5(fixed)	1.1	33.5	—
u_{146}	O(6)...H(17)	403.6(78)	15.6(fixed)	-2.3	15.6	—
u_{124}	C(7)...H(16)	405.3(58)	15.7(fixed)	-2.8	15.7	—
u_{98}	H(10)...H(13)	406.1(136)	48.1(fixed)	24.3	48.1	—
u_{137}	C(1)...C(8)	408.3(56)	16.8(fixed)	-2.3	16.8	—
u_{131}	H(9)...H(13)	409.7(110)	59.6(fixed)	0.4	59.6	—
u_{158}	H(13)...H(16)	411.8(138)	63.4(fixed)	1.7	63.4	—
u_{167}	H(15)...H(18)	411.9(83)	22.6(fixed)	-1.2	22.6	—
u_{151}	H(11)...H(20)	413.8(127)	48.6(fixed)	10.6	48.6	—
u_{119}	H(9)...H(14)	414.3(125)	52.5(fixed)	15.4	52.5	—
u_{135}	O(4)...H(9)	417.2(60)	19.1(fixed)	-11.3	19.1	—
u_{126}	C(2)...C(8)	417.8(37)	21.2(fixed)	-1.0	21.2	—
u_{122}	C(3)...H(19)	419.3(30)	17.2(fixed)	-2.5	17.2	—
u_{164}	C(7)...H(10)	422.2(86)	38.9(fixed)	-11.4	38.9	—
u_{140}	C(2)...C(7)	422.3(22)	13.6(fixed)	-1.8	13.6	—
u_{136}	C(7)...H(12)	423.6(50)	30.4(fixed)	8.0	30.4	—
u_{150}	C(7)...H(9)	424.3(89)	44.4(fixed)	-8.9	44.4	—
u_{155}	O(6)...H(16)	424.9(57)	13.4(fixed)	-4.8	13.4	—

u_{162}	H(11)...H(18)	424.9(101)	42.0(fixed)	10.0	42.0	—
u_{149}	C(3)...H(18)	429.9(39)	11.5(fixed)	-2.3	11.5	—
u_{87}	H(10)...H(17)	431.3(138)	59.0(fixed)	20.7	59.0	—
u_{143}	C(7)...H(17)	434.4(45)	11.8(fixed)	-2.8	11.8	—
u_{144}	C(1)...H(12)	435.0(45)	15.6(fixed)	-8.1	15.6	—
u_{145}	C(2)...H(11)	436.3(33)	16.0(fixed)	-9.0	16.0	—
u_{111}	C(1)...H(17)	437.7(89)	31.4(fixed)	3.1	31.4	—
u_{157}	H(15)...H(19)	438.1(55)	18.2(fixed)	-3.7	18.2	—
u_{118}	C(2)...H(21)	439.2(58)	36.2(fixed)	0.4	36.2	—
u_{133}	H(10)...H(14)	439.2(113)	59.9(fixed)	-0.5	59.9	—
u_{165}	C(8)...H(10)	439.3(101)	46.0(fixed)	-5.9	46.0	—
u_{128}	C(1)...C(3)	441.2(67)	21.7(fixed)	-1.4	21.7	—
u_{180}	C(1)...H(20)	445.7(79)	26.3(fixed)	-3.7	26.3	—
u_{121}	C(3)...H(10)	447.2(119)	53.7(fixed)	8.3	53.7	—
u_{195}	H(10)...H(20)	460.7(127)	59.6(fixed)	-7.6	59.6	—
u_{183}	C(1)...H(18)	460.8(61)	22.1(fixed)	-3.9	22.1	—
u_{159}	H(10)...H(12)	465.5(97)	33.0(fixed)	-5.7	33.0	—
u_{179}	C(7)...H(14)	467.6(67)	36.0(fixed)	-6.5	36.0	—
u_{139}	H(16)...H(19)	468.1(53)	26.2(fixed)	-2.8	26.2	—
u_{173}	H(16)...H(18)	468.2(83)	19.6(fixed)	-3.2	19.6	—
u_{141}	C(3)...H(11)	470.4(112)	54.9(fixed)	-0.4	54.9	—
u_{161}	H(11)...H(13)	471.2(72)	32.3(fixed)	-7.6	32.3	—
u_{153}	C(8)...H(13)	471.9(75)	46.9(fixed)	-5.4	46.9	—
u_{177}	H(11)...H(14)	474.3(78)	30.8(fixed)	-11.3	30.8	—
u_{178}	H(9)...H(12)	475.5(58)	32.1(fixed)	-10.1	32.1	—
u_{182}	C(2)...H(19)	477.1(34)	15.2(fixed)	-3.5	15.2	—
u_{176}	C(1)...H(15)	480.2(100)	27.6(fixed)	-4.1	27.6	—
u_{123}	H(11)...H(17)	480.7(123)	66.3(fixed)	-1.5	66.3	—
u_{184}	C(8)...H(14)	487.0(64)	33.8(fixed)	-10.9	33.8	—
u_{154}	H(17)...H(19)	487.1(55)	22.5(fixed)	-3.2	22.5	—
u_{207}	H(14)...H(16)	489.1(132)	31.2(fixed)	-18.9	31.2	—
u_{174}	H(12)...H(18)	490.7(77)	39.9(fixed)	10.2	39.9	—
u_{191}	C(8)...H(9)	491.0(69)	28.2(fixed)	-12.5	28.2	—
u_{187}	H(11)...H(21)	492.9(100)	32.6(fixed)	4.1	32.6	—
u_{181}	H(12)...H(20)	494.6(85)	43.8(fixed)	8.9	43.8	—
u_{148}	H(13)...H(21)	494.9(97)	60.6(fixed)	-6.6	60.6	—
u_{189}	H(12)...H(19)	495.3(47)	26.7(fixed)	2.7	26.7	—
u_{188}	C(7)...H(13)	495.9(44)	28.3(fixed)	-8.7	28.3	—
u_{194}	H(11)...H(12)	497.1(46)	20.8(fixed)	-12.2	20.8	—
u_{186}	C(2)...H(18)	500.5(41)	21.3(fixed)	-2.3	21.3	—
u_{185}	C(1)...H(21)	502.2(58)	16.1(fixed)	-3.1	16.1	—
u_{175}	H(14)...H(21)	503.9(98)	51.1(fixed)	-11.0	51.1	—
u_{171}	H(9)...H(17)	504.0(99)	39.6(fixed)	-11.3	39.6	—
u_{170}	H(10)...H(15)	507.0(135)	50.8(fixed)	5.4	50.8	—
u_{190}	C(2)...H(20)	510.2(57)	22.1(fixed)	-2.7	22.1	—
u_{193}	H(11)...H(15)	511.9(110)	50.0(fixed)	-5.7	50.0	—
u_{198}	H(9)...H(18)	515.3(101)	49.1(fixed)	-9.5	49.1	—
u_{192}	C(3)...H(9)	515.8(67)	25.5(fixed)	-15.1	25.5	—
u_{160}	H(10)...H(16)	518.2(138)	66.3(fixed)	4.1	66.3	—
u_{196}	H(17)...H(18)	519.0(53)	13.5(fixed)	-4.1	13.5	—

u_{200}	H(14)...H(19)	522.5(61)	30.1(fixed)	-7.3	30.1	—
u_{172}	C(1)...H(16)	523.6(80)	31.0(fixed)	-4.0	31.0	—
u_{205}	H(10)...H(18)	526.6(88)	38.1(fixed)	-14.5	38.1	—
u_{206}	H(9)...H(20)	532.8(87)	36.5(fixed)	-16.8	36.5	—
u_{201}	H(14)...H(18)	534.2(92)	47.9(fixed)	-7.0	47.9	—
u_{197}	H(10)...H(21)	537.2(101)	39.2(fixed)	-5.1	39.2	—
u_{202}	H(13)...H(19)	542.9(55)	27.3(fixed)	-8.4	27.3	—
u_{166}	H(11)...H(16)	543.9(129)	65.2(fixed)	1.2	65.2	—
u_{204}	H(9)...H(15)	544.2(119)	33.1(fixed)	-15.5	33.1	—
u_{199}	H(13)...H(20)	553.8(94)	50.6(fixed)	-5.8	50.6	—
u_{208}	H(13)...H(18)	580.2(52)	33.6(fixed)	-11.9	33.6	—
u_{203}	H(9)...H(21)	582.0(72)	24.8(fixed)	-11.6	24.8	—
u_{210}	H(14)...H(20)	583.2(62)	32.1(fixed)	-14.0	32.1	—
u_{209}	H(9)...H(16)	602.8(75)	33.7(fixed)	-20.5	33.7	—

^a Estimated standard deviations, as obtained in the least squares refinement, are given in parentheses. ^b Amplitudes not refined were fixed at the values obtained using the force field calculated at the B3LYP/6-311+G* level.

Table S7 Interatomic distances (r_a / pm), refined and calculated amplitudes of vibration (u_{h1} / pm) and distance corrections (k_{h1}) for the SARACEN-restrained GED structure of $[\text{Me}_2\text{GaO}^t\text{Bu}]_2$ (**32**).^a

	Atom pair	r_a	$u_{h1}(\text{exp.})^b$	k_{h1}	$u_{h1}(\text{calc.})$	Restraint
u_3	C(31)-H(34)	110.4(3)	6.0(tied to u_1)	0.4	7.7	–
u_8	C(31)-H(32)	110.4(3)	6.1(tied to u_1)	0.4	7.7	–
u_6	C(31)-H(33)	110.4(3)	6.0(tied to u_1)	0.4	7.7	–
u_1	C(7)-H(12)	110.4(3)	6.0(4)	0.4	7.7	–
u_4	C(6)-H(11)	110.4(3)	6.0(tied to u_1)	0.4	7.7	–
u_7	C(7)-H(13)	110.4(3)	6.0(tied to u_1)	0.4	7.7	–
u_5	C(6)-H(10)	110.4(3)	6.0(tied to u_1)	0.4	7.7	–
u_2	C(6)-H(9)	110.4(3)	6.0(tied to u_1)	0.4	7.7	–
u_9	O(2)-C(5)	144.4(5)	4.8(tied to u_{10})	0.1	5.2	–
u_{11}	C(5)-C(7)	153.7(4)	4.9(tied to u_{10})	0.2	5.3	–
u_{10}	C(5)-C(6)	154.0(3)	4.9(7)	0.2	5.3	–
u_{12}	H(32)...H(33)	172.8(37)	12.6(fixed)	-0.3	12.6	–
u_{16}	H(32)...H(34)	177.4(13)	12.5(fixed)	-0.3	12.5	–
u_{15}	H(33)...H(34)	177.7(13)	12.5(fixed)	-0.3	12.5	–
u_{19}	H(9)...H(10)	178.1(11)	12.4(fixed)	-0.1	12.4	–
u_{14}	H(12)...H(14)	178.2(11)	12.4(fixed)	-0.1	12.4	–
u_{13}	H(10)...H(11)	178.2(11)	12.4(fixed)	0.0	12.4	–
u_{18}	H(9)...H(11)	178.2(11)	12.4(fixed)	0.0	12.4	–
u_{17}	H(12)...H(13)	178.3(11)	12.4(fixed)	0.0	12.4	–
u_{20}	Ga(1)-C(39)	196.5(3)	5.3(tied to u_{21})	0.2	5.8	–
u_{21}	Ga(1)-O(2)	197.9(2)	6.2(3)	0.2	6.8	–
u_{24}	C(5)...H(12)	217.5(12)	11.0(fixed)	-0.2	11.0	–
u_{25}	C(5)...H(13)	217.7(12)	11.0(fixed)	-0.1	11.0	–
u_{22}	C(5)...H(9)	217.8(12)	11.0(fixed)	-0.2	11.0	–
u_{23}	C(18)...H(25)	217.8(12)	11.0(fixed)	-0.2	11.0	–
u_{26}	C(5)...H(10)	217.8(12)	11.0(fixed)	-0.2	11.0	–
u_{27}	O(2)...C(6)	241.4(9)	6.4(6)	0.1	7.2	–
u_{28}	O(2)...C(7)	244.6(10)	6.6(tied to u_{27})	0.1	7.4	–
u_{30}	C(6)...C(7)	248.9(13)	6.8(tied to u_{27})	-0.1	7.7	–
u_{33}	H(10)...H(14)	249.5(44)	25.9(fixed)	3.8	25.9	–
u_{38}	H(11)...H(13)	254.1(41)	27.4(fixed)	3.5	27.4	–
u_{32}	O(2)...O(3)	256.5(9)	7.2(tied to u_{27})	-1.7	8.1	–
u_{37}	Ga(1)...H(42)	257.2(12)	12.0(tied to u_{27})	-0.4	13.5	–
u_{35}	Ga(1)...H(40)	257.7(12)	11.9(tied to u_{27})	-0.1	13.5	–
u_{29}	C(6)...C(8)	258.4(26)	6.7(tied to u_{27})	-0.1	7.6	–
u_{36}	Ga(1)...H(41)	259.3(12)	11.9(tied to u_{27})	-0.5	13.4	–
u_{50}	H(10)...H(32)	264.6(96)	81.3(fixed)	18.3	81.3	–
u_{42}	O(2)...H(10)	266.6(17)	17.7(fixed)	0.2	17.7	–
u_{39}	O(2)...H(9)	266.7(17)	17.9(fixed)	0.3	17.9	–
u_{31}	H(11)...H(15)	268.1(47)	25.8(fixed)	3.4	25.8	–
u_{41}	H(12)...H(41)	268.7(72)	74.6(fixed)	19.7	74.6	–
u_{34}	H(9)...H(17)	268.8(60)	25.2(fixed)	3.4	25.2	–
u_{40}	O(2)...H(12)	270.6(19)	19.1(fixed)	0.4	19.1	–
u_{47}	C(6)...H(14)	270.7(24)	17.8(fixed)	0.4	17.8	–
u_{45}	C(7)...H(10)	272.0(24)	17.2(fixed)	0.3	17.2	–
u_{49}	C(7)...H(11)	272.8(23)	18.1(fixed)	0.1	18.1	–

u_{48}	C(6)...H(13)	274.2(23)	18.8(fixed)	0.4	18.8	—
u_{43}	H(12)...H(42)	278.4(102)	65.9(fixed)	22.2	65.9	—
u_{44}	C(6)...H(15)	284.3(31)	17.7(fixed)	0.3	17.7	—
u_{46}	C(6)...H(17)	284.6(38)	17.2(fixed)	0.2	17.2	—
u_{53}	Ga(1)...H(16)	295.6(22)	29.9(tied to u_{55})	6.6	31.3	—
u_{55}	Ga(1)...Ga(4)	299.5(5)	7.1(4)	-0.3	7.4	—
u_{59}	H(11)...H(14)	302.6(28)	29.5(fixed)	-1.0	29.5	—
u_{54}	H(12)...C(39)	304.4(57)	50.7(fixed)	15.7	50.7	—
u_{56}	H(10)...H(13)	306.5(27)	30.2(fixed)	-0.7	30.2	—
u_{51}	H(9)...H(38)	309.3(82)	67.0(fixed)	23.6	67.0	—
u_{58}	Ga(1)...C(5)	309.6(5)	9.0(tied to u_{55})	-1.0	9.4	—
u_{52}	H(10)...H(38)	311.2(91)	64.7(fixed)	26.5	64.7	—
u_{67}	H(10)...C(31)	315.9(71)	63.9(fixed)	5.2	63.9	—
u_{57}	H(9)...H(15)	318.4(40)	29.0(fixed)	-0.8	29.0	—
u_{62}	O(2)...C(31)	323.4(40)	13.2(tied to u_{55})	-1.6	13.8	—
u_{61}	O(2)...C(35)	326.7(38)	13.2(tied to u_{55})	0.8	13.8	—
u_{65}	Ga(1)...C(8)	333.0(14)	20.6(tied to u_{55})	1.3	21.5	—
u_{60}	H(9)...H(36)	333.6(106)	69.1(fixed)	15.8	69.1	—
u_{64}	O(2)...H(36)	335.5(59)	31.1(fixed)	4.8	31.1	—
u_{66}	O(2)...H(11)	336.1(10)	10.3(fixed)	-1.5	10.3	—
u_{68}	O(2)...H(13)	338.1(11)	10.4(fixed)	-1.9	10.4	—
u_{71}	O(2)...H(34)	338.1(60)	31.0(fixed)	1.2	31.0	—
u_{72}	Ga(1)...H(17)	340.6(24)	36.3(tied to u_{55})	-0.2	38.0	—
u_{69}	Ga(1)...H(12)	342.7(37)	36.2(tied to u_{55})	4.6	37.9	—
u_{78}	C(31)...C(35)	343.1(27)	12.6(tied to u_{55})	-0.5	13.2	—
u_{63}	H(9)...C(35)	343.3(65)	46.5(fixed)	12.6	46.5	—
u_{76}	C(6)...H(12)	344.1(13)	10.7(fixed)	-2.0	10.7	—
u_{75}	C(7)...H(9)	344.4(13)	10.6(fixed)	-1.7	10.6	—
u_{73}	H(10)...C(35)	346.6(69)	47.5(fixed)	10.3	47.5	—
u_{74}	C(6)...H(16)	351.4(19)	10.6(fixed)	-1.7	10.6	—
u_{77}	H(34)...H(42)	354.9(80)	87.2(fixed)	26.8	87.2	—
u_{79}	C(7)...H(34)	355.5(92)	60.3(fixed)	8.6	60.3	—
u_{80}	O(2)...H(32)	355.9(49)	32.0(fixed)	-1.4	32.0	—
u_{83}	H(12)...H(34)	359.2(81)	84.8(fixed)	8.9	84.8	—
u_{70}	C(6)...H(38)	359.8(82)	49.1(fixed)	19.7	49.1	—
u_{82}	C(7)...H(32)	360.2(66)	62.6(fixed)	4.8	62.6	—
u_{92}	C(6)...H(32)	361.8(84)	65.7(fixed)	6.5	65.7	—
u_{100}	H(10)...H(34)	362.1(93)	74.8(fixed)	-3.2	74.8	—
u_{81}	O(2)...H(38)	366.2(47)	32.5(fixed)	1.1	32.5	—
u_{90}	C(31)...H(38)	366.3(41)	28.7(fixed)	1.6	28.7	—
u_{89}	H(10)...H(12)	370.5(27)	18.6(fixed)	-2.3	18.6	—
u_{87}	H(9)...H(14)	370.7(27)	18.7(fixed)	-1.8	18.7	—
u_{84}	H(32)...H(38)	370.9(52)	44.6(fixed)	10.2	44.6	—
u_{93}	H(11)...H(12)	373.1(26)	19.1(fixed)	-2.4	19.1	—
u_{94}	H(9)...H(13)	373.9(26)	19.1(fixed)	-1.9	19.1	—
u_{85}	Ga(1)...C(7)	374.5(22)	20.6(13)	-0.7	25.6	—
u_{95}	C(31)...H(37)	374.6(39)	29.9(fixed)	0.9	29.9	—
u_{97}	H(10)...H(36)	379.9(94)	69.2(fixed)	1.2	69.2	—
u_{96}	C(7)...C(31)	381.3(52)	33.1(tied to u_{85})	2.3	41.2	—
u_{86}	H(10)...H(15)	382.5(30)	18.6(fixed)	-1.9	18.6	—

u_{91}	H(9)...H(16)	382.8(37)	18.2(fixed)	-2.1	18.2	—
u_{98}	C(5)...H(32)	384.3(67)	43.1(fixed)	1.5	43.1	—
u_{88}	C(6)...C(35)	385.7(64)	24.3(tied to u_{85})	7.5	30.3	—
u_{105}	H(33)...H(38)	386.6(70)	47.3(fixed)	-0.1	47.3	—
u_{101}	C(5)...C(31)	388.4(52)	15.9(tied to u_{85})	-2.3	19.8	—
u_{99}	C(6)...H(36)	395.0(97)	58.1(fixed)	5.4	58.1	—
u_{103}	C(5)...H(34)	395.3(82)	41.8(fixed)	-0.6	41.8	—
u_{107}	C(6)...C(31)	397.5(63)	37.0(tied to u_{85})	-2.3	46.2	—
u_{102}	O(2)...C(18)	397.5(10)	7.4(tied to u_{85})	-3.4	9.2	—
u_{117}	H(10)...H(33)	400.0(65)	67.7(fixed)	-0.3	67.7	—
u_{104}	H(12)...H(40)	403.1(62)	53.1(fixed)	5.9	53.1	—
u_{106}	Ga(1)...H(14)	405.4(29)	42.3(tied to u_{124})	-3.4	41.6	—
u_{116}	H(12)...H(32)	406.1(60)	81.4(fixed)	-5.2	81.4	—
u_{111}	H(12)...C(31)	406.1(45)	67.8(fixed)	-2.7	67.8	—
u_{113}	H(32)...H(37)	410.1(66)	48.7(fixed)	-1.6	48.7	—
u_{114}	O(2)...H(33)	413.4(33)	16.0(fixed)	-7.1	16.0	—
u_{109}	Ga(1)...H(34)	414.9(31)	41.3(tied to u_{124})	4.8	40.6	—
u_{112}	O(2)...H(37)	414.9(34)	17.1(fixed)	-5.6	17.1	—
u_{127}	H(9)...H(32)	415.8(84)	76.3(fixed)	-0.8	76.3	—
u_{108}	C(5)...C(35)	416.6(50)	18.8(tied to u_{124})	0.0	18.5	—
u_{115}	C(5)...H(36)	423.5(78)	41.9(fixed)	1.8	41.9	—
u_{110}	C(5)...H(38)	425.2(65)	39.9(fixed)	4.6	39.9	—
u_{118}	C(31)...H(42)	425.5(65)	72.4(fixed)	9.3	72.4	—
u_{124}	Ga(1)...C(31)	427.4(19)	23.2(10)	-2.1	22.8	—
u_{130}	C(31)...H(36)	428.2(22)	14.5(fixed)	-5.9	14.5	—
u_{120}	H(9)...H(12)	429.3(20)	14.3(fixed)	-3.1	14.3	—
u_{122}	Ga(1)...C(6)	429.3(8)	12.9(tied to u_{124})	-4.4	12.7	—
u_{134}	H(11)...H(32)	429.4(86)	70.8(fixed)	6.6	70.8	—
u_{123}	H(13)...H(32)	429.8(70)	65.1(fixed)	4.2	65.1	—
u_{135}	C(6)...H(34)	431.9(87)	56.5(fixed)	-6.5	56.5	—
u_{121}	H(10)...H(16)	432.4(21)	14.0(fixed)	-2.8	14.0	—
u_{125}	H(10)...H(37)	434.8(61)	48.6(fixed)	3.5	48.6	—
u_{128}	Ga(1)...H(15)	437.4(13)	22.6(tied to u_{124})	-1.3	22.2	—
u_{131}	Ga(1)...H(9)	439.5(21)	30.8(tied to u_{124})	-4.5	30.3	—
u_{137}	H(9)...C(31)	440.2(62)	57.9(fixed)	-7.5	57.9	—
u_{126}	H(9)...H(37)	441.2(65)	49.4(fixed)	1.8	49.4	—
u_{133}	H(13)...H(34)	442.7(95)	63.0(fixed)	2.6	63.0	—
u_{132}	O(2)...H(22)	447.1(46)	35.4(fixed)	0.1	35.4	—
u_{119}	H(11)...H(38)	448.7(87)	52.9(fixed)	17.9	52.9	—
u_{129}	H(9)...H(45)	449.5(79)	75.5(fixed)	10.4	75.5	—
u_{136}	O(2)...C(19)	457.4(33)	20.5(tied to u_{124})	-1.9	20.2	—
u_{139}	Ga(1)...H(10)	458.5(18)	20.0(tied to u_{124})	-5.4	19.7	—
u_{142}	H(33)...H(36)	459.3(36)	27.7(fixed)	-6.0	27.7	—
u_{144}	H(32)...H(36)	462.4(34)	29.0(fixed)	-6.4	29.0	—
u_{138}	O(2)...H(27)	462.7(22)	27.3(fixed)	-2.8	27.3	—
u_{140}	H(13)...C(31)	465.5(55)	41.7(fixed)	-1.6	41.7	—
u_{141}	Ga(1)...H(13)	470.1(20)	24.6(tied to u_{124})	-3.4	24.2	—
u_{143}	O(2)...C(20)	474.0(12)	14.0(tied to u_{124})	-4.5	13.8	—
u_{145}	O(2)...H(25)	477.8(26)	27.5(fixed)	-5.0	27.5	—
u_{157}	H(11)...C(31)	478.1(65)	49.4(fixed)	-4.0	49.4	—

u_{149}	C(31)...C(39)	480.4(51)	55.5(tied to u_{124})	-3.2	54.6	—
u_{153}	C(7)...H(33)	481.0(54)	43.4(fixed)	-7.1	43.4	—
u_{147}	C(6)...H(37)	481.1(58)	32.5(fixed)	-1.7	32.5	—
u_{154}	H(32)...H(42)	483.4(74)	83.1(fixed)	1.7	83.1	—
u_{161}	C(6)...H(33)	484.4(55)	50.6(fixed)	-9.1	50.6	—
u_{146}	H(11)...C(35)	484.7(66)	34.2(fixed)	4.2	34.2	—
u_{159}	C(5)...H(33)	486.4(45)	21.3(fixed)	-10.1	21.3	—
u_{148}	H(9)...C(43)	487.7(48)	56.6(fixed)	-0.6	56.6	—
u_{155}	H(12)...C(43)	488.6(59)	50.3(fixed)	-1.9	50.3	—
u_{151}	H(12)...H(46)	488.8(76)	68.7(fixed)	3.8	68.7	—
u_{160}	Ga(1)...H(32)	491.7(32)	34.3(tied to u_{124})	-6.9	33.7	—
u_{158}	H(33)...H(42)	492.8(74)	83.8(fixed)	2.2	83.8	—
u_{164}	H(9)...H(34)	493.1(78)	57.7(fixed)	-12.3	57.7	—
u_{152}	H(11)...H(36)	493.5(100)	63.0(fixed)	2.0	63.0	—
u_{150}	C(6)...H(45)	495.8(76)	57.4(fixed)	3.4	57.4	—
u_{162}	Ga(1)...H(33)	498.6(29)	33.4(tied to u_{124})	-6.7	32.8	—
u_{156}	H(9)...H(46)	498.9(66)	74.8(fixed)	-0.8	74.8	—
u_{165}	H(34)...H(36)	504.2(24)	18.6(fixed)	-9.1	18.6	—
u_{171}	H(12)...H(33)	505.2(52)	71.4(fixed)	-11.8	71.4	—
u_{172}	H(11)...H(34)	506.2(94)	62.7(fixed)	-8.3	62.7	—
u_{166}	C(5)...H(37)	512.4(42)	19.6(fixed)	-8.2	19.6	—
u_{163}	C(6)...C(43)	515.1(45)	33.9(fixed)	-3.3	33.9	—
u_{167}	C(7)...C(35)	515.2(53)	30.6(fixed)	-4.2	30.6	—
u_{169}	Ga(1)...H(11)	516.3(11)	15.7(fixed)	-6.3	15.7	—
u_{178}	H(9)...H(33)	518.9(53)	64.7(fixed)	-13.1	64.7	—
u_{168}	C(7)...H(38)	521.1(70)	49.5(fixed)	0.8	49.5	—
u_{170}	C(6)...H(46)	527.1(62)	53.5(fixed)	-1.5	53.5	—
u_{174}	C(6)...H(42)	529.1(76)	43.5(fixed)	-5.1	43.5	—
u_{175}	C(6)...C(39)	529.1(48)	19.1(fixed)	-8.0	19.1	—
u_{176}	C(6)...H(41)	531.9(66)	43.2(fixed)	-5.8	43.2	—
u_{177}	H(12)...H(45)	535.2(74)	50.1(fixed)	-7.2	50.1	—
u_{181}	H(10)...H(42)	536.4(76)	57.0(fixed)	-2.5	57.0	—
u_{173}	C(5)...C(18)	538.8(12)	9.9(fixed)	-5.6	9.9	—
u_{182}	C(31)...H(41)	540.5(61)	65.2(fixed)	-9.9	65.2	—
u_{179}	C(7)...H(36)	542.8(73)	39.8(fixed)	-5.7	39.8	—
u_{180}	H(10)...H(45)	546.3(66)	57.1(fixed)	-0.4	57.1	—
u_{185}	C(31)...H(40)	551.7(58)	65.7(fixed)	-9.8	65.7	—
u_{186}	H(10)...C(39)	553.3(49)	32.8(fixed)	-8.7	32.8	—
u_{183}	O(2)...H(24)	562.3(30)	20.4(fixed)	-5.8	20.4	—
u_{191}	H(13)...H(33)	563.6(59)	45.3(fixed)	-11.9	45.3	—
u_{204}	H(11)...H(33)	565.8(61)	55.7(fixed)	-12.3	55.7	—
u_{188}	H(10)...C(43)	566.1(41)	33.8(fixed)	-7.3	33.8	—
u_{190}	H(12)...H(44)	566.4(48)	54.8(fixed)	-6.6	54.8	—
u_{189}	H(12)...C(35)	566.5(49)	35.4(fixed)	-8.7	35.4	—
u_{199}	H(10)...H(41)	569.4(64)	48.2(fixed)	-9.2	48.2	—
u_{196}	H(9)...C(39)	570.1(50)	26.8(fixed)	-10.4	26.8	—
u_{193}	H(10)...H(30)	571.8(45)	49.3(fixed)	7.8	49.3	—
u_{184}	H(9)...H(22)	575.9(44)	62.6(fixed)	10.1	62.6	—
u_{192}	O(2)...H(26)	576.6(12)	14.9(fixed)	-7.3	14.9	—
u_{201}	H(9)...H(41)	578.6(69)	46.9(fixed)	-8.1	46.9	—

u_{195}	H(11)...H(37)	578.8(62)	37.6(fixed)	-5.4	37.6	-
u_{187}	H(11)...H(45)	579.1(83)	62.6(fixed)	0.2	62.6	-
u_{194}	C(5)...H(22)	580.6(42)	39.4(fixed)	-2.6	39.4	-
u_{205}	H(11)...H(41)	583.8(75)	49.1(fixed)	-5.4	49.1	-
u_{206}	H(9)...H(42)	584.5(72)	39.1(fixed)	-9.4	39.1	-
u_{200}	H(9)...H(44)	584.6(52)	59.3(fixed)	-10.8	59.3	-
u_{220}	H(32)...H(41)	586.3(96)	78.9(fixed)	-14.5	78.9	-
u_{203}	H(12)...H(38)	587.7(64)	50.2(fixed)	-6.9	50.2	-
u_{198}	H(13)...H(38)	588.8(77)	52.4(fixed)	1.9	52.4	-
u_{208}	H(12)...H(36)	590.7(68)	38.5(fixed)	-8.4	38.5	-
u_{211}	C(5)...H(27)	591.1(24)	29.2(fixed)	-4.9	29.2	-
u_{216}	C(31)...C(43)	592.4(27)	16.7(fixed)	-5.7	16.7	-
u_{210}	H(10)...H(46)	593.2(58)	50.8(fixed)	-7.9	50.8	-
u_{218}	H(11)...H(42)	593.6(87)	49.7(fixed)	-7.3	49.7	-
u_{197}	H(11)...H(46)	594.5(70)	57.6(fixed)	-1.0	57.6	-
u_{212}	H(13)...C(35)	595.8(57)	32.2(fixed)	-5.4	32.2	-
u_{202}	H(11)...C(43)	595.9(51)	37.5(fixed)	-5.2	37.5	-
u_{219}	H(11)...C(39)	596.1(56)	24.9(fixed)	-9.7	24.9	-
u_{215}	C(31)...H(45)	596.7(34)	33.0(fixed)	-1.8	33.0	-
u_{207}	C(5)...C(19)	596.8(30)	23.3(fixed)	-4.7	23.3	-
u_{209}	H(10)...H(22)	598.8(53)	53.3(fixed)	4.1	53.3	-
u_{221}	C(7)...H(37)	601.9(41)	33.9(fixed)	-11.0	33.9	-
u_{214}	C(5)...H(25)	602.5(23)	33.0(fixed)	-6.7	33.0	-
u_{213}	H(9)...H(23)	606.0(41)	72.5(fixed)	1.5	72.5	-
u_{222}	C(5)...C(20)	608.3(13)	16.5(fixed)	-6.8	16.5	-
u_{225}	H(9)...H(30)	609.3(47)	59.7(fixed)	-1.7	59.7	-
u_{229}	H(33)...H(40)	611.5(87)	80.0(fixed)	-14.6	80.0	-
u_{224}	C(6)...H(44)	612.2(43)	35.2(fixed)	-12.9	35.2	-
u_{217}	C(6)...H(22)	613.4(44)	48.3(fixed)	3.3	48.3	-
u_{226}	H(34)...H(45)	617.5(45)	34.5(fixed)	-2.4	34.5	-
u_{228}	C(6)...H(30)	617.9(36)	42.2(fixed)	-0.4	42.2	-
u_{227}	H(13)...H(36)	620.2(81)	45.9(fixed)	-7.1	45.9	-
u_{231}	H(32)...H(40)	620.3(60)	72.1(fixed)	-19.0	72.1	-
u_{223}	C(7)...H(25)	621.5(34)	52.1(fixed)	0.5	52.1	-
u_{232}	C(6)...H(40)	625.5(41)	20.9(fixed)	-16.6	20.9	-
u_{233}	C(7)...H(27)	641.6(40)	40.6(fixed)	-4.2	40.6	-
u_{230}	C(6)...H(23)	641.8(39)	54.8(fixed)	-4.1	54.8	-
u_{235}	H(10)...H(23)	648.0(47)	58.1(fixed)	-8.2	58.1	-
u_{237}	H(12)...H(37)	648.3(39)	40.7(fixed)	-15.3	40.7	-
u_{244}	H(10)...H(40)	648.6(46)	35.5(fixed)	-17.7	35.5	-
u_{234}	C(6)...C(19)	650.5(32)	35.0(fixed)	-3.7	35.0	-
u_{242}	C(31)...H(44)	652.9(33)	28.4(fixed)	-9.8	28.4	-
u_{236}	H(32)...H(45)	652.9(43)	40.9(fixed)	-4.2	40.9	-
u_{239}	C(6)...H(29)	656.4(36)	42.9(fixed)	-8.4	42.9	-
u_{240}	H(33)...H(45)	657.0(42)	41.6(fixed)	-4.2	41.6	-
u_{243}	C(31)...H(46)	657.2(31)	27.8(fixed)	-9.7	27.8	-
u_{238}	C(6)...C(21)	657.2(26)	28.5(fixed)	-6.2	28.5	-
u_{245}	H(10)...H(44)	657.6(41)	36.3(fixed)	-16.4	36.3	-
u_{247}	H(9)...H(40)	660.2(40)	30.5(fixed)	-17.9	30.5	-
u_{241}	H(12)...H(23)	662.8(73)	42.4(fixed)	-7.7	42.4	-

u_{248}	H(9)...H(29)	671.2(46)	49.7(fixed)	-13.5	49.7	—
u_{246}	C(7)...H(22)	674.1(58)	33.3(fixed)	-8.9	33.3	—
u_{249}	C(7)...C(19)	680.9(48)	19.9(fixed)	-8.8	19.9	—
u_{250}	H(12)...H(22)	681.8(69)	40.1(fixed)	-12.5	40.1	—
u_{251}	H(13)...H(37)	684.7(46)	35.8(fixed)	-13.5	35.8	—
u_{253}	H(9)...H(27)	689.1(41)	49.8(fixed)	-12.4	49.8	—
u_{255}	C(6)...H(27)	692.7(28)	31.6(fixed)	-11.9	31.6	—
u_{259}	H(11)...H(40)	693.9(50)	26.9(fixed)	-19.4	26.9	—
u_{252}	H(11)...H(44)	694.5(48)	38.3(fixed)	-15.7	38.3	—
u_{263}	H(10)...H(27)	700.1(41)	34.4(fixed)	-14.3	34.4	—
u_{256}	C(6)...C(20)	700.7(20)	16.7(fixed)	-12.1	16.7	—
u_{254}	C(5)...H(24)	701.9(29)	23.3(fixed)	-9.0	23.3	—
u_{257}	C(6)...H(25)	702.5(29)	32.3(fixed)	-13.7	32.3	—
u_{262}	H(32)...H(46)	708.5(46)	41.8(fixed)	-12.1	41.8	—
u_{260}	C(5)...H(26)	712.5(13)	17.3(fixed)	-10.1	17.3	—
u_{258}	H(11)...H(22)	718.9(43)	50.7(fixed)	-0.8	50.7	—
u_{264}	H(9)...H(25)	719.5(41)	33.9(fixed)	-17.6	33.9	—
u_{265}	H(10)...H(28)	721.5(36)	42.9(fixed)	-4.1	42.9	—
u_{266}	H(32)...H(44)	721.7(47)	33.3(fixed)	-16.7	33.3	—
u_{261}	H(9)...H(24)	723.5(35)	54.5(fixed)	-5.1	54.5	—
u_{268}	H(33)...H(46)	729.3(43)	32.4(fixed)	-16.7	32.4	—
u_{269}	H(10)...H(24)	741.8(39)	41.1(fixed)	-8.4	41.1	—
u_{267}	H(11)...H(23)	744.1(39)	56.4(fixed)	-7.3	56.4	—
u_{271}	C(6)...H(24)	754.2(31)	35.9(fixed)	-8.7	35.9	—
u_{272}	H(9)...H(28)	754.9(34)	45.0(fixed)	-11.5	45.0	—
u_{270}	C(7)...H(26)	755.9(31)	36.6(fixed)	-7.4	36.6	—
u_{273}	C(6)...H(28)	760.7(26)	29.3(fixed)	-9.7	29.3	—
u_{274}	H(12)...H(24)	772.0(56)	35.6(fixed)	-11.6	35.6	—
u_{275}	C(7)...H(24)	782.3(44)	21.1(fixed)	-12.2	21.1	—
u_{276}	H(10)...H(26)	787.8(31)	33.5(fixed)	-14.9	33.5	—
u_{277}	H(9)...H(26)	796.1(30)	35.8(fixed)	-16.6	35.8	—
u_{278}	C(6)...H(26)	799.3(19)	19.0(fixed)	-15.4	19.0	—
u_{279}	H(11)...H(24)	859.6(31)	37.8(fixed)	-12.8	37.8	—
u_{280}	H(11)...H(28)	864.5(26)	30.1(fixed)	-13.7	30.1	—
u_{281}	H(13)...H(24)	884.4(43)	21.6(fixed)	-16.2	21.6	—
u_{282}	H(11)...H(26)	899.4(20)	20.7(fixed)	-19.1	20.7	—

^a Estimated standard deviations, as obtained in the least squares refinement, are given in parentheses. ^b Amplitudes not refined were fixed at the values obtained using the force field calculated at the B3LYP/6-311+G* level.

Table S8 Least-squares correlation matrix ($\times 100$) for $\text{Me}_2\text{GaOCH}_2\text{CH}_2\text{NMe}_2$ (**30a**).^a

	p_{22}	p_{23}	p_{24}	p_{25}	p_{26}	u_{17}	u_{36}	k_1	k_2
p_2							54		
p_4									57
p_{10}	52								
p_{11}									
p_{12}			57						
p_{13}		-51	53						
p_{16}				-50	-74				
p_{21}	68								
p_{23}		100		52	51				
p_{25}				100	81				
u_1						56		69	60
u_{17}						100		64	
k_1								100	65

^a Only elements with absolute values $\geq 50\%$ are shown.**Table S9** Least-squares correlation matrix ($\times 100$) for $\text{Me}_2\text{GaOCH}_2\text{CH}_2\text{OMe}$ (**31a**).^a

	p_3	p_4	p_{28}	p_{29}	p_{30}	p_{32}
p_1		52				
p_2	-54					
p_9				67		
p_{10}						
p_{11}			50		-65	
p_{12}			63		-70	
p_{28}			100		-55	
p_{31}						-61

^a Only elements with absolute values $\geq 50\%$ are shown.**Table S10** Least-squares correlation matrix ($\times 100$) for $[\text{Me}_2\text{GaO}^t\text{Bu}]_2$ (**32**).^a

	p_{19}	u_{21}	u_{27}	k_2
p_7			55	
p_{10}	-79			
u_1		54		
u_{21}		100	85	

^a Only elements with absolute values $\geq 50\%$ are shown. k_2 is a scale factor.

Table S11 GED coordinates (in Å) for Me₂GaOCH₂CH₂NMe₂ (**30a**).

Atom	<i>x</i>	<i>y</i>	<i>z</i>
C(1)	1.7386	1.9461	3.0477
C(2)	1.2864	4.0551	0.1823
C(3)	-1.7980	3.2018	0.5985
Ga(4)	1.1479	2.3115	1.1653
O(5)	1.1653	0.8031	0.0000
C(6)	0.0000	0.0000	0.0000
C(7)	-1.2717	0.8765	0.0000
H(8)	2.8089	2.0875	3.1493
H(9)	1.2424	2.6141	3.7431
H(10)	1.5042	0.9266	3.3334
H(11)	0.8419	3.9771	-0.8038
H(12)	0.7734	4.8431	0.7225
H(13)	2.3237	4.3478	0.0627
H(14)	-1.3314	3.5688	-0.3090
H(15)	-2.8515	3.0433	0.3960
H(16)	-1.7122	3.9716	1.3573
H(17)	0.0000	-0.6471	-0.8702
H(18)	0.0000	-0.6471	0.8702
H(19)	-2.1480	0.2748	0.2150
H(20)	-1.4029	1.3559	-0.9638
N(21)	-1.1519	1.9401	1.0511
C(22)	-1.5070	1.3876	2.3885
H(23)	-0.8384	0.5709	2.6375
H(24)	-1.4176	2.1628	3.1415
H(25)	-2.5256	1.0156	2.3929

Table S12 Calculated coordinates [MP2(full)/6-311+G*] for Me₂GaOCH₂CH₂NMe₂ (**30a**).

Atom	x	y	z
C(1)	-1.5511	-0.0374	1.8724
C(2)	-1.7348	-0.9389	-1.4900
C(3)	1.4189	-1.8337	-0.5950
Ga(4)	-0.9184	0.0576	0.0037
O(5)	-0.2770	1.7407	-0.5274
C(6)	1.0969	1.8797	-0.3170
C(7)	1.8055	0.5712	-0.6672
H(8)	-2.6077	0.2448	1.9171
H(9)	-1.4773	-1.0455	2.2931
H(10)	-1.0091	0.6461	2.5314
H(11)	-1.1740	-0.8099	-2.4201
H(12)	-1.8247	-2.0110	-1.2886
H(13)	-2.7466	-0.5643	-1.6757
H(14)	1.0163	-1.8076	-1.6072
H(15)	2.4954	-2.0436	-0.6373
H(16)	0.9236	-2.6340	-0.0412
H(17)	1.4999	2.6720	-0.9623
H(18)	1.3297	2.1710	0.7221
H(19)	2.8860	0.5929	-0.4587
H(20)	1.6581	0.3813	-1.7343
N(21)	1.1632	-0.5461	0.0708
C(22)	1.6658	-0.6084	1.4553
H(23)	1.5002	0.3441	1.9563
H(24)	1.1280	-1.3825	2.0037
H(25)	2.7394	-0.8372	1.4614

Energy = -2290.99283 Hartrees (not corrected for ZPE).

Table S13 GED coordinates (in Å) for Me₂GaOCH₂CH₂OMe (**31a**).

Atom	<i>x</i>	<i>y</i>	<i>z</i>
C(1)	1.3657	1.2332	3.1499
C(2)	1.6648	3.8540	0.6273
C(3)	-1.2407	3.3348	0.2398
O(4)	-0.8826	2.0559	0.8478
Ga(5)	1.2104	2.0911	1.3823
O(6)	1.1656	0.8403	0.0000
C(7)	0.0000	0.0000	0.0000
C(8)	-1.2586	0.9073	0.0000
H(9)	2.4228	1.1880	3.4465
H(10)	0.8041	1.8157	3.8933
H(11)	0.9575	0.2141	3.1026
H(12)	1.0769	4.0263	-0.2849
H(13)	1.4486	4.6617	1.3402
H(14)	2.7446	3.8759	0.4247
H(15)	-0.6510	3.4350	-0.6820
H(16)	-2.3117	3.3702	-0.0034
H(17)	-0.9921	4.1595	0.9220
H(18)	0.0000	-0.6523	-0.8842
H(19)	0.0000	-0.6523	0.8842
H(20)	-2.1325	0.3985	0.4301
H(21)	-1.5125	1.2585	-1.0098

Table S14 Calculated coordinates [MP2(full)/6-311+G*] for Me₂GaOCH₂CH₂OMe (31a)

Atom	x	y	z
C(1)	1.6127	-0.5355	1.6742
C(2)	1.4298	1.2764	-1.3481
C(3)	-1.5261	1.9563	0.5392
O(4)	-1.1498	0.5798	0.5478
Ga(5)	0.8318	-0.0939	-0.0729
O(6)	-0.1579	-1.4513	-0.8855
C(7)	-1.3983	-1.6246	-0.2591
C(8)	-2.0912	-0.2783	-0.1276
H(9)	2.6530	-0.8583	1.5709
H(10)	1.6083	0.3283	2.3458
H(11)	1.0613	-1.3434	2.1614
H(12)	0.6288	1.5474	-2.0409
H(13)	1.7874	2.1866	-0.8582
H(14)	2.2565	0.8907	-1.9527
H(15)	-1.5931	2.3287	-0.4874
H(16)	-2.4881	2.0783	1.0436
H(17)	-0.7556	2.5030	1.0807
H(18)	-2.0326	-2.2909	-0.8576
H(19)	-1.3007	-2.0714	0.7444
H(20)	-3.0147	-0.3218	0.4617
H(21)	-2.2955	0.1395	-1.1206

Energy = -2271.63890 Hartrees (not corrected for ZPE).

Table S15 GED coordinates (in Å) for [Me₂GaO^tBu]₂ (**32**).

Atom	<i>x</i>	<i>y</i>	<i>z</i>
Ga(1)	0.0000	0.0000	1.4994
O(2)	-1.2922	0.0000	0.0000
O(3)	1.2922	0.0000	0.0000
Ga(4)	0.0000	0.0000	-1.4994
C(5)	-2.7074	-0.2896	0.0000
C(6)	-3.3105	0.2876	-1.2935
C(7)	-2.9394	-1.8089	0.0000
C(8)	-3.3105	0.2876	1.2935
H(9)	-3.1535	1.3791	-1.3389
H(10)	-2.8363	-0.1708	-2.1784
H(11)	-4.3952	0.0885	-1.3358
H(12)	-2.4865	-2.2684	0.8955
H(13)	-4.0197	-2.0343	0.0000
H(14)	-2.4865	-2.2684	-0.8955
H(15)	-4.3952	0.0885	1.3358
H(16)	-2.8363	-0.1708	2.1784
H(17)	-3.1535	1.3791	1.3389
C(18)	2.7074	0.2896	0.0000
C(19)	2.9394	1.8089	0.0000
C(20)	3.3105	-0.2876	1.2935
C(21)	3.3105	-0.2876	-1.2935
H(22)	2.4865	2.2684	-0.8955
H(23)	2.4865	2.2684	0.8955
H(24)	4.0197	2.0343	0.0000
H(25)	3.1535	-1.3791	1.3389
H(26)	4.3952	-0.0885	1.3358
H(27)	2.8363	0.1708	2.1784
H(28)	4.3952	-0.0885	-1.3358
H(29)	3.1535	-1.3791	-1.3389
H(30)	2.8363	0.1708	-2.1784
C(31)	-0.0113	-1.7202	-2.4494
H(32)	-0.9215	-1.8725	-3.0547
H(33)	0.8125	-1.7855	-3.1809
H(34)	0.0797	-2.5686	-1.7493
C(35)	0.0113	1.7202	-2.4494
H(36)	-0.0797	2.5686	-1.7493
H(37)	0.9215	1.8725	-3.0547
H(38)	-0.8125	1.7855	-3.1809
C(39)	-0.0113	-1.7202	2.4494
H(40)	0.8125	-1.7855	3.1809
H(41)	-0.9215	-1.8725	3.0547
H(42)	0.0797	-2.5686	1.7493
C(43)	0.0113	1.7202	2.4494
H(44)	0.9215	1.8725	3.0547
H(45)	-0.0797	2.5686	1.7493
H(46)	-0.8125	1.7855	3.1809

Table S16 Calculated coordinates [MP2(full)/6-311+G*] for [Me₂GaO^tBu]₂ (**32**).

Atom	<i>x</i>	<i>y</i>	<i>z</i>
Ga(1)	0.0000	0.0000	1.5216
O(2)	-0.0868	1.2485	0.0000
O(3)	0.0868	-1.2485	0.0000
Ga(4)	0.0000	0.0000	-1.5216
C(5)	-0.5509	2.6094	0.0000
C(6)	0.0000	3.2857	-1.2493
C(7)	-2.0759	2.6341	0.0000
C(8)	0.0000	3.2857	1.2493
H(9)	1.0904	3.2109	-1.2703
H(10)	-0.3997	2.8189	-2.1553
H(11)	-0.2789	4.3433	-1.2724
H(12)	-2.4688	2.1291	0.8856
H(13)	-2.4449	3.6648	0.0000
H(14)	-2.4688	2.1291	-0.8856
H(15)	-0.2789	4.3433	1.2724
H(16)	-0.3997	2.8189	2.1553
H(17)	1.0904	3.2109	1.2703
C(18)	0.5509	-2.6094	0.0000
C(19)	2.0759	-2.6341	0.0000
C(20)	0.0000	-3.2857	1.2493
C(21)	0.0000	-3.2857	-1.2493
H(22)	2.4688	-2.1291	-0.8856
H(23)	2.4688	-2.1291	0.8856
H(24)	2.4449	-3.6648	0.0000
H(25)	-1.0904	-3.2109	1.2703
H(26)	0.2789	-4.3433	1.2724
H(27)	0.3997	-2.8189	2.1553
H(28)	0.2789	-4.3433	-1.2724
H(29)	-1.0904	-3.2109	-1.2703
H(30)	0.3997	-2.8189	-2.1553
C(31)	-1.7538	-0.1926	-2.3936
H(32)	-2.0433	0.6999	-2.9573
H(33)	-1.7465	-1.0269	-3.1023
H(34)	-2.5345	-0.3919	-1.6540
C(35)	1.7538	0.1926	-2.3936
H(36)	2.5345	0.3919	-1.6540
H(37)	2.0433	-0.6999	-2.9573
H(38)	1.7465	1.0269	-3.1023
C(39)	-1.7538	-0.1926	2.3936
H(40)	-1.7465	-1.0269	3.1023
H(41)	-2.0433	0.6999	2.9573
H(42)	-2.5345	-0.3919	1.6540
C(43)	1.7538	0.1926	2.3936
H(44)	2.0433	-0.6999	2.9573
H(45)	2.5345	0.3919	1.6540
H(46)	1.7465	1.0269	3.1023

Energy = -4471.60983 Hartrees (not corrected for ZPE).